UNIVERSITÀ DEGLI STUDI DI MILANO

SCUOLA DI DOTTORATO
TERRA, AMBIENTE E BIODIVERSITÀ

DIPARTIMENTO DI SCIENZE DELLA TERRA
"Ardito Desio"

Dottorato di Ricerca in Scienze della Terra
Ciclo XXVI

STRUCTURE AND PETROGENESIS OF PLAGIOCLASE-BEARING MANTLE PERIDOTITES FROM THE ROMANCHE TRANSFORM (EQUATORIAL ATLANTIC OCEAN)

GEO/07

Domitilla Santi
Matricola R09363

Tutor **Prof.ssa Paola Tartarotti**

Co-tutor: **Dott. Daniele Brunelli**

Coordinatore: **Prof.ssa Elisabetta Erba**

A.A. 2012/2013

Index

Abstract

The Romanche Fracture Zone is a lens-shaped, 900 km-long, 100 km-wide multifault deformation zone, the major transform fault that offsets the Equatorial Mid-Atlantic Ridge and one of the longest of the worldwide ridge system. It looks different from "classic" oceanic transform boundaries, which are characterized by a single, few-kilometers-wide, strike-slip deformation zone, so that it has been defined as "megatransform" plate-boundary (Ligi et al., 2002). The Romanche FZ peridotites represent residua of a relatively cold mantle related to a strong cold edge effect, an possibly regional lower mantle temperatures, hence experiencing among the lowest degrees of melting (<10%) of the whole mid-ocean ridge system, in which frequently part of the percolating melts may be retained and crystallize within the lithospheric mantle (Seyler & Bonatti, 1997; Bonatti et al., 2001; Tartarotti et al., 2002).

Textural, geochemical and petrological data of abyssal plagioclase-bearing peridotites sampled in the central and western parts of the Romanche FZ during the oceanographic expedition PRIMAR-96 (Russian R/V Gelendzhik) are here reported. Petrography reveals that rocks of Group1 and Group2 represent mantle residua showing protogranular to porphyroclastic textures possibly with relics of equigranular textures, developed during upwelling throughout asthenospheric and lithospheric environments simultaneously to melting and melt percolation. These textures appear to have been diffusively superimposed by further, deep melt percolation at the shallowest levels in mantle, leading to crystallization of large amounts of plagioclase (up to 16%) and new clinopyroxene from the trapped melts. As melting ceases when mantle approaches the conductive layer of the lithosphere, in fact, continuous melt supply from deeper levels by diffuse porous flow results in reactive impregnation, which may start in the shallowest levels of the spinel stability field and then proceeds in the plagioclase stability field, leading to crystallization of new minerals pockets, made of (cpx+ol) or (plag+cpx) depending on pressure conditions. New mineral pockets will exploit the rock porosity, i.e. zone of pervasive grain-size reduction developed in asthenospheric environments, and lithospheric brittle/ductile deformation structures, e.g. fractures, gashes, kink bands, micro-faults. Reactive impregnation may involve total amounts of impregnating melts up to 25%.

Major and trace elements of fresh minerals (ol, opx, opx, cpx, sp and pl) have been determined by EMPA and LA-ICP-MS techniques. Geochemistry attests for the rims of the coarser-grained pyroxene to have equilibrated in the plagioclase stability field. Trace elements modeling allows to determine the degree of melting of the peridotites and compositions of the melts which percolated the rock source during its melting

and post-melting histories. Percolating melts pertain to two main compositional families, namely: i) enriched melts relatively aggregated with strongly variable garnet fingerprint and ii) markedly depleted melts. Degrees of melting from 8% to 14% have been inferred for rocks of Group1 and Group2; this suggest plagioclase-bearing peridotites of the Romanche FZ to be the result of refertilization of previously depleted peridotites rather than pure residues after low degree of partial melting, therefore the observed scarcity of erupted basalts at the seafloor in this region (Bonatti et al., 2001) may be due to strong melt retention rather than low melt production. This is in contrast with sample of Group3, which attests for significant degrees of melting (18% according to modeling) combined with very low melt retention and weak, nearly negligible post-melting reactive impregnation, suggesting efficient mechanisms of melt production and extraction, thus a scenario more similar to channeled melt transport rather than diffuse porous flow. This type of rock may thus represent an example of efficiently channelized melt extraction that early collects deep melts and re-distributes them partially into the rock, resulting in E-MORB extrusion at the seafloor with significant garnet-fingerprint (Ligi et al., 2005), confirming that channelization of deep melt portions can be strongly efficient from the early melt stages in the deep regions.

Chapter 1
Geological background

1.1 Equatorial Atlantic

The equatorial region of the Atlantic Ocean is geologically peculiar. The axis of the Mid Atlantic Ridge (MAR) is broken in short (200 km), roughly N-S trending, segments separated by closely-spaced, long offset (>300 km), E-W transform faults, forming altogether an east-west megashear belt (about 2000 km of total offset, fig. 1.1.1). This is clearly seen in satellite radar altimetry elaborations or in maps reporting the distribution of earthquakes epicenters. They include: the St. Paul, the Romanche and the Chain fracture zones (FZ). The largest transform is the Romanche FZ (about 900 km offset), located very close to the equator. The St. Paul transform (offset about 400 km) is located between 1°N and 2°N, i.e. roughly 180 km north of the Romanche, whereas the Chain FZ (offset about 300 km) is located about 180 km south of the Romanche (fig. 1.1.2).

Each of these transforms has a strong topographic signature, generally a deep transform valley bordered by prominent transverse ridges. Transverse ridges constitute major topography anomalies relative to the thermal subsidence curve for the oceanic lithosphere. The topographic signature of each of these major transforms can be traced outside the ridge/ridge offset, and can be shown to extend as fracture zones from one side to the other of the Atlantic. Given the above, the equatorial Atlantic may be considered as a large latitudinal megashear zone that crosses the ocean from coast to coast.

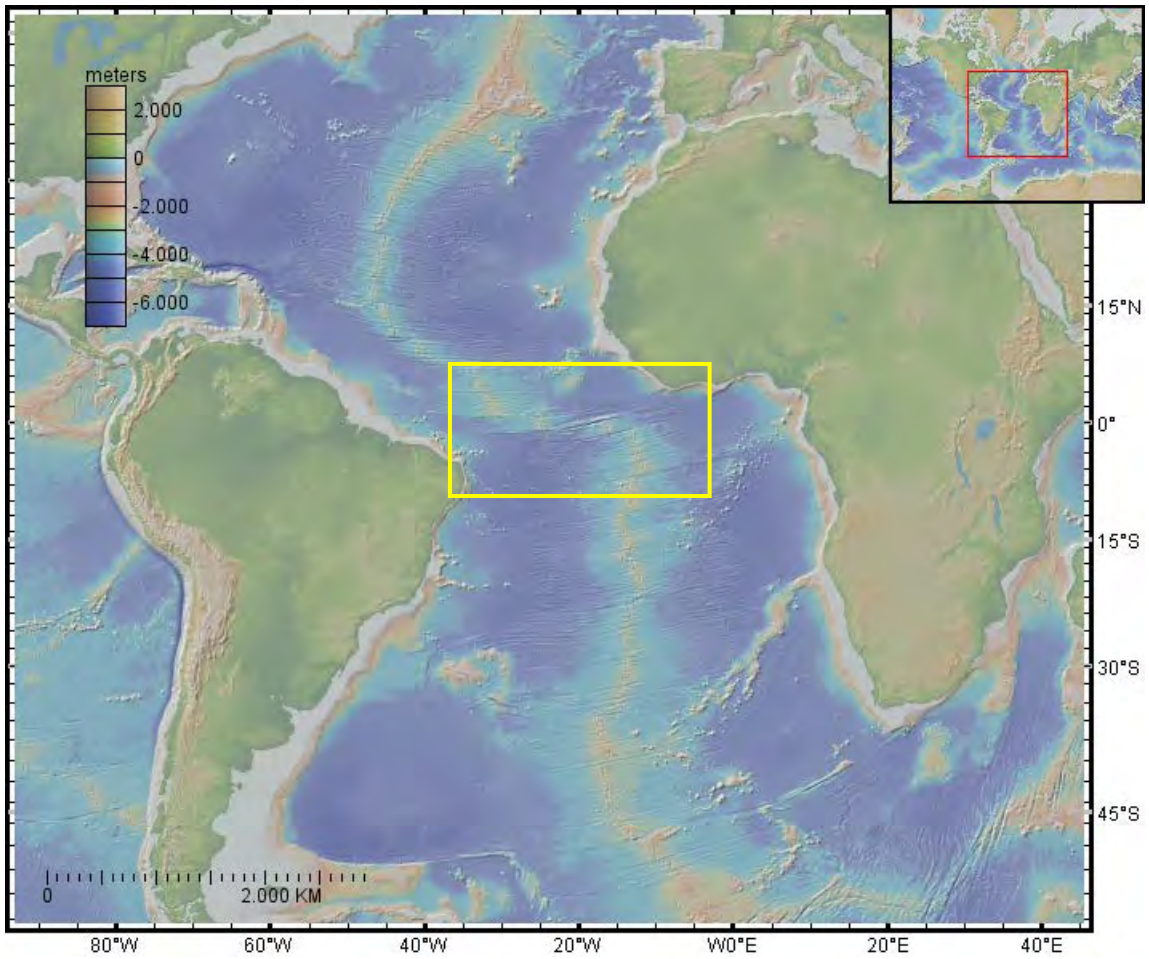

Fig. 1.1.1 - Bathymetric and topographic map of Atlantic ocean. The Equatorial Atlantic in the yellow rectangle. (From GeoMapApp©).

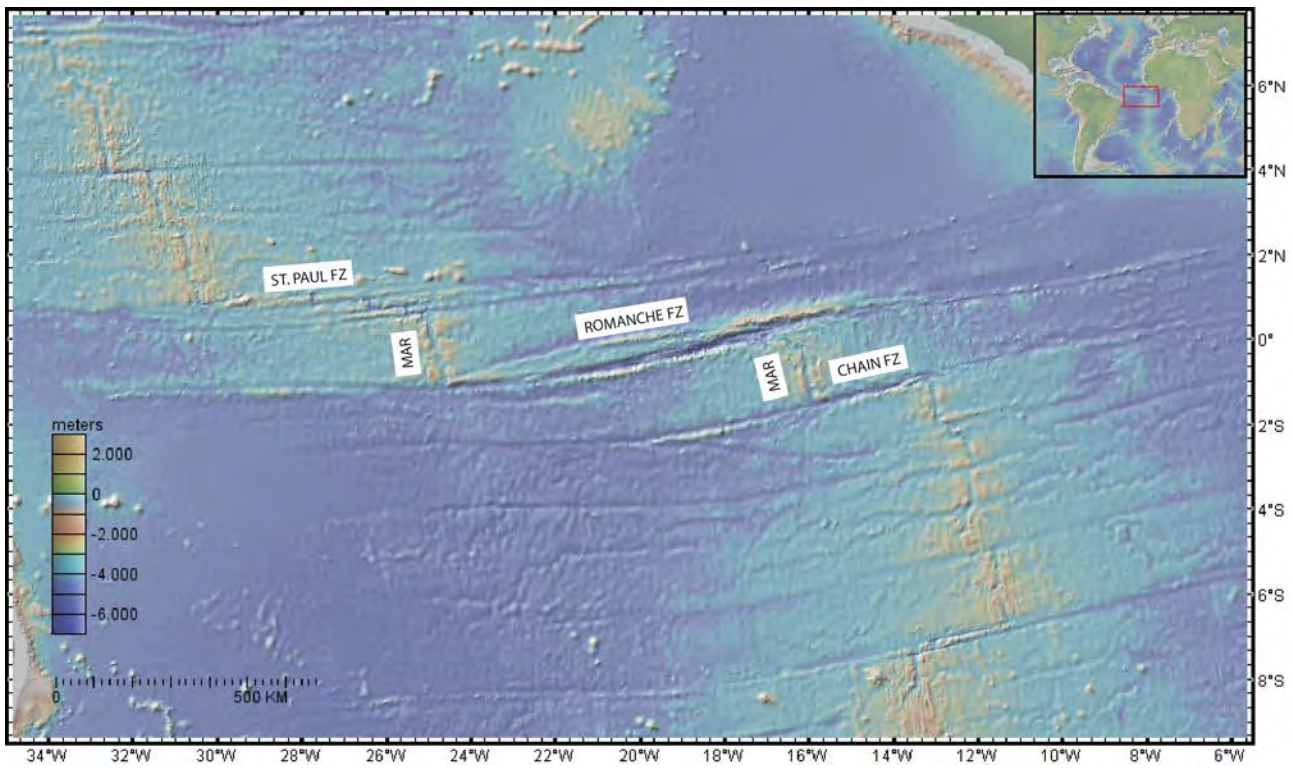

Fig. 1.1.2 - Bathymetric and topographic map of equatorial Atlantic ocean, which comprises St. Paul FZ, Romanche FZ and Chain FZ. MAR means Mid-Atlantic Ridge. (from GeoMapApp©).

1.2 The Romanche Fracture Zone

In the first half of the 90s three oceanographic expeditions were carried out to the Romanche FZ: PRIMAR I and PRIMAR II (in 1991 and 1992, respectively) cruises, by R/V A.N. Strakhov and G96 Cruise by the R/V Gelendzhik (1996). These works were carried out in the frame of the Russian-Italian Mid-Atlantic Ridge Project (PRIMAR) in which Russian Academy of Sciences of Moscow and Bologna's Institute of Marine Geology (IGM) of the Italian Research Council (CNR) collaborated. Broadly, the first two expeditions focused on the eastern part of the transform zone and the second one mainly focused on the western part. In order to identify and describe the main morphostructures of the Romanche transform, during such expeditions morphobathymetric, magnetometric, seismic reflection, gravimetric data and rock samples were collected, whose results and interpretations can be consulted in many publications (Bonatti et al., 1991, 1994, 1996a and 1996b; Gasperini et al. 1997a and 1997b; Ligi et al., 2002; Tartarotti et al., 2002) and integrated with others previous works (Monti and Mercier, 1991; Honnorez et al., 1991; Searle et al., 1994; Heezen et al. 1964; Gorini, 1977; Chermak, 1979).

The Romanche FZ (fig. 1.2.1) is the largest transform fault that offsets the equatorial MAR and one of the major structures of the entire world ridge system. It is a lens-shaped, 900 km-long, 100 km-wide multi-fault deformation zone characterized by a deep, roughly E-W trending valley flanked on both sides by two prominent ridges and by a system of secondary parallel troughs and ridges (Heezen et al., 1964; Gorini,1977; Chermak, 1979). The tips of the lens-shaped deformed region correspond to the eastern and western ridge - transform intersections (RTI).

The Romanche transform has an average half spreading rate of 17 mm/yr (slow ridge) according to Cande et al. (1988), thus a corresponding age offset of ~52 My (Bonatti et al., 2001). This means that the oceanic crust fronting each ridge axis is aged of about 50 My, and it is thus formed by a thick (about 30 km) cold lithosphere. The Romanche transform can be traced by satellite gravimetry to the South American and African continental margins, with approximately east-west offsets of the coast-lines. Hence, the Romanche has acted as a transform plate boundary since the early stages of continental separation.

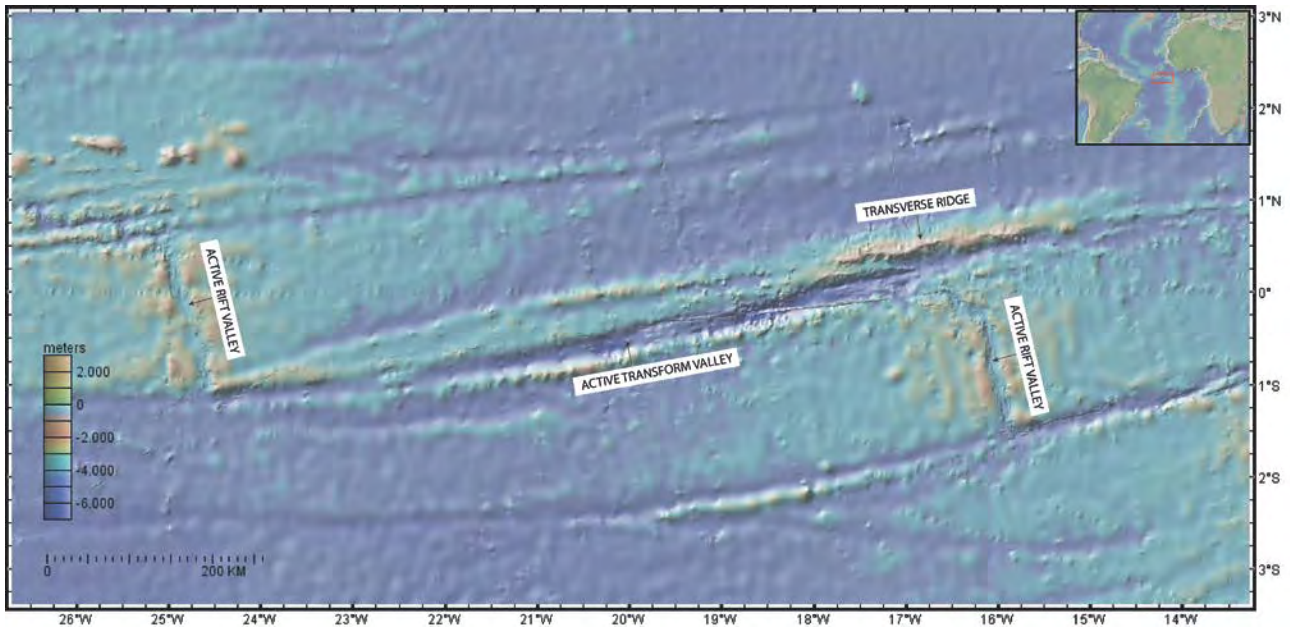

Fig. 1.2.1 - Bathymetric and topographic map of Romanche FZ (from GeoMapApp©) and location of the active main boundaries and the transverse ridge.

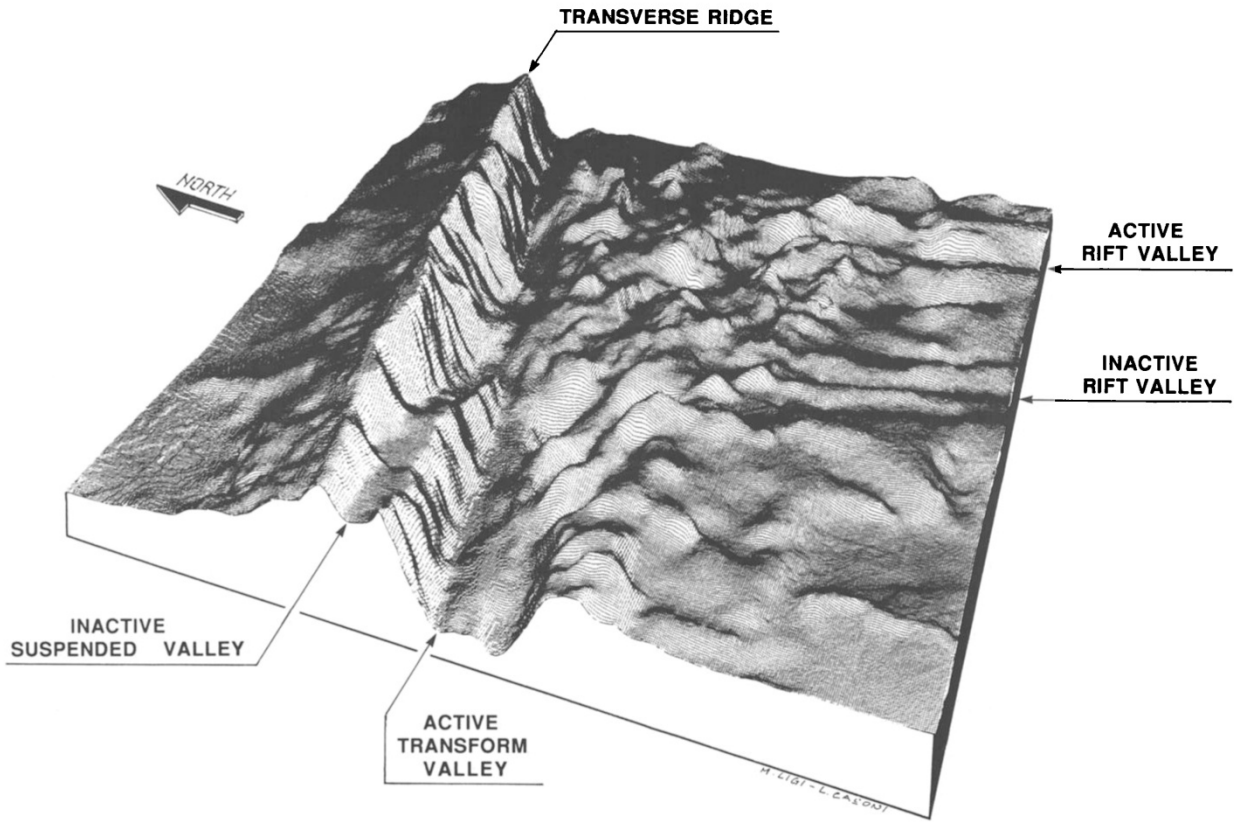

Fig. 1.2.2 - Three-dimensional morphobathymetric image of the eastern part of the Romanche transform. Vertical exaggeration is about 12.5 times. (From Bonatti et al., 1994).

1.2.1 The southern valley and the northern valley: the active transform boundary

The southern valley is the major valley of the Romanche system, and it joins the two ridge-transform-intersections in the southern part of the deformed region. North of this valley there is another valley (the northern valley) which extends into the northern part of the deformed region. The northern and the southern valleys are not parallel, but their orientation differs by up to about 15° (fig. 1.2.2). The southern valley is roughly E-W striking and towards the eastern part it turns to ENE-WSW striking; its width ranges from 20 km in the western part to 60 km in the eastern part. Its depth reaches 5000 m below sea level in the western RTI, whereas in the eastern RTI it reaches 5500 m below sea level. The deepest part of the valley, reaching about 7.8 km below sea level, is located between 18° and 19° W (7856 m below sea level at 18°30' W). The northern valley extends for about 800 km from the vicinity of the eastern RTI to about 150 km from the western MAR segment. Its eastern part is suspended on the southern slope of the major transverse ridge and converges with the southern valley, both merging in the eastern RTI area. Sketches of the topographic and tectonic setting of the Romanche transform are shown in figs. 1.2.1.1 and 1.2.1.2. In these figures, the main morphostructures so far recognized and defined by Authors are reported. Descriptions of these morphostructures are described in the following.

Based on earthquakes distribution in the Romanche area, covering more or less the last forty years (Bohnenstiehl et al., 2000; McGuire et al., 1996; Forsyth et al., 1986) argued that the southern valley marks the present-day principal transform boundary, which is characterized by right-lateral strike-slip motion on east-west faults, as suggested by the focal mechanism of the earthquakes (McGuire et al., 1996; Forsyth et al., 1986). However, although most of earthquake epicenters are recorded along the southern valley, a lower seismicity affects the northern valley, maybe partly triggered by earthquakes of the principal boundary, suggesting present-day strike-slip motion also in correspondence of the northern valley. Moreover, multichannel seismic reflection profiles, collected near some of the largest past earthquakes, show recent extension normal to the transform, i.e. transtension.

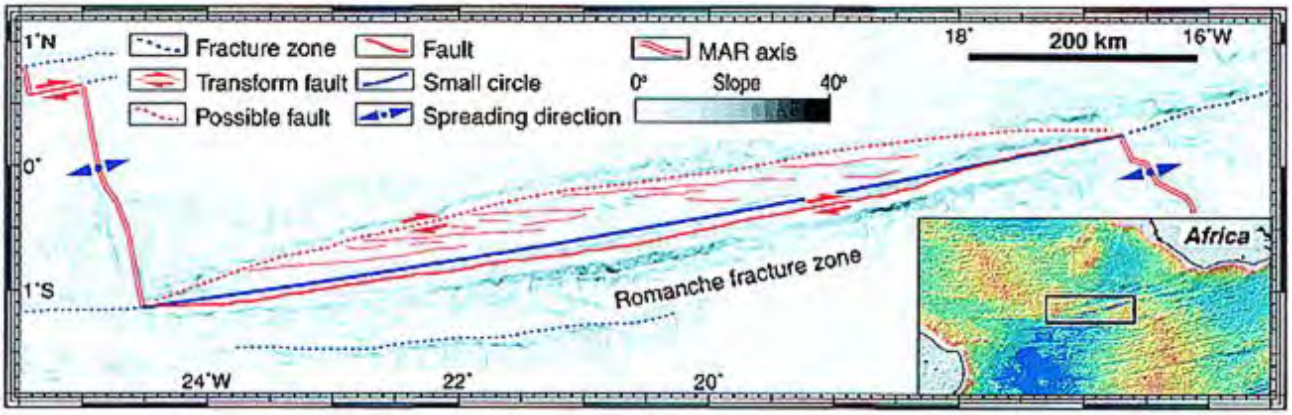

Fig. 1.2.1.1 - Map of maximum topographic slopes and sketch of the structural setting of the area. Predicted bathymetry of equatorial area is shown in inset. (From Ligi et al., 2002)

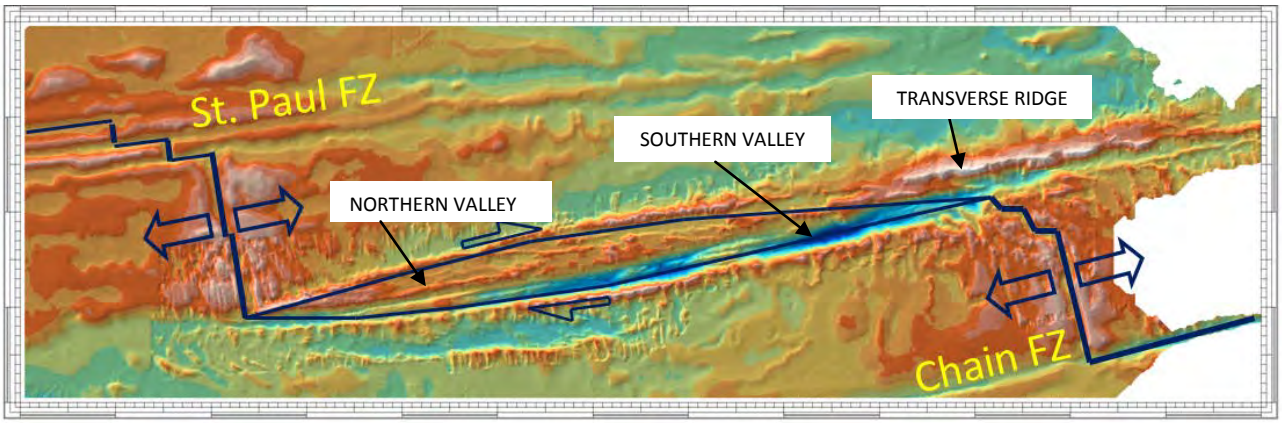

Fig. 1.2.1.2 - Sketch of the active transform boundary of the Romanche FZ: trace of the present-day main inferred deformation zones (blue line) and position of the northern and the southern valleys and the major transverse ridge. Shaded relief map based on multibeam coverage obtained during cruises G-96 (R/V Gelendzhik), and S-13, S-16, and S-19 (R/V Akademik Strakhov) and those of Monti and Mercier (1991). Depth ranges from 7800 m (dark blue) to 1000 m (light gray). Mercator projection at 08. (From Ligi et al., 2002). (Scale: see fig. 1.2.1.1).

This morphotectonic scenario affecting the Romanche area lead Ligi and coauthors (2002) to infer a ridge-ridge broad diffuse transform boundary consisting of a semistationary deformed microplate with strike-slip motion distributed mainly along two major faults, one of which prevails at present (the southern one). Thus, they suggested that the Romanche FZ can be defined as a "megatransform", i.e. a complex multiple oceanic transform boundary, rather than a "classic" oceanic transform boundary (Wilson, 1965), i.e. a single, few-kilometers-wide strike-slip deformation zone (Fox and Gallo, 1984). Another example of "megatransforms" is the Andrew Bain FZ (Grindlay et al., 1996; Sclater et al., 1998), in correspondence of which the Southwest Indian Ridge is offset by an 750-km-long, 120-km-wide, lens-shaped transform zone (fig. 1.2.1.3). The slip rate is 15 mm/yr, therefore, the age offset is 100 m.y. The Romanche and Andrew Bain transforms show length/width ratios lower than what is observed in "normal" oceanic transforms, being instead within the range of continental strike-slip deformation zone (i.e. 5-10; England et al., 1985). According to numerical modeling, the development of such wide multiple, lens-shaped transform boundaries may occur when the

age offset is above the threshold value of about 30 m.y., i.e. in extra long (>500 km) slow-slip transforms (Ligi et al. 2002).

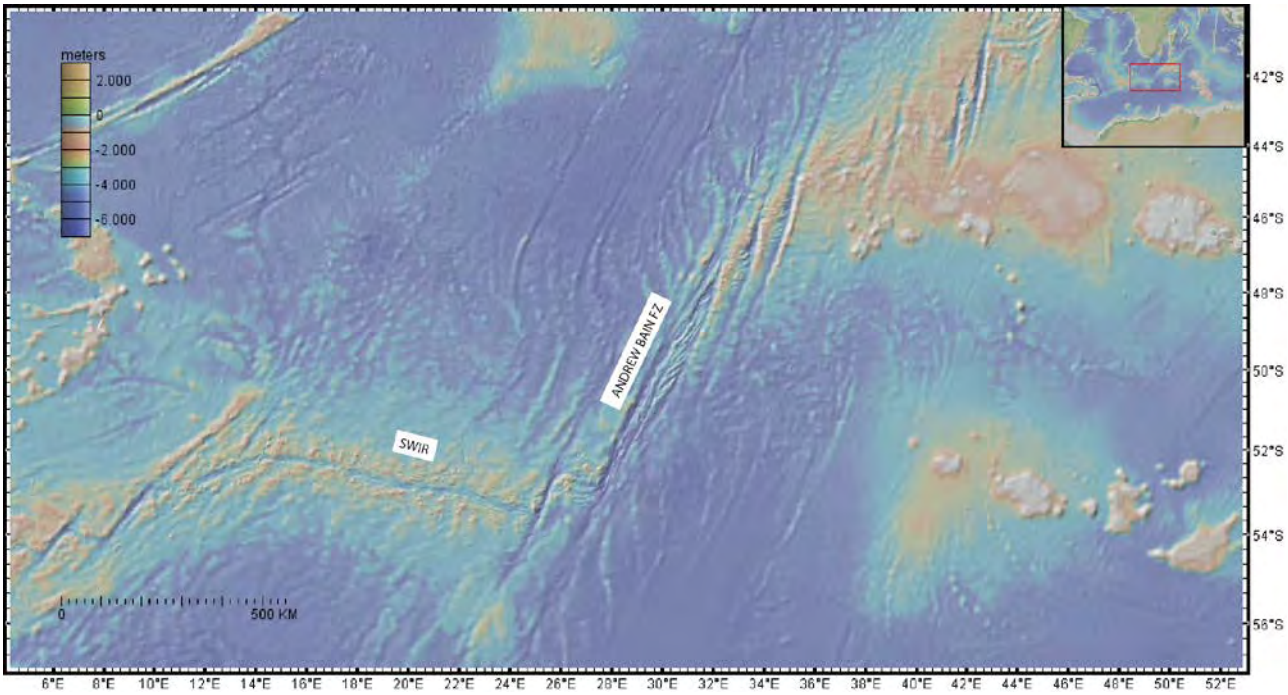

Fig. 1.2.1.3 - Bathymetric and topographic map of Andrew Bain FZ, Southwest Indian Ridge (from GeoMapApp©).

The fact that at present the northern valley contains as much as 1 km of turbiditic sediments, whereas only 300 m are observed in the southern valley, may suggest that the former is older than the latter; Bonatti et al. (1994) proposed as a possible interpretation that the northern valley is the trace of an earlier transform boundary (the PaleoRomanche) that ceased to be active about 8-10 Ma, and then migrated and rotated towards the present position of the southern valley. According to Searle's method (1981), Bonatti and coauthors (1994) calculated that the best fit pole of rotation relative to the PaleoRomanche is at 75° 20'N and 62° 77'W. The geotectonic upheaval related to this process involved other important events, such as ridge propagation on the western RTI, ridge jumping on the eastern RTI and the uplift of lithospheric blocks (the major transverse ridge).

1.2.2 The transverse ridge

In the Romanche F.Z., the most prominent topographic anomaly is represented by the transverse ridge located near the eastern Ridge-Transform Intersection (E-RTI; fig. 1.2.2). This transverse ridge propagates up to 6°30'W and it is characterized by a set of roughly E-W elongated peaks (Gasperini et al., 1997 (b) and 2001), in correspondence of which it reaches the shallowest depth of the whole transform system (up to 900 m below sea level, i.e. less than 2000 m below sea level), that corresponds to ≈ 4 km above the depth

predicted by the thermal contraction depth age law (fig. 1.2.2.1) (Bonatti and Chermak, 1981; Bonatti et al., 1993 and 1996b). Some authors indicated that the summit of the transverse ridge was above the sea level up to about 5 m.y. before present and subsided since then at a rate one order magnitude faster than the plate thermal subsidence rate (Bonatti et al. 1979, Bonatti and Chermak 1981).

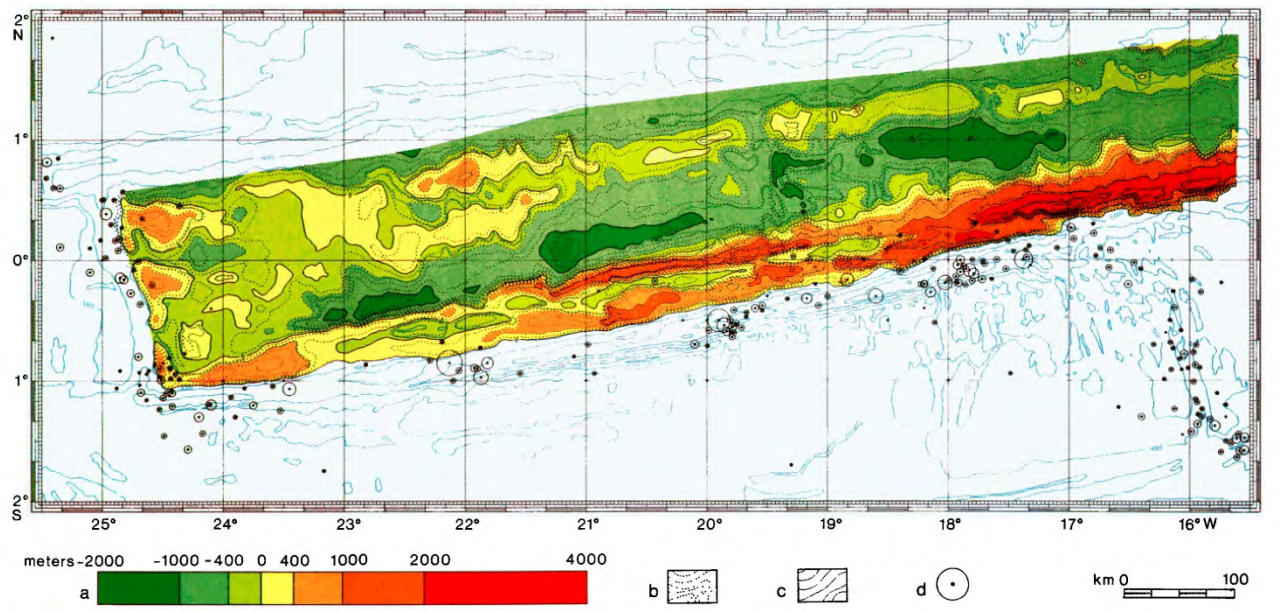

Fig. 1.2.2.1 - Topographic anomaly contour map relative to the theoretical thermal contraction level of the crust (Parsons and Sclater, 1977) for the northern side of the Romanche transform. a) Range of topographic anomalies (in meters) plus or minus the theoretical level; b) isoanomaly curves (in meteres), interval 200 m; c) bathymetric curves (in meters), interval 1000 m; d) earthquakes epicenters, 1960-1990. (From Bonatti et al., 1994)

The transverse ridge flanks the northern slope of the transform and is characterized by an asymmetric profile (Fig. 1.2.2): its north-facing slope appears less steep than the south-facing one, which is interrupted by a suspended valley (the northern valley) striking about 10°-15° from the present active transform valley (the southern valley).

Bonatti and coauthors (1994) interpreted the transverse ridge as a sliver of lithosphere which underwent vertical tectonism during the process of transform migration. Alternating transpressional and transtensional events - related to non-straight transform boundaries and non-steady state ridge-transform-ridge geometries, and involving slight changes in the direction of spreading - caused respectively the uplift of the transverse ridge above sea level (up to about 5 m.y ago) and then active subsidence to the present-day level. This is consistent with Bonatti et al. (1994) and Ligi et al. (2002) who found evidences of recent transtensional motion in this area.

On the basis of high resolution seismic reflection and multibeam detailed surveys and study of rock samples, Gasperini and coauthors (1997b) proposed a stratigraphic and paleoenvironmental reconstruction of the transverse ridge peak "A" (the one on the west), providing for a shallow-water, 300-400-m-thick carbonate platform lying on the sub-horizontal surface of the basement, constituted by oceanic crust. Given that,

according to ages derived from microfossils, the base of the carbonate platform dates from 17-25 m.y. ago and the sinking of the platform started between 18 and 13 m.y., estimates of tectonic subsidence rates range between 0.03 and 0.04 mm/yr, starting in an age ranging from 20 to 21 Ma, whereas the estimated average thermal cooling rate of subsidence is 0.028 mm/yr. Being the former significantly higher than the latter, thermal cooling alone cannot cause the fast sinking of the transverse ridge as well as its strong uplift: other mechanisms must be took in account, such as aforementioned transform related vertical tectonics due to transpression and transtension (Bonatti et al., 1994).

From multichannel seismic reflection profiles and rock sampling emerged that east of about 15°30', roughly 100 km east from the eastern RTI, the transverse ridge is capped by a >4 km-thick and >200 km-long sedimentary sequence (the Romanche Sedimentary Sequence, RSS; Bonatti et al., 1996 a), including Mayolica-type pelagic limestones with calpionellids of Lower Creataceous (about 140 Myr), and an overlying unit of continent-derived quartzitic siltstones of Middle Paleocene and Middle Eocene age (Bonatti et al., 1996a; Gasperini et al., 2001). On the other hand, according to paleogeographic reconstructions, the equatorial Atlantic Ocean basin started to open in the Cretaceous period, not earlier than 120 Myr ago (Rabinowitz and LaBrecque, 1979; Cande et al., 1988; Nürnberg and Müller, 1991); in addition, the predicted age of the oceanic crust below this unit should be not older than 60 Myr. The contradictory finding of the 140 Myr deposit could thus explaned by two mechanism (Gasperini et al., 2001): 1) oscillatory spreading (Bonatti and Crane, 1982), by which, due to following migration and reorientation events of an oceanic transform boundary, a block of lithosphere may be transferred from one plate to another adjacent plate, thus reversing its direction of motion. Actually, the Romanche FZ probably underwent transform boundary migration and rotation, as mentioned above (Bonatti et al., 1994); 2) the broad multiple transform system affecting the Romanche FZ (and other *megatransforms*, e.g. Andrew Bain FZ), which may have led to the development of a semistationary microplate located between the African and the South American plates (thus providing ages older than those predicted by standard sea-floor spreading models).

1.2.3 The Romanche Ridge-Transform Intersections

The southern part of the MAR segment between the Romanche and the Chain transforms is traced by a well developed axial rift valley, which gradually fades out moving northward to the intersection with the Romanche transform (i.e., the E-RTI). According to Monti and Mercier (1991), Mamaloukas-Frangoulis (1992), and Searle et al. (1994), at 80 km from the transform, the ridge is replaced by a set of short, oblique (about 25°) en echelon segments. Before reaching the transform valley, at 30 km from it, from 17° to 17°10'W, these en echelon segments completely disappear. Therefore, a ridge-transform intersection lacking a well-defined morphological signature is resulting in the eastern part of the fracture zone. Furthermore, given that: *i)* magnetic anomalies are subdued or absent in the equatorial region; *ii)* a diffuse seismicity affects this area; *iii)* the basaltic coverage is scant; *iv)* an active nodal deep (namely the typical topographic

depression occurring where the rift valley enters the transform valley) and an inner corner high (namely a topographic high commonly observed at the transform side of the rift valley as it approaches the transform valley) were not identified, then it's hard to locate unequivocally the spreading center opening into the transform valley and where they intersect each other, in contrast with the well-developed RTIs observed in other Atlantic transforms. For these reasons Bonatti et al. (1996a) proposed a diffuse rifted zone rather than a normal rifted axis of spreading at the E-RTI. However, Bonatti and coauthors (1994) had tried to identify the E-RTI at about 16°30'W, and argued that the well-formed aseismic valley opening into the transform valley about 80 km west of the inferred location of the present RTI was probably a fossil axial valley, strengthening the hypothesis of an eastwards RTI-and-ridge-jumping within the last 3-4 m.y., that followed the transform migration from the PaleoRomanche to the present active transform valley. We cannot exclude that the presently E-RTI area represents an embryonic stage of development and that a new portion of ridge axis is going to establish and to propagate towards the transform.

The MAR segment between the Chain and the Romanche FZ is over 4 km below sea level, i.e. significantly deeper than the "normal" zero-age level reached by the MAR outside the equatorial region. Moreover, moving along the segment, approaching the E-RTI of the Romanche, the seafloor appears to shallow slightly, then it drops precipitously when it reaches the edge of the transform valley. This contrasts with the gradual deepening of the same ridge segment as it approaches the Chain FZ to the south and with the common behavior of other long offset/slowly slipping oceanic transforms (Fox and Gallo, 1984). For example, in a transform with an age offset of 20-25 m.y. such as Vema FZ, this deepening is roughly 1 km per 30 km horizontally (Phipps Morgan and Forsyth, 1988), whereas the 30-km-wide band of the seafloor at the edge of the Romanche transform valley is slightly more elevated than the area farther away from the transform. In addition, this area shows a scanty basaltic crust and the dominance of mantle-derived ultramafics (Bonatti and Honnorez, 1976). These effects are related to the juxtaposition of a thick lithospheric edge against a hot ridge axis tip, that causes the cooling and thus the thermal contraction of the sub-ridge upper mantle near the RTI (the so called transform cold edge effect) and the reduction of the production of melt, that results in the topographic lowering of the ridge axis (Fox and Gallo, 1984; Forsyth and Wilson, 1984). According to thess mechanism, the higher the age offset of the transform, i.e. the age contrast of juxtaposed lithosphere at the RTI, the higher the extent of deepening of a ridge segment approaching a RTI. In addition, the thermal structure of the upper mantle beneath the equatorial Mid Atlantic Ridge appears to be affected by a negative thermal anomaly, centered in the region between the St. Paul and the Chain fracture zones (Bonatti et al., 1996b; Schilling et al., 1995). On the other hand, the ridge segment lacks of topographic deepening of the ridge axis towards the Romanche E-RTI, despite the large age offset (about 50 m.y.): this anomaly has been interpreted as due to massive serpentinization of the mantle peridotite layer exposed on the seafloor, in absence of the "protection" of an overlying basaltic coverage, with consequent decrease of density and possible increase of volume (Bonatti et al., 1996b).

The western part of the Romanche transform (W-RTI) was poorly known until the G96 expedition was carried out in 1996 (Gasperini et al. 1997a). It came to light the presence of an equally complex system of

transverse ridges and valleys that represent en echelon transtensional zones. This area is characterized by a prominent east-west, >200-km-long scarp, south of the lens-shaped deformed zone, that probably marks another older fossil transform (Ligi et al. 2002). As it was observed at the eastern RTI, the western RTI lacks some of the typical features observed at RTIs of other oceanic transforms, i.e. high inside corner and nodal deep.

1.3 Sampling

The studied samples were collected during the G96 Cruise of the R/V Gelendzhik, carried out in May and June 1996 by the Russian-Italian Mid-Atlantic Ridge Project (PRIMAR) in which the Russian Academy of Sciences in Moscow and the Bologna's Institute of Marine Geology (IGM) of the Italian Research Council (CNR) have collaborated.

Dredge stations were located in the central and the western part of the Romanche transform, except for dredge #27 which was carried out to the east of the eastern RTI.

The most relevant morphostructures related to the transform domain have been sampled, i.e. the active transform zone and its western intersection with the MAR; the inactive western sector; the north and south paleo-transform zones, and transverse ridges. Dredges #29 through #36 were located along a narrow, north-south trending profile near 21° W between 0° and 1° S, in order to investigate the three main transform structures, i.e. the north and south paleo-Romanche and the active Romanche F.Z. Twenty dredge stations were carried out during this expedition. The sampled rocks include (Table 1.3.1): serpentinized peridotite, gabbro, basalt, dolerite, metasomatic rocks, limestone, serpentinite breccia, gabbro breccia, basaltic breccia, hyaloclastite breccia, sedimentary breccia, ophicalcite breccia. The most widespread lithological types are peridotite and basalt.

The samples studied in this thesis consist only of peridotite and pertain to dredge #32, #33 and #39 (Fig. 1.3.1 and Table 1.3.1).

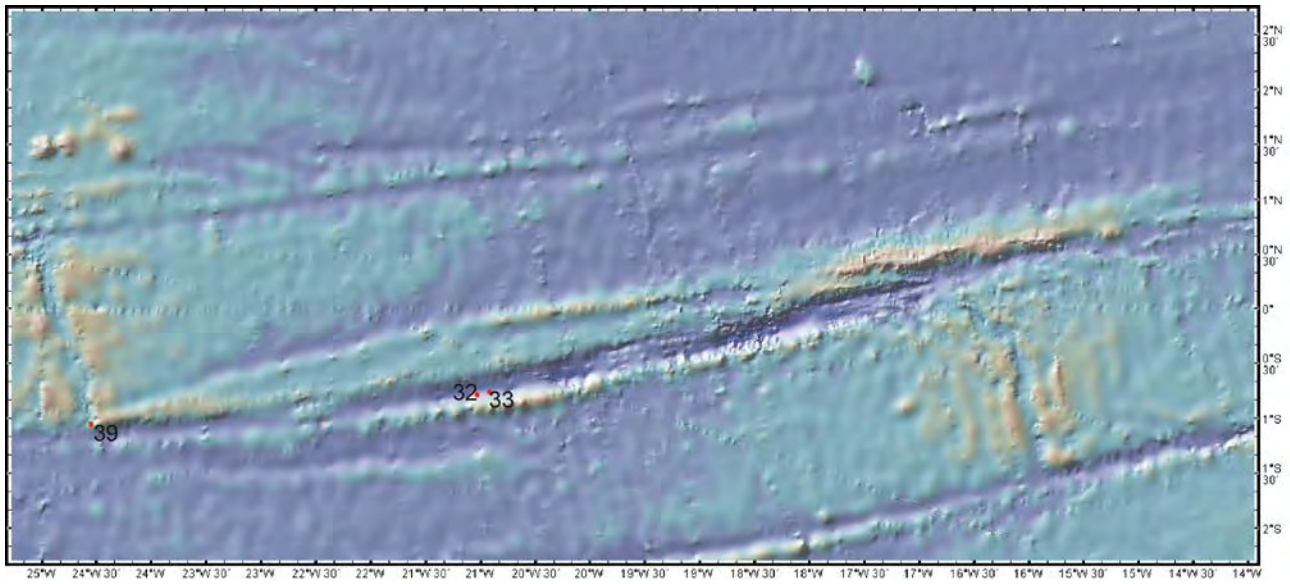

Fig. 1.3.1 - Dredging site position of the studied samples: dredges #32, #33 and #39.

Table 1.3.1 - Dredging of G96 CRUISE

LOCATION		DREDGES #	LITHOLOGY
northern paleo-Romanche	north wall	36, 45	ophicalcite breccia
	south wall	35	basalts
Romanche FZ	north wall	34	basalts, hyaloclastite breccia, sedimentary breccia
	south wall	31, 32, 33, 38, 42, 43	peridotites,serp. Breccia, metasomatic rocks, basalts, dolerites, sedim. Breccia, hyaloclastite breccia
Southern paleo-Romanche	north wall	29, 41	basalts, dolerites, hyaloclastite, breccia, peridotites, gabbros, limestones
	south wall	28	(empty dredge)
High inside corner (HIC) of the western RTI	south slope	39	peridotites, gabbros, basalts, basaltic breccias, sedim. Breccias
Oblique structure south-west of the western RTI		37	(empty dredge)
Romanche FZ west of the western RTI	north wall	40	(empty dredge)
southern transverse ridge	south slope	30	gabbros, sedim. Breccia
median ridge	south slope	44	(empty dredge)
northern transverse ridge west of the western RTI	north slope	46	peridotites, serp. Breccia, sedim. Breccia: evidence of faulting
(RTI) = Ridge-Transform Intersection			

Chapter 2
Petrography

2.1 Samples description and modal analysis

Peridotites collected during G96 cruise (Table 2.1.1) show various degrees of serpentinization (from 26% to 70% of total rock; Susini, PhD thesis 1997). On average serpentinization is always higher than 50% and fresh primary olivine is present only in few samples. The studied rocks are plagioclase-bearing spinel-peridotites, i.e. they typically consist of olivine + orthopyroxene + clinopyroxene + spinel + plagioclase.

Table 2.1.1 Main lithotypes sampled in dredges G9632, G9633 and G9639 during G96 cruise.

dredge	lithotype
G9632	Altered peridotites, breccias with serpentinitic material and Fe-Mn crust.
G9633	Altered peridotites and serpentinitic breccias, with Fe-Mn crust
G9639	Altered basalts, serpentinized peridotites and some foliated, sedimentary breccias.

According to modal analysis, the studied samples consist of lherzolites (modal clinopyroxene from 6.7% in sample 39-36 to 24% in sample 33-01; table 2.1.2). Modal composition of sample 32-22 lies very close to the compositional fields of olivine-websterites (fig.2.1.1). Note that the terms "harzburgite" and "lherzolite" are used only referring to the modal description, not to the history of the rock.

Table 2.1.2. Modal composition of the studied samples and estimated degree of impregnation

Sample	Ol%	Opx%	Cpx%	Sp%	Pl%	Imp%
G96-32/03	63.6	16.6	12.5	2.1	5.2	12
G96-32/07	59.6	15.6	6.5	1.9	16.4	30
G96-32/14	63.8	13.6	12.5	2.8	7.2	17
G96-32/22	34.6	33.5	15.7	0.7	15.5	28
G96-32/32	47.8	16.4	21.1	2.1	12.6	23
G96-33/01	59.5	8.5	24.3	2.1	5.6	13
G96-33/05	62.5	15	12.5	1.4	8.5	20
G96-39/36	67.1	24.5	6.7	1.4	0.4	0.9
G96-39/28	65.2	19.0	6.9	1.8	7.1	13
G96-39/27	66.0	25.3	6.2	1.6	0.9	2
G96-43/03	59.4	6.3	23.2	1.6	9.5	17

Modal composition and estimated degrees of impregnation of the studied samples were obtained by counting a minimum 1000 points at a 0.2-mm spacing for each thin section. Values refer to the total amount of each phase, regardless of the genesis, and they were calculated according to the following assumptions: (i) serpentine in mesh-texture replacing olivine and magnetite were calculated as olivine; (ii) bastite replacing orthopyroxene was calculated as orthopyroxene; (iii) magnetite at the rim of spinel was attributed to spinel; (iv) late tensional veins filled with serpentine fibres, carbonate or secondary minerals were not counted; (v) corrections for volume expansion due to serpentinization were not considered; (vi) residual and magmatic pyroxenes and plagioclase were not distinguished.

The impregnation degree (Imp%) was calculated with a proportion on the basis of the modal plagioclase of the rock and assuming a modal plagioclase for abyssal basalts of about 55% (Bryan and Dick, 1982; Dick, 1989).

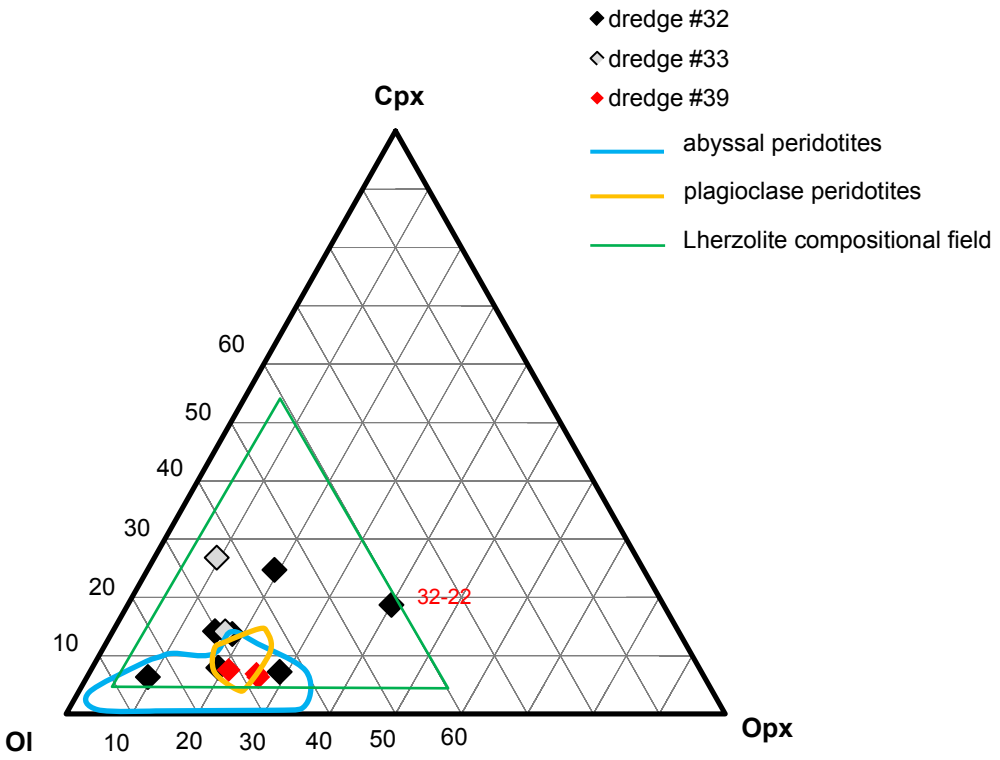

Fig. 2.1.1 - Ternary plot of modal composition of the studied samples, grouped by dredge. Black dots are compositions of samples of dredge #32, grey dots are compositions of samples of dredge #33 and red dots are compositions of samples of dredge #39. Modal field of plagioclase peridotites (orange line) (Seyler & Bonatti, 1997) and of plagioclase-free peridotites (blue line) (MICHAEL & BONATTI, 1985; Seyler & Bonatti, 1997) are also reported.

2.2 Petrography and textures

2.2.1 Samples description

Henceforth in the text, the terms *protogranular*, *porphyroclastic* and *equigranular* are used according to the meaning of Ceuleneer and Cannat (1997) and Dick et al. (2010), whereas definition of the grain size - coarse (≈ 5 mm), medium (≈ 1 mm) and fine (≈ 0.25 mm) - of each sample is based on the work of Ceuleneer and Cannat (1997).
For detailed description and illustration of plagioclase peculiar textures see next paragraph (§ 2.2.2).

Dredge G9639

Dredge #39 was sampled at the southern wall of the western high inside corner of the transform. From this dredge two samples have been selected: 39-36 and 39-28.

Sample 39-36: sample 39-36 is a spinel-lherzolite (opx 24.5% and clinopyroxene 6.7%) containing plagioclase (0.4%) the estimated degree of impregnation is 0.9%.
The olivine groundmass consists of i) coarse-grained crystals, whose average size ranges from 5 mm up to 10 mm, ii) medium-grained crystals, which displays an average size of ≈1 mm, and, less frequently, iii) fine-grained (around 0.25 mm) small aggregates. Olivine also occurs in very fine-grained (up to ≈0.03 m) poly-mineral aggregates together with opx, clinopyroxene and spinel.
Coarse-grained olivine displays elongated shapes and defines preferred orientation (fig. 2.2.1.1). Locally, coarse-grained olivine fades into medium-grained olivine, which occurs in clusters of anhedral, sub-rounded crystals. Fine-grained olivine is rarer, occasionally appearing in small clusters of sub-euhedral items. Finally, very fine-grained olivine forms equigranular poly-mineralic aggregates which mainly develop along coarse opx grain boundaries or fractures. Coarse-grained olivine may show wavy extinction (fig. 2.2.1.2). Coarse-grained olivine crystals show reciprocal smooth and curvilinear grain boundaries, whereas smooth and quite straight grain boundaries occur when in contact with pyroxene (fig. 2.2.1.2). As a whole, the olivine matrix appears rather fresh or, at worst, affected by incipient alteration into serpentine, being characterized by fresh portions of olivine trapped by a pervasive network of serpentine veins.
Opx may occur as medium- to coarse-grained (up to 9 mm) crystals showing ovoid to elongated to complex shapes, with curvilinear and/or jagged outlines and several embayments at the rim; opx also forms fine- to very fine-grained (around 0.25 mm and less, up to 0.03 mm), euhedral, equigranular aggregates with common 120° triple junctions, sometimes associated with ol and sp , generally developing along coarse opx grain boundaries or fractures. Largest crystals may appear broken by wedge-shaped fractures filled with olivine or embed olivine patches (fig. 2.2.1.3); the most elongated items suggest slight preferred orientation

concordant with the foliation of the olivine matrix. Some evidence of weak brittle deformation, i.e. kink band, are also present.

Clinopyroxene is not very abundant and mostly occurs as medium-grained (up to 3 mm), disjointed, complex-shaped crystals with embayed and jagged rims.

Cr-spinel occurs as fresh, small and reddish grains, displaying either holly-leaf or vermicular habit. Holly leaf-shaped spinel forms isolated items; moreover it may occur as interstitial small grains in ol+px very fine-grained aggregates (fig. 2.2.1.6). Vermicular spinel occurs in sp+opx±cpx symplectitic intergrowths (fig. 2.2.1.7).

Only two quite fresh plagioclase grains were found; apart from those, plagioclase mainly appears totally replaced by alteration products. However, the textural features of plagioclase are preserved. It occurs in swarms of anhedral, elongated patches (length up to 2 mm) crosscutting the rock; they appear strongly isoriented in concordance with the rock foliation and mostly gathered along bands. Smaller interstitial patches also may occur in very fine-grained ol+px aggregates.

Sample 39-28: sample 39-28 is a spinel-lherzolite (opx 19.0% and cpx 6.9%) containing plagioclase (7.1%), with an estimated degree of impregnation of 13%.

The olivine groundmass mainly consists of medium-grained items with sub-rounded habit and curvilinear grain boundaries; locally, medium-grained olivine fades into clusters of euhedral, fine-grained (from 0.1 to 0.4 mm) crystals which show 120° triple junctions (fig. 2.2.1.4); finally, several coarse-grained, elongated crystals are also present, which define preferred orientation. Coarse- and medium grained olivine may display wavy extinction. The olivine matrix is affected by incipient serpentinization; the degree of alteration locally may be quite high, with almost total replacement of olivine by serpentine.

Opx may occur as coarse-, medium- and fine-grained crystals. Coarse and medium crystals are strongly fractured, displaying ovoid to elongated to complex shapes, with embayed and/or jagged outlines and, occasionally, may be partially re-crystallized in fine-grained neoblasts, or partially replaced by equigranular, euhedral fine-grained poly-mineralic aggregates. Very fine-grained orthopyroxene is also present; it occurs as equigranular, euhedral aggregates, sometimes together with olivine and interstitial sp, developing along opx grain boundaries or along fractures inside coarse orthopyroxene.

Clinopyroxene mainly displays medium to fine grain size; it may occur as isolated medium-grained irregular "shreds" or sub-euhedral crystals, showing features similar to those of coarse- and medium-grained orthopyroxene. Some crystals may be affected by incipient replacement by fine- and very fine-grained clinopyroxene or affected by mechanical twinnings. Fine-grained clinopyroxene also occurs in poly-mineralic, heterogranular, euhedral aggregates together with ol and orthopyroxene (fig. 2.2.1.5).

Cr-spinel forms quite large (up to 2.5 mm) holly-leaf-shaped grains; it appears almost totally opaque under the plain light, i.e. it is much altered. In one case one crystals is rimmed by a plagioclase corona (fig. 2.2.1.8).

Plagioclase occurs in swarms of interstitial patches (up to 2-mm-sized), that show preferred orientation concordant with the rock foliation; patches appear totally replaced by alteration products, probably sericite for the most part and secondly clay minerals.

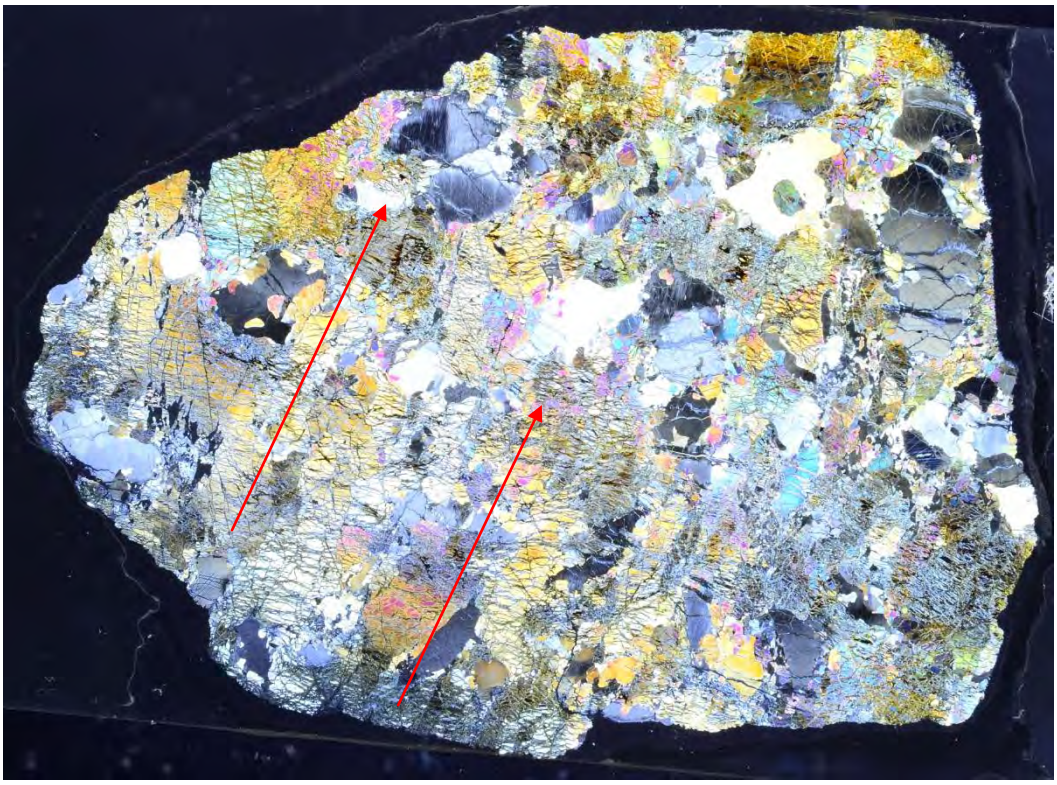

Fig. 2.2.1.1 - Thin section of sample 39-26: Coarse, elongated crystals of olivine show preferred orientation and define the rock foliation (red arrows).

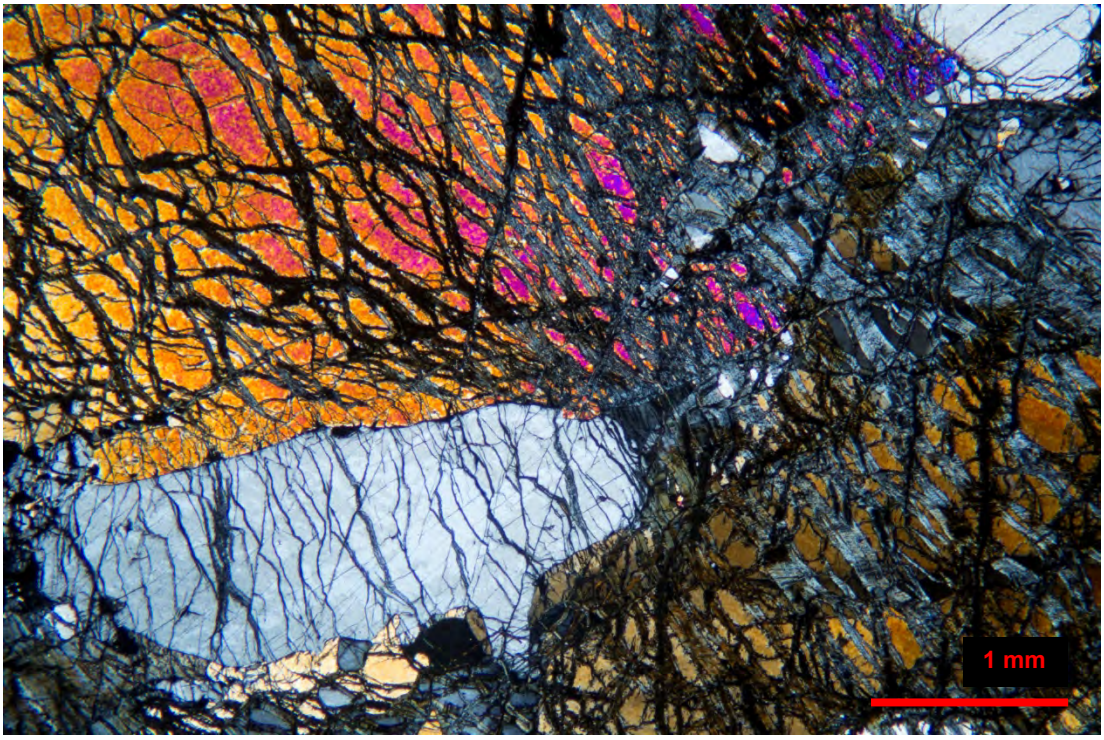

Fig. 2.2.1.2 - Coarse-grained olivine (orange zone) showing straight grain boundaries against ≈3 mm ovoid opx; on the other side the opx shows embayed and irregular rims being in contact with fine-grained olivine. Coarse olivine is affected by wavy extinction (on the right corner). Sample 39-36. Crossed nicols.

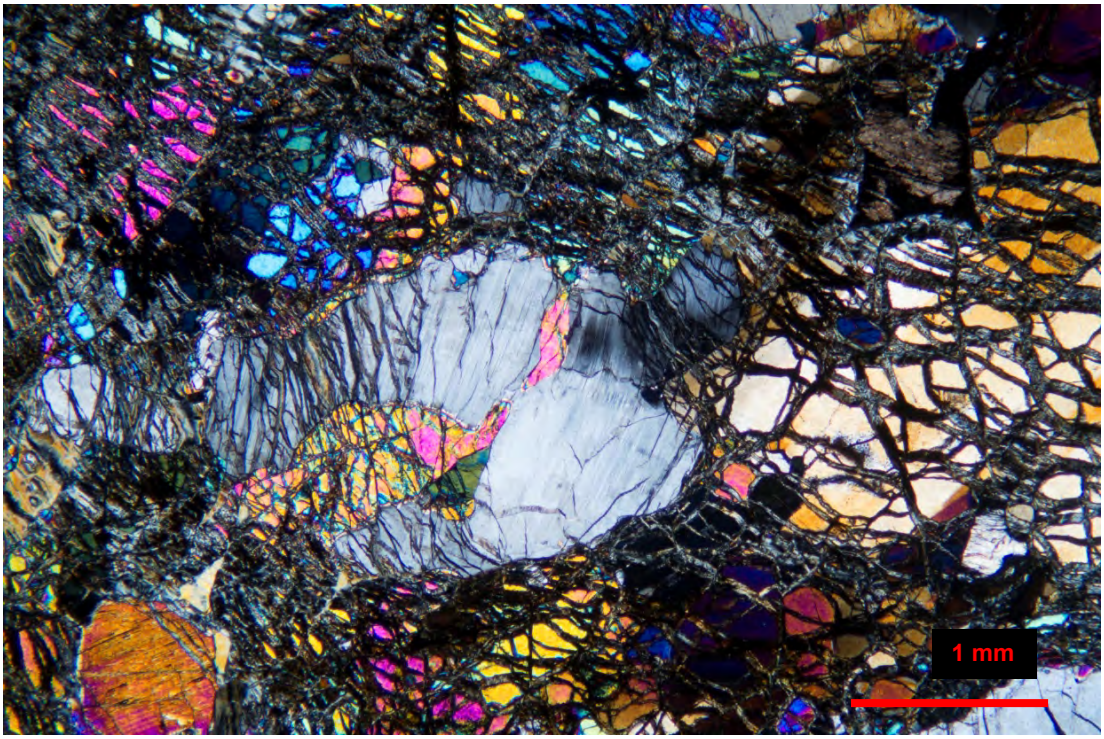

Fig. 2.2.1.3 - ≈2.5 mm irregular orthopyroxene surrounded and penetrated by medium-grained mosaic of elongated olivines; a larger crystal of olivine showing wavy extinction is visible on the right. Sample 39-36. Crossed nicols.

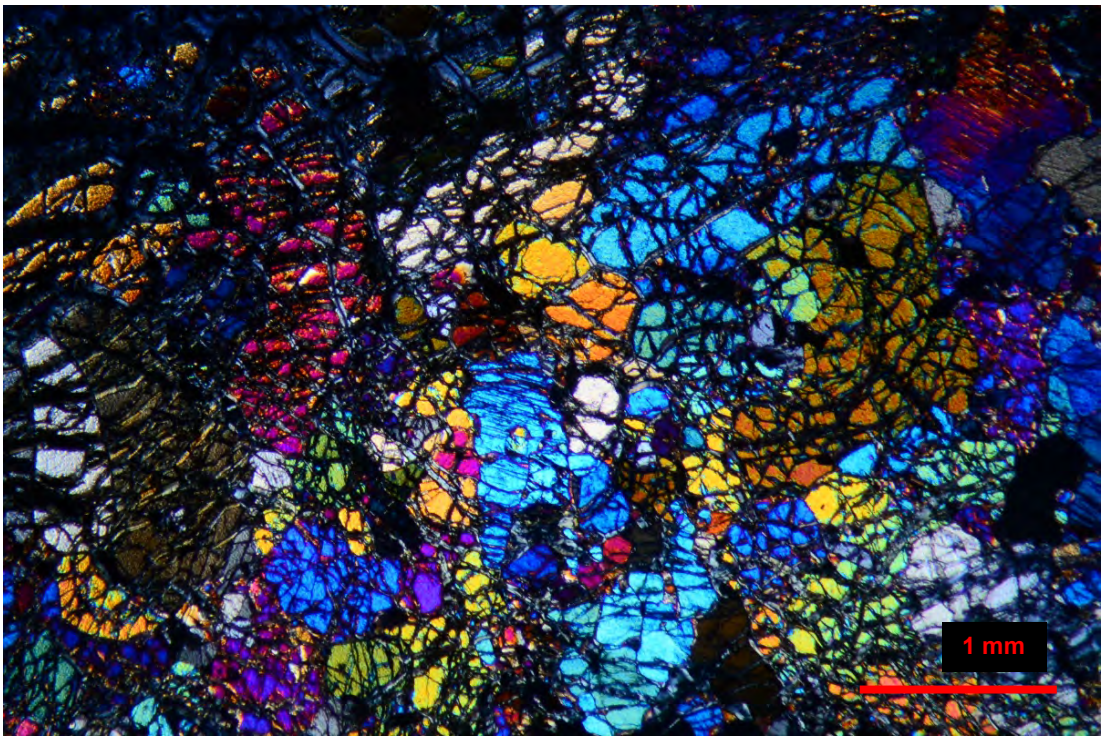

Fig. 2.2.1.4 - Heterogranular medium- to fine-grained mosaic of olivine forming the rock groundmass. Scattered clinopyroxene crystals are also present. Sample 39-28. Crossed nicols.

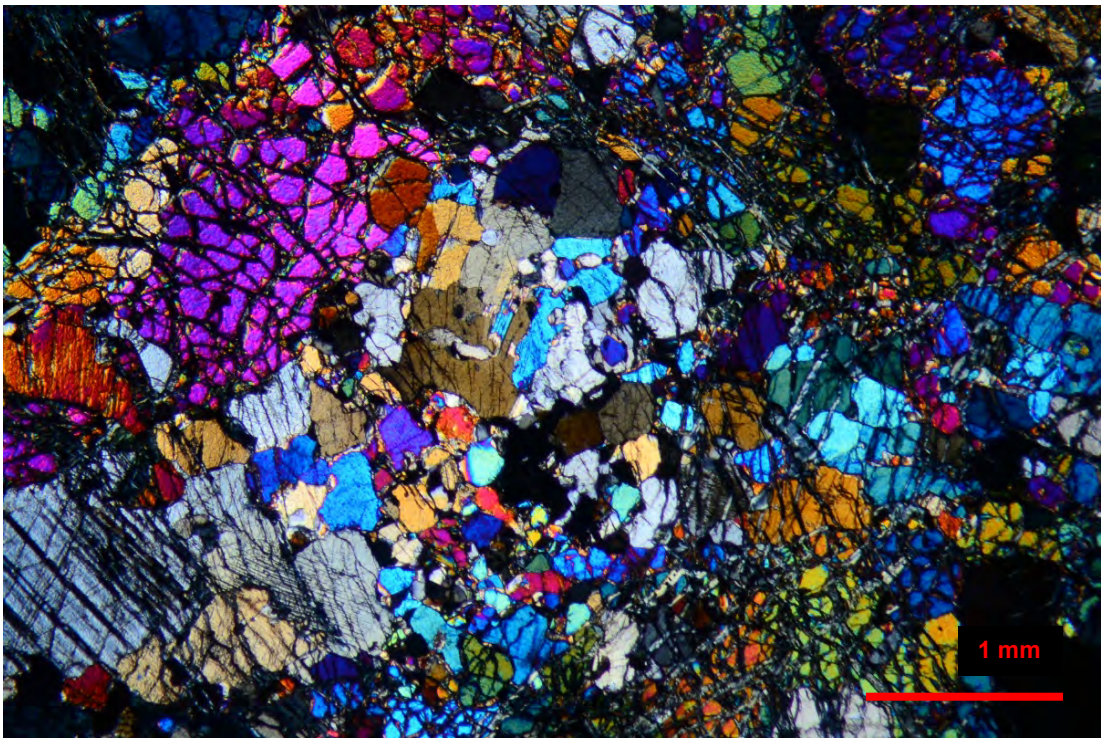

Fig. 2.2.1.5 - Heterogranular medium- to fine-grained mosaic containing ol+cpx. Sample 39-28. Crossed nicols.

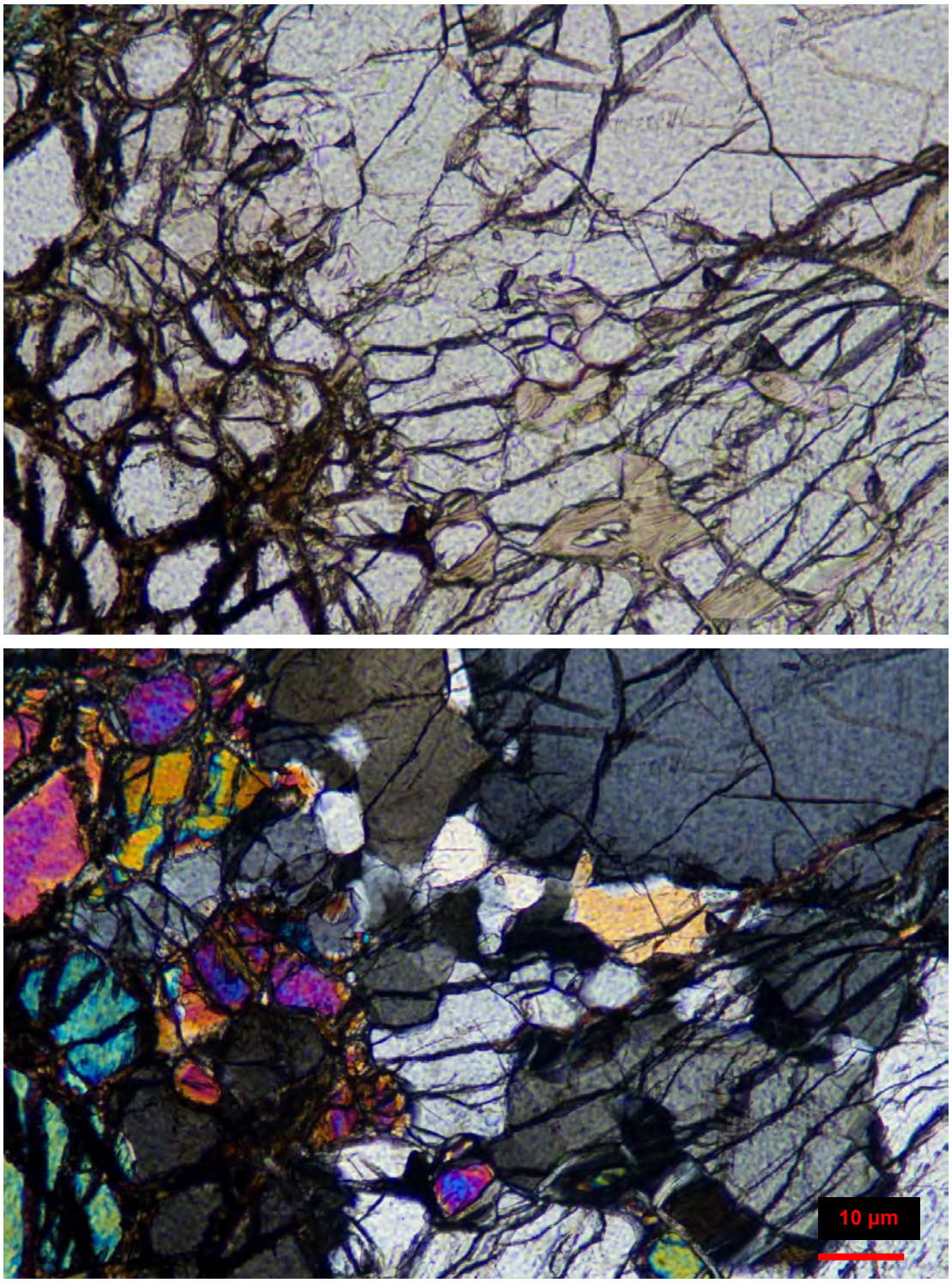

Fig. 2.2.1.6 - Plain light (upper) and crossed nicol (lower) images of fine-grained ol+opx+sp developed along ol-opx contact; fine-grained orthopyroxene shows subhedral to euhedral near-equilibrium texture with common 120° triple junctions; olivine shows anhedral habit, spinel is interstitial. Sample 39-36.

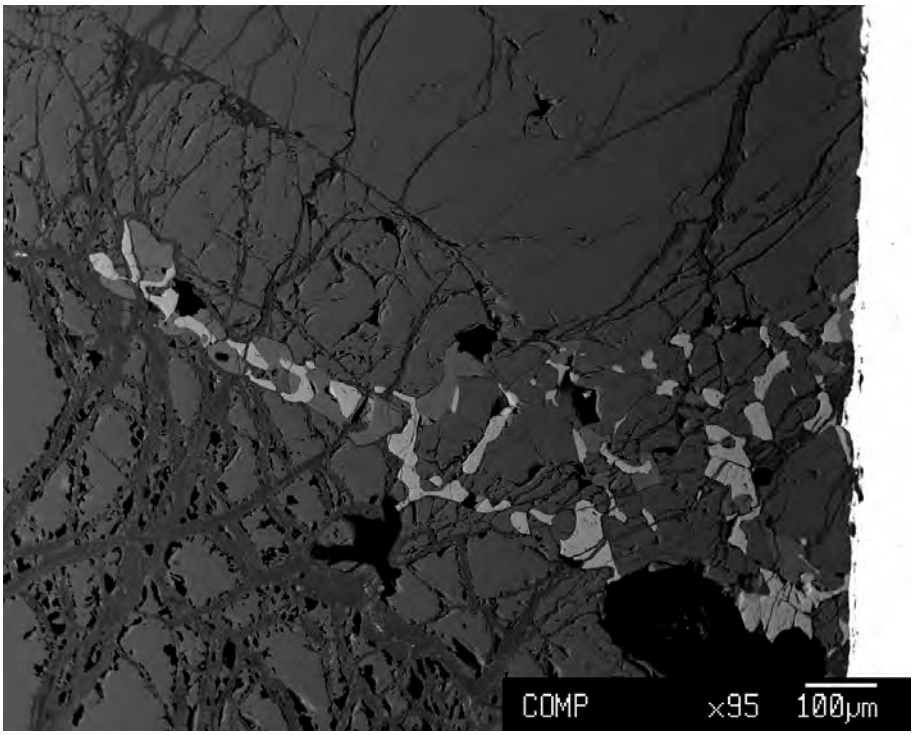

Fig. 2.2.1.7 - Backscattered electron image of a symplectitic pockets along opx-ol interface formed by vermicular spinel (white) ± clinopyroxene (light grey) ± opx (grey), the assemblage extend laterally with a cpx + sp intergrowth forming a veinlet in the olivine matrix. Sample 39-36.

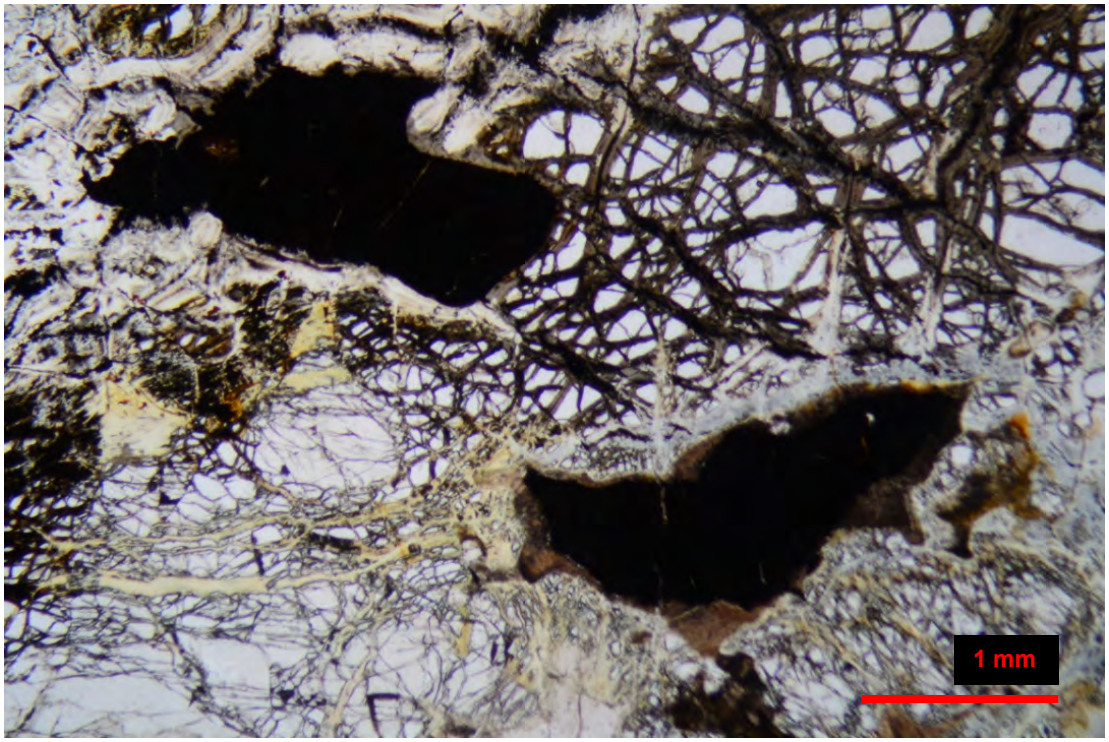

Fig. 2.2.1.8 - Holly-leaf-shaped crystals of dark spinel. The crystal on the right is rimmed by a thin (altered) plagioclase corona. Sample 39-28. Plain light.

Dredges G9632 and G9633

Dredges #32 and #33 were collected from the southern wall of the active transform valley (the southern valley) of the Romanche FZ, on the western part. From these dredges samples 32-03, -07, -14, -22 and -32 were selected.

In these samples olivine is completely altered. The groundmass is made of brownish Fe-hydroxides + clay minerals which totally replaced serpentine. Dick et al. (2010) described similar "argillitized relict olivine" after serpentinization due to seafloor weathering. The substitution is pseudomorphic on an earlier serpentinitic matrix as suggested by the pervasive network of veins (fig. 2.2.3.1, see § 2.2.3). Estimation of the grain-size of olivine is thus prevented. However, for the purpose of the petrographic description the altered groundmass is treated as olivine, as well as the modal analysis and textural relationships with other phases and relative grain boundaries.

Sample 32-03: sample 32-03 is a spinel-lherzolite (clinopyroxene 12.5% and opx 16.6%) containing plagioclase (5.2%) with an estimated degree of impregnation of 12%.

Olivine appears totally replaced by alteration products, i.e. a homogeneous groundmass made of brownish Fe-hydroxides, in which the preserved pervasive network of veins suggests the presence of an earlier serpentinitic matrix.

Orthopyroxene occurs as coarse-, medium- and fine-grained crystals. Coarse-grained orthopyroxene is scarce; coarse and medium grains have similar features, showing strong fracturing (with occasional wedge-shaped fractures), complex-shapes, more rarely sub-euhedral or elongated shapes, irregular outlines (curvilinear and/or jagged rims with several embayments), and often appear disjointed in several "shreds". Elongated items define a slight foliation; in one case deformation by kink-banding is present. Fine-grained crystals show sub-euhedral habit and may occur in heterogranular poly-mineral aggregates.

Clinopyroxene occurs as medium- to fine-grained crystals; medium-grained clinopyroxene mainly occurs as complex-shaped crystals but also may display sub-euhedral or ovoid shapes, usually showing irregular outlines and being surrounded by fine-grained aggregates. Deformed items show mechanical twinnings, bending, and some appear replaced by fine- and very fine-grained clinopyroxene aggregates. Fine-grained clinopyroxene may forms pockets of euhedral crystals or occur in heterogranular poly-mineral aggregates. Moreover, clinopyroxene may forms medium- to fine-grained clusters of interstitial grains within the rock groundmass (fig. 2.2.1.10), sometimes interweaved with, or bordering, plagioclase interstitial patches (fig. 2.2.1.11).

Cr-spinel (2.1%) occurs as spread, small holly-leaf-shaped grains, sometimes with plagioclase patches. They are almost completely opaque under the plain light because of their deep alteration.

Plagioclase forms quite fresh interstitial patches which permeate the whole rock, locally showing preferred orientation (at the scale of the thin section).

Sample 32-07: sample 32-07 is a spinel-lherzolite (clinopyroxene 6.5% and opx 15.6%) containing plagioclase (16.4%) with an estimated degree of impregnation of 30%.

Olivine appears totally replaced by alteration products, i.e. a homogeneous groundmass made of brownish Fe-hydroxides, in which the preserved pervasive network of veins suggests an earlier serpentinitic matrix.

Orthopyroxene may occur as coarse-, medium- and fine-grained crystals. Coarse- to medium-grained items mainly display complex shapes and irregular outlines (fig. 2.2.1.9), sometimes appearing disjointed in several "shreds"; some sub-rounded to ovoid crystals with quite smooth boundaries are also present. Medium-to fine-grained crystals occur in heterogranular poly-mineralic aggregates. Very fine-grained equigranular opx aggregates develop along fractures inside orthopyroxene or along orthopyroxene boundaries.

Clinopyroxene occurs as medium- to fine-grained sub-rounded to complex-shaped grains characterized by irregular outlines. Largest clinopyroxene may appear affected by incipient replacement by fine- and very-fine-grained clinopyroxene aggregates. Fine-grained clinopyroxene may occur in heterogranular poly-mineralic aggregates, as clusters of small interstitial grains, occasionally texturally associated with plagioclase patches. Both orthopyroxene and clinopyroxene larger occurrences may appear strongly fractured; apart from that, orthopyroxene is rather undeformed, except one case in which a slight bending (wavy extinction) is present; more often clinopyroxene displays evidences of deformation, such as slight bending and mechanical twinnings.

Cr-spinel (1.9% modal) is holly-leaf textured, quite altered (almost totally black under plain light), mostly occurring isolated in the former olivine matrix or, occasionally, totally or partially embedded in patches of plagioclase.

Plagioclase is pretty fresh; it occurs as interstitial patches, randomly spread in the olivine groundmass, permeating the interstices of heterogranular poly-mineral aggregates, superimposing forming patches associated with orthopyroxene inside large clinopyroxene, or filling veinlets.

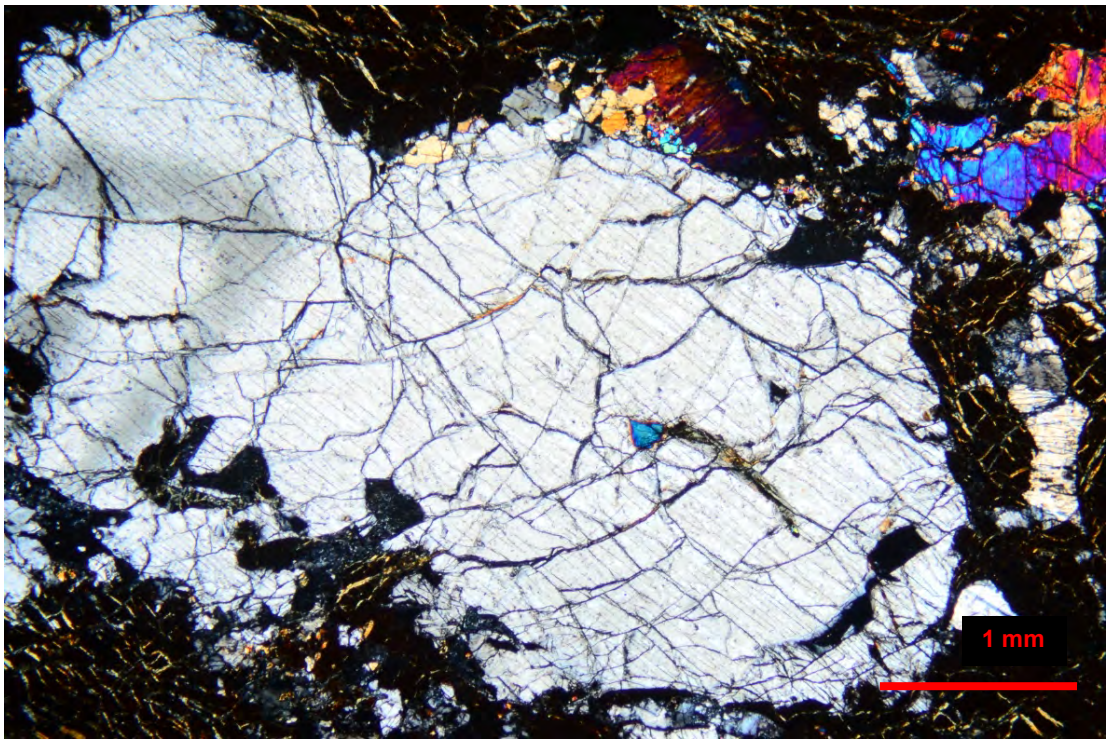

Fig. 2.2.1.9 - Coarse-grained complex-shaped orthopyroxene with irregular rims and irregular sharp embayments. Some very-fine-grained aggregates are present along the rim. Dark zones inside the orthopyroxene are altered olivine. Sample 32-07. Crossed nicols.

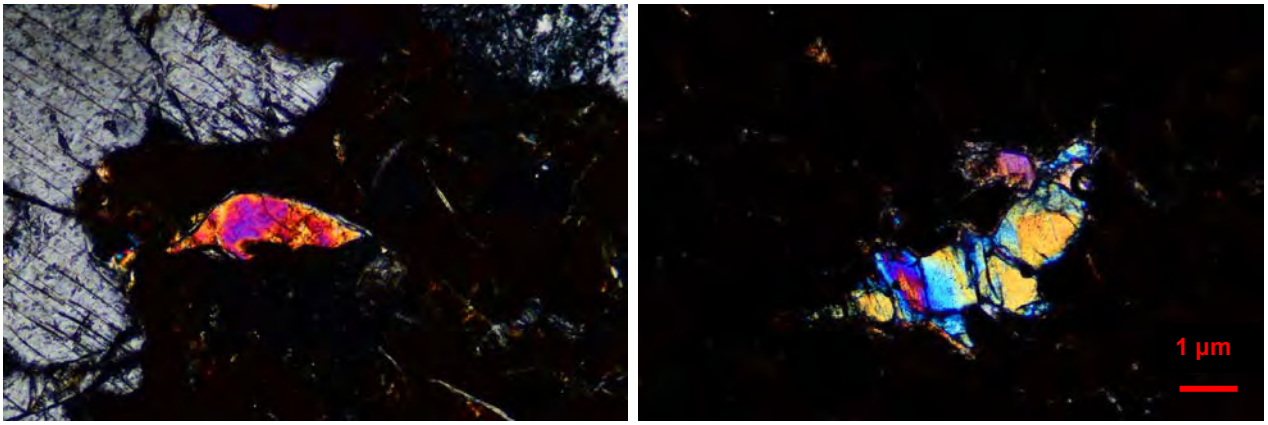

Fig. 2.2.1.10 - Small interstitial grains of clinopyroxene, within the olivine matrix now replaced by alteration products (dark stuff). Sample 32-07 (left) and sample 32-03 (right). Crossed nicols.

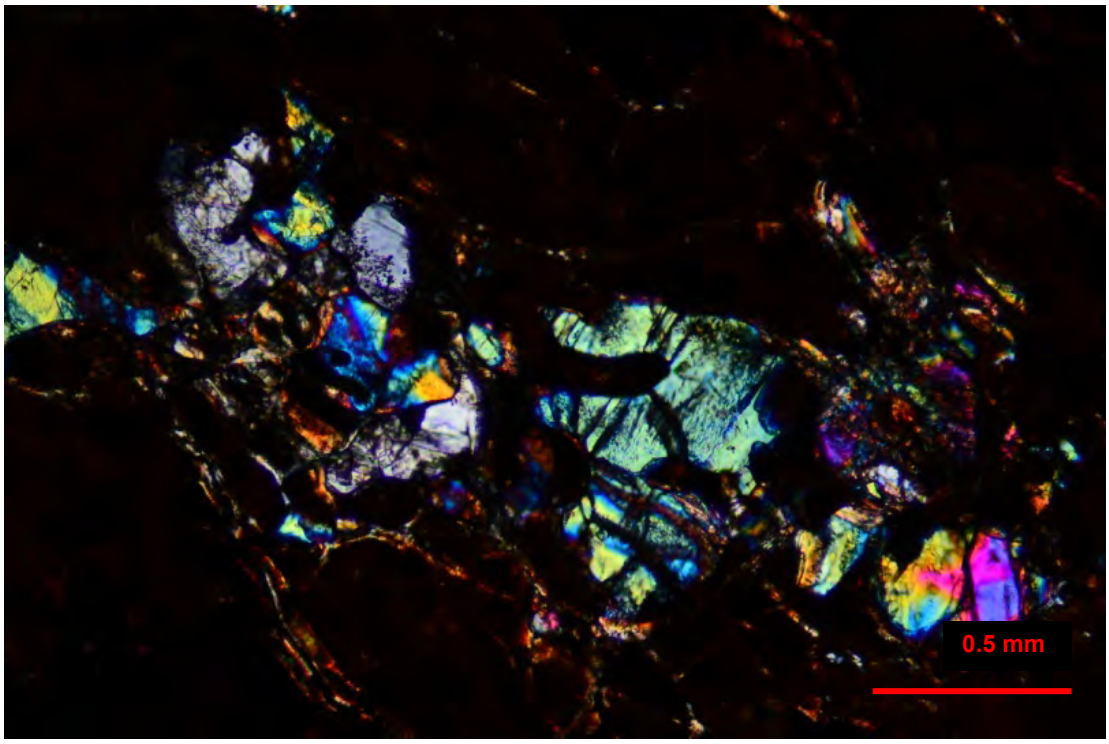

Fig. 2.2.1.11 - Cluster of small interstitial grains of clinopyroxene, interweaved with similar-sized interstitial plagioclase, within the olivine matrix now replaced by alteration products (dark stuff). Sample 32-03. Crossed nicols.

Sample 32-14: sample 32-14 is a spinel-lherzolite (clinopyroxene 12.5% and opx 13.6%) containing plagioclase (7.2%) with an estimated degree of impregnation of 17%.

Olivine appears totally replaced by alteration products, i.e. a homogeneous groundmass made of clay minerals? + brownish Fe-hydroxides, in which the preserved pervasive network of veins suggests the occurrence of an earlier serpentinitic matrix.

Orthopyroxene occurs as coarse-, medium- and fine-grained crystals. Coarse grains are scarce; more frequently orthopyroxene displays intermediate sizes between coarse and medium. Coarse- to medium-grained orthopyroxene may occur either as complex-shaped "shreds" or as elongated to ovoid crystals, mostly showing irregular outlines (smooth rims only in ovoid crystals). Elongated occurrences define a weak foliation. Coarser crystals may show strong kink-banding or wavy extinction.

Coarse clinopyroxene is absent; clinopyroxene mostly occurs as coarse- to medium-grained crystals, showing features similar to those of coarse- to medium-grained orthopyroxene. Furthermore, some deformed clinopyroxene crystals are present, showing mechanical twinning and strong bending (wavy extinction). Occasionally, orthopyroxene and clinopyroxene may show inner intergrowths of Fe-Ni-sulfides (as evidenced by EDS). Fine-grained orthopyroxene and clinopyroxene show similar features, both occurring in fine- to very-fine grained poly-mineralic aggregates.

Cr-spinel (2.8%) occurs as spread, small holly-leaf-shaped grains, which appear rather altered.

Plagioclase forms interstitial fresh patches, showing either elongated or sub-rounded shapes. Elongated patches locally may show preferred orientation or display sub-alignment.

Sample 32-22: sample 32-22 is a spinel-lherzolite (clinopyroxene 15.7% and opx 33.5%) containing plagioclase (16.4%) with an estimated degree of impregnation of 30%.

Despite the overall high degree of alteration of the earlier olivine matrix, replaced by clay minerals? + brownish Fe-hydroxides, locally some fresh olivine relics are preserved. It is noticeable the presence of medium-grained olivine, affected by incipient alteration into serpentine, whereas many fine-grained, sub-euhedral crystals may occur in poly-mineral aggregates.

Orthopyroxene and clinopyroxene occurs in a wide range of sizes, from coarse to very fine. Coarse orthopyroxene and clinopyroxene appear strongly fractured, disjointed, from complex-shapes with irregular rims to, more rarely, ovoid with quite smooth rims. Medium-grained orthopyroxene and clinopyroxene occurs as complex-shaped and strongly fractured "shreds". Usually, coarse pyroxene show coronas of fine- and very fine-grained poly-mineralic aggregates, which may also develop along px-px contact or fractures (fig. 2.2.1.15). Locally, medium- to fine-grained px aggregates seamless permeate the gap amongst several coarse crystals of pyroxene. Clinopyroxene and orthopyroxene also occur as clusters of small interstitial grains, occasionally texturally associated with plagioclase patches. Generally, coarse and medium clinopyroxene display mechanical twinning and heavy bending, whereas coarse orthopyroxene mainly display kink band. Moreover, both coarse- and medium-grained pyroxene may show inner Fe-Ni-sulfides intergrowths (as evidenced by EDS; see fig. 2.2.1.13).

Cr-spinel is not very abundant (0.7%), only occurring in spread small holly-leaf-shaped grains.

Plagioclase is, instead, rather abundant. It forms fresh interstitial patches which randomly permeate the whole rock and occurs: i) as isolated patch within the ex-olivine matrix, ii) in the interstices of poly-mineralic aggregates, iii) bordering coarse pyroxene, as well as, iv) permeating fractures or forming patches associated with orthopyroxene inside coarse clinopyroxene crystals.

Sample 32-32: sample 32-32 is a spinel-lherzolite (clinopyroxene 6.5% and opx 16.6%) containing plagioclase (12.6%) with an estimated degree of impregnation of 23%.

Olivine is nearly totally altered into brownish Fe-hydroxides except for some fresh fine grains occurring in poly-mineral aggregates.

Orthopyroxene occurs as coarse-, medium- and fine-grained items. Coarse and very coarse (up to 9 mm) orthopyroxene mostly appears complex-shaped, sometimes disjointed in several "shreds", showing irregular outlines, inner fractures, blanks and wedge-shaped fractures (fig. 2.2.1.12). Orthopyroxene occurs in medium- to fine- to very fine (up to 0.03 mm)-grained poly-mineralic aggregates; very-fine orthopyroxene aggregates ±cpx±ol±pl±sp mostly develop along fractures inside large orthopyroxene or along orthopyroxene grain boundaries (figs. 2.2.1.14 and 2.2.1.15). Moreover, small interstitial patches of orthopyroxene may occur isolated or associated with plagioclase patches.

Clinopyroxene mostly occurs as medium-grained crystals (less than 5 mm) with features similar to coarse and medium orthopyroxene. Moreover, clinopyroxene often appears totally embedded in very-fine-grained mineral aggregates. Modal composition of very-fine-grained aggregates is difficult to establish under the

optical microscope due to the small size. In other cases, medium-grained clinopyroxene appears partially replaced by fine-grained clinopyroxene aggregates. Clinopyroxene also occurs as clusters of small interstitial grains, occasionally texturally associated with plagioclase patches. Some coarse orthopyroxene crystals are kinked; clinopyroxene, instead, mainly appears affected by bending, mechanical twinnings and replacement by finer neoblasts (figs. 2.2.1.17 and 2.2.1.18). Both orthopyroxene and clinopyroxene are occasionally spotted by Fe-Ni-sulfides fine grain clusters.

Cr-spinel forms holly leaf-shaped crystals which appears quite altered. Some elongated items show sub-alignment forming trails together with plagioclase and orthopyroxene. In one case spinel forms exolution lamellae associated with clinopyroxene inside a coarse crystal of orthopyroxene (fig. 2.2.1.16).

Plagioclase is rather abundant and fresh. It occurs as interstitial patches permeating the whole rock, displaying a wide range of textures (see sample 32-22).

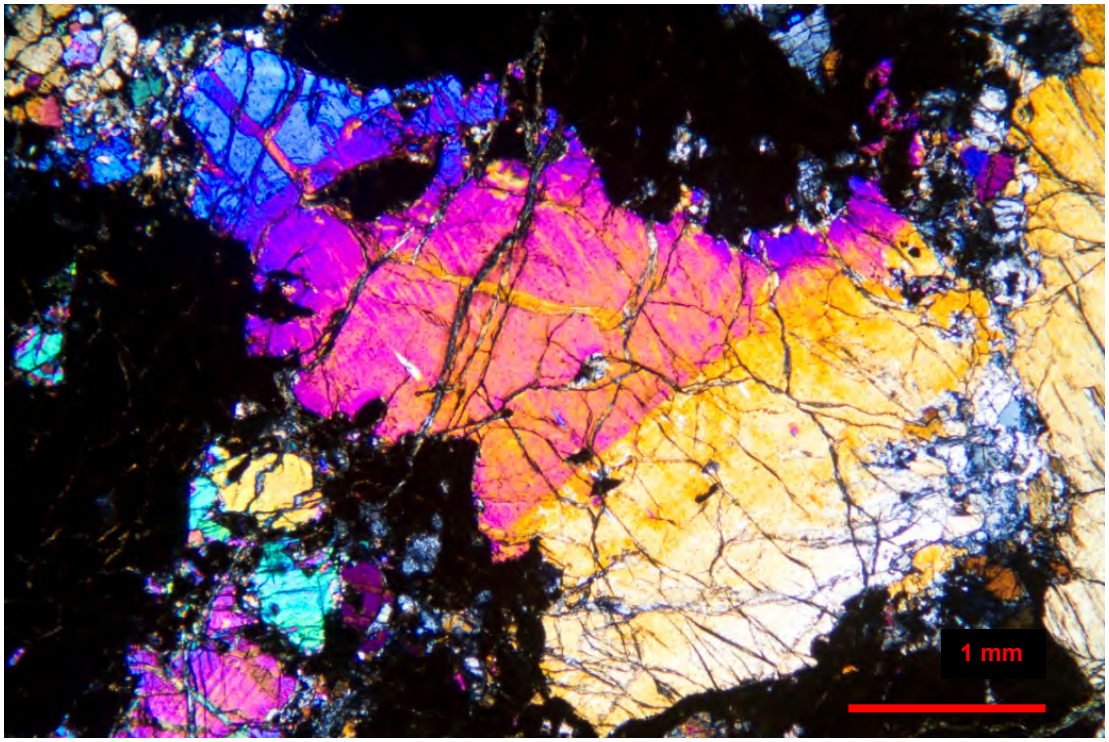

Fig. 2.2.1.12 - Coarse-grained complex-shaped orthopyroxene with irregular rims. Inner dark patch is filled by altered olivine. Poly-mineralic aggregate develops along opx-opx contact (on the right). Sample 32-32. Crossed nicols.

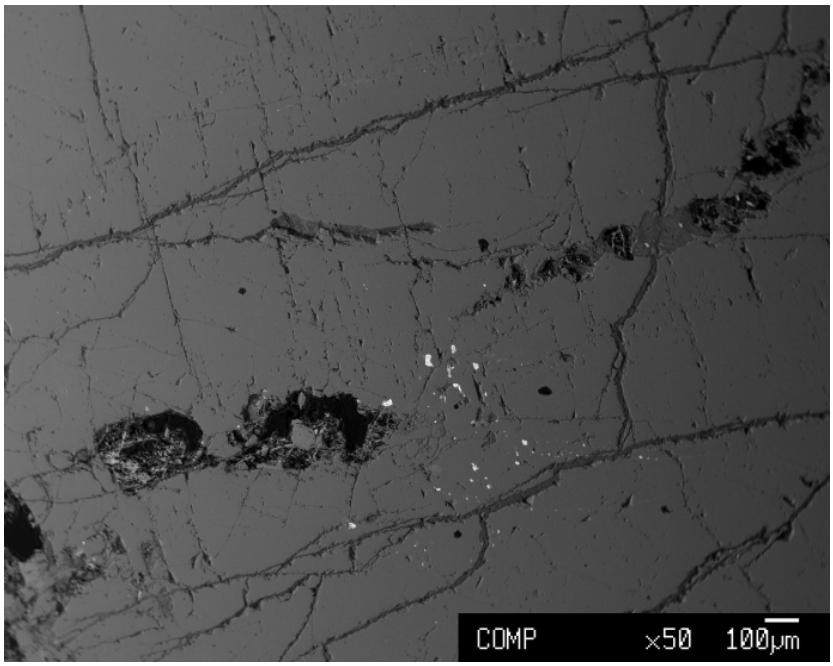

Fig. 2.2.1.13 - Backscattered electron images of Fe-Ni sulfides (white grains) spotting coarse orthopyroxene (grey groundmass). Dark patches are altered olivine. Sample 32-22.

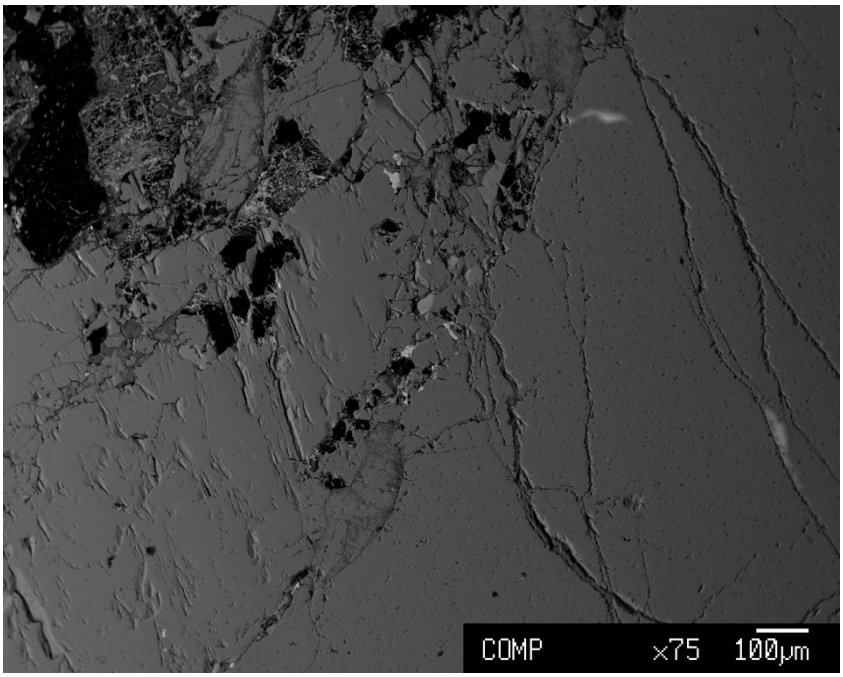

Fig. 2.2.1.14 - Backscattered electron image of opx (grey) + cpx (light grey) + pl (mottled grey) + sp (white) aggregate developed along opx-opx contact. Sample 32-32.

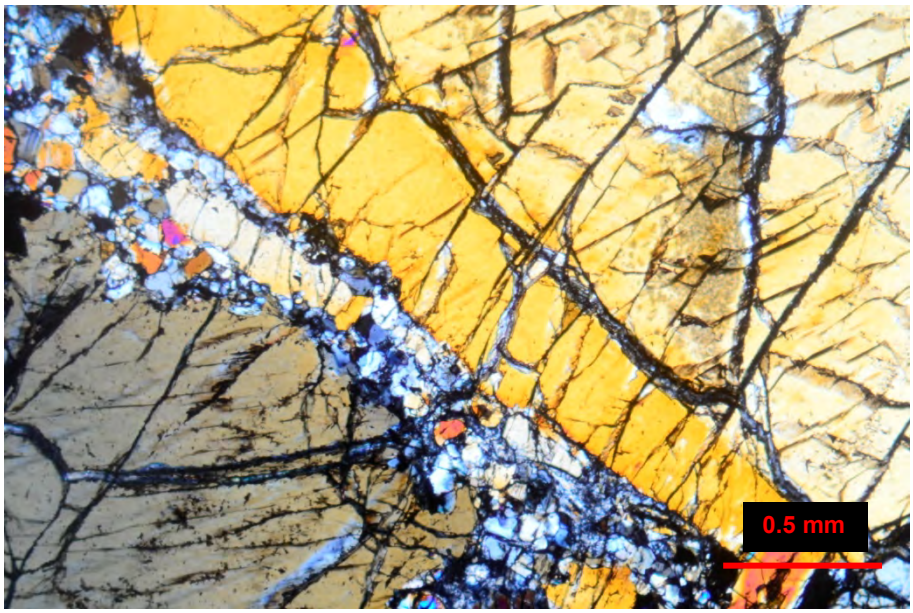

Fig. 2.2.1.15 - Fine-grained aggregate containing opx+cpx+ol+sp+pl, developed along opx-opx contact (or fracture?). Sample 32.22. Crossed nicols.

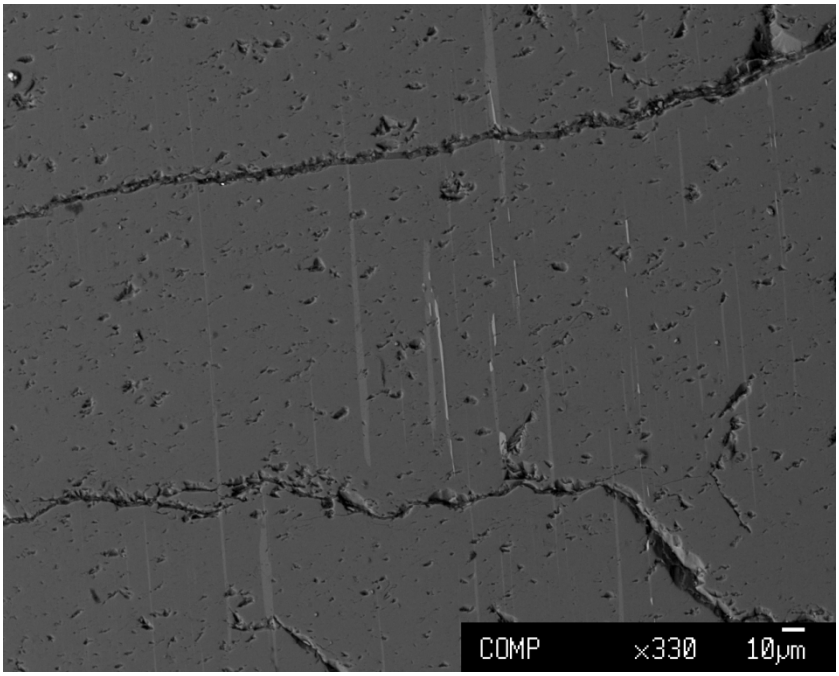

Fig. 2.2.1.16 - Backscattered electron image of opx (grey groundmass) in which are present cpx (light grey) + sp (white) exolution lamellae. Sample 32-32.

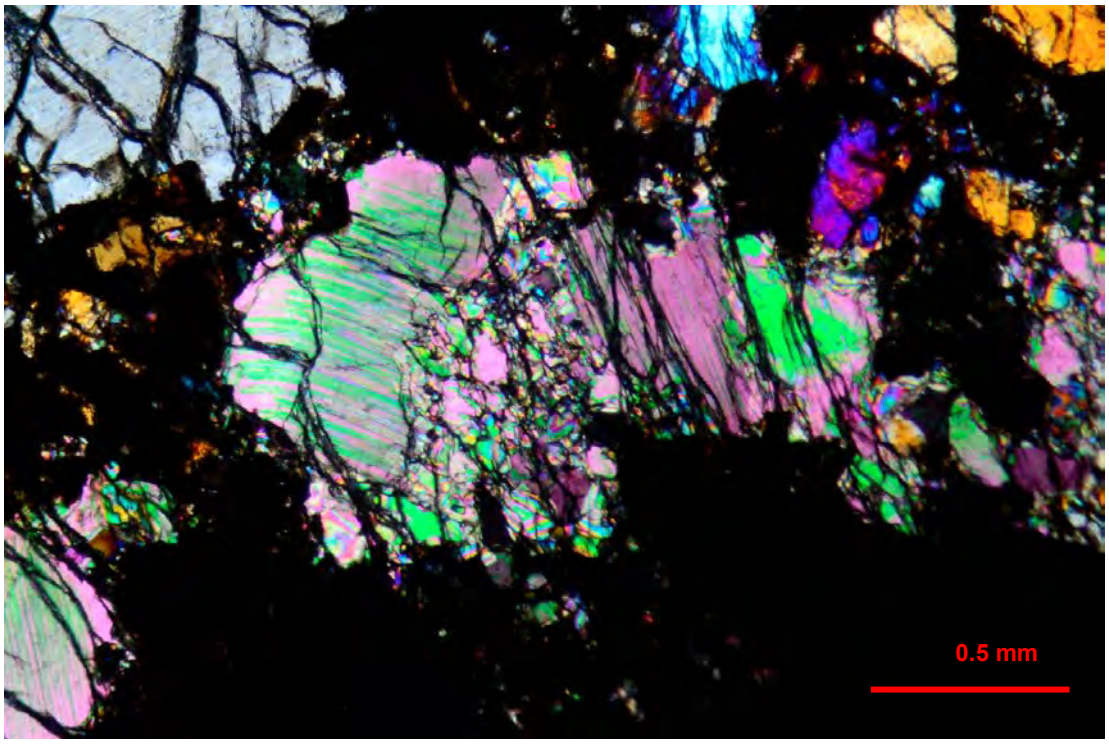

Fig. 2.2.1.17 - Medium-grained complex-shaped clinopyroxene with jagged rims, affected by partial replacement by very fine -grained neoblasts, and showing mechanical twinning and slight bending. Sample 32-32. Crossed nicols.

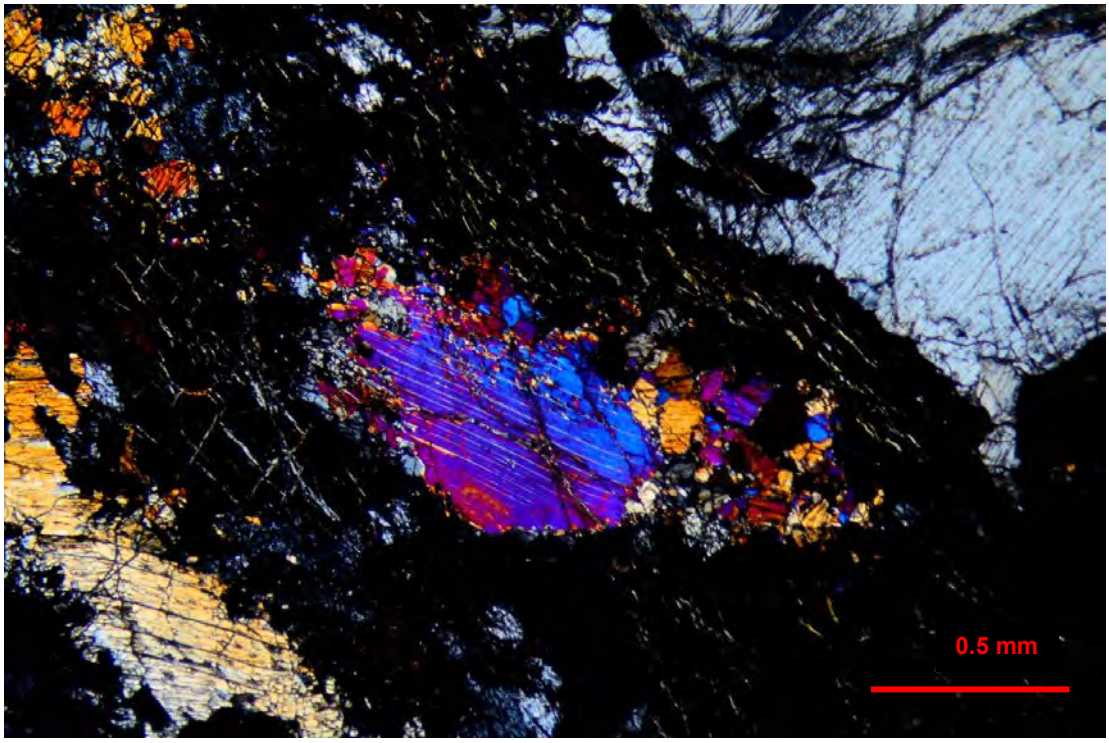

Fig. 2.2.1.18 - Medium-grained sub-ovoid clinopyroxene affected by partial replacement by very fine -grained neoblasts, showing mechanical twinning and slight bending. Sample 32-32. Crossed nicols.

Sample 33-01: sample 32-01 is a spinel-lherzolite (clinopyroxene 24.3% and opx 8.5%) containing plagioclase (5.6%) with an estimated degree of impregnation of 13%.

Olivine appears totally replaced by alteration products, i.e. a homogeneous groundmass made of brownish Fe-hydroxides (± clay minerals?), in which the preserved pervasive network of veins suggests the presence of an earlier serpentinitic matrix.

Orthopyroxene displays coarse to medium to fine grain-size. Coarse- to medium- grained orthopyroxene mostly occur as complex-shaped, irregular-rimmed, disjointed items, occasionally showing wedge-shaped fractures, but some elongated crystals are also present. Coarse orthopyroxene often appear surrounded by fine-grained poly-mineral aggregates. Coarse-grained clinopyroxene is absent; it mostly occurs as medium-grained crystals showing complex and disjointed shapes, or, more rarely, sub-rounded with quite straight rims; moreover, many clusters of small interstitial grains are also present. Larger clinopyroxene may contain inner sulfides intergrowths.

Spinel mostly occurs closely associated to plagioclase; it forms either isolated holly-leaf-shaped crystals (up to 2 mm), sometimes embedded in plagioclase patches, or swarms of small vermicular (or interstitial?) grains isoriented and gathered in bands. Plagioclase forms patches permeating the whole rock and locally isoriented. Often patches have elongated and sinuous shapes, sometimes resembling deformation gashes (foto). Locally spinel together with plagioclase may from bands of isoriented patches.

Sample 33-05: sample 33-05 is a spinel-lherzolite (clinopyroxene 24.3% and opx 8.5%) containing plagioclase (8.5%) with an estimated degree of impregnation of 20%.

Olivine appears totally replaced by alteration products, i.e. a homogeneous groundmass made of brownish Fe-hydroxides (± clay minerals?), in which the preserved pervasive network of veins suggests the occurrence of an earlier serpentinitic matrix.

Orthopyroxene occurs as coarse- to medium- to fine-grained crystals. Coarser orthopyroxene appears complex-shaped, irregular-rimmed and often disjointed in several shreds. Coarse- to medium-grained items also may show more regular shapes such as ovoid and elongated with quite smooth rims. Medium- to fine-grained orthopyroxene mainly occurs in poly-mineral aggregates.

Clinopyroxene occurs as medium- to fine-grained crystals. Medium clinopyroxene shows features similar to medium orthopyroxene as regards the shape; medium- to fine-grained clinopyroxene occasionally form pockets of sub-euhedral crystals, whereas many clusters of interstitial small grains occur scattered throughout the rock.

Cr-spinel forms holly-leaf-shaped crystals often associated with plagioclase.

Plagioclase is pretty fresh and forms clusters of sub-rounded to elongated patches spread throughout the rock, locally interweaved with interstitial clinopyroxene grains and/or associated with spinel.

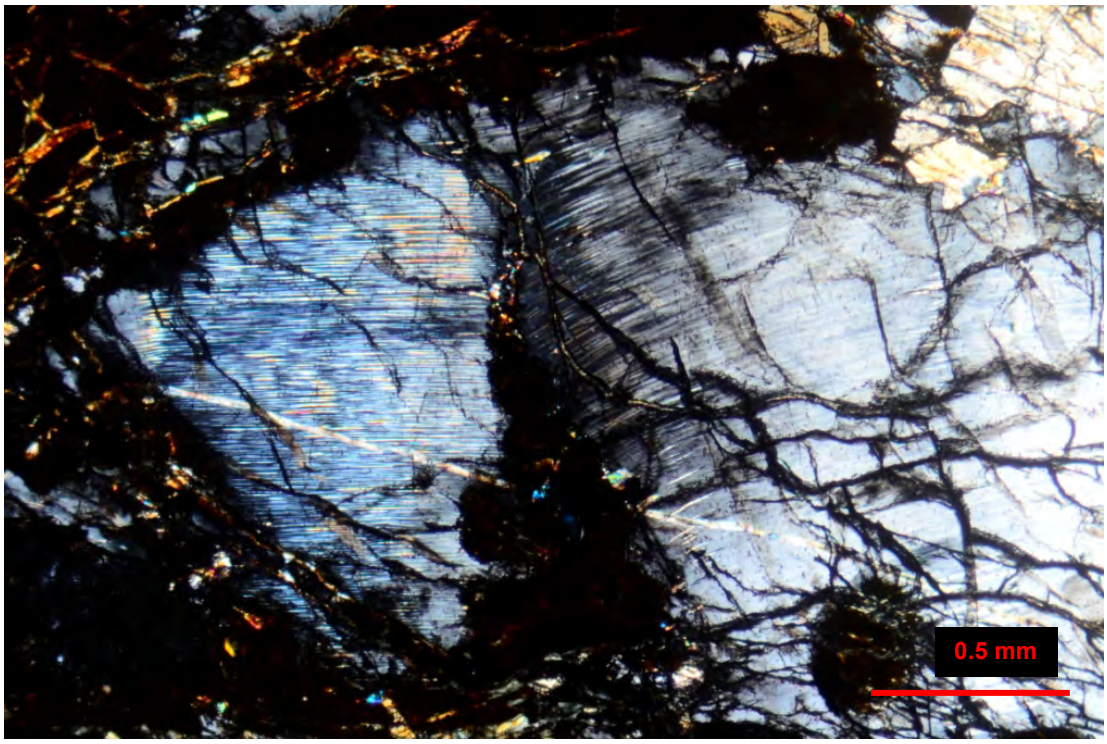

Fig. 2.2.1.19 - Irregular-shaped coarse orthopyroxene disjointed by a wedge-shaped fracture filled with olivine, now totally altered. Sample 32-05. Crossed nicols.

2.2.2 Plagioclase textures

The peculiarity of these rocks is the presence of plagioclase (from 0.4% in sample 39-36 to 16.4% in sample 32-07), occurring in several different textural types and mineral assemblages.

As a rule, plagioclase occurs as interstitial patches randomly spread throughout the rock, tracing out an interstitial network: i) along ol-ol grain boundaries, ii) along ol-pyroxene and pyroxene-pyroxene grain boundaries, iii) inside coarse clinopyroxene associated with orthopyroxene, and iv) inside dikelets and fractures within the serpentine matrix and within large pyroxene.

Plagioclase appears highly variable as regards to grain size and shape, both of which may depend on the site of crystallization. Size varies from less than 1 mm up to 2-3 mm. Plagioclase mainly forms clusters of partially interconnected, sub-triangular or blebby patches, which permeate both olivine groundmass (figs. 2.2.2.1 and 2.2.2.2) and granular px±ol mosaics (fig. 2.2.2.3). Patches may show preferred orientation, either locally or at the scale of the thin section. Plagioclase may develop along olivine-large pyroxene contacts, resulting in embayments in the pyroxene rims due to the penetration of blebby patches (fig. 2.2.2.4). Furthermore, plagioclase is also found within thin dikelets and sigmoidal en echelon fractures in the olivine matrix (figs. 2.2.2.5 and 2.2.2.6), or within displacements in large pyroxene.

Plagioclase patches often occur texturally associated with small amount of pyroxene, which may forms thin belts partially bordering plagioclase patches (figs. 2.2.2.5, 2.2.2.6 2.2.2.9 and 2.2.2.10), or forms small interstitial grains interweaved with plagioclase patches. Plagioclase associated with orthopyroxene may occur in patches inside large clinopyroxene (fig. 2.2.2.8). Occasionally, holly-leaf spinel may be partially or totally embedded in plagioclase patches, or bordered by thin plagioclase coronas, or form tiny grains texturally associated with plagioclase.

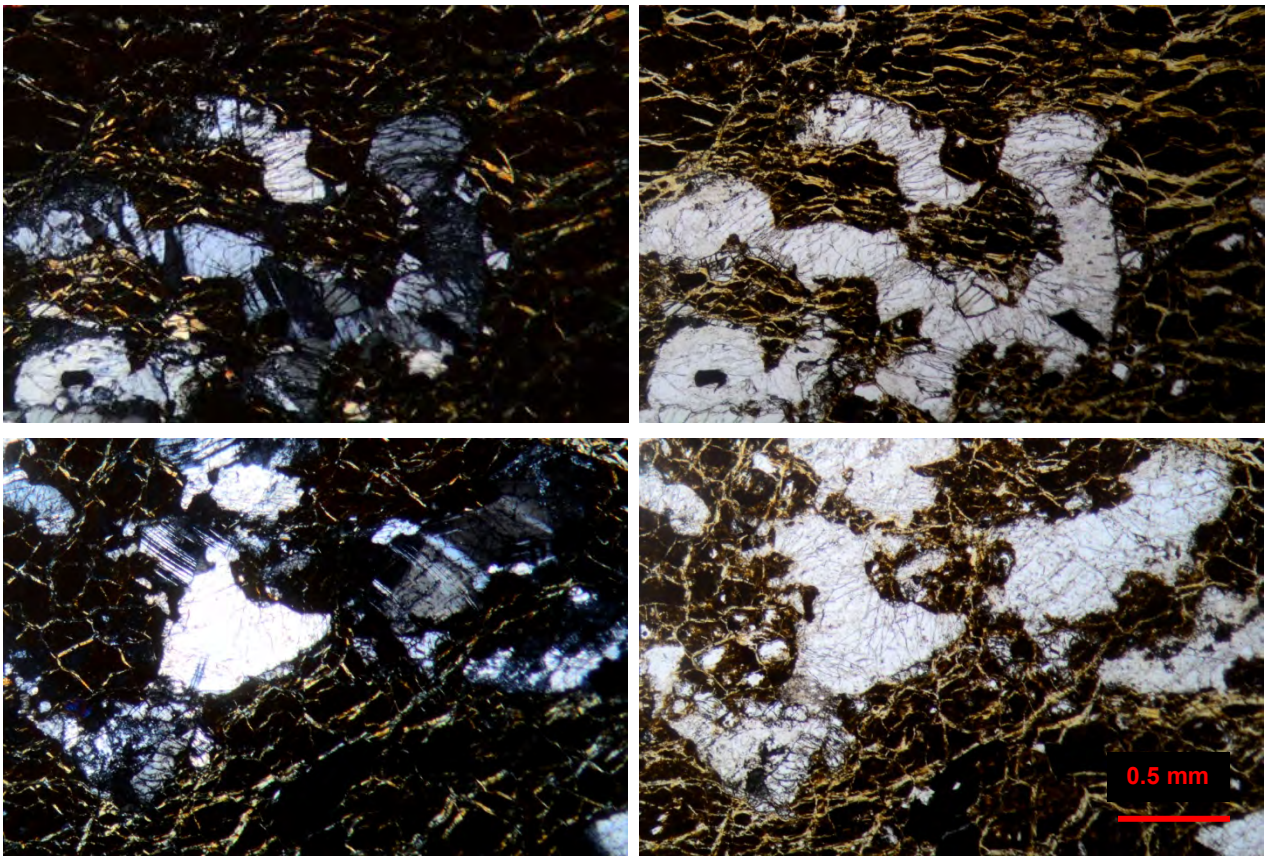

Fig. 2.2.2.1 - Sub-triangular partially interconnected plagioclase patches developed along ol-ol grain boundaries; olivine has been replaced later by alteration products (brown groundmass). Sample 32-07. Crossed nicols (on the left) and plain light (on the right).

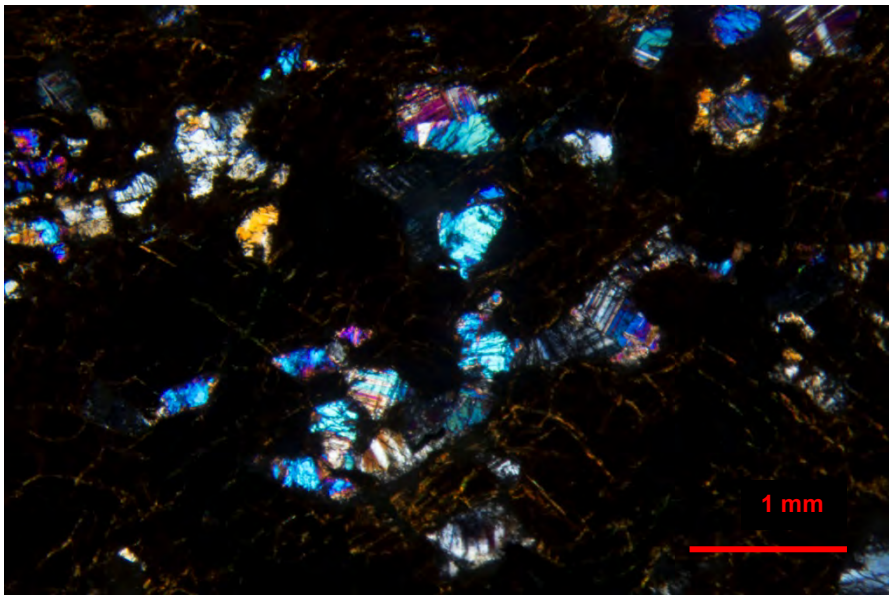

Fig. 2.2.2.2 - Sub-triangular partially interconnected plagioclase patches developed along ol-ol grain boundaries; olivine has been replaced later by alteration products (brown groundmass). High interference colors of plagioclase are due to slightly higher thickness of the thin section. Sample 33-05. Crossed nicols

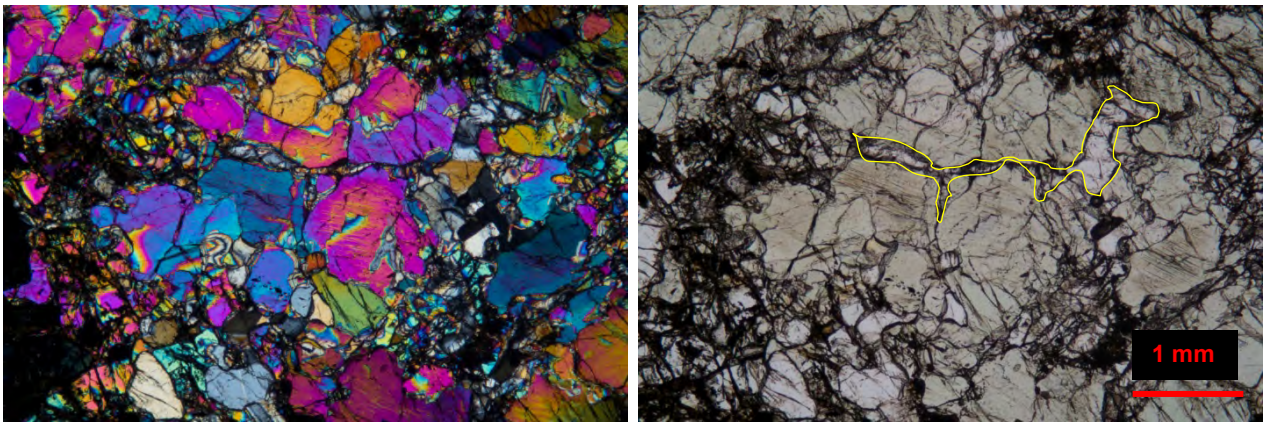

Fig. 2.2.2.3 - Plagioclase patches (yellow outline in the right) penetrating the interstices of medium- to fine-grained granular mosaic containing px+ol. Sample 32-22. Crossed nicols (left) and plain light (right).

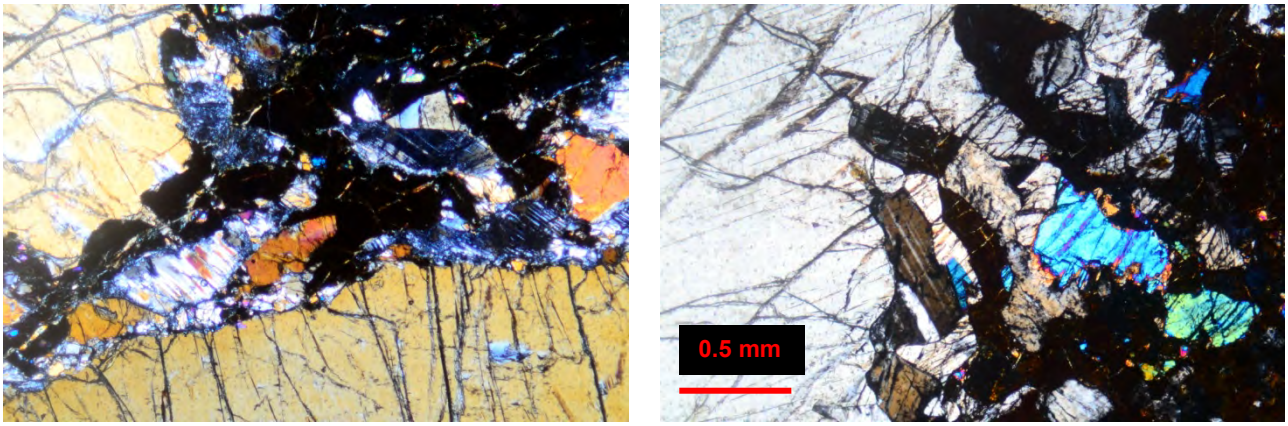

Fig. 2.2.2.4 - Plagioclase patches developing along opx-ol grain boundaries, ad penetrating the orthopyroxene rim (right). Crossed nicols.

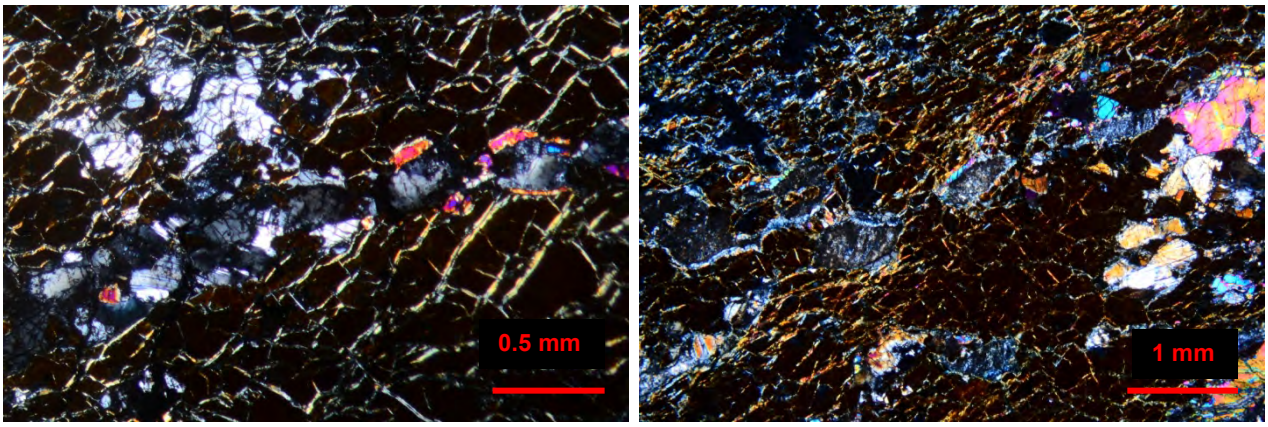

Fig. 2.2.2.5 - Deformation structures within the olivine groundmass filled by plagioclase and clinopyroxene: thin dikelet (left, sample 32-07) and en echelon small fractures (right, sample33-05). Crossed nicols.

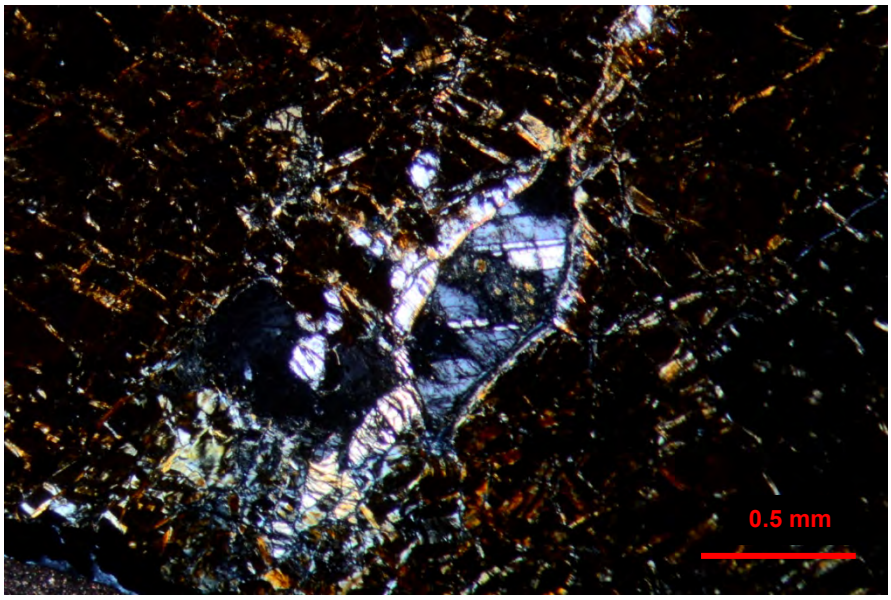

Fig. 2.2.2.6 - Sigmoidal fracture within the altered olivine matrix (brown groundmass) filled with rather fresh plagioclase partially bordered by altered pyroxene. Plagioclase crystallization might be subsequent to fracturing. Sample 33-01. Crossed nicols.

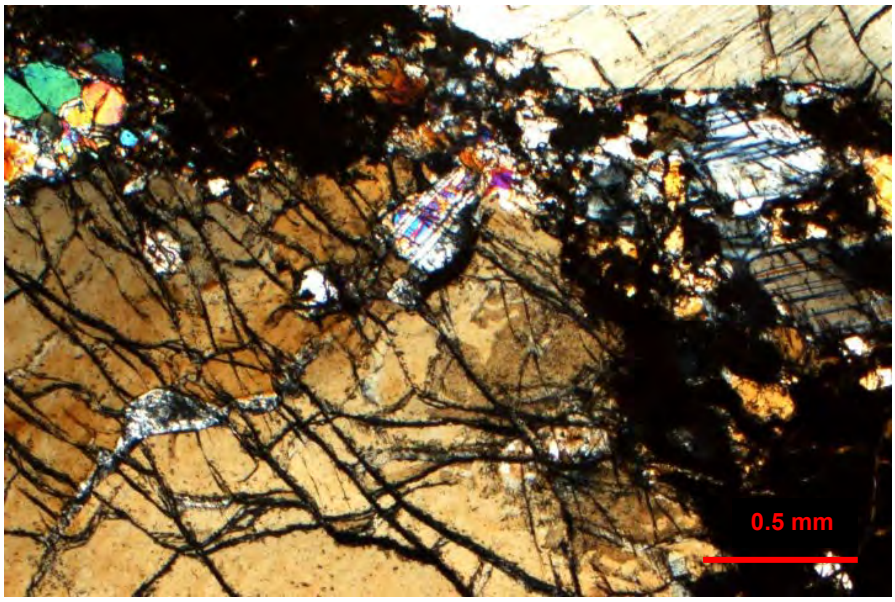

Fig. 2.2.2.7 - Plagioclase penetrating within a fracture in coarse orthopyroxene crystal. Sample 32-32. Crossed nicols.

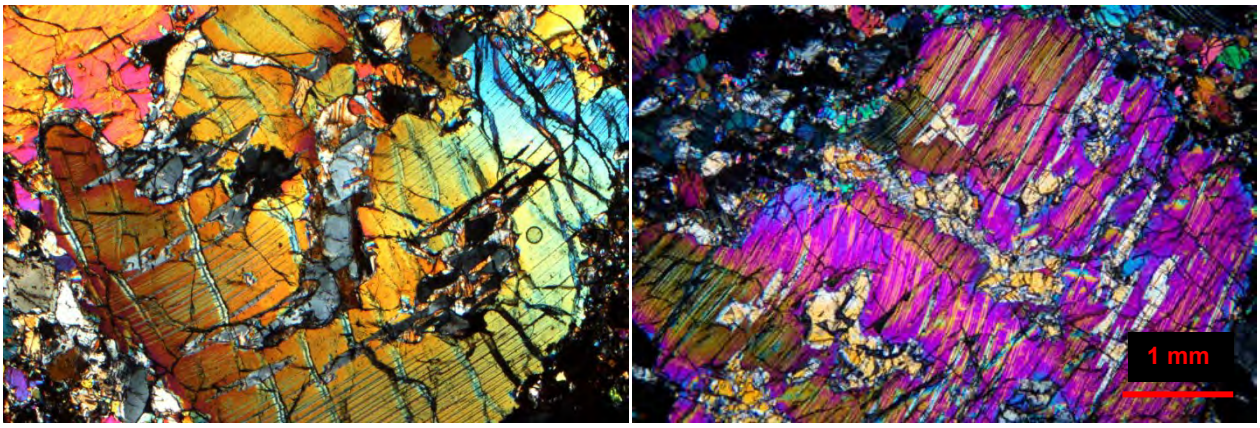

Fig. 2.2.2.8 - Coarse-grained cpx, surrounded by halos of fine-grained poly-mineralic aggregates; plagioclase together with orthopyroxene forms patches inside the coarse cpx. Sample 32-22. Crossed nicols.

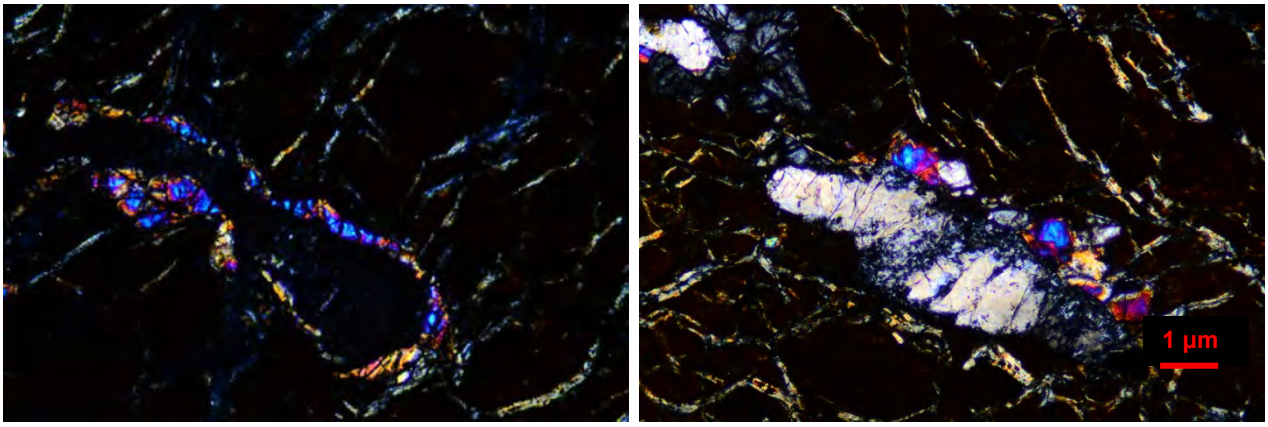

Fig. 2.2.2.9 - Partially altered plagioclase patches surrounded (on the left) and partially bordered (on the right) by thin belts of clinopyroxene, within the altered olivine matrix. Sample 32-07. Crossed nicols.

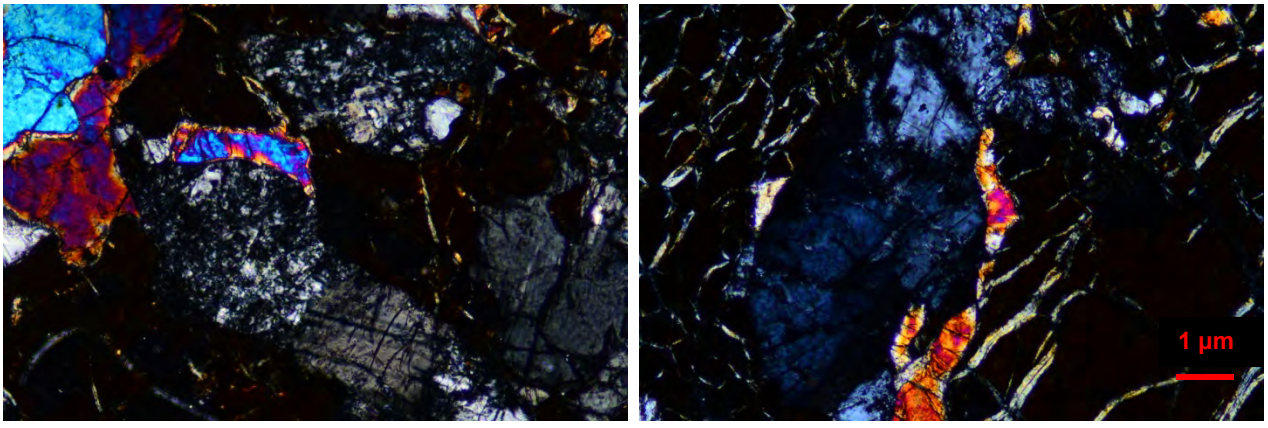

Fig. 2.2.2.10 - Partially altered plagioclase patches partially bordered by thin belts of clinopyroxene, within the altered olivine matrix. Sample 32-07. Crossed nicols.

2.2.3 Rock alteration

Olivine appears almost completely altered and thus replaced by serpentine in the typical *mesh structure* (Aumento and Loubat, 1971; Wicks and Wittaker, 1977; Prichard, 1979) ± magnetite. In some samples the rock groundmass is made of brownish Fe-hydroxides ± clay minerals, due to pseudomorphic substitution on the earlier serpentinitic matrix as suggested by the preserved pervasive network of veins (fig. 2.2.3.1). Orthopyroxene appears less altered than olivine, being sometimes partially replaced by pseudomorphic fibrous-yellowish bastite or, rarely, by serpentine. Alteration mainly affects the rim of the large orthopyroxene or fills fractures, and rarely replaces the entire crystal. When present, exsolution lamellae of clinopyroxene inside bastite replacing residual orthopyroxene can be preserved nearly fresh because of the higher resistance of clinopyroxene to alteration with respect to orthopyroxene. Rock alteration also involves spinel, which appears gradually replaced by magnetite from rim to core. Plagioclase may occur from totally altered to pretty fresh, with well-defined typical twinnings. Mineral composition of alteration products of plagioclase cannot be detected by the observation at the optical microscope, but they probably consist of an ensemble of clay minerals, phillosilicates (micas and others), hydro-garnet and sericite.

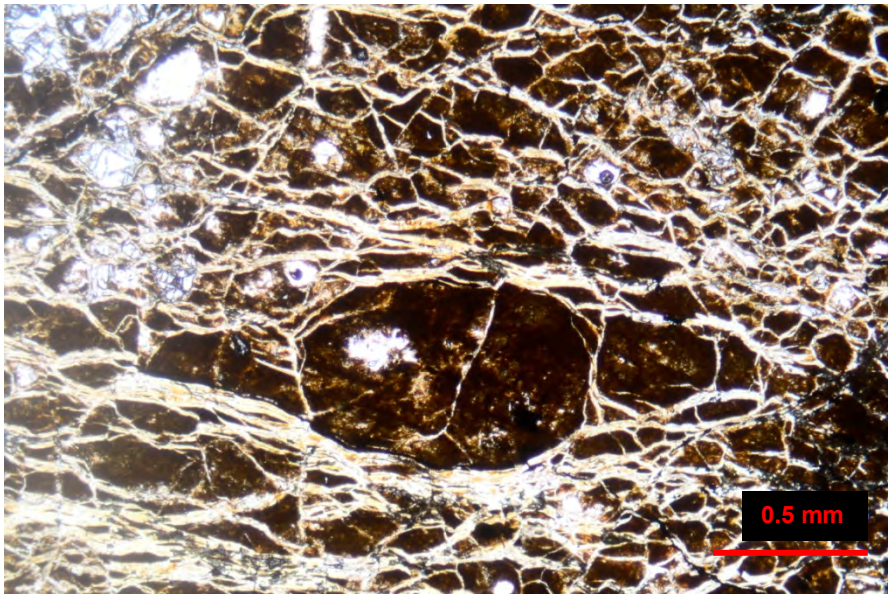

Fig. 2.2.3.1 - Pervasive network of alteration veins affecting the brownish Fe-hydroxides groundmass, suggesting pseudomorphic substitution of an earlier mesh-structured serpentinitic matrix. Sample 32-07- Plain light.

2.2.4 Brittle and ductile intracrystalline deformation

Intracrystalline deformation mostly affects residual pyroxenes; brittle deformation results in kink bands (fig. 2.2.4.1), micro-faults, micro-fractures. Often these structures are superimposed by the precipitation of plagioclase (fig. 2.2.4.2) or by dissolution for the benefit of olivine. Evidences of ductile deformation of orthopyroxene are also present: the most frequent structures are wavy extinction due to bending and mechanical twinning (in clinopyroxene); dynamic re-crystallization of neoblasts may also occurs. Coarse-grained olivine may be affected by wavy extinction and gliding. Rarely plagioclase patches shows evidences of slight deformation, i.e. undulouse extinction and tapering lamellar twins (Dijkstra et al., 2001) (fig. 2.2.4.3).

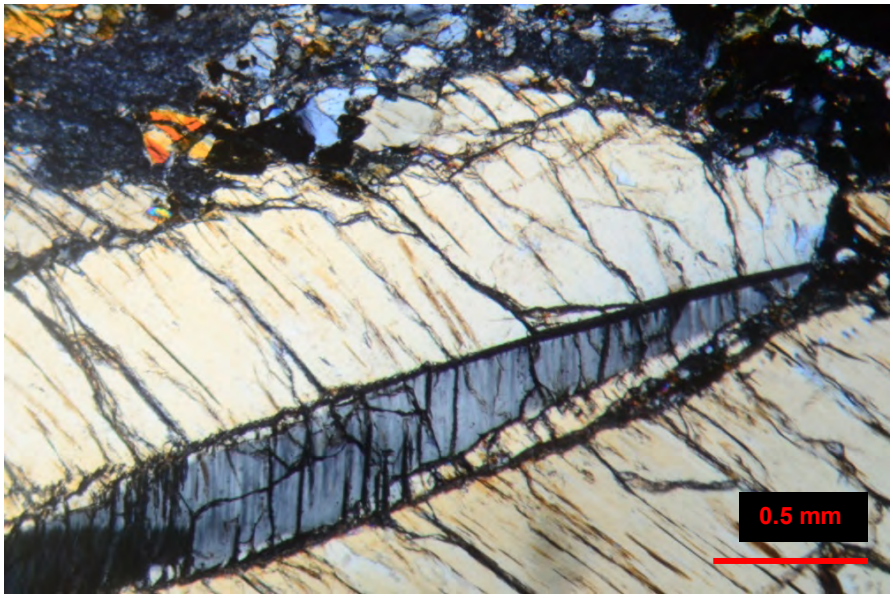

Fig. 2.2.4.1 - Kink band in a large orthopyroxene. Fine-grained orthopyroxene aggregate develops along the suture line of the kink. Sample 32-14. Crossed nicols.

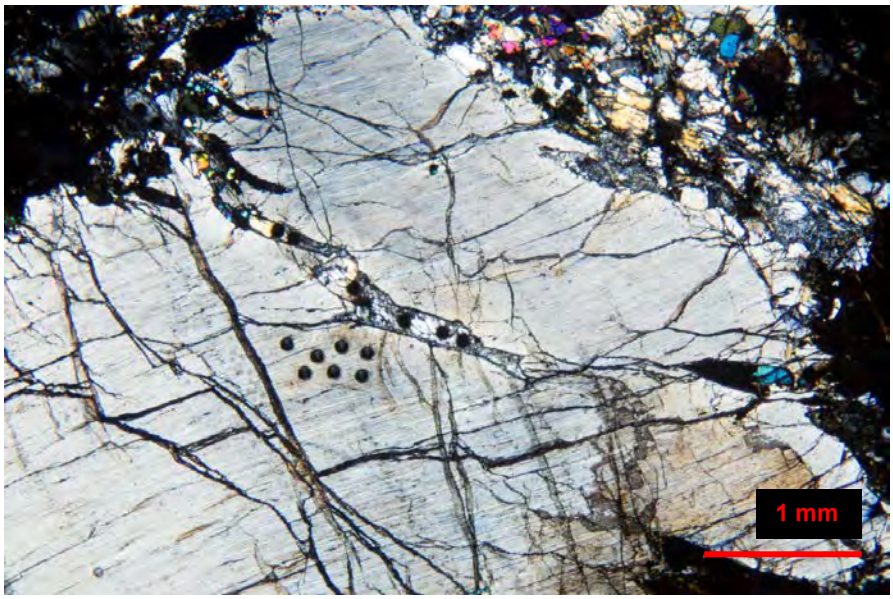

Fig. 2.2.4.2 - Fracture (and displacement) in a large orthopyroxene filled by plagioclase, +opx+cpx+ol+sp. Plagioclase precipitation might be later with respect to fracturing. Dark spots are due to laser ablation. Sample 32-22. Crossed nicols.

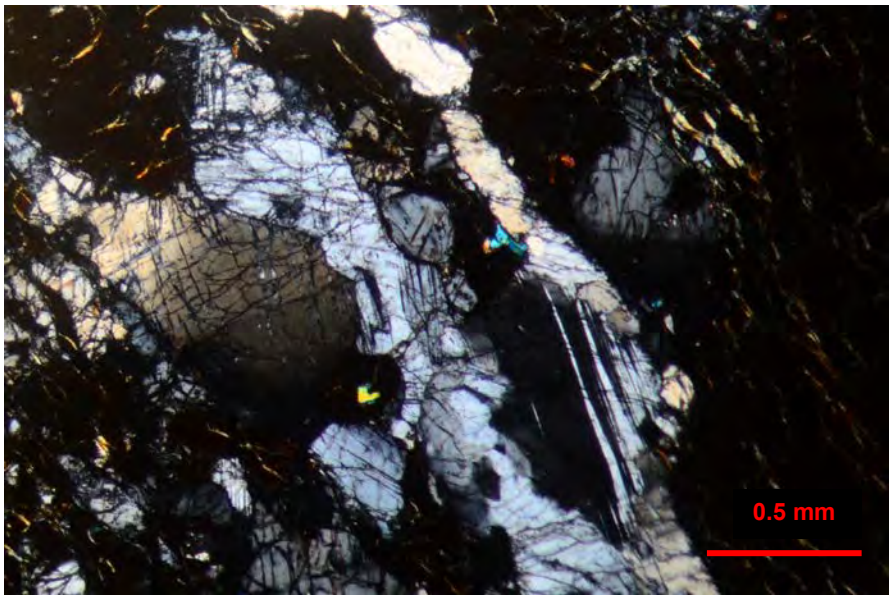

Fig. 2.2.4.3 - Fresh plagioclase patch affected by undulouse extinction, suggesting slight intracrystalline deformation. Sample 32-07. Crossed nicols.

2.3 Summary

2.3.1 Petrography

Studied samples consist of plagioclase-bearing spinel-lherzolites, with plagioclase ranging from 0.4% (sample 39-36) to 15.5% (sample 32-22).

By macro- and microscopic observation of the studied samples, it appears that samples of dredge #39 differ from samples of dredges #32 and #33 for the degree of alteration of the olivine groundmass, being rather fresh in samples of dredge 39, whereas completely altered in samples of dredges #32 and #33. Therefore the textural features of olivine are described on the basis of samples 39-28 and 39-36.

The olivine groundmass consists of a heterogranular mosaic which displays trimodal grain-size distribution. Coarse-grained (up to 10 mm) elongated olivine crystals show smooth and curvilinear grain boundaries and lattice preferred orientation, defining the rock foliation. Both medium- (around 5 mm) and fine- (around 1 mm) grained olivine form equigranular clusters of sub-rounded (medium) and sub-euhedral (fine) crystals, but elongated and anhedral grains of both grain-sizes are also present. Medium- to fine-grained olivine mainly develop along ol-ol, but also ol-pyroxene grain boundaries, locally replacing coarse- (the former) and medium-grained (the latter) olivine. Fine-grained olivine is rare in sample 39-36, whereas it is relatively abundant in sample 39-28, in which it forms heterogranular, euhedral mosaics, occasionally associated with pyroxene and sp (fig. 2.3.1.1). In both samples, very-fine grained (up to 0.03 mm) ol may occur in aggregates together with orthopyroxene and occasionally interstitial sp, mostly developing along opx-opx or ol-opx grain boundaries or along fractures inside orthopyroxene.

In samples of dredges #32 and #33 the olivine texture is totally obscured by a homogeneous brownish mass, in which lie several pyroxene crystals of various size, the largest of which usually show halos of finer-grained aggregates.

Apart from the different degree of alteration of the olivine matrix, the two groups of samples show similar textures and structures as regards pyroxenes. As a rule, in all samples pyroxenes mainly display trimodal grain-size distribution (coarse, medium and fine). Coarse- to medium-grained pyroxene may have strongly unsettled appearance, showing complex shapes, dismemberments in two or more shreds of various sizes, embayed and jagged outlines, together with evidences of brittle and ductile deformation, such as kink-banding and strong fracturing for the former and bending and wavy extinction for the latter. They may also appear affected by partial replacement by finer neoblasts. Then, medium- to fine-grained pyroxene are also present, displaying a wide range of textures - from completely disjointed and irregular-shaped to sub-euhedral and sub-rounded with quite smooth rims - and sometimes occurring in poly-mineralic aggregates associated with ol, pl and/or sp.

In samples of dredge #39 the occurrence of medium- to fine-grained clusters of olivine along ol-pyroxene contacts results in the development of embayed and jagged outlines in pyroxene, due to penetration of olivine grains into the rims of pyroxenes. Moreover, when in contact with the fine-grained olivine mosaic,

coarse to medium pyroxene appear disjointed, irregular-shaped and partially replaced by equigranular, euhedral, fine-grained aggregates of orthopyroxene (in orthopyroxene) and clinopyroxene (in clinopyroxene) + ol, overall resulting in the development of distinct zones (at the scale of the thin section) of pervasive grain-size reduction (from coarse to medium to fine), mainly involving olivine and secondly orthopyroxene and clinopyroxene (fig. 2.3.1.2).

Therefore, it can be inferred that embayed and jagged outlines characterizing coarse- to medium- grained pyroxene in samples of dredge #32 and #33 are due to the growth of medium- to fine- grained olivine along ol-pyroxene grain boundaries, by analogy with samples of dredge #39. Moreover, although in samples of dredge #32 and #33 the olivine texture appears obscured by alteration products, grain-size distribution and habit of olivine might be locally inferred from sizes and shapes of given embayments on pyroxene rims. Similarly, the extremely complex shapes affecting medium- to fine-grained pyroxene in samples of dredge #32 and #33 could be explained considering them as residual shreds of earlier coarse crystals, which underwent pervasive grain-size reduction occurring simultaneously with crystallization of either medium- or fine-grained olivine (as clearly observed in samples of dredge #39) (fig. 2.3.1.1), which later have been totally replaced by alteration products (fig. 2.3.1.2).

In all samples spinel generally appears as holly-leaf-shaped grains spread throughout the rock, occasionally associated with patches of plagioclase or rimmed by plagioclase coronas. However, sample 39-36 represents an exception, being the only sample containing vermicular spinel, together with several other small holly-leaf-shaped grains. Vermicular spinel occurs in cpx+opx+sp symplectitic intergrowths developing along opx-ol grain boundaries or within the serpentinitic matrix, respectively resembling "S2" and "S1" symplectites described by Seyler et al. (2007).

Plagioclase appears almost totally replaced by alteration products in samples of dredge #39, whereas it displays a wide range of degree of alteration in samples of dredge #32 and #33": from extremely fresh to totally altered. Anyway, plagioclase displays similar textural environments in both groups of samples. In samples of dredge #39, being the olivine fabric almost totally preserved, it is noticeable that plagioclase patches mostly show preferred orientation concordant with the rock foliation, and, moreover, that patches tend to gather in zones of pervasive grain-size reduction of both olivine and pyroxenes, mostly permeating the interstices of the granular mosaics (fig. 2.3.1.3).

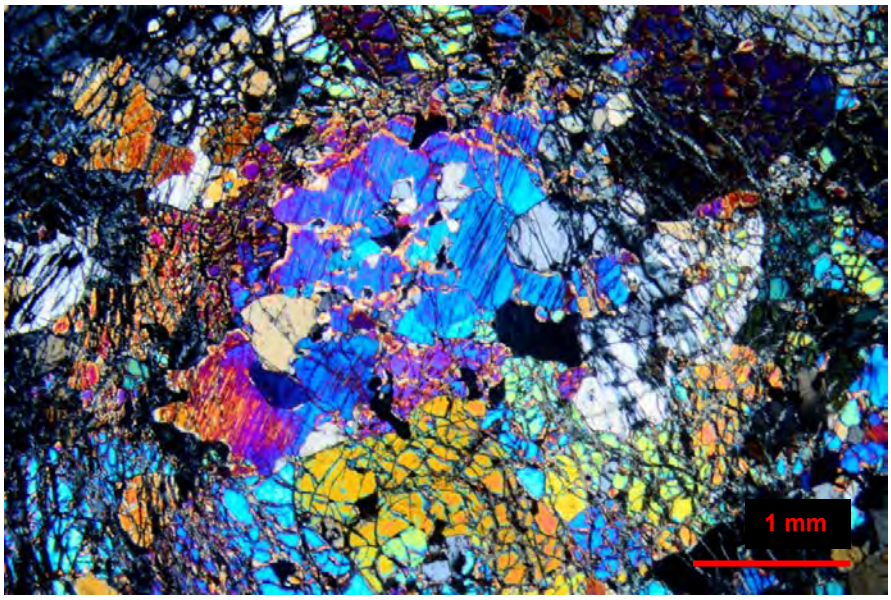

Fig. 2.3.1.1 - Heterogranular medium- to fine-grained mosaic of ol+cpx. Blue clinopyroxene probably represents an earlier coarse-grained crystal which have been unsettled by growth of medium- to fine grained olivine and dynamic re-crystallization of neoblasts. Sample 39-28. Crossed nicols.

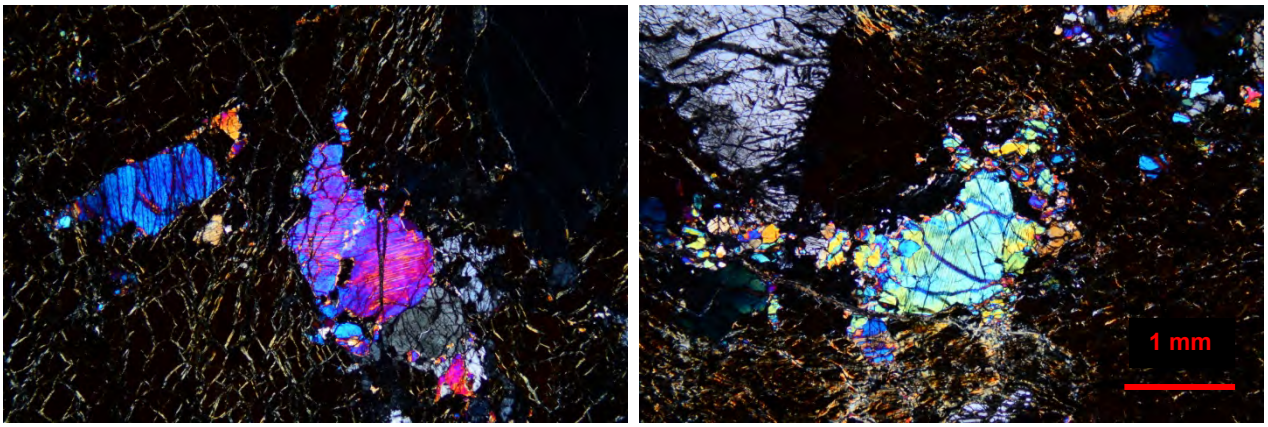

Fig. 2.3.1.2 - Irregular-shaped, medium-grained "shreds" of clinopyroxene, probably representing earlier coarse-grained crystals which have been unsettled by growth of medium- to fine grained olivine, now totally altered, and dynamic re-crystallization of neoblasts. Sample 32-07 (left) and 32-03 (right). Crossed nicols.

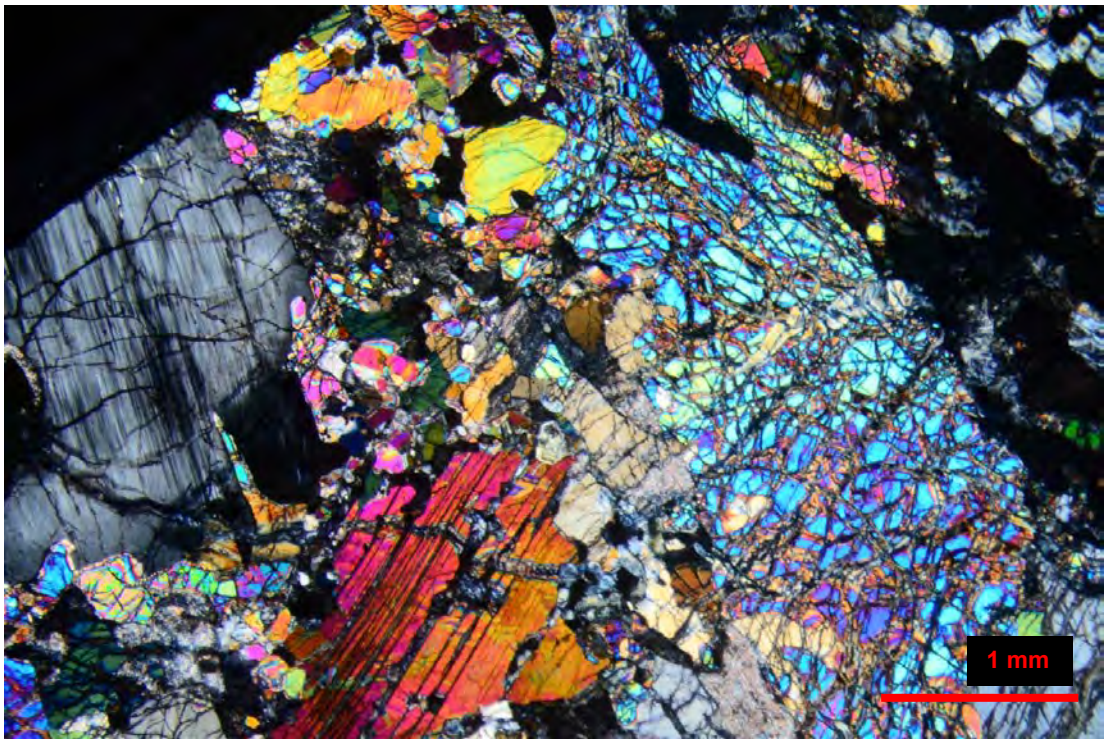

Fig. 2.3.1.3 - Contact between a coarse crystal of olivine (turquoise band) and a zone of pervasive grain-size reduction (in the middle left), in which some residual shreds of opx and cpx are present; the zone of pervasive grain size reduction appears permeated by several isoriented patches of plagioclase (altered). Sample 39-28. Crossed nicols.

Chapter 3
Major elements

3.1 Methods

Major element composition of relict primary and secondary phases has been determined by in situ quantitative analysis using the electron microprobe Jeol JXA8200 at the University of Milan, Italy. Mineral phases were measured using an acceleration potential of 15 kV, a beam current of 5 nA and a spot size of 1 and 5 μm. Acquisition time is 30 seconds per each element, except for Na that has been analyzed for 20 seconds. A set of international standards have been used for internal linearization (tab. 3.1.1).

Table 3.1.1 -. List of the international standards

Element	Standard
Si	Wollastonite
Ca	Anorthite 137
Al	Anorthite 137
Fe	Fayalite 143
Mg	Olivine 153
Na	Omphacite 154
Mn	Rodonite
Ni	Niccolite
Ti	Ilmenite
Cr	Pure

In order to define the micro-chemical features of the studied rocks, four best representative samples were selected on the basis of least degrees of alteration and wider range of occurring micro-textures. Selected samples are: 32-07, 32-22, 32-32 and 39-36.

All the analytical results of major elements are reported in Appendix A.

3.2 Major elements compositions of the studied samples

Major and minor element compositions of the main phases ol, orthopyroxene, clinopyroxene, spinel and plagioclase have been measured in samples 32-07, 32-22, 32-32 and 39-36. In order to obtain as wide as possible ranges of compositions, each point in the following plots represents a single measure.

The observed values are then compared with the fields of compositional variability of published mid-ocean ridge plagioclase-free (Michael and Bonatti, 1985) (Dick, 1989) (Brunelli et al., 2006) and plagioclase-bearing peridotites (Dick et al., 2010); (Tartarotti et al., 2002).

3.2.1 Olivine

Fresh olivine has been detected in all the studied samples but one (sample 32-07).
Olivine analyses have been grouped after discriminating coarse- to medium-grained crystals from fine grains. Coarse- to medium- grained crystals have been detected only in samples 39-36 and 32-22, whereas fine grains were detected in all samples.
In all samples olivine shows very homogeneous Fo content, regardless of textural position, ranging from 89 to 90, and values appear slightly lower compared to other plagioclase-free abyssal peridotites, except for sample 39-36. Olivine chemical data of other published plagioclase-bearing peridotites are not available for comparison.
NiO, that behaves as compatible element, appears homogenously spread in all samples, ranging from 0.30% wt. to 0.48% wt. Samples are slightly enriched in NiO with respect to other plagioclase-free abyssal peridotites (Figure 3.2.1). Fo and NiO contents do not show any clear correlation.
Depending on data availability, as regards olivine the observed values were compared only with those of plagioclase-free abyssal peridotites from Dick (1989).

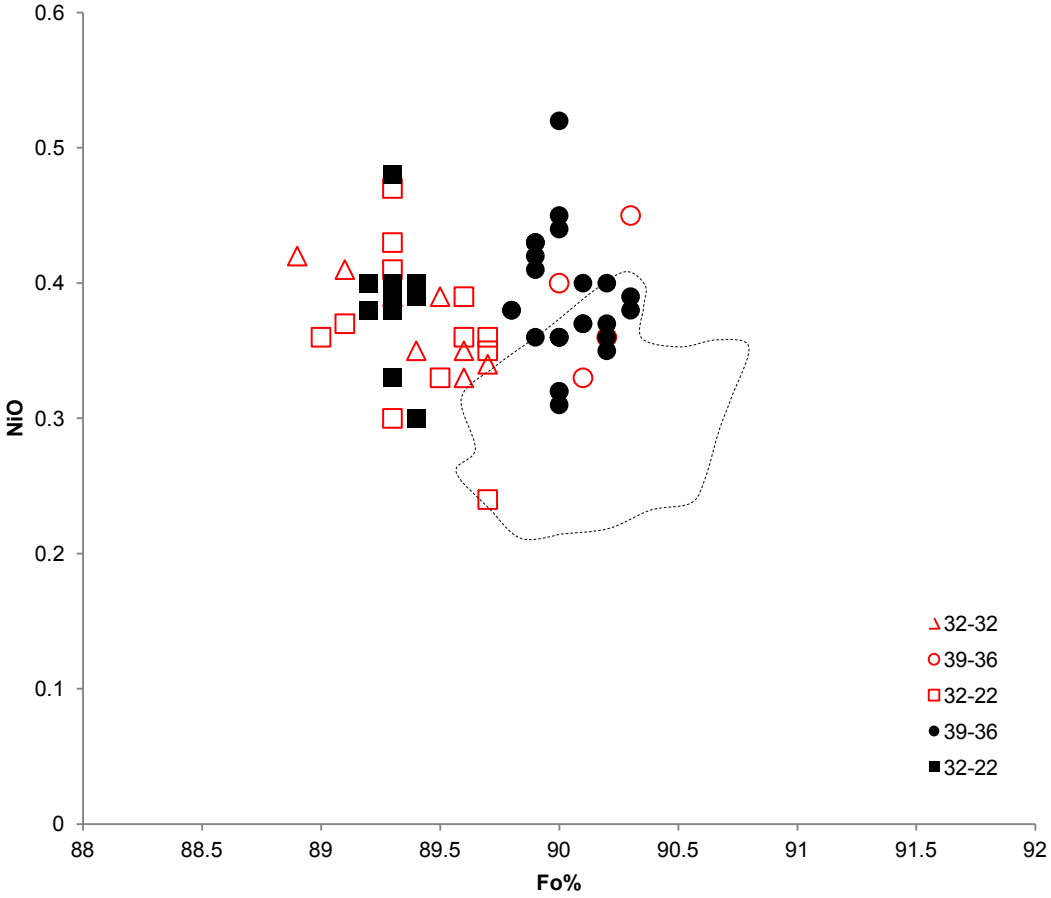

Figure 3.2.1 - NiO vs. Fo% in olivine of analysed samples. Red open symbols represent fine-grained crystals whereas black solid symbols represent medium and coarse crystals. Dashed area represents the compositional field defined by plagioclase-free abyssal peridotites from Dick (1989).

3.2.2 Pyroxene

Major element composition of pyroxenes have been analyzed in all studied samples. Pyroxenes are present in form of medium- to coarse-sized residual and deformed crystals, of which distinct measurements of cores and rims have been determined, or in form of medium- to fine-grained crystals, often occurring in poly-mineralic aggregates, without distinction between core and rim due to the small size.

Orthopyroxene

Orthopyroxene Al_2O_3 ranges from 1.59% wt (sample 39-36) to 5.47% wt. (sample 32-32); the core of the coarse crystals are enriched in Al_2O_3 compared to their rims, whereas the small grains record the lowest values of all.

Mg# ([100 x Mg/(Cr + Fe)] with all Fe as Fe^{2+}) ranges from 89.1 (sample 32-22) to 91.2 (sample 39-36) with no significant differences among the different textural environments; however, sample 39-36 shows

distinctly higher values with respect to samples of dredge #32 Cr# [100 x Cr/(Cr + Al)] is slightly more variable, but as much homogenous, with both the highest and the lowest values recorded in sample 32-32 (from 9.23 to 19.27). No evident correlation between Mg# and Cr# is observable (Figure 3.2.2.1).

Cr_2O_3 ranges from 0.29% wt. (sample 32-22) to 1.07% wt. (sample 39-36), generally decreasing from core to rim in the coarse crystals, whereas the small grains record the highest depletion. In all samples Al_2O_3 and Cr_2O_3 positively correlate up to Al_2O_3 ~ 3,5%; then, for Al_2O_3 values higher than 3,5%, Cr_2O_3 content is almost homogeneous (Fig. 3.2.2.2). As exceptions, few points show negative correlation, i.e. the cores of the coarse crystals in sample 32-22 and few cores and rims in sample 32-32.(Fig. 3.2.2.3)

The studied samples of dredge #32 show TiO_2 values evenly distributed among the different textural environments. TiO_2 content in samples of dredge #32 ranges from 0.11% wt. (sample 32-32) to 0.32% wt. (sample 32-07), whereas sample 39-36 is strongly depleted in TiO_2 with respect to the other samples, with a maximum value of 0.09% wt. and negligible values in many cases. Samples of dredge #32 display TiO_2 contents comparable (or even slightly higher) to those of other plagioclase-bearing abyssal peridotites, whereas sample 39-36 shows values more similar to those of plagioclase-free abyssal peridotites.

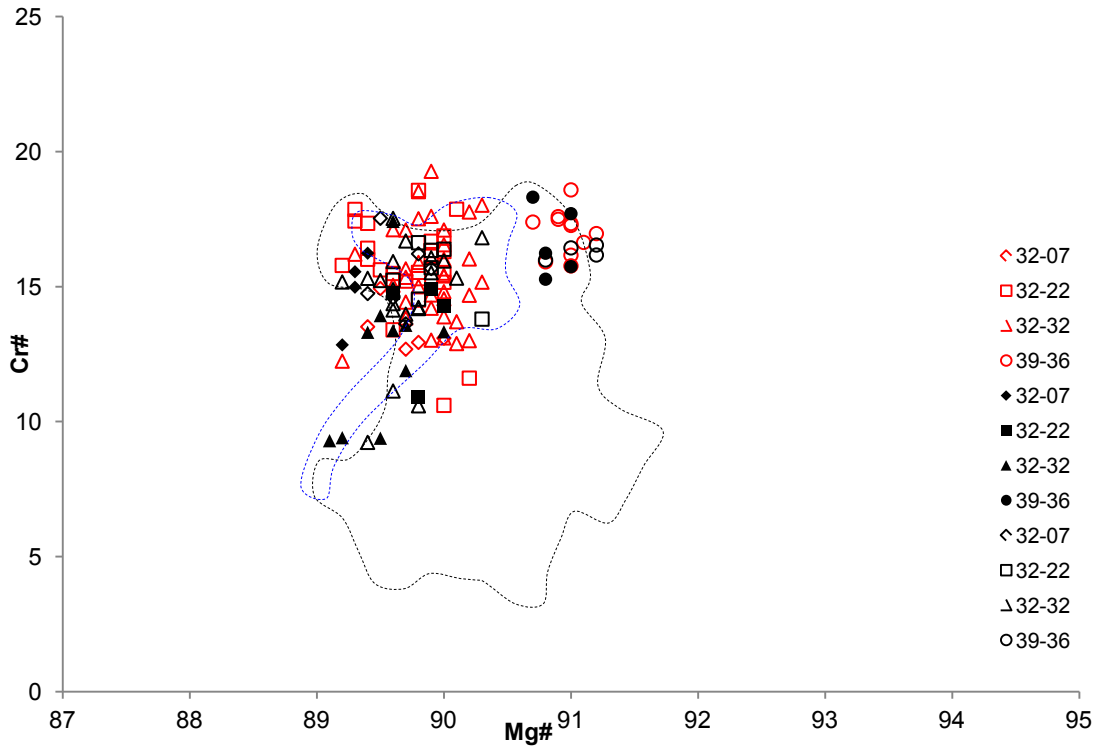

Figure 3.2.2.1 - Cr# vs Mg# in orthopyroxene in the analyzed samples. Red open symbols represent fine-grained crystals, whereas black open symbols represent the rims of the coarse crystals and black solid symbols represent the cores of the coarse crystals. Dashed black line represents compositional field of plagioclase-free abyssal peridotites, whereas dashed blue line represents compositional fields of plagioclase-bearing abyssal peridotites.

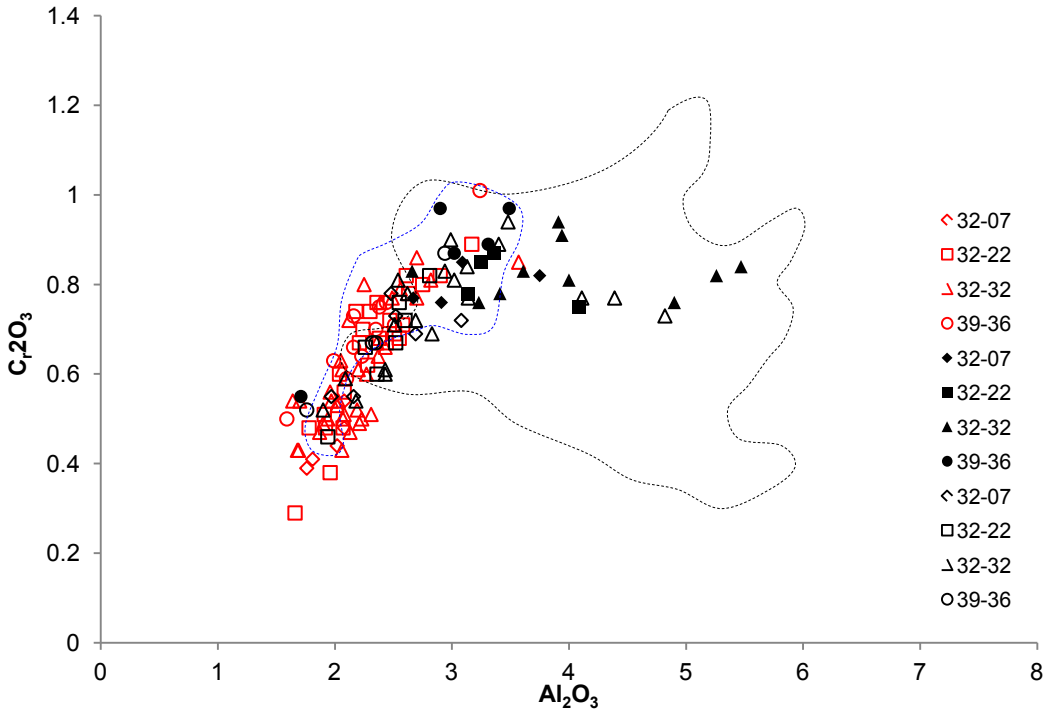

Figure 3.2.2.2 - Cr_2O_3 vs. Al_2O_3 in orthopyroxene of the analyzed samples. Red open symbols represent fine-grained crystals, whereas black open symbols represent the rims of the coarse crystals and black solid symbols represent the cores of the coarse crystals. Dashed black line represents compositional field of plagioclase-free abyssal peridotites, whereas dashed blue line represents compositional fields of plagioclase-bearing abyssal peridotites.

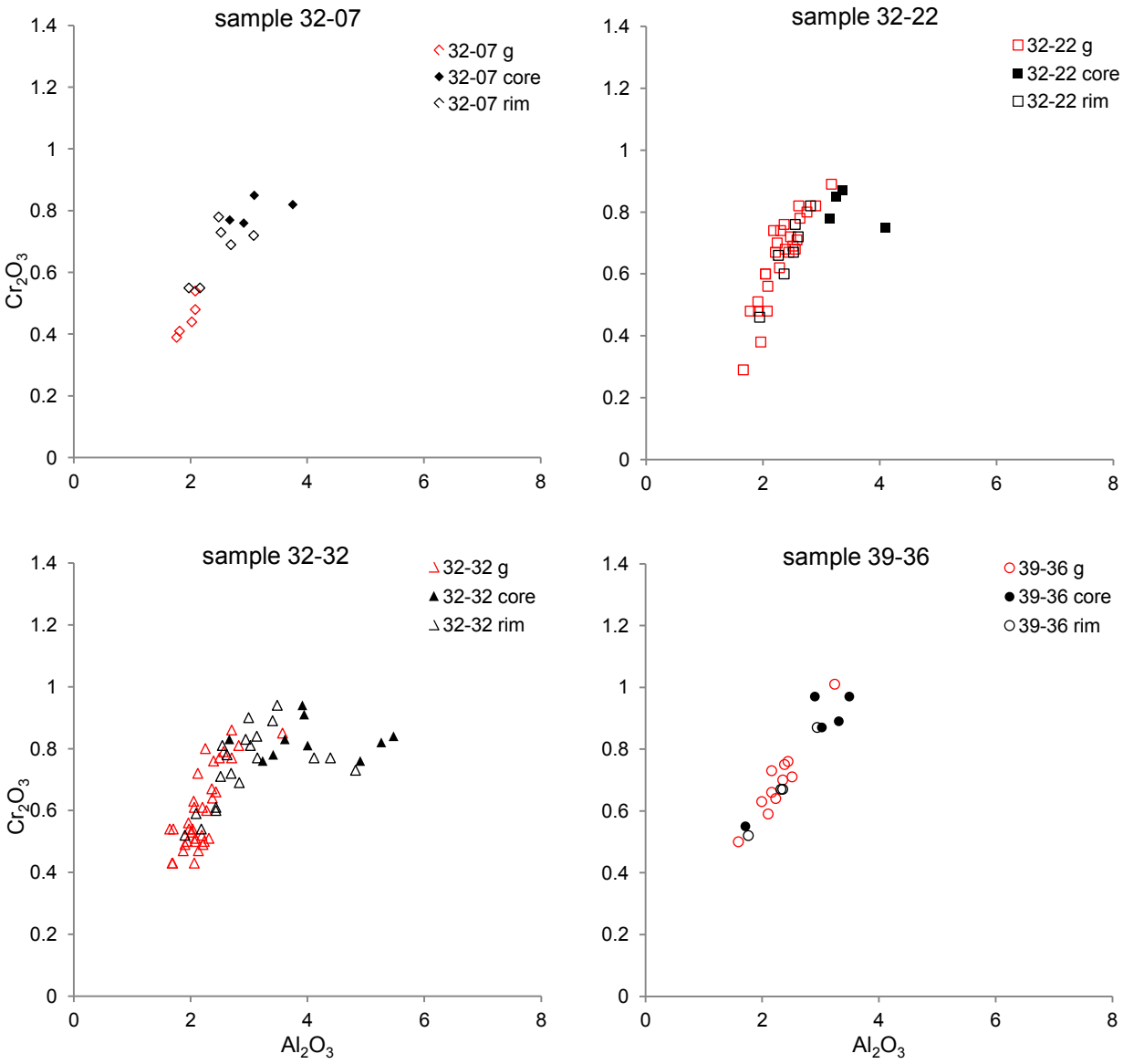

Figure 3.2.2.3 - Cr_2O_3 vs. Al_2O_3correlation in orthopyroxene, distinguished by sample. Red open symbols represent fine-grained crystals, whereas black open symbols represent the rims of the coarse crystals and black solid symbols represent the cores of the coarse crystals.

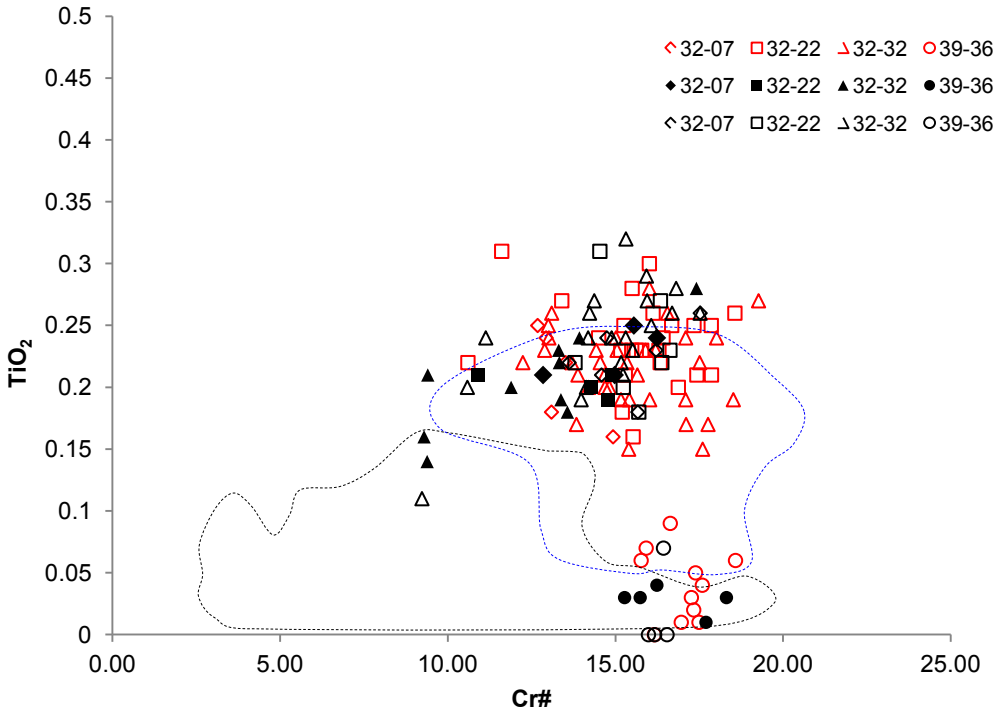

Figure 3.2.2.4 - TiO_2 vs. Cr# in orthopyroxene from studied samples. Red open symbols represent fine-grained crystals, whereas black open symbols represent the rims of the coarse crystals and black solid symbols represent the cores of the coarse crystals. Dashed black line represents compositional field of plagioclase-free abyssal peridotites, whereas dashed blue line represents compositional fields of plagioclase-bearing abyssal peridotites.

Clinopyroxene

In clinopyroxene Al_2O_3 ranges from 2.12% wt (sample 32-07) to 7.49% wt. (sample 32-22), and the core of the coarse crystals are enriched in Al_2O_3 compared to their rims; the small grains record the lowest values. Most of the cores, indeed, displays Al_2O_3 contents more similar, or even higher, to those of plagioclase-free abyssal peridotites.

Mg# and Cr# are rather variable (Mg # from 87.7 to 94.1, Cr# from 9 to 24.3), being lower in the cores of the coarse crystals with respect to their rims, and recording the highest values in the small grains, and positively correlate in agreement with other abyssal peridotites. Cr#-Mg# trend appears to be shifted from the arrays of both plagioclase-free and plagioclase-bearing peridotites towards lower values of both Mg# and Cr#, except for sample 39-36 which shows higher values of both Cr# and Mg# compared to the other samples (Figure 3.2.2.5).

FeO ranges from 3.97 wt.% (sample 32-22) to 1.86 wt.% (sample 39-36), with the cores of the coarse crystals barely enriched with respect to the corresponding rims, and the small grains recording intermediate values. Sample 39-36 appears depleted in FeO compared to samples of dredge #32.

Cr_2O_3 ranges from 0.78% wt. (sample 32-22) to 1.70% wt. (sample 32-22), and generally increases from core to rim, except for sample 39-36, with small grains displaying intermediate values. Sample 39-36 displays slightly higher values with respect to the other samples.

Overall in the analyzed clinopyroxene, Al_2O_3 and Cr_2O_3 correlation distinctly define both positive and negative trends (Figure 3.2.2.7). With the exception of sample 39-36, in which Al_2O_3 and Cr_2O_3 are positively correlated in any case; generally, the cores of the coarse crystals show negative correlation, whereas in the small grains Al_2O_3 and Cr_2O_3 are clearly positively correlated; the rims of the coarse crystals show both trends.

As already observed for orthopyroxene, the studied samples form two distinct groups as regards TiO_2contents in clinopyroxene: samples of the dredge #32 show TiO_2 values evenly distributed among the different textural environments, ranging from 0.31% wt. (sample 32-32) to 1.07% wt. (sample 32-22). In sample 39-36 clinopyroxene is, instead, strongly depleted in TiO_2 with respect to the other samples, ranging from 0.01% wt to 0.11% wt.

TiO_2 contents in clinopyroxene are mostly comparable to those of other plagioclase-bearing abyssal peridotites, with some small grains and some rims showing higher values, whereas sample 39-36 shows values typical of plagioclase-free abyssal peridotites.

Na_2O in sample 39-36 ranges from 0.29 wt.% to 0.39 wt.%, whereas samples of dredge #32 appear slightly enriched with values ranging from 0.33 wt.% to 0.66 wt.% No noteworthy differences between the different textures are observed. Sample 39-36 globally displays lower content of Na_2O, as well as TiO_2, compared to samples of dredge #32, but no correlation between them is observed considering the single samples (Figure 3.2.2.11). In samples of the dredge #32, Na_2O and TiO_2 partially fit the compositional field of plagioclase-bearing peridotites, whereas sample 39-36 fall in the compositional field of plagioclase-free peridotites.

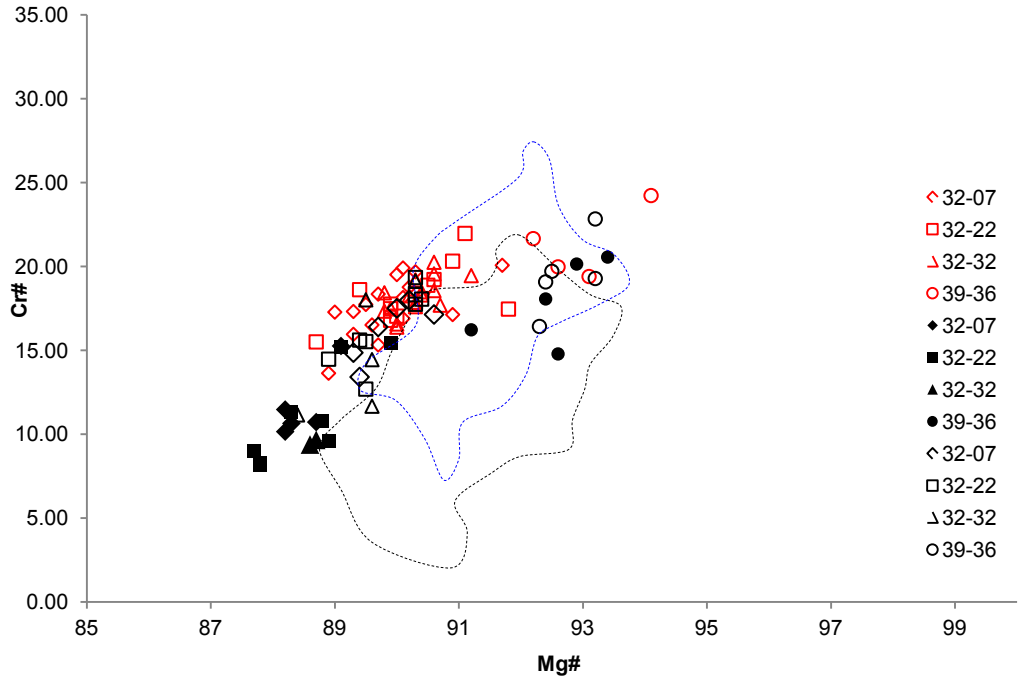

Figure 3.2.2.5 - Cr# vs Mg# in clinopyroxene of the studied samples. Red open symbols represent fine-grained crystals, whereas black open symbols represent the rims of the coarse crystals and black solid symbols represent the cores of the coarse crystals. Dashed black line represents compositional field of plagioclase-free abyssal peridotites, whereas dashed blue line represents compositional fields of plagioclase-bearing abyssal peridotites.

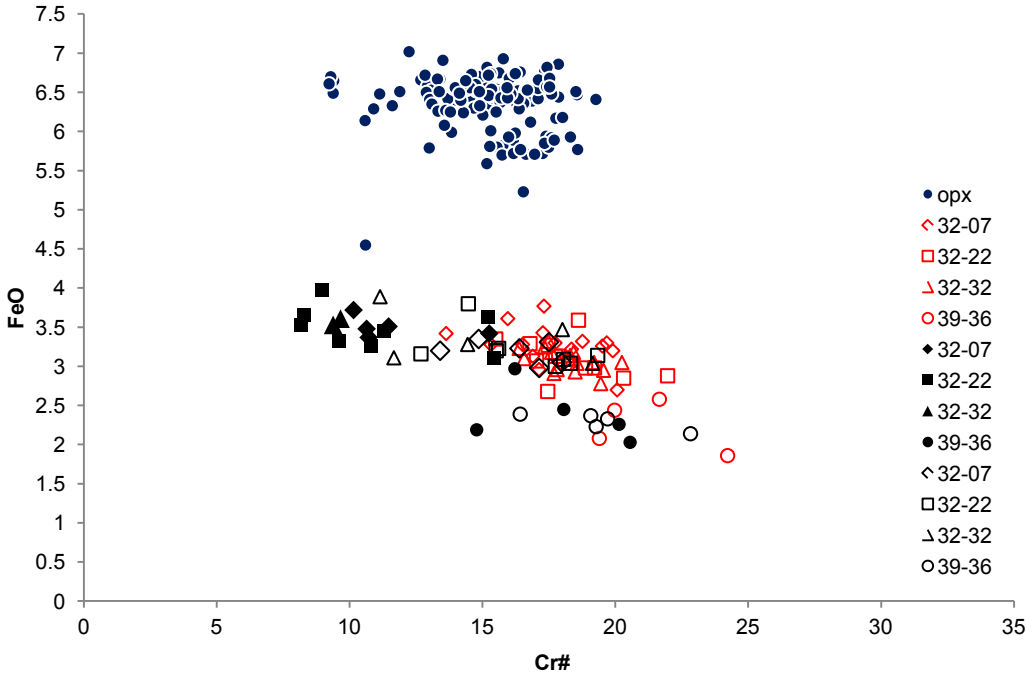

Figure 3.2.2.6 - FeO vs Cr# in clinopyroxene of the analyzed samples. Red open symbols represent fine-grained crystals, whereas black open symbols represent the rims of the coarse crystals and black solid symbols represent the cores of the coarse crystals. Orthopyroxene FeO vs. Cr# contents of the studied samples are also reported for comparison (blue dots).

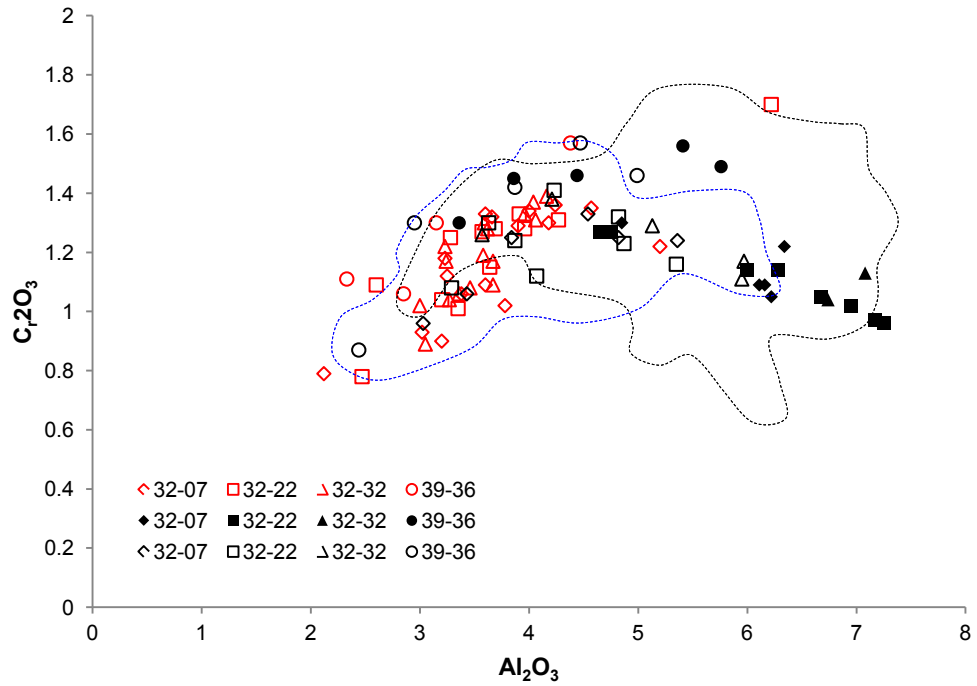

Figure 3.2.2.7 - Cr_2O_3 vs. Al_2O_3 in clinopyroxene. Red open symbols represent fine-grained crystals, whereas black open symbols represent the rims of the coarse crystals and black solid symbols represent the cores of the coarse crystals. Dashed black line represents compositional field of plagioclase-free abyssal peridotites, whereas dashed blue line represents compositional fields of plagioclase-bearing abyssal peridotites.

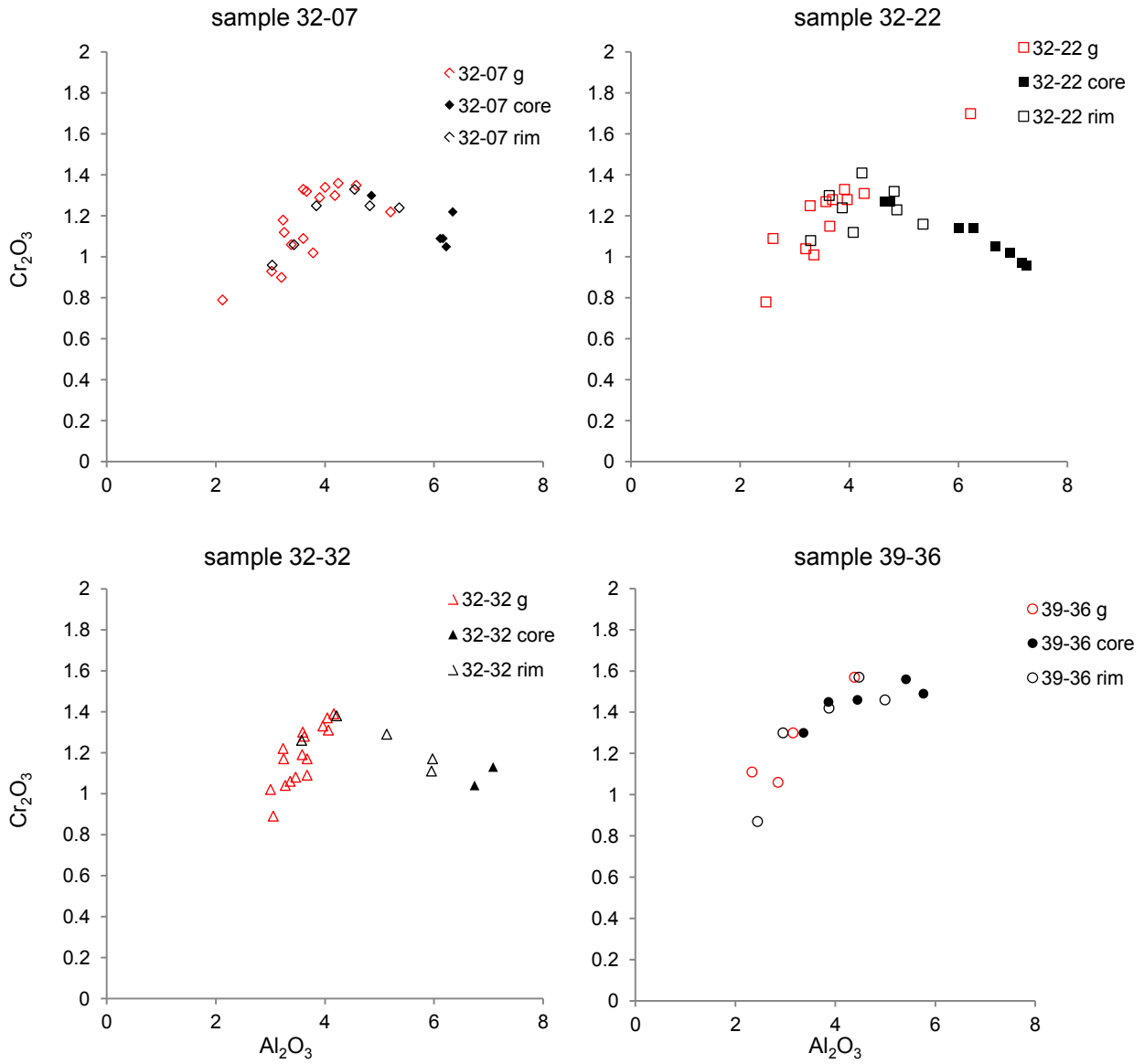

Figure 3.2.2.8 - Cr_2O_3 vs. Al_2O_3 in clinopyroxene in the studied samples distinguished by sample. Red open symbols represent fine-grained crystals, whereas black solid symbols represent the rims of the coarse crystals and black solid symbols represent the cores of the coarse crystals.

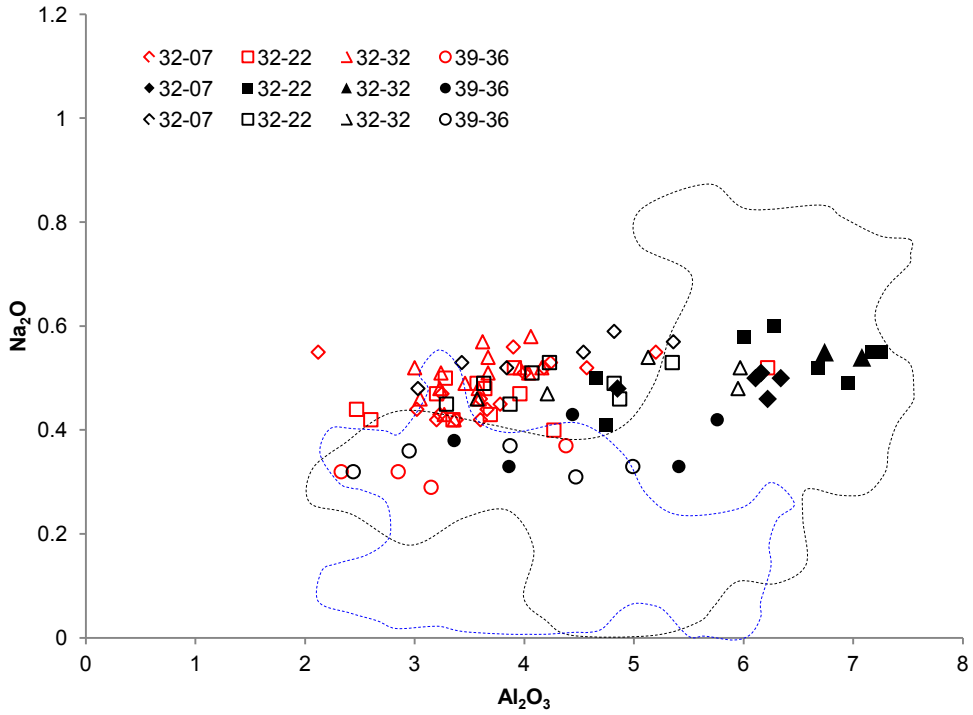

Figure 3.2.2.9 - Na_2O vs. Al_2O_3 in clinopyroxene from the analyzed samples. Red open symbols represent fine-grained crystals, whereas black open symbols represent the rims of the coarse crystals and black solid symbols represent the cores of the coarse crystals. Dashed black line represents compositional field of plagioclase-free abyssal peridotites, whereas dashed blue line represents compositional fields of plagioclase-bearing abyssal peridotites.

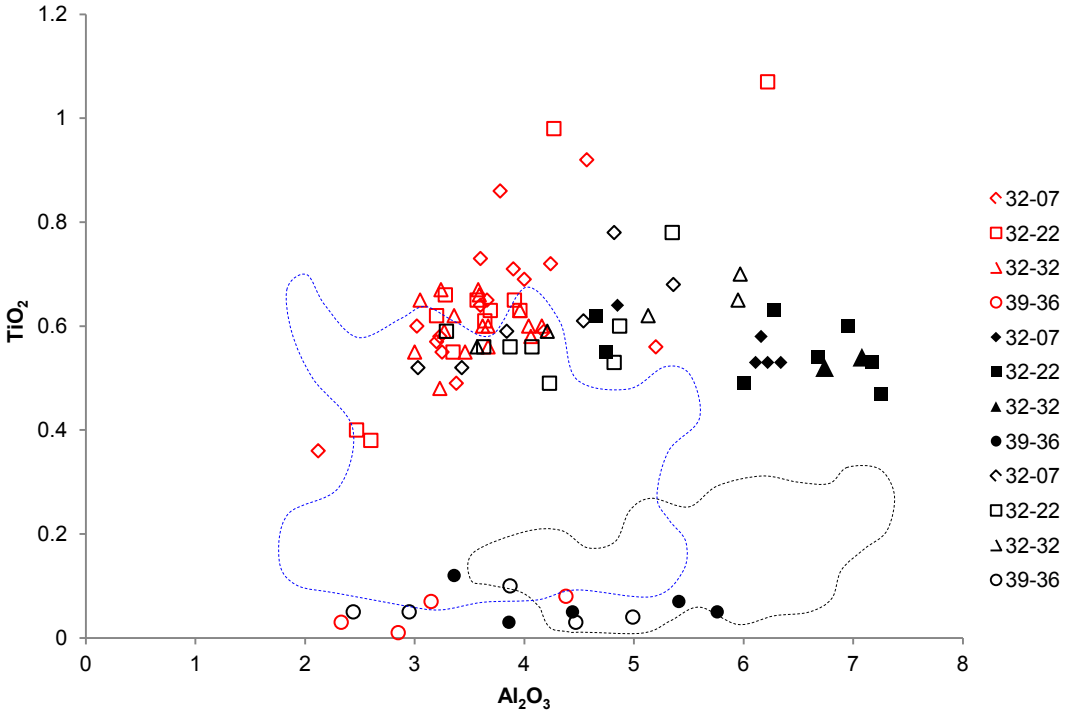

Figure 3.2.2.10 - TiO_2 vs. Al_2O_3 in clinopyroxene. Red open symbols represent fine-grained crystals, whereas black open symbols represent the rims of the coarse crystals and black solid symbols represent the cores of the coarse crystals. Dashed black line represents compositional field of plagioclase-free abyssal peridotites, whereas dashed blue line represents compositional fields of plagioclase-bearing abyssal peridotites.

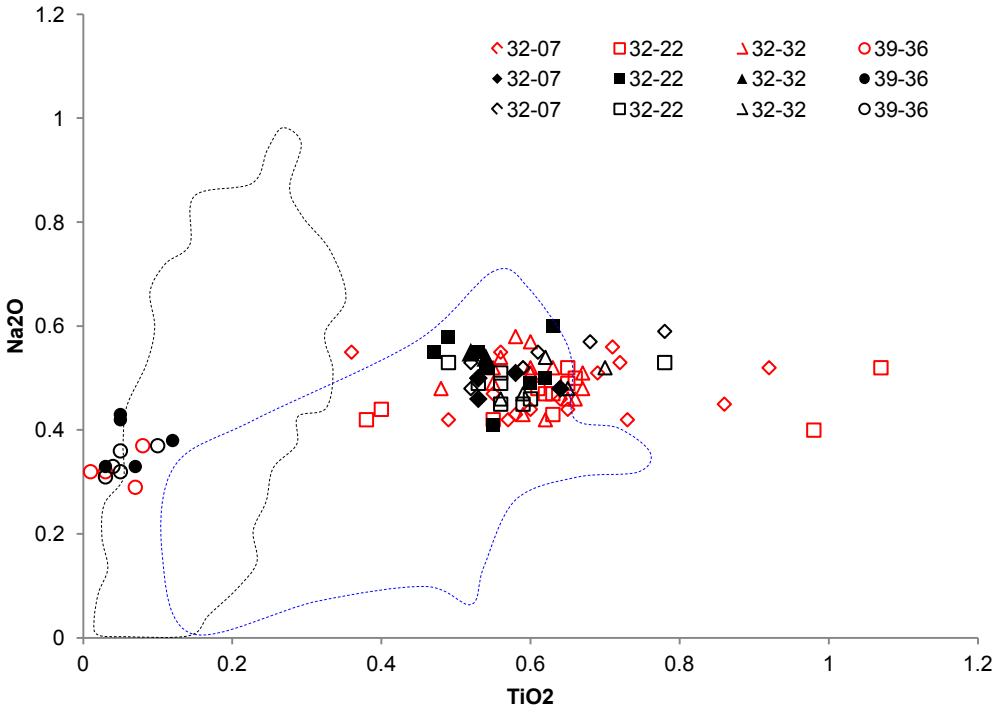

Figure 3.2.2.11 - Na_2O vs. TiO_2 in clinopyroxene from the studied samples. Red open symbols represent fine-grained crystals, whereas black open symbols represent the rims of the coarse crystals and black solid symbols represent the cores of the coarse crystals. Dashed black line represents compositional field of plagioclase-free abyssal peridotites, whereas dashed blue line represents compositional fields of plagioclase-bearing abyssal peridotites.

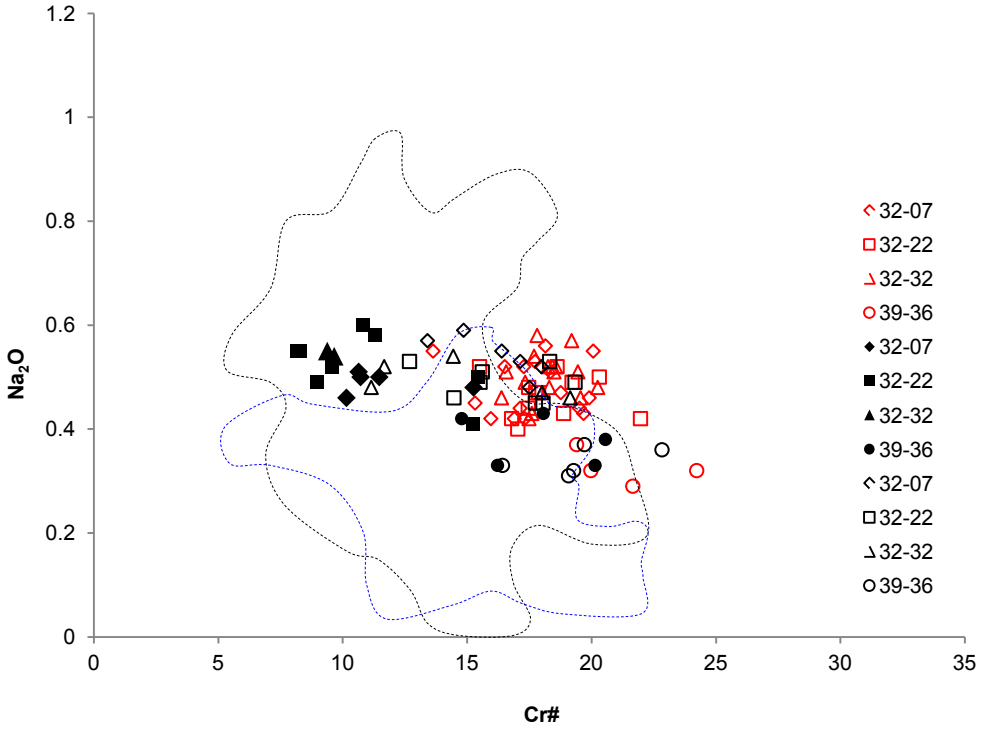

Figure 3.2.2.12 - Na_2O vs. Cr# in clinopyroxene. Red open symbols represent fine-grained crystals, whereas black open symbols represent the rims of the coarse crystals and black solid symbols represent the cores of the coarse crystals. Dashed black line represents compositional field of plagioclase-free abyssal peridotites, whereas dashed blue line represents compositional fields of plagioclase-bearing abyssal peridotites.

3.2.3 Spinel

Spinel has been detected in all the studied samples. Chemical analysis are distinguished on larger spinel crystals (up to around 3 mm), which may appear either vermicular or holly-leaf-shaped, tiny spinel grains which generally occur in poly-mineral aggregates. Further, there is one analysis relative to spinel occurring in exolution lamallae together with clinopyroxene, inside orthopyroxene (sample 32-32).

Spinel in exolution lamellae shows the highest Mg# (63.5) and the lowest Cr# (39.3) among all measured grains. In the other occurrences Cr# ranges from 42.7 (sample 39-36) to 52.8 (sample 32-32), whereas Mg# ranges from 41.7 (sample 39-36) to 61.7 (sample 39-36), well fitting the field of plagioclase-bearing abyssal peridotites. Tiny grains show lower Mg# and slightly higher Cr# compared to the larger crystals (fig. 3.2.3.1). Cr# and Mg# display rather homogeneous values among samples, with sample 39-36 exhibiting the lowest Cr# and the highest Mg#, and show rather flat negative correlation in agreement with other plagioclase-bearing abyssal peridotites trend.

TiO_2 ranges from 0 wt.% (sample 39-36) to 1.24 wt.% (sample 32-32); as well as clinopyroxene and orthopyroxene, spinel displays strong TiO_2 depletion in sample 39-36 (from 0 wt.% to 0.08 wt.%) with respect to samples of dredge #32 (from 0.43 wt.% to 1.24 wt.%), whose TiO_2 contents are even higher than those of other plagioclase-bearing peridotites with rare exceptions (fig. 3.2.3.2). TiO_2 contents of sample 39-36 are comparable to those of plagioclase-free abyssal peridotite. It is noteworthy that, among samples of dredge #32, the lowest TiO_2 content is recorded in spinel inside exolution lamellae (sample 32-32). No evident differences between large crystals and tiny grains are present, except for the fact that TiO_2 displays rather homogeneous values in large crystals whereas in tiny grains values appear more scattered, and no clear correlation with Cr# is observed.

NiO is highly variable, ranging from 0 wt. % (sample 39-36) to 0.28 wt.% (sample 32-32), with average lower content in sample 39-36. Spinel in exolution lamellae is the most enriched in NiO (fig. 3.2.3.3).

On the whole no noteworthy differences between vermicular and holly leaf spinel have been noticed.

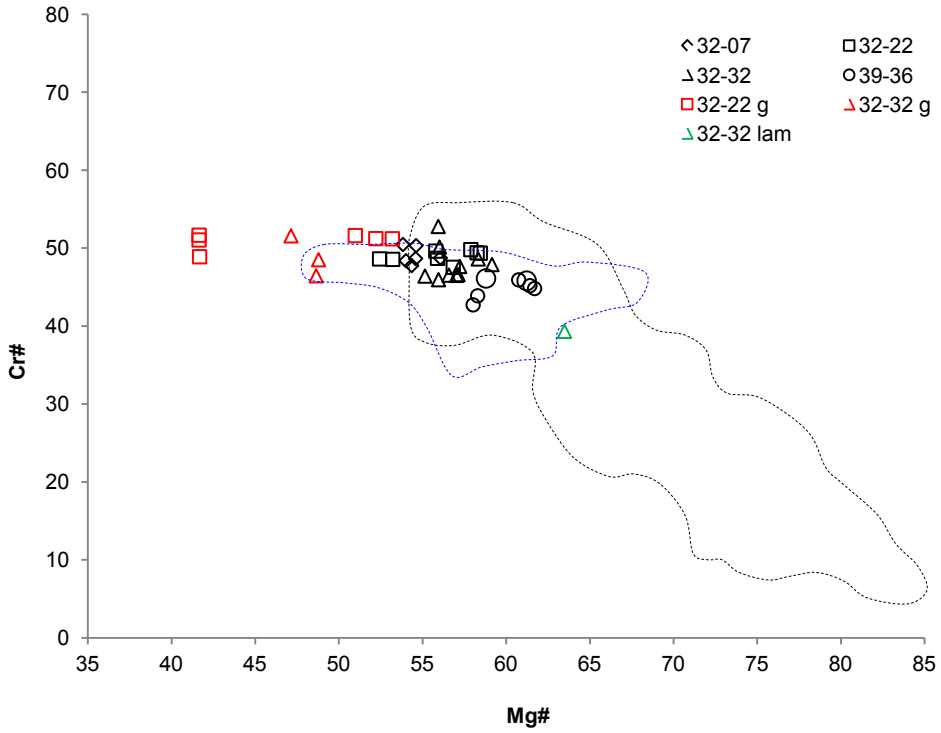

Figure 3.2.3.1 - Cr# vs. Mg# in the analyzed spinel. Black open symbols represent large crystals, whereas red open symbols represent tiny grains. Green symbol represents spinel in exsolution lamellae. As regards sample 39-36 it has been distinguished vermicular spinel (large circles) from holly leaf spinel (small circles). In the other samples spinel is always holly-leaf-textured. Dashed black line represents compositional field of plagioclase-free abyssal peridotites, whereas dashed blue line represents compositional fields of plagioclase-bearing abyssal peridotites.

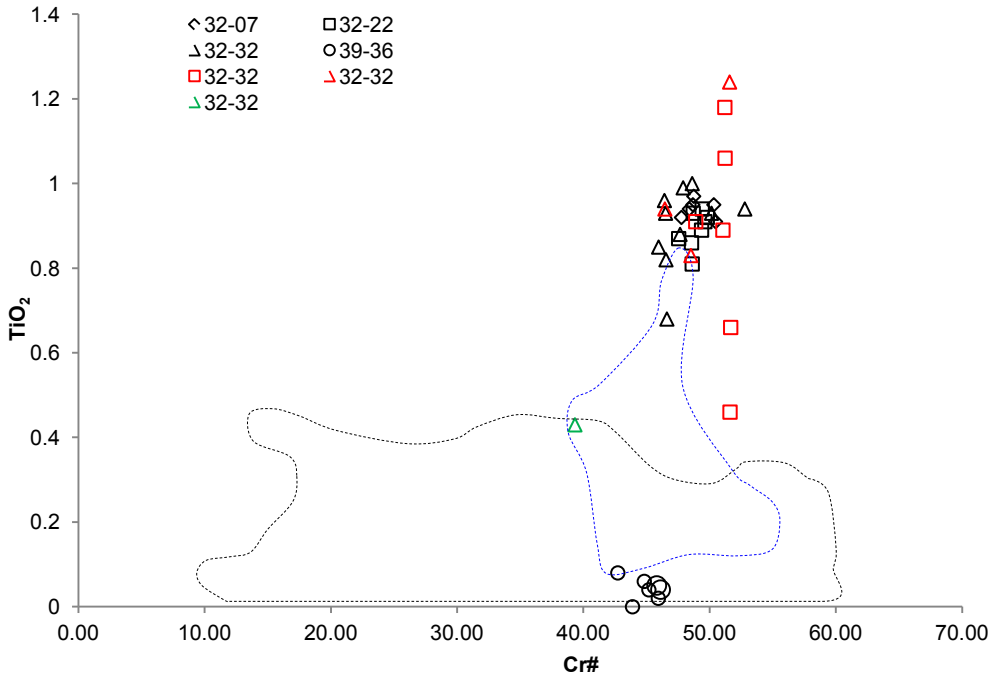

Figure 3.2.3.2 - TiO_2 vs. Cr# in spinel. Black open symbols represent large crystals, whereas red open symbols represent tiny grains. Green symbol represents spinel in exsolution lamellae. As regards sample 39-36 it has been distinguished vermicular spinel (large circles) from holly leaf spinel (small circles). In the other samples spinel is always holly-leaf-textured. Dashed black line represents compositional field of plagioclase-free abyssal peridotites, whereas dashed blue line represents compositional fields of plagioclase-bearing abyssal peridotites.

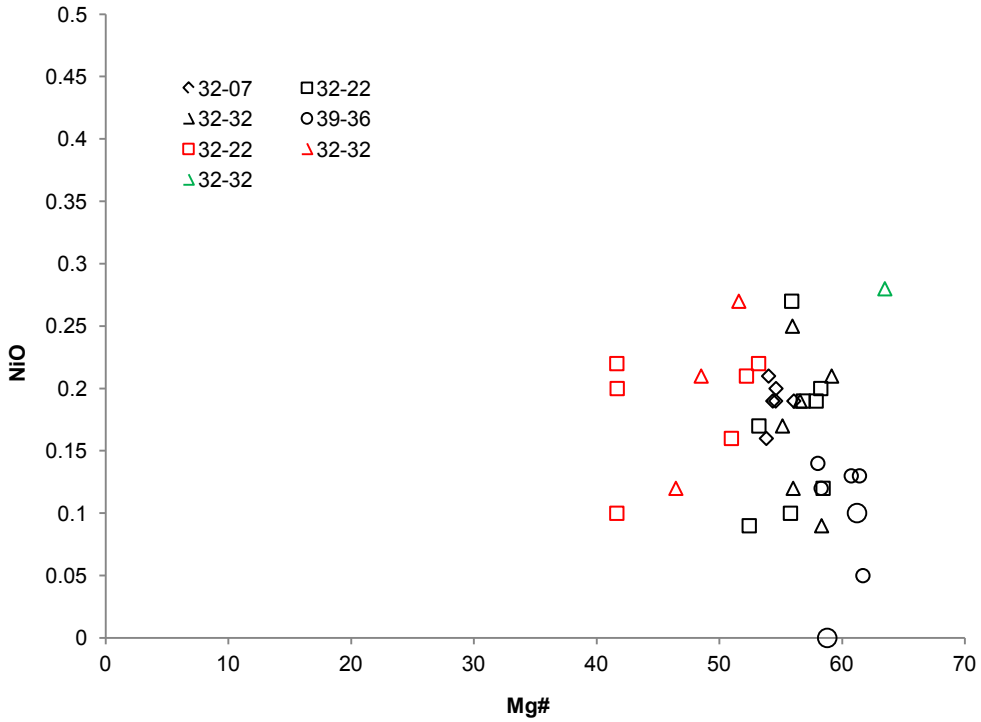

Figure 3.2.3.3 - Mg# vs. NiO in spinel. Black open symbols represent large crystals, whereas red open symbols represent tiny grains. Green symbol represents spinel in exsolution lamellae. As regards sample 39-36 it has been distinguished vermicular spinel (large circles) from holly-leaf spinel (small circles). In the other samples spinel is always holly-leaf-textured.

3.2.4 Plagioclase

Plagioclase mineral chemistry has been analyzed in all the studied samples. Unfortunately in sample 39-36 only one fresh patch of plagioclase was present. No distinction has been made between core and rim due to the small size of plagioclase crystals.

Plagioclase shows Anorthite contents ranging from 67% (sample 32-22) to 86% (sample 39-36). An values appear rather homogenous in samples of dredge #32 (from 67% to 78.5%) with no inter-sample evident variations, whereas sample 39-36 displays the highest An (86%). Plagioclase in sample 39-36, moreover, is clearly depleted in Fe; as regards dredge #32, instead, Fe appears homogeneously distributed among samples, except for two outliers with strongly higher values, corresponding to a plagioclase patch partially filling a fracture inside a large orthopyroxene (sample 32-32).

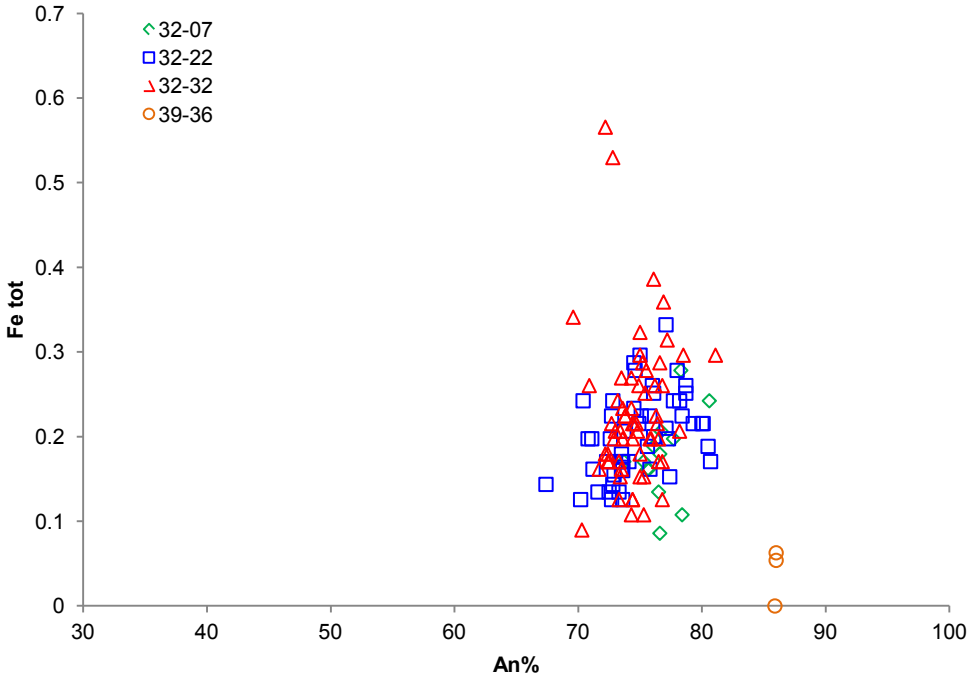

Figure 3.2.4.1 - Fe tot vs. An% in plagioclase.

3.3 Summary

Forsterite in olivine is very homogeneous, regardless of textural features, ranging from 0.89 to 0.90. Also NiO appears homogenously spread in all samples, ranging from 0.3% wt. to 0.48% wt, with no evident correlation with Fo.

In the coarse crystals of orthopyroxene, Al_2O_3 and Cr_2O_3 decreasing from core to rim is coupled with increasing MgO; the small grains are, instead, the most depleted in Al_2O_3 and Cr_2O_3 and the most enriched in MgO. Moreover, Al_2O_3 in coarse orthopyroxene decreases when approaching internal fractures filled by fine-grained poly-mineral aggregates containing plagioclase ±opx±cpx±ol±sp. Except for few cases, Al_2O_3 and Cr_2O_3 are positively correlated. Orthopyroxene in sample 39-36 appears strongly depleted in TiO_2 and shows higher values of Mg# with respect to samples of dredge #32.

Coarse clinopyroxenes display cores enriched in Al_2O_3, FeO, Na_2O and depleted in Cr_2O_3 with respect to their rims; the lowest Al_2O_3, FeO, Na_2O are recorded in the small grains. Mg# and Cr#, instead, increases from core to rim and record the highest values in the small grains; moreover, Mg# and Cr# define a positive correlation trend, in agreement with other abyssal peridotites. Concerning TiO_2 contents in clinopyroxene, sample 39-36 appears strongly depleted compared to samples of dredge #32. Overall in the analyzed clinopyroxene, Al_2O_3 and Cr_2O_3 correlation distinctly defines both positive and negative trends. With the exception of sample 39-36, in which Al_2O_3 and Cr_2O_3 are positively correlated in any case, as a whole the cores of the coarse crystals usually show negative correlation, whereas in small grains Al_2O_3 and Cr_2O_3 are clearly positively correlated; the rims of the coarse crystals show both trends.

Spinel in clinopyroxene exolution lamellae inside orthopyroxene displays the highest Mg# and the lowest Cr# of all. Apart from that, tiny grains have lower Mg# and higher Cr# compared to the large crystals. Spinel in sample 39-36 is strongly depleted in TiO_2 and slightly depleted in NiO with respect to samples of dredge #32, and overall there are no evident differences between large crystals and tiny grains. Spinel in exolution lamellae inside orthopyroxene is the most depleted in TiO_2 and the most enriched in NiO among samples of dredge #32. No noteworthy differences between vermicular and holly leaf spinel in sample 39-36 have been detected.

3.3.1 Comparison of the studied samples

As a whole, when compared to samples of dredge #32, sample 39-36 exhibits orthopyroxene, clinopyroxene and spinelstrongly depleted in TiO_2, accompanied by higher values of both Cr# and Mg#. Moreover, sample 39-36 clinopyroxene shows slight enrichment in Cr_2O_3, plus low depletion in FeO and Na_2O, whereas spinel also appears a little bit depleted in NiO and records the lowest Cr#. Finally, plagioclase in sample 39-36 is more anorthitic than in samples of dredge #32.

3.3.2 Comparison with other abyssal peridotites

From comparing the studied samples with other plagioclase-free and plagioclase-bearing peridotites, we can point out that:
i) olivine displays slightly lower Fo, except for sample 39-36, and slightly higher NiO compared to plagioclase-free abyssal peridotites;
ii) coarse clinopyroxene cores display Al_2O_3 and Cr# values similar to those of plagioclase-free abyssal peridotites; also some coarse orthopyroxene cores display Al_2O_3 content similar to those of plagioclase-free abyssal peridotites; iii) leaving out sample 39-36, clinopyroxene from other samples displays Cr# vs. Mg# trend that is shifted from abyssal peridotites arrays, due to lower Mg# and Cr#;
iv) TiO_2 contents in minerals from sample 39-36 lie within the plagioclase-free abyssal peridotites ranges; on the contrary, samples of dredge #32 generally exhibits TiO_2 contents comparable to those of other plagioclase-bearing abyssal peridotites, except for strong enrichment in spinel and in few clinopyroxene small grains and rims; v) orthopyroxene small grains show moderate depletion in Cr_2O_3.

3.3.3 Mineral equilibrium in the studied peridotites

In order to estimate mineral equilibrium conditions, Cr# of orthopyroxene, clinopyroxene and spinel of the studied samples are reported together with those of plagioclase-free abyssal peridotites from the Vema FZ (Brunelli et al., 2006) for comparison. As a whole, the observed values exhibit two different sub-parallel positive trends: one is defined by values of the rims of the coarse crystals and the small grains which partially overlap with the Vema FZ plagioclase-free abyssal peridotites but reaching higher values of Cr#; the other one is defined by values of the cores of the coarse crystals. This may suggest that the rims and the small grains well equilibrated under the P-T conditions of the spinel peridotite field, in agreement with the composition of plagioclase-free abyssal peridotites (Brunelli et al., 2006).

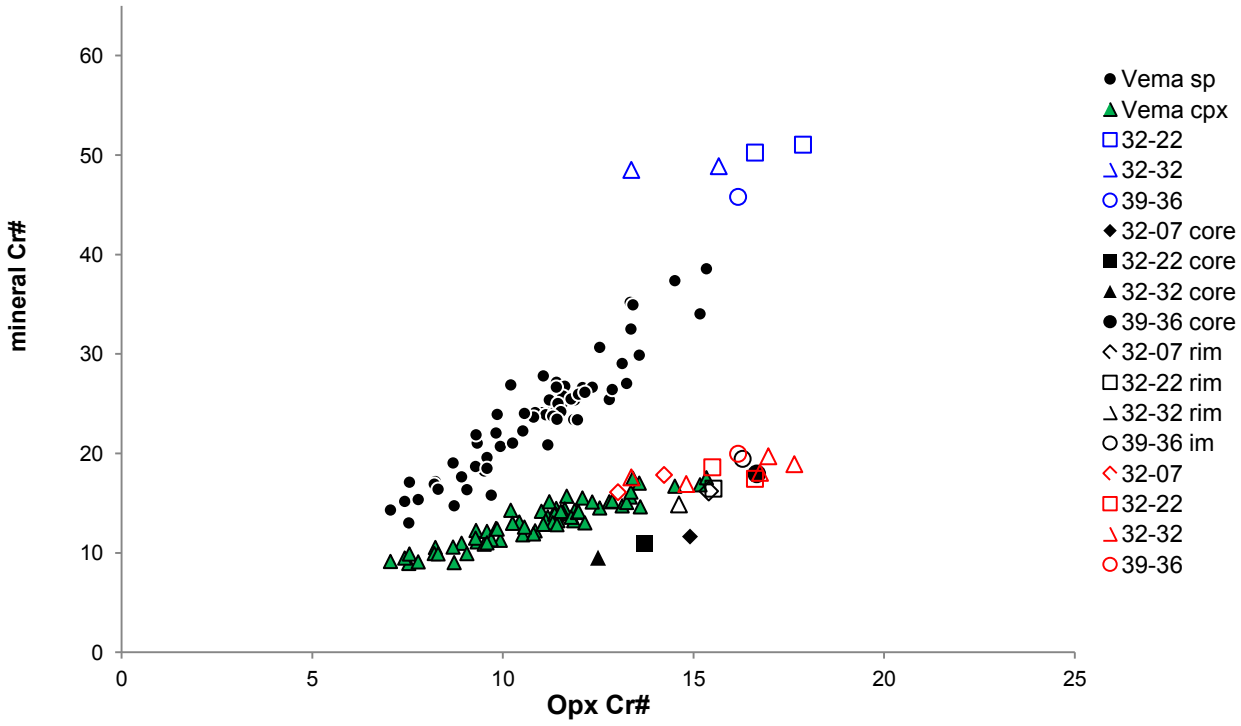

Figure 3.3.3.1 - Orthopyroxene vs. spinel and clinopyroxene Cr# [100 x Cr/(Cr + Al)]. Red open symbols represent fine-grained pyroxene crystals, whereas black open symbols represent the rims of the coarse pyroxene crystals and black solid symbols represent the cores of the coarse pyroxene crystals. Blue open symbol represent fine-grained orthopyroxene and sp. Black dots are spinel Cr# of plagioclase-free abyssal peridotites and green symbols are cpx Cr# of plagioclase-free abyssal peridotites (from Brunelli et al., 2006).

Chapter 4
Trace elements

4.1 Methods

Trace elements data have been collected at the University of Modena with a Thermo Finnigan X-Series II ICP-MS coupled with a laser ablation system (LA-ICP-MS).
Laser ablation-inductively coupled with? plasma-mass spectrometry (LA-ICP-MS) is an analytical technique that in the last three decades has been widely accepted in many fields, with geology being an area in which there are many excellent applications, i.e. quantitative trace element determinations in geological samples.
LA-ICPM-MS, as the acronym suggests, consists of three main components (table 4.1.1)

Table 4.1.1 - Main components of ICP-MS analytical technique

Laser Ablation (LA)	Laser Focussing, homogenization, beam steering, power control, power monitoring, sample observation Sample cell, computer driven movable sample stage Transport tubing
Inductively Coupled Plasma (ICP)	Ion source
Mass Spectrometer (MS)	Vacuum system Interface and ion lenses Analyzer (Quadrupole, Sector, Time of Flight, etc.) Detector (Transducer) Data Acquisition System and software

The first part of the LA-ICP-MS is the LA (laser ablation), which consists of a laser with associated optics, an airtight sample cell suitable for containing the sample and tubing to transport the sample to the ICP by means of a flow of gas. The most commonly used laser energies today are based upon the *Nd: YAG (Neodymium: Yttrium Alluminium Garnet)* laser, a solid state laser in which a garnet rod is excited using a flash lamp. The laser's fundamental energy output is at a wavelength of 1064 nm in the near infrared (NIR).
The sample is transformed in the cell by the laser into an aerosol of small particles which are carried in a flow of gas to the ICP (inductively coupled plasma). In the ICP, the gas (Ar often combined with He) is electrically heated to a high temperature (around 8000°C) forming a plasma. Plasma is a fluid similar to a gas, but containing a large number of free electron ions. The sample aerosol is carried into this plasma where it is further vaporized, atomized and finally ionized. The next part, the MS (mass spectrometer), which operates in vacuum, separates these ions based upon their mass to charge ratio. The intensity (ions per second or current) of this ion beam is converted to an electrical signal which is measured and recorded. The mass/charges identifies the elemental composition and the intensity is functionally related to the concentration. One of the especially attractive characteristic of LA-ICP-MS is that the LA is optimized for sampling, the ICP for ion production, and MS for separating the ions. Finally the ICP-MS has a detector system, computer interface and computer.
The ICP is where the ions are formed for subsequent analysis. The great achievement of ICP-MS instrumentation was to extract these ions into a vacuum where the pressure was low enough to produce good resolution of ions with differing mass to charge ratios.
The most commonly used laser energies today are based upon the *Nd: YAG (Neodymium: Yttrium Alluminium Garnet)* laser. This is a solid state laser in which the garnet rod is excited using a flash lamp and the laser's fundamental energy output is at a wavelength of 1064 nm in the near infrared (NIR).

ICP-MS data have been collected using a 100 μm diameter pre-ablation beam for a period of 5 seconds and with a frequency of 2Hz. Laser fluency is about 25 J/cm2. Once pre-ablation has finished, measurements start with an 80 μm diameter ablation beam that works for a period of 30 seconds and with a fire frequency of 20 Hz. A flux of helium of 600 ml/min is used to transport ablated aerosol from laser ablation sample holder to the plasma torch. Plasma is produced by a flux of argon cooling gas of 13 liters/min plus an auxiliary flux of 0.9 l/min and a nebulizer flux of 0.8 l/min, using a RF power set up at 1400 Watts. Acquisition lasts 30 seconds during which the quadrupole analyses all the chosen analytes, changing potential configuration each 30 msec. These working conditions are mean values because the day by day instrumental tuning slightly differs. Machine tuning is performed by maximizing the 139La and 232Th signals, keeping oxides formations under 1%.

4.2 Trace elements composition of the studied samples

Trace elements analysis of clinopyroxene, orthopyroxene and plagioclase have been performed in samples 32-07, 32-22, 32-32 and 39-36. Generally, in each crystal both core and rim trace elements compositions have been determined, and each reported value represents the mean value between at least three neighboring measurements. Distinction between core and rim is prevented in the smaller crystals.
All the analytical results of major elements are reported in Appendix B.

Trace elements concentrations have been normalized to C1 chondrite of Anders and Grevesse (1988).

4.2.1 Clinopyroxene

From the obtained patterns of clinopyroxene trace elements compositions (fig. 4.2.1.1), we can observe that sample 39-36 is affected by a strong depletion in all elements with respect to samples of dredge #32.
Clinopyroxene trace elements compositions of samples from dredge #32 are very homogeneous: they define a rather narrow compositional range characterized by pronounced Sr, Zr and Ti negative anomalies and showing the narrower and the wider ranges respectively for Ti and Sr, the latter reaching the overall minimum concentrations (up to 0.2xC1; however not as low as in sample 39-36 where Sr content is 0.03xC1). Noteworthy inter-samples variations occur in correspondence to LREE, HREE and Zr, in which sample 32-22 and sample 32-07 represent the most enriched and the most depleted, respectively. All samples from dredge #32 show LREE depletion (Ce_N/Yb_N=0.21) relative to MREE and HREE and near-flat MREE to HREE patterns (Sm_N/Yb_N=1.19 and Dy_N/Yb_N=1.29) with ≈ 10-25 x C1 abundances. As a whole, a weak negative Eu anomaly (defined as $Eu_{(N)}/Eu^*$, with $Eu^*=(Sm_{(N)}xGd_{(N)})^{1/2}$) affects all the analyzed crystals, although with variable extents (Eu/Eu*= 0.70-0.99), in agreement with equilibrium phases in the presence of plagioclase.
Sample 39-36, of which only one clinopyroxene crystal has been analyzed, shows less pronounced Eu anomaly (average Eu/Eu*=0.55 between rim and core), whereas Ti anomaly is nearly absent; REE regularly increase from LREE (Ce_N/Yb_N=0.04) to MREE (Sm_N/Yb_N=0.16) to HREE (Dy_N/Yb_N=0.78), and the most enriched compositions roughly start from Gd, reaching 4-5 x C1 HREE abundances, arranging in a spoon-shaped pattern (Seyler et al. 2011) (Fig. 4.2.1.2).

The extent of the 1σ intra-crystal variability in sample 32-22 is reported as an example in fig. 4.2.1.5.

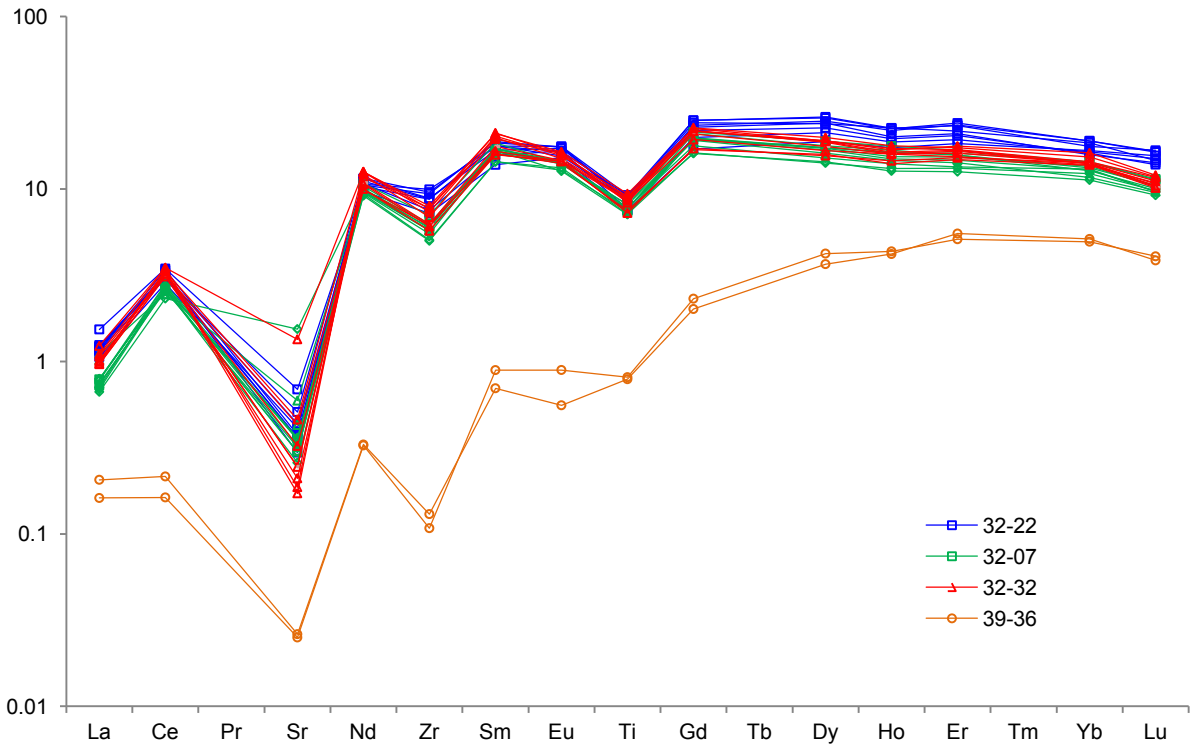

Fig. 4.2.1.1 - Extended clinopyroxene trace elements spiderdiagram of the studied samples; patterns are color-coded by sample: green (sample 32-07), blue (sample 32-22), red (sample 32-32) and orange (sample 39-36).

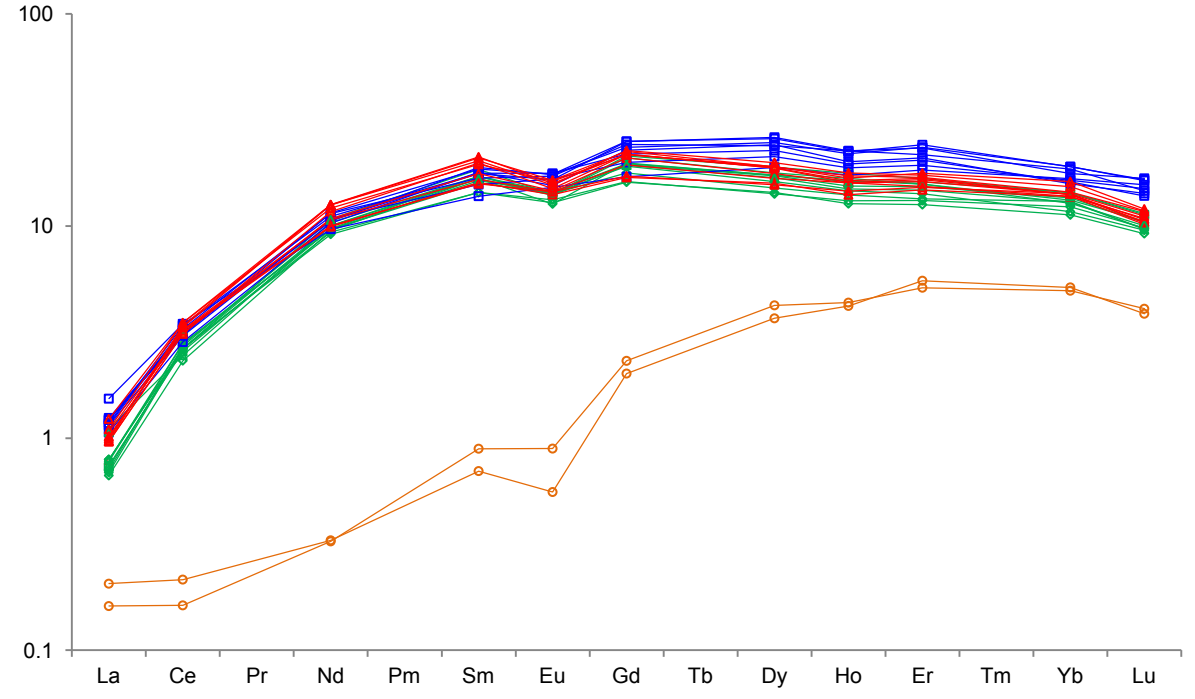

Fig. 4.2.1.2 - Rare Earth Elements (REE) clinopyroxene patterns of the studied samples. Patterns are color-coded by sample: green (sample 32-07), blue (sample 32-22), red (sample 32-32) and orange (sample 39-36).

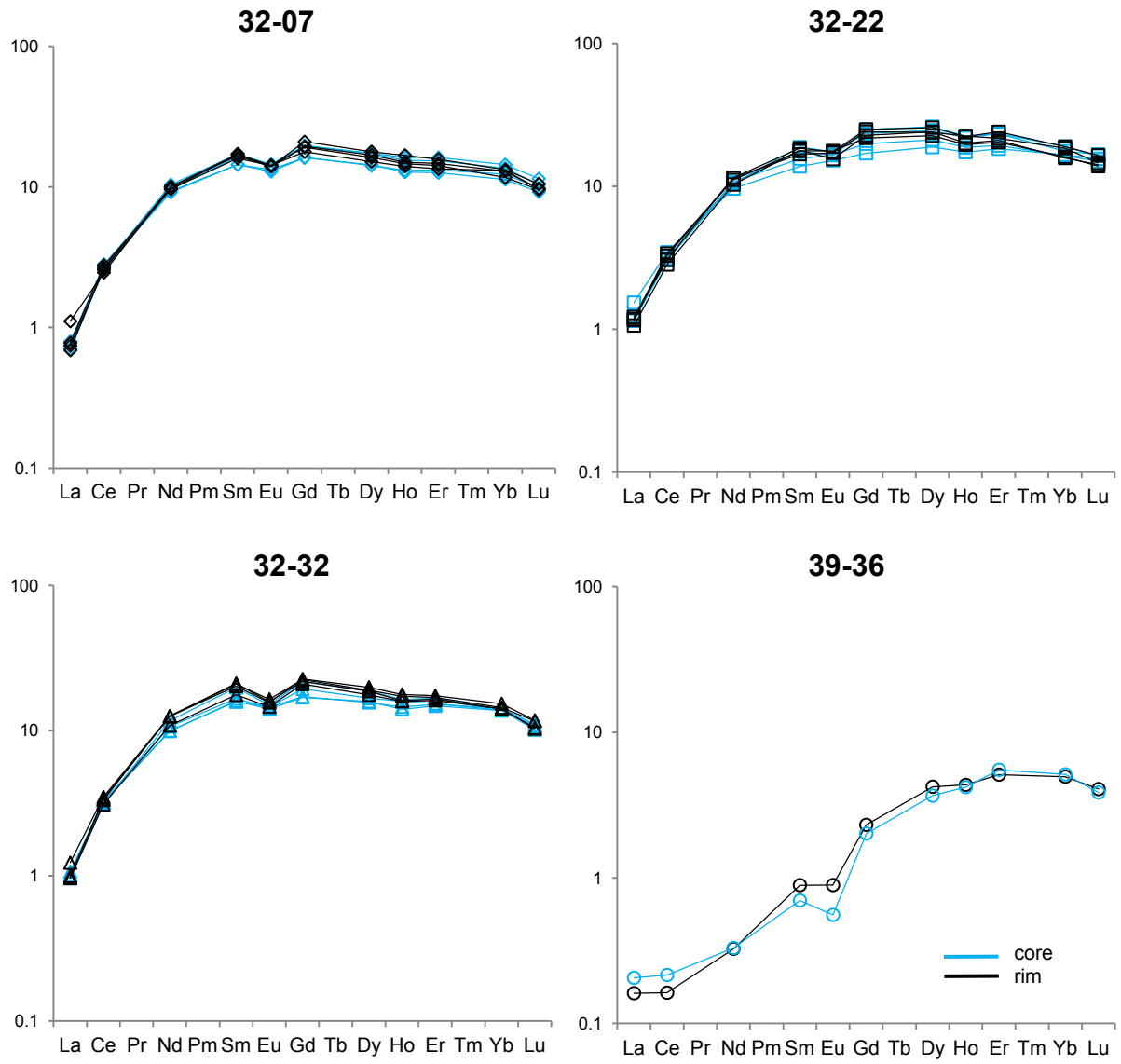

Fig. 4.2.1.3 - Rare Earth Elements (REE) clinopyroxene patterns of the studied samples, sample by sample. Patterns are color-coded by core (light blue) and rim (black).

Clinopyroxene trace elements compositions of the studied samples do not show prominent variations from core to rim (fig. 4.2.1.3); however, appreciable variability (up to 2-3 chondritic in sample 32-22) generally occurs in correspondence to MREE, with depleted cores compared to the rims. Moreover, sample 39-36 records core enrichment in the lighter REE (La, Ce) with respect to the corresponding rim. Noteworthy variations also concern the negative Eu anomaly, which may vary from crystal to crystal at the sample scale, but anyhow tends to weaken from rim to core, thus defining positive correlation with Al2O3 and negative correlation with Cr# (fig. 4.2.1.4). On the contrary, in sample 39-36 Eu negative anomaly increases from rim to core.

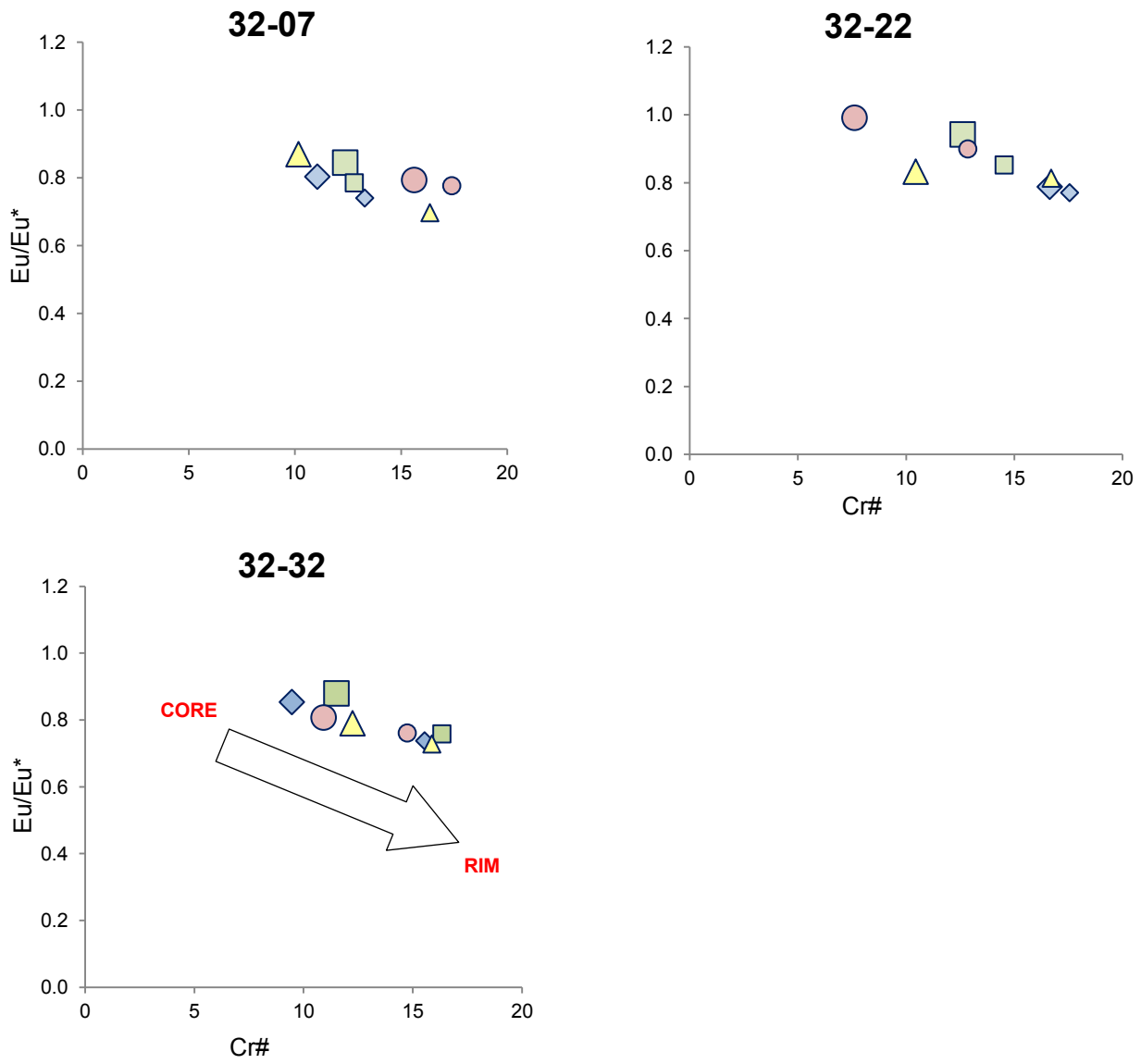

Fig. 4.2.1.4 - Eu anomaly (Eu/Eu) vs. Cr# in clinopyroxene, sample by sample (sample 39-36 is omitted); each colored symbol represents a single crystal: larger symbols represent the cores whereas the smaller ones represent the corresponding rims.*

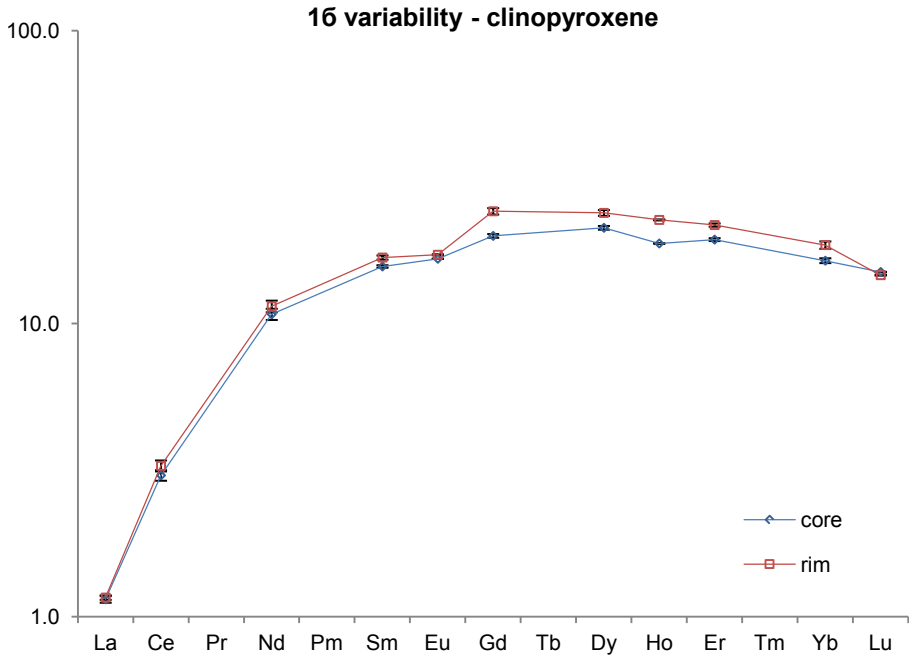

Fig. 4.2.1.5 - REE patterns of a clinopyroxene crystal (rim and core; sample 32-22) in which the error bars indicate 1σ variability. Each reported value represents the average of three neighboring measurements. Values are normalized to C1 chondrite of Anders & Grevesse (1989).

4.2.2 Orthopyroxene

From the obtained patterns of orthopyroxene trace element compositions (fig. 4.2.2.1), we can observe that sample 39-36 is affected by a general depletion with respect to samples of dredge #32, except for La and Ce.
Orthopyroxene trace elements composition of samples of dredge #32 are variably homogeneous: they define a rather narrow compositional range for MREE and HREE (from Eu to Lu), whereas data appear more scattered for the most incompatible elements, i.e. LREE and Sr. Positive Ti and Zr anomalies affect all samples, as well as a negative Sr anomaly, although with a wider span. Moderate inter-samples variations occur in correspondence to Zr, Ti and from MREE to HREE, in which sample 32-32 and sample 32-07 represent the most enriched and the most depleted, respectively. Samples of dredge #32 show REE regular increasing from LREE (Ce_N/Yb_N=0.015) to HREE (Dy_N/Yb_N=0.49), with the greater enrichment up to 5xC1 abundances of Yb.
Except for few cases, a moderate negative Eu anomaly affects all the analyzed crystals (Eu/Eu*= 0.58-1.28 in samples of dredge #32 and Eu/Eu*=0.18-0.85 in sample 39-36), in agreement with equilibrium phases in the presence of plagioclase.

The extent of the 1б intra-crystal variability in sample 32-22 is reported as an example in fig. 4.2.2.4.

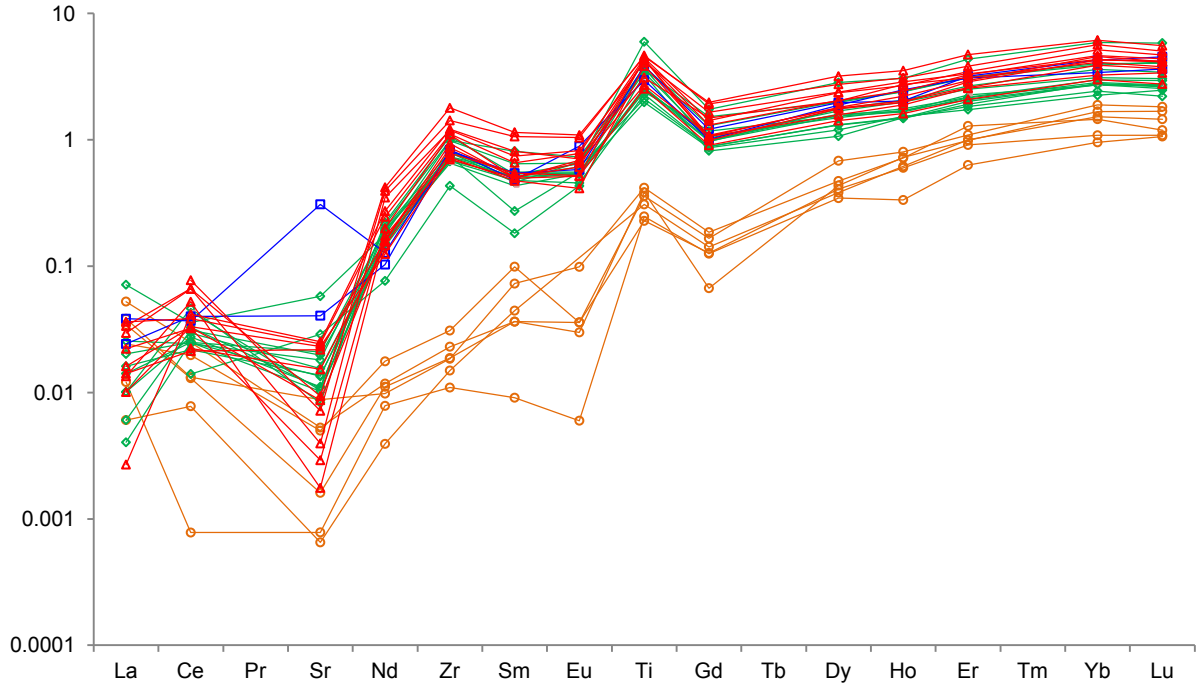

Fig. 4.2.2.1 - Extended orthopyroxene trace elements spiderdiagram of the studied samples; patterns are color-coded by sample: green (sample 32-07), blue (sample 32-22), red (sample 32-32) and orange (sample 39-36).

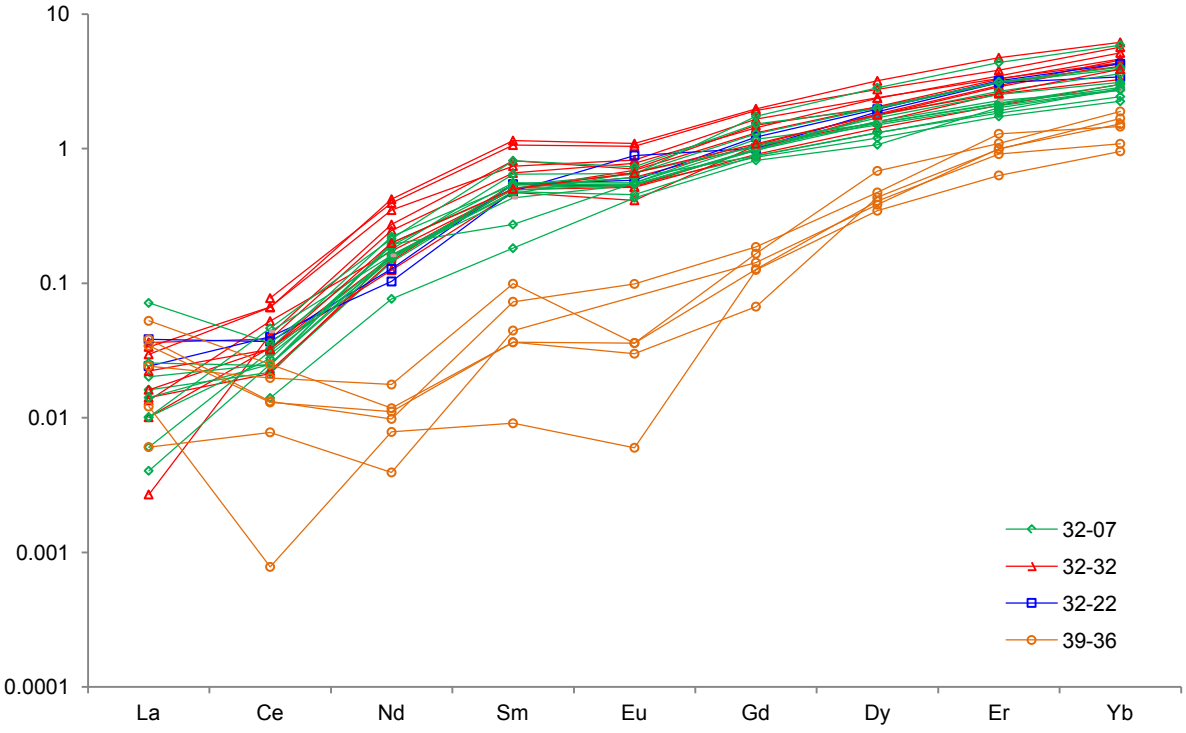

Fig. 4.2.2.2 - Rare Earth Elements (REE) patterns in orthopyroxene from the studied samples. Patterns are color-coded by sample: green (sample 32-07), blue (sample 32-22), red (sample 32-32) and orange (sample 39-36).

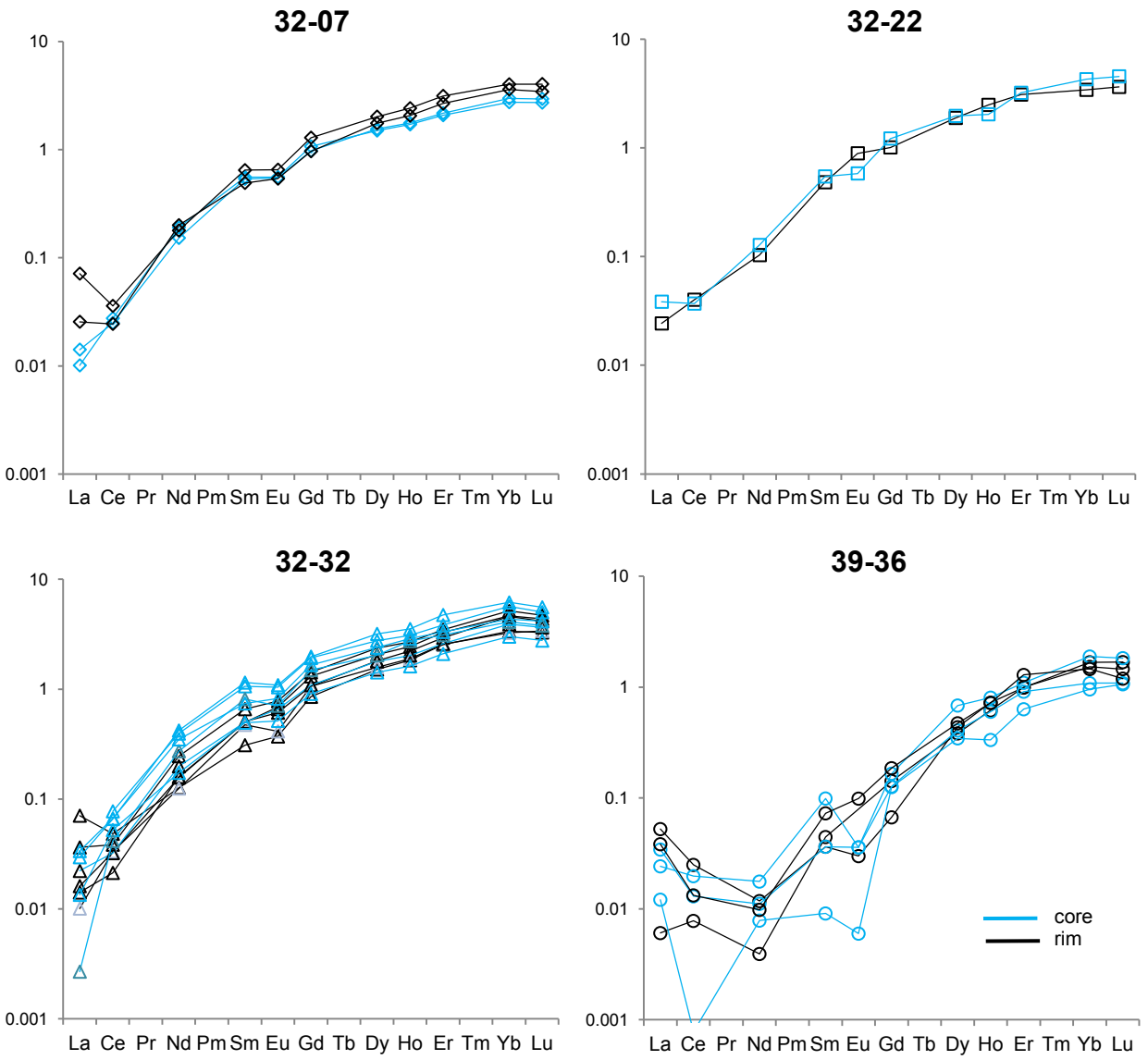

Fig. 4.2.2.3 - Rare Earth Elements (REE) patterns in orthopyroxene from the studied samples, sample by sample. Patterns are color-coded by core (light blue) and rim (black).

Orthopyroxene trace elements compositions of the studied samples show moderate variability moving from core to rim (fig. 4.2.2.3). On the average, cores define slightly enriched patterns compared to the rims in samples 32-22 and 32-32; vice versa in sample 32-07, the rims records the higher concentrations. In sample 39-36 data appear more scattered. Eu negative anomaly may either increase or decrease from core to rim.

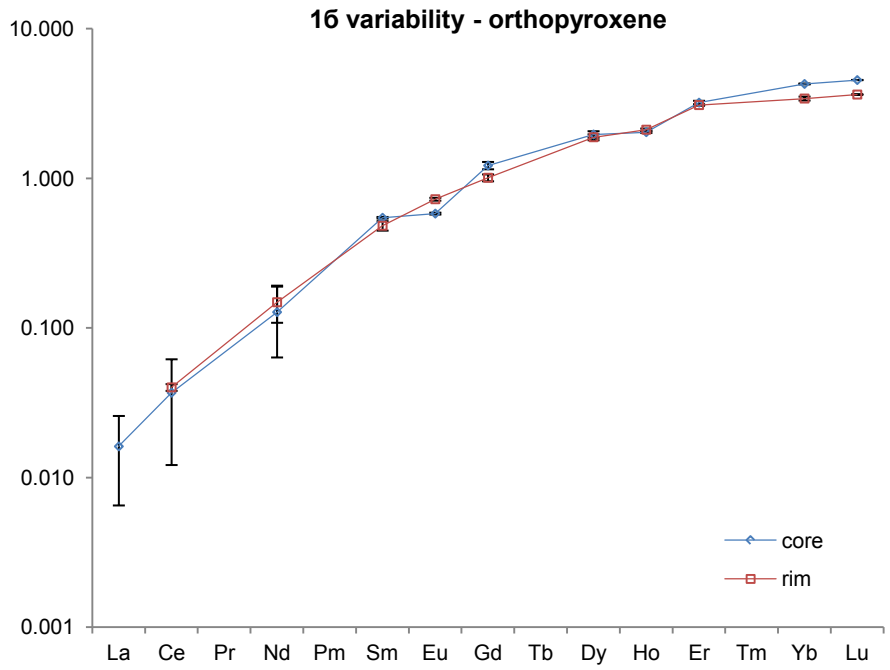

Fig. 4.2.2.4 - REE patterns of an orthopyroxene crystal (rim and core; sample 32-22) in which the error bars indicate 1σ variability. Each reported value represents the average of three neighboring measurements. Values are normalized to C1 chondrite of Anders & Grevesse (1989).

4.2.3 Plagioclase

Plagioclase trace elements compositions of the studied samples (fig. 4.2.3.1) are moderately homogeneous; the corresponding patterns appear variously scattered, especially as regards Zr and HREE. Sample 39-36, of which one single plagioclase crystal has been analyzed, is the most depleted in all elements..
Plagioclase appears generally affected by positive Eu and Sr anomalies and strong negative Zr anomaly, except for sample 39-36 and most crystals of sample 32-22. As concerns REE, intra-sample variability is generally quite low in samples of dredge #32. LREE reveal slight inter-sample variation, with sample 32-22 and sample 32-07 being the most enriched and the most depleted, respectively. Plagioclase generally exhibits LREE-enriched spectra (Ce_N/Sm_N=1.39-2.60), and, excluding the Eu positive anomaly, REE regular decreasing from Ce (up to 3xC1 abundances) to Dy.

The extent of the 1б intra-crystal variability in sample 32-22 is reported as an example in fig. 4.2.3.3.

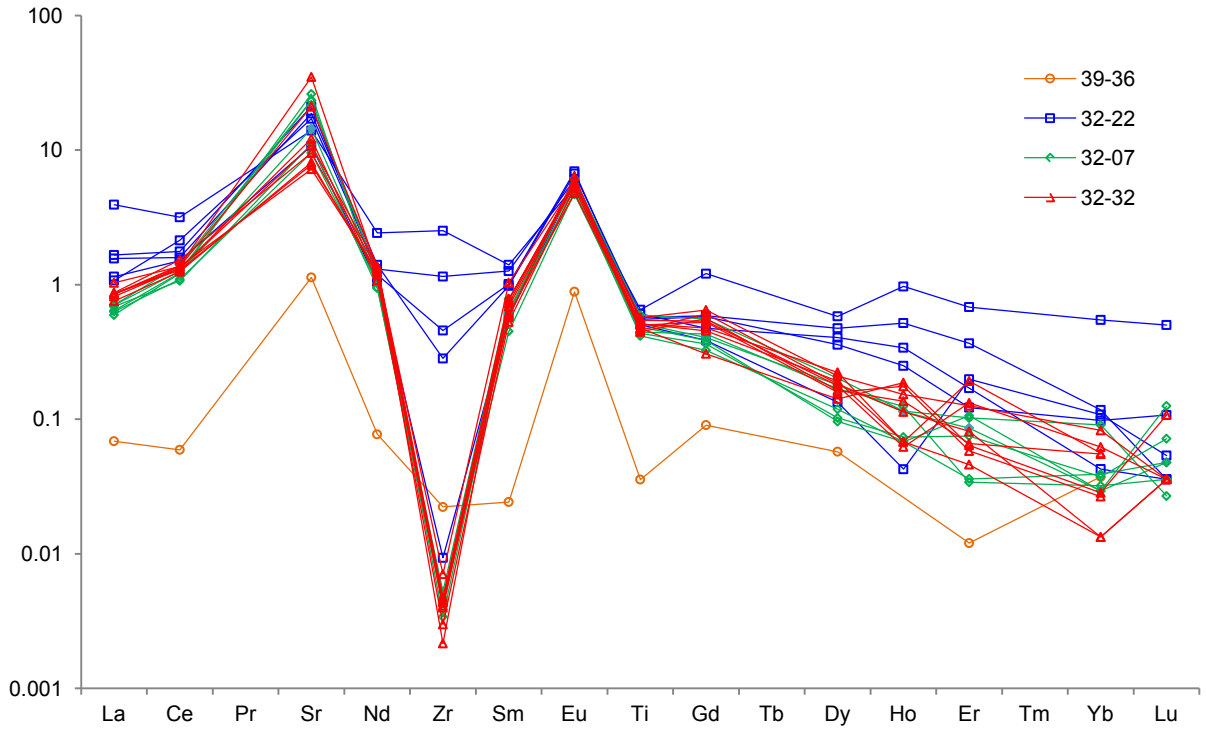

Fig. 4.2.3.1 - Extended plagioclase trace elements spiderdiagram of the studied samples; patterns are color-coded by sample: green (sample 32-07), blue (sample 32-22), red (sample 32-32) and orange (sample 39-36).

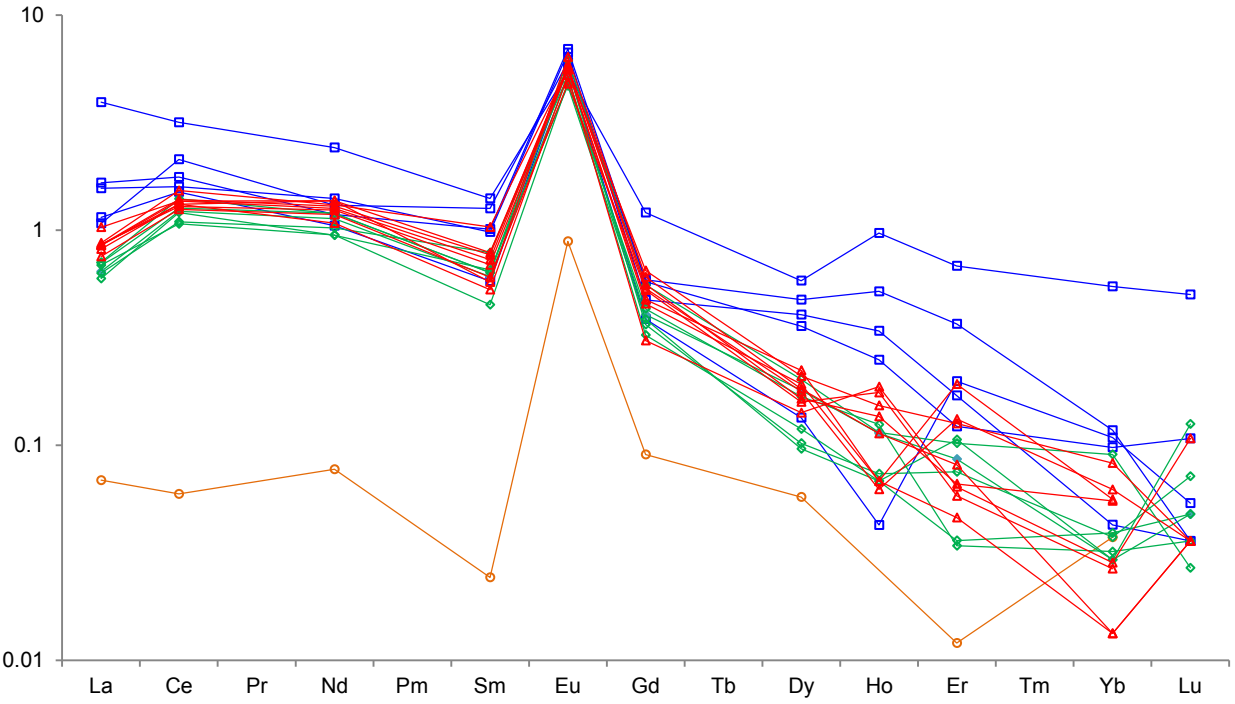

Fig. 4.2.3.2 - Plagioclase REE patterns of the studied samples; patterns are color-coded by sample: green (sample 32-07), blue (sample 32-22), red (sample 32-32) and orange (sample 39-36).

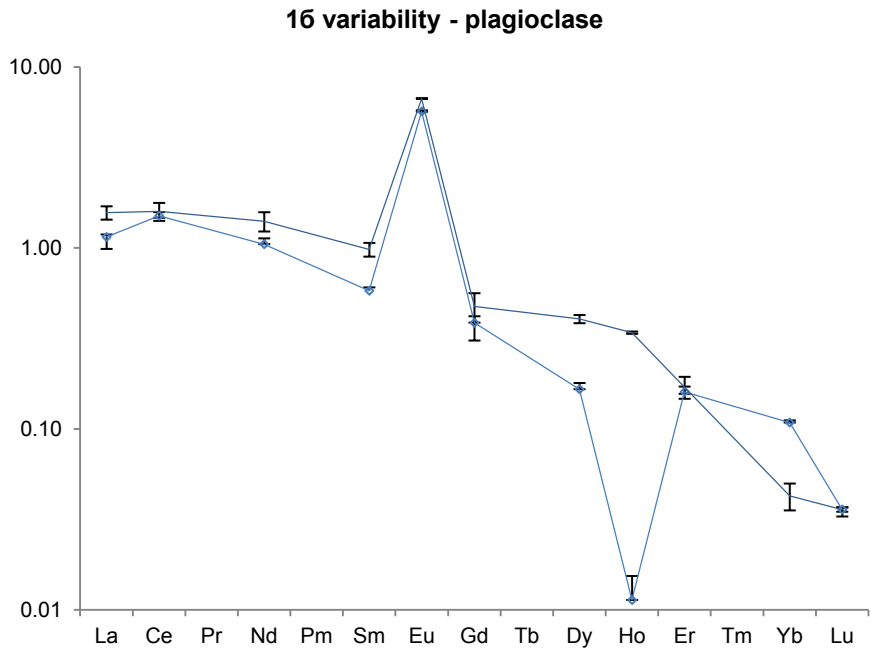

Fig. 4.2.3.3 - REE patterns of a plagioclase crystal (sample 32-22) in which the error bars indicate 1σ variability. Each reported value represents the average of three neighboring measurements. Values are normalized to C1 chondrite of Anders & Grevesse (1989).

4.3 Comparison with data from literature

Two out of four of the analyzed samples pertaining the present work (sample 32-22 and sample 39-36) have been already analyzed by Tartarotti and co-authors (2002), whose work dealt with a set of samples collected along the Romanche FZ during the cruise G96. In the following figures, pyroxenes trace elements compositions of samples 32-22 and 39-36, obtained in the present work and in Tartarotti and co-authors' one, are reported for comparison.

Trace elements concentrations from Tartarotti et al. (2002) were determined with ion microprobe analyses by means of a Cameca IMS 4f ion microprobe at the C.N.R- CSCC of Pavia.

The two data sets appear quite well in agreement, especially as regards clinopyroxene concentrations of sample 32-22; major incongruities may occur in correspondence to the lowest concentrations (e.g. La, Ce, Sr) and Ce.

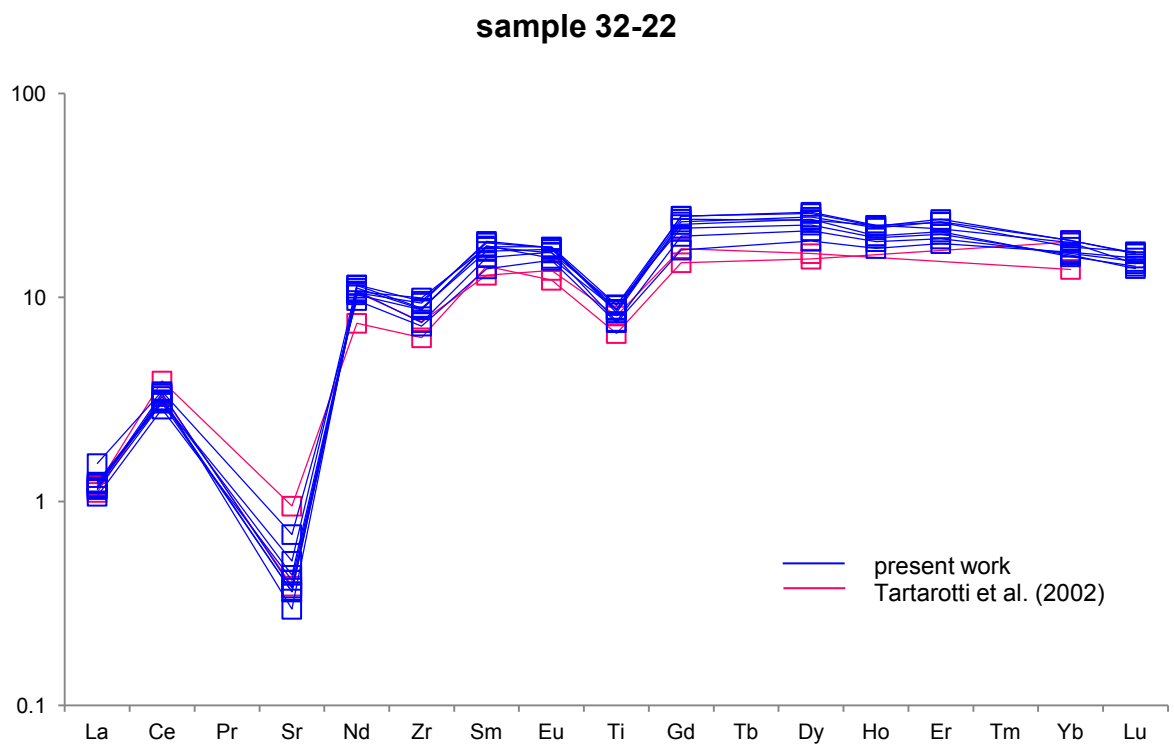

Fig. 4.3.1 - Clinopyroxene trace elements patterns of sample 32-22: reported data are from the present work (blue) and from Tartarotti et al. (2002) (pink).

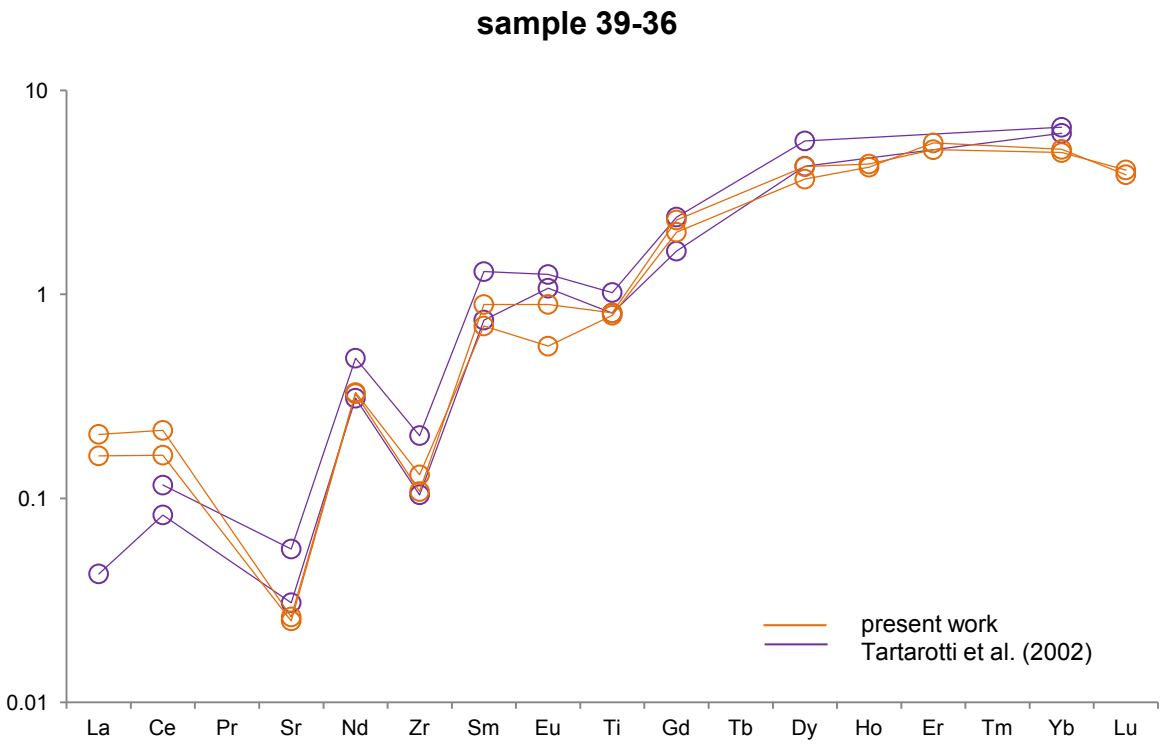

Fig. 4.3.2 - Clinopyroxene trace elements patterns of sample 39-36: reported data are from the present work (orange) and from Tartarotti et al. (2002) (violet).

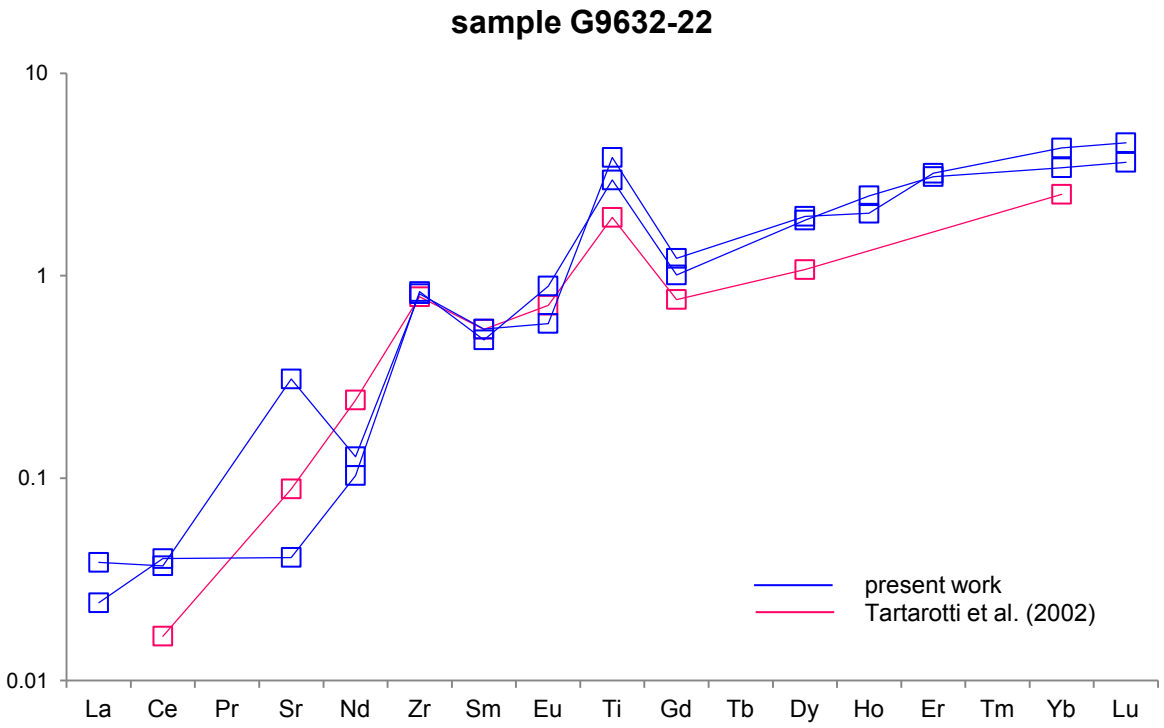

Fig. 4.3.3 - Orthopyroxene trace elements patterns of sample 32-22: reported data are from the present work (blue) and from Tartarotti et al. (2002) (pink).

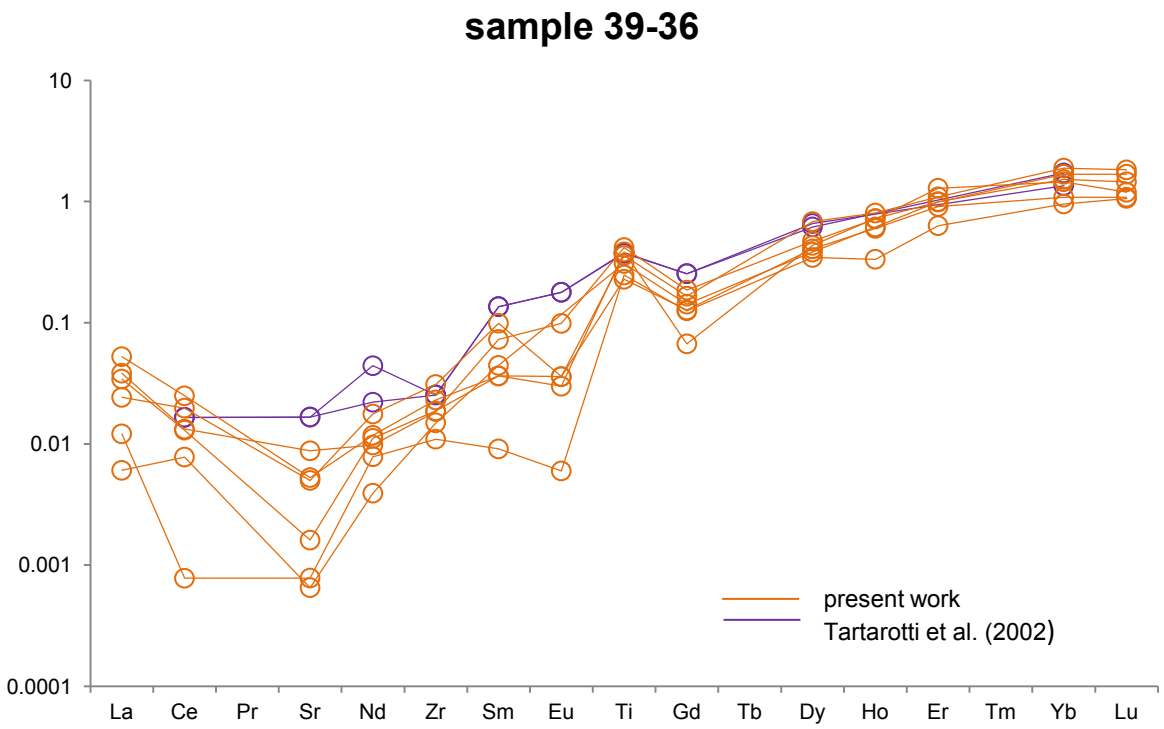

Fig. 4.3.4 - Orthopyroxene trace elements patterns of sample 39-36: reported data are from the present work (orange) and from Tartarotti et al. (2002) (violet).

REE pyroxenes abundances of the studied samples have been compared to compositional ranges of mid-ocean ridge plagioclase-free (Johnson et al., 1990; Seyler and Bonatti 1997; Brunelli et al. 2006; Seyler et al. 2011) and plagioclase-bearing (Seyler and Bonatti 1997; Tartarotti et al. 2002, of which samples 32-22 and 39-36 have not been included) peridotites, and to those of plagioclase-bearing peridotites from Apennines ophiolites (Piccardo et al., 2007; Rampone et al., 2008); orthopyroxene data are not available from authors Brunelli et al. (2006), Johnson et al., (1990) and Seyler and Bonatti (1997); finally, due to the current lack of trace elements plagioclase data from abyssal peridotites in literature, plagioclase abundances of the studied samples have been compared to those from oceanic gabbros (Brunelli, unpublished), ol-troctolites (Drouin et al., 2009) and plagioclase-peridotites from Apennines ophiolites (Piccardo et al., 2007; Rampone et al., 2008).

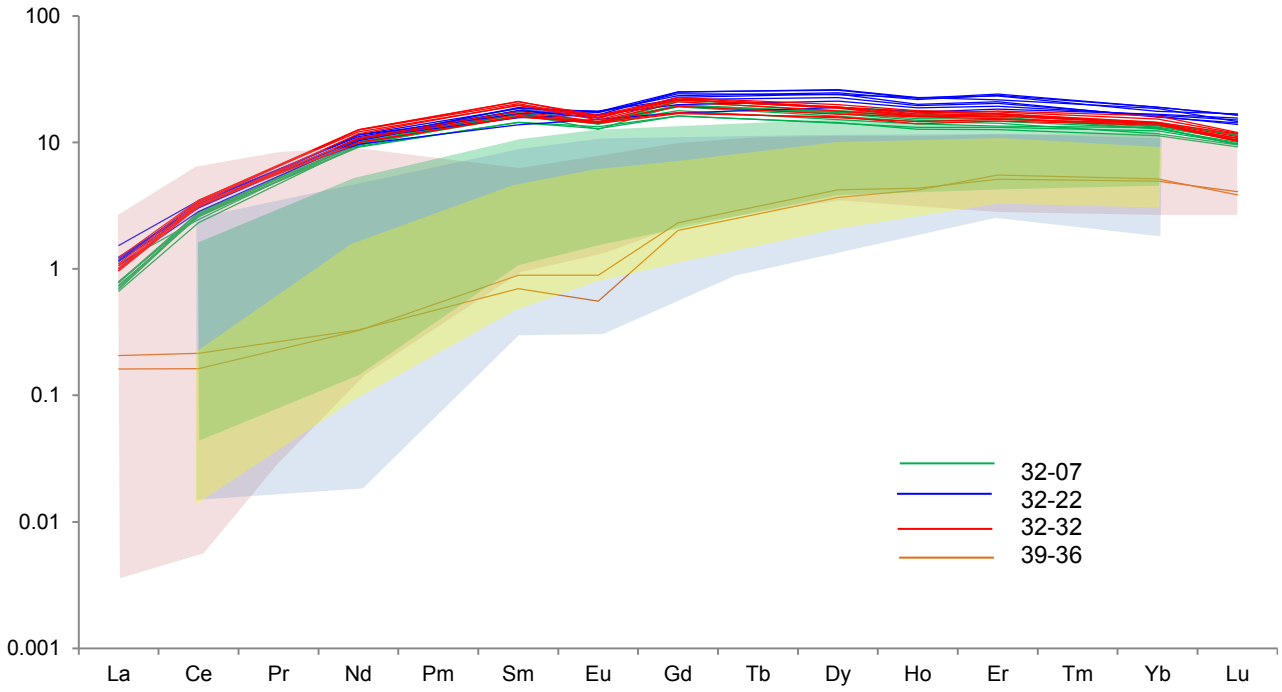

Fig. 4.3.5 - Clinopyroxene Rare Earth Elements patterns of the studied samples compared with those from plagioclase-free abyssal peridotites, from Johnson et al. (1990) (blue field), Seyler & Bonatti (Ro1 group, green field), Seyler e al. (2011) (red field) and Brunelli et al. (2006) (yellow field).

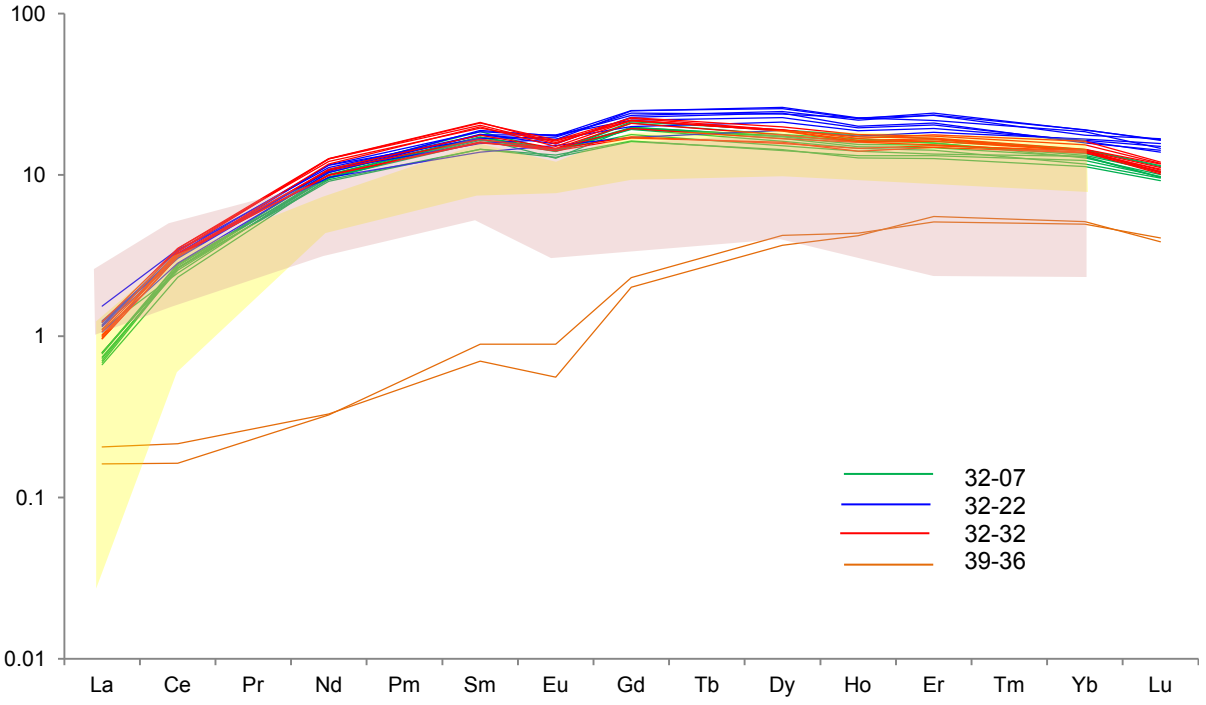

Fig. 4.3.6 - Clinopyroxene Rare Earth Elements patterns of the studied samples compared with those from plagioclase-bearing abyssal peridotites, from Seyler and Bonatti (1997) (Ro2 group; red field) and Tartarotti et al. (2002) (yellow field).

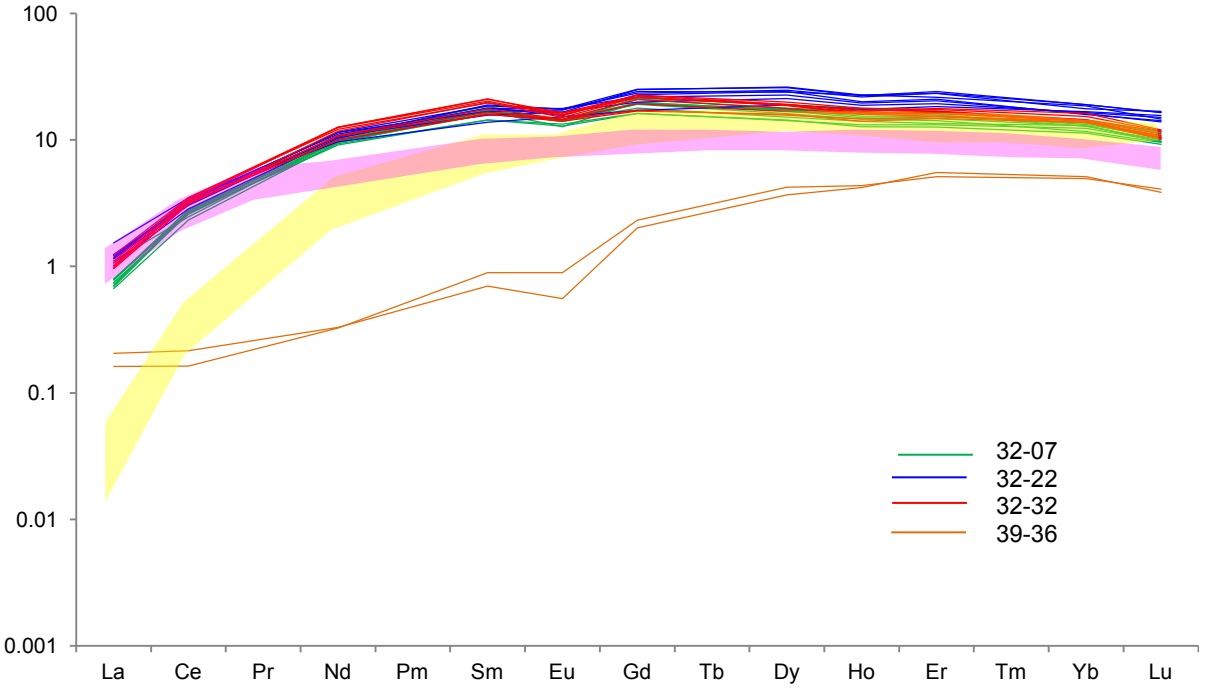

Fig. 4.3.7 - Clinopyroxene Rare Earth Elements patterns of the studied samples compared with those from plagioclase-bearing peridotite of Apennines ophiolites, from Piccardo et al. (2007) (pink field) and Rampone et al. (2008) (yellow field).

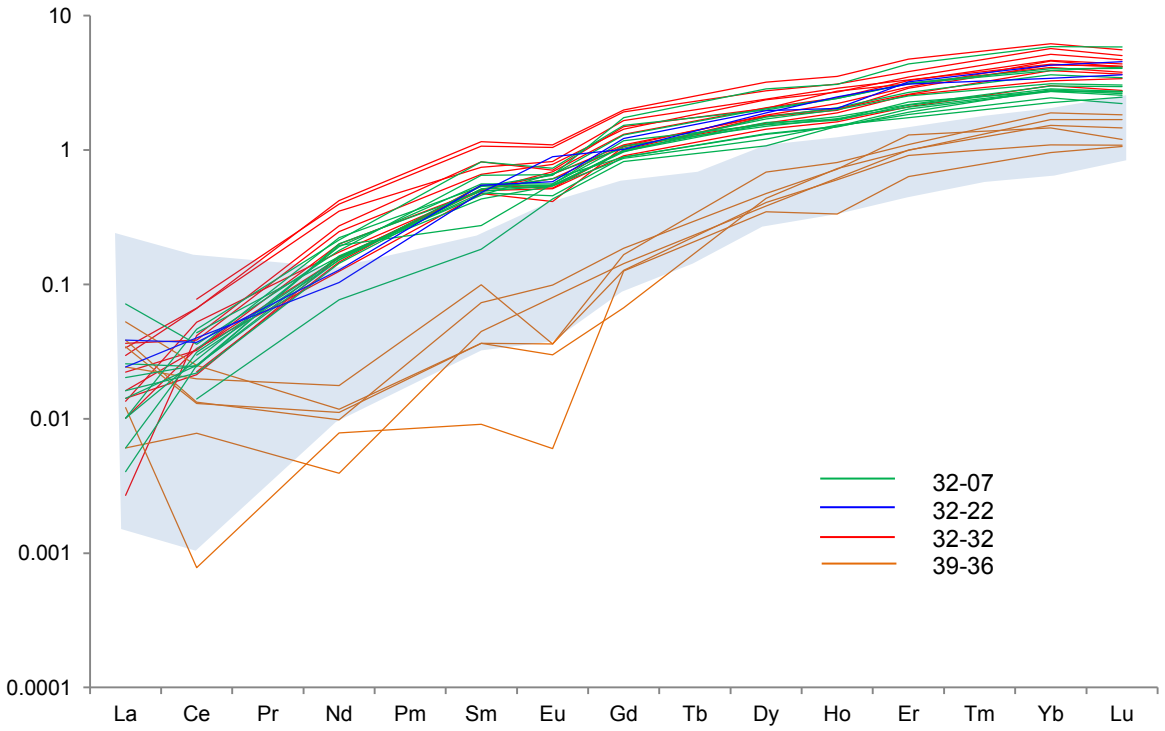

Fig. 4.3.8 - Orthopyroxene Rare Earth Elements patterns of the studied samples compared with those from plagioclase-free abyssal peridotites, from Seyler et al. (2011) (blue field).

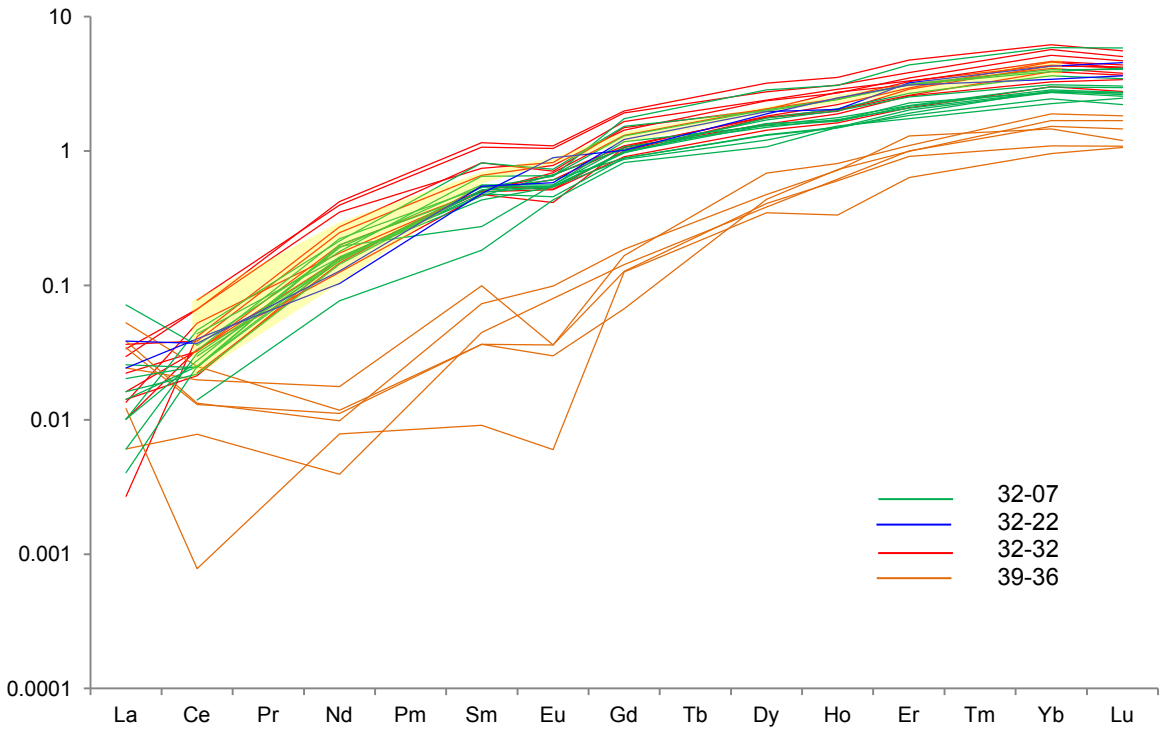

Fig. 4.3.9 - Orthopyroxene Rare Earth Elements patterns of the studied samples compared with those from plagioclase-bearing abyssal peridotites, from Tartarotti et al. (2002) (yellow field).

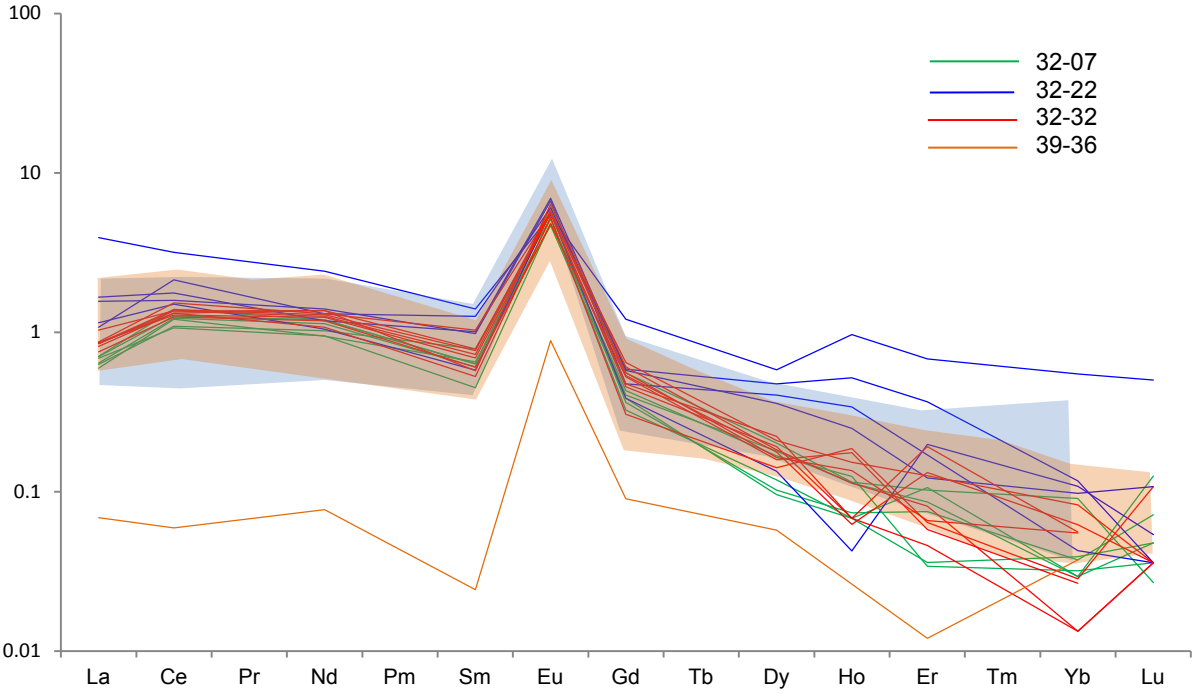

Fig. 4.3.10 - Plagioclase Rare Earth Elements patterns of the studied samples compared with those from oceanic gabbros (Brunelli, unpublished data; blue field) and from oceanic ol-troctolites (Drouin et al., 2009; red field).

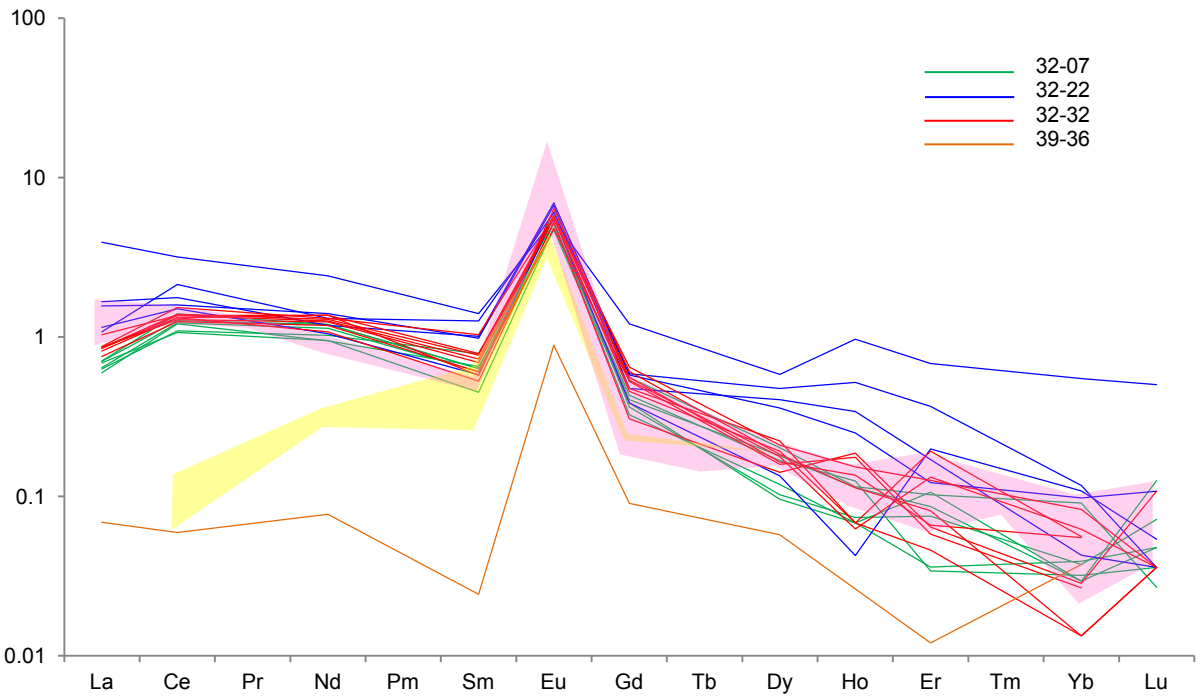

Fig. 4.3.11 - Plagioclase Rare Earth Elements patterns of the studied samples compared with those from Apennines ophiolites, from Piccardo et al. (2007) (pink field) and Rampone et al. (2008) (yellow field).

From comparison with data from literature, it comes to light that pyroxenes REE concentrations of the studied samples generally appear in agreement with those of other plagioclase-bearing abyssal peridotites

(with even higher concentrations from MREE to HREE in sample 32-22), i.e. generally enriched with respect to plagioclase-free abyssal peridotites. Sample 39-36, instead, which is the most depleted of the studied samples, exhibits trace elements concentrations that fall in the compositional field of abyssal plagioclase-free peridotites. As regards plagioclase, REE patterns of the studied samples fit well with those from oceanic gabbros and ol-troctolites and partially with those of plagioclase-peridotites from Apennines ophiolites , unless the strong depletion affecting sample 39-36.

4.4 Comparison of G96 data

In the following figures, clinopyroxene rare earth elements data of the present work are reported together with data from Tartarotti et al. (2002), of which samples 32-22 and 39-36 have been renamed adding abbreviation "TA" (table 4.4.1). Samples have been divided in three groups on the basis of their REE pattern shape.

In figure 4.4.1 we can observe that Group1 (samples 32-07, 32-22, 32-22TA and 32-32, sea-green lines) is characterized by near-flat MREE to HREE patterns (Sm_N/Yb_N=1.19 and Dy_N/Yb_N=1.29), with relative moderate depletion in LREE (Ce_N/Yb_N=0.21). Group2 (samples 39-27, 39-28 and 43-03; pink lines) is characterized by near-flat HREE patterns (Sm_N/Yb_N=1.04 and Dy_N/Yb_N=1.29), showing 12-28xC1 abundances similar to those of Group1, with relative strong depletion in LREE (Ce_N/Yb_N=0.09) (fig. 4.4.3A). Group3 (sample 39-36 and 39-36TA; orange lines) characterized by REE regular increasing from LREE (Ce_N/Yb_N=0.04) to MREE (Sm_N/Yb_N=0.16) to HREE (Dy_N/Yb_N=0.78), up to 4-5 x C1 HREE abundances.

In the light of this grouping, we can also observe that samples of Group1 and Group2 are characterized by Ti and Zr enrichment, whereas Group3 records a strong depletion (fig. 4.4.2), as also major elements analysis confirmed (titanium concentrations measured by EMPA and LA-ICP-Ms are well in agreement, with average $Ti_{EMPA}/Ti_{LA\text{-}ICP\text{-}MS} \approx 1.05$); on the other hand, as shown in figure 4.4.4, Group2 samples are affected by Na2O depletion with respect to Group1, showing values in agreement with, or even higher than, those of Group3, coupled with Sr depletion, although still not reaching the low concentrations of Group3.

Table 4.4.1 - List of G96 samples

G96 samples list	
present work	*Tartarotti et al. (2002)*
G9632-07	G9632-22TA
G9632-22	G9639-27
G9632-32	G9639-28
G9639-36	G9639-36TA
	G9643-03

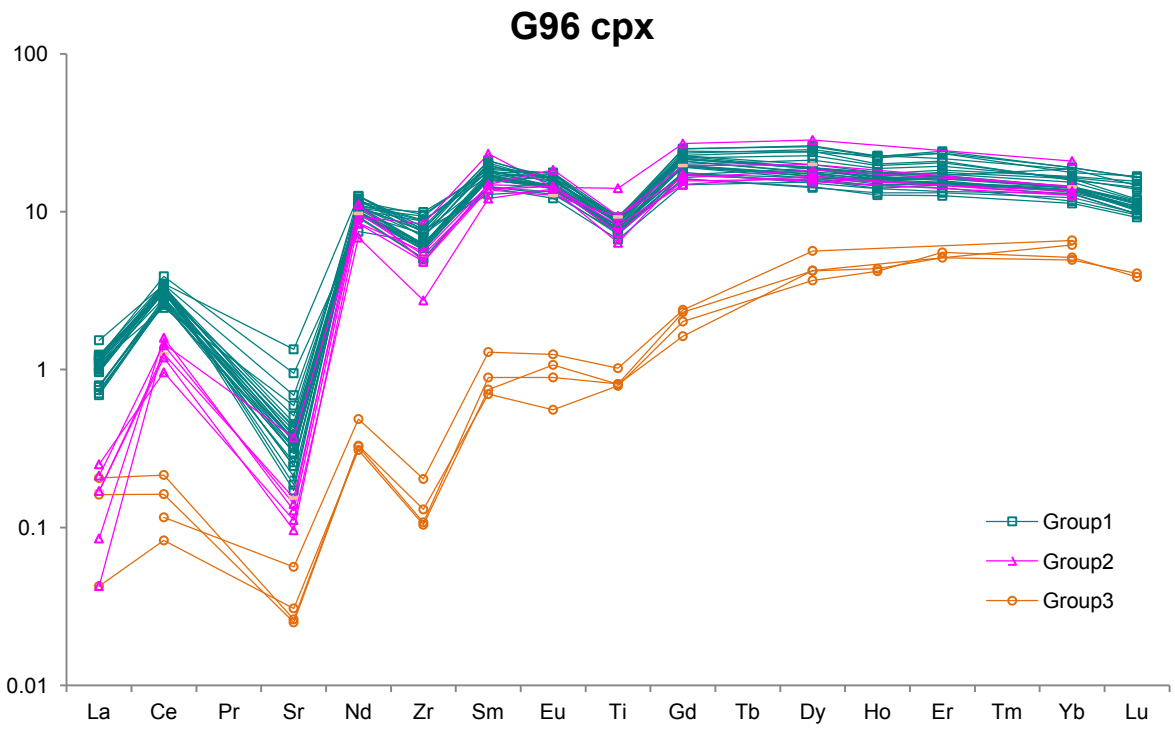

Fig. 4.4.1 - Clinopyroxene REE patterns of the studied samples integrated with data from Tartarotti et al., (2002); samples have been divided in three groups on the basis of their pattern shape: Group1 (sea-green), Group2 (pink) and Group3 (orange).

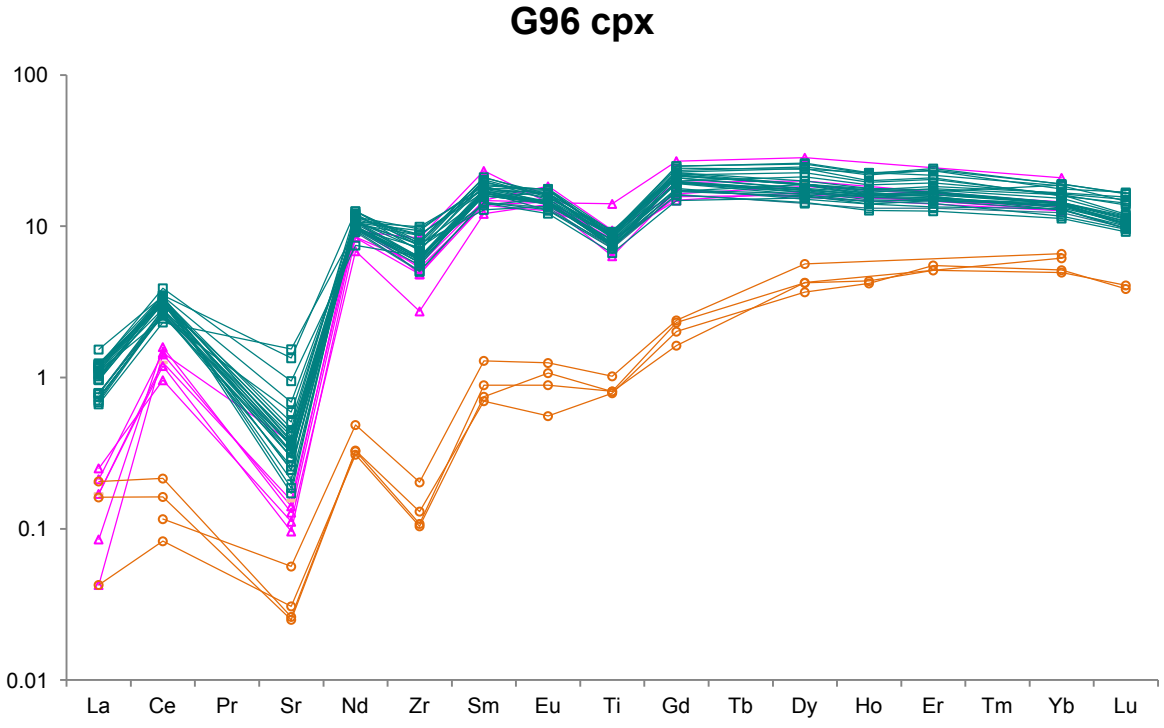

Fig. 4.4.2 - Clinopyroxene trace elements spiderdiagram of the studied samples integrated with data from Tartarotti et al., (2002); samples are color-coded by groups on the basis of their REE pattern shape (see text): Group1 (sea-green), Group2 (pink) and Group3 (orange).

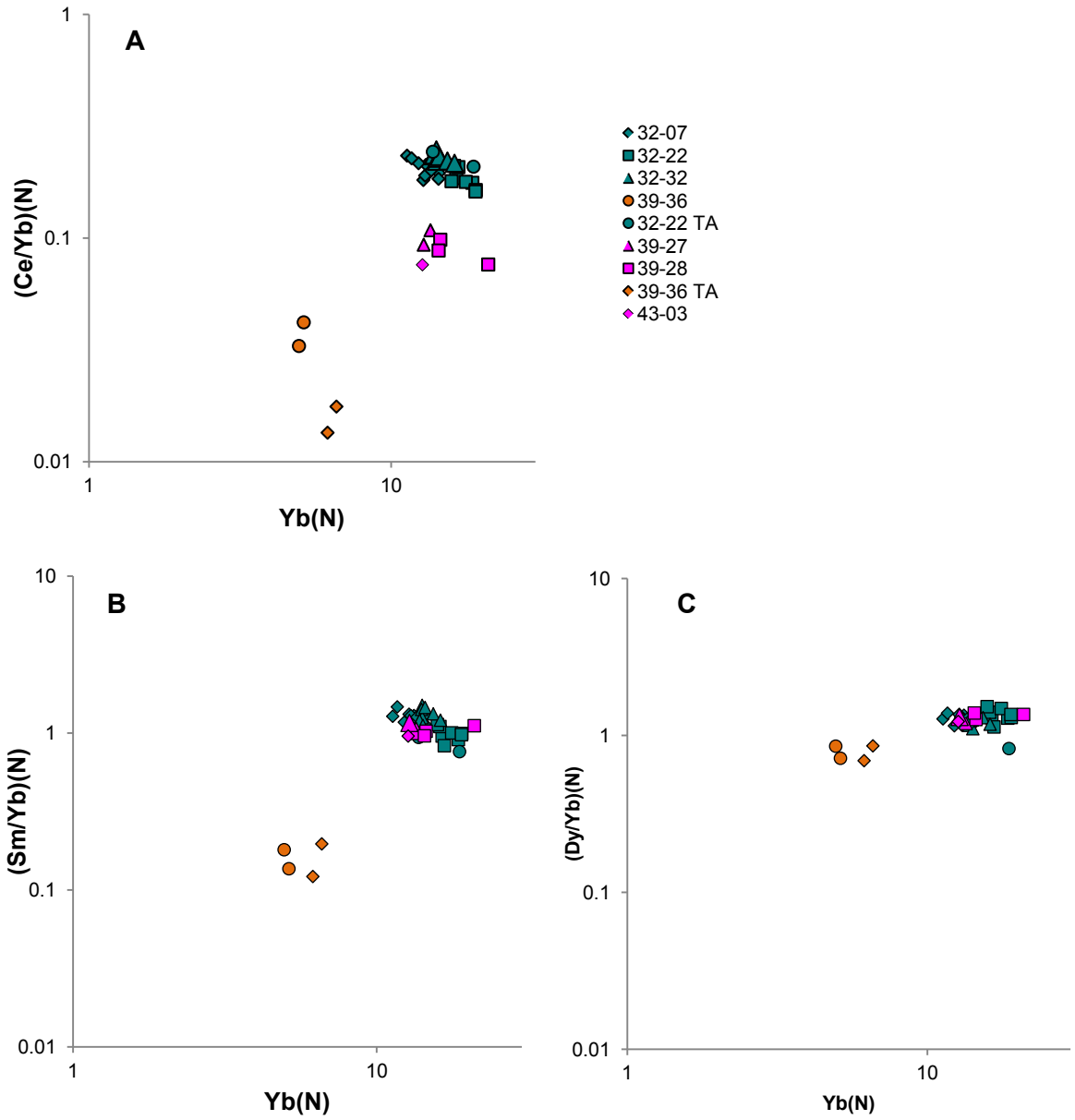

Fig. 4.4.3 - Variation of Ce/Yb (A), Sm/Yb (B) and Dy/Yb (C) vs. Yb of the studied samples integrated with data from Tartarotti et al. (2002); samples are color-coded by groups on the basis of their REE pattern shape (see text): Group1 (sea-green), Group2 (pink) and Group3 (orange). Values are normalized to C1 chondrite of Anders and Grevesse (1989).

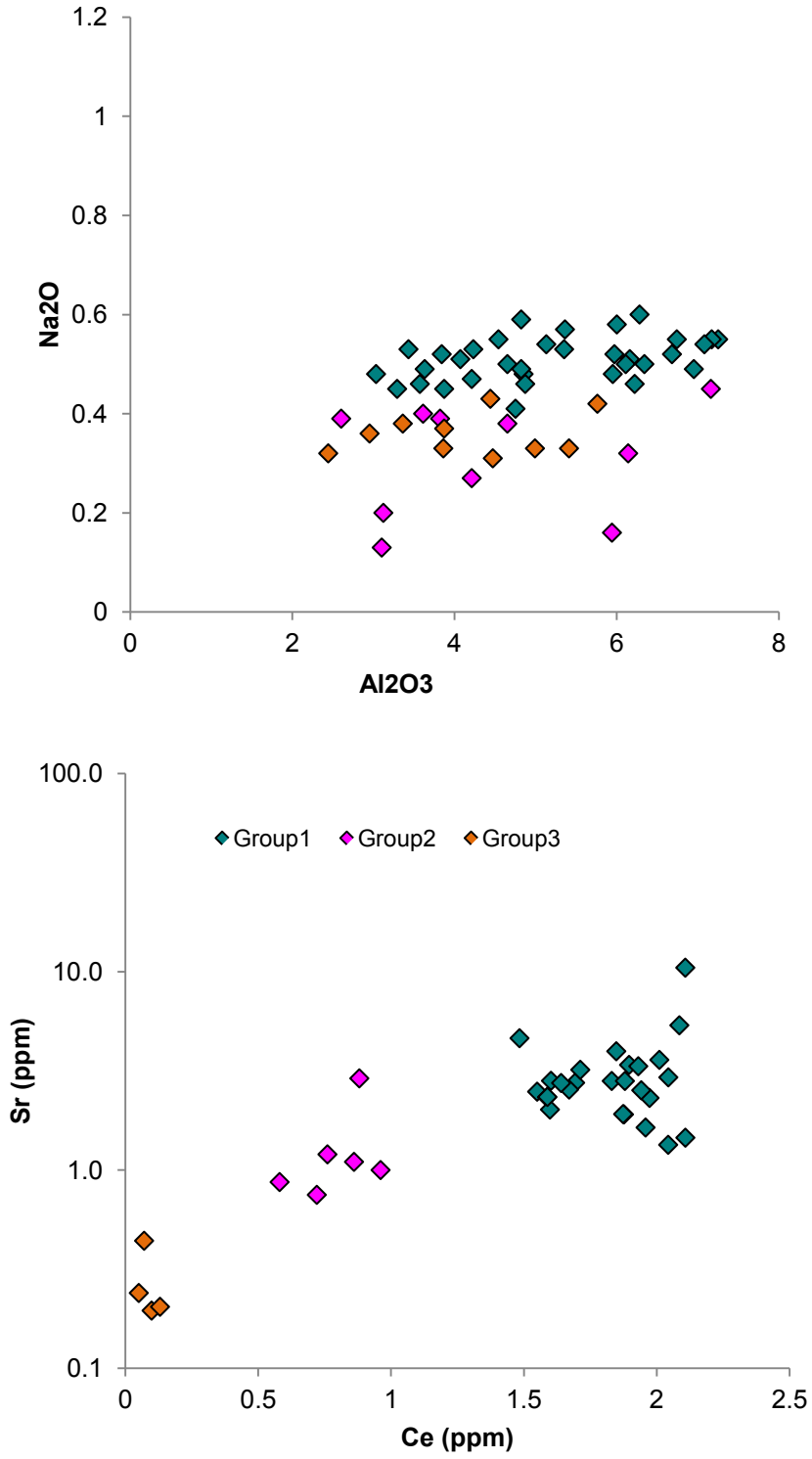

Fig. 4.4.4 -Na2O vs Al2O3 and Sr (ppm) vs. Ce (ppm) in clinopyroxene of G96 samples; samples are color-coded by groups on the basis of their REE pattern shape (see text): Group1 (sea-green), Group2 (pink) and Group3 (orange).

Chapter 5
Modeling

5.1 Dynamic melting and open-system melting

The trace element composition of residual mantle is an important tool not only for documenting the chemical composition of the mantle, but also to describe the nature of the melting process that the mantle has undergone. Generally, mantle partial melting process can be represented by means of three main models: batch melting, fractional melting (Schilling & Winchester, 1967; Gast, 1968; Shaw, 1970), and dynamic melting (Langmuir et al., 1977; Mckenzie, 1985; Liang, 2008; Shaw, 2000; Albarède, 1995; Johnson & Dick, 1992; Zou, 1998).

The batch melting model assumes that the melt remains in equilibrium with the solid throughout the melting event, whereas the fractional melting model assumes that (i) the melt is removed from the initial source as it forms, (ii) only the last drop of melt is in equilibrium with the residue, and (iii) there is no residual melt. Dynamic melting, instead, accounts for a critical threshold for melt extraction: when the melt mass fraction in the residue is less than the critical value for melt separation, there is no melt extraction (as in batch melting), and when the melt fraction in the residue is greater than the critical value for melt separation, any infinitesimal excess of melt will be extracted from the matrix. At the end of the process the melt mass corresponding to the critical mass fraction is retained in the mantle residue.

Dynamic melting is generally agreed to be the more realistic scenario concerning melting during adiabatic upwelling (Richter and McKenzie, 1984; Ribe, 1988; Williams and Gill, 1989; Hémond et al., 1994; Zou and Zindler, 1996). Trace elements (REE, Ti and Zr) data of most abyssal peridotites do not match equilibrium conditions with MORB; the composition of MORB and residual peridotites appear to be, instead, closely approximated by repeated melting and segregations of small increments (≤0.1%) of a Depleted MORB Mantle (DMM) source (Johnson et al.,1990). The melt formed, which cannot be perfectly extracted from the residue, will probably be retained at grain boundaries or in interstices between minerals; this residual melt porosity has been estimated to be in the range of 0.1-1% (Langmuir et al., 1992; Spiegelman & Elliott, 1993; Lundstromet al., 2000). Such trapped melts play an important role in the melting process as they are partially responsible for a weak refertilization of the melting source (Brunelli et al. 2006; Hellebrand et al. 2002).

Moreover, melting starting in the garnet stability field and then continuing in the spinel stability field is thought to be a common process that abyssal peridotites experience beneath mid-ocean ridges (Hellebrand et al. 2002). Dynamic melting model consists of three subsystems: the residual melt, the extracted melt and the residual solid; a dynamic melting process keeping a constant fraction of each solid phase and a constant bulk distribution coefficient is called modal dynamic melting and nonmodal dynamic melting, otherwise.
Highly incompatible elements, e.g. LREEs, are useful to assess late-stage processes such as entrapment, melt-rock reaction and veining; for example dynamic melting model is consistent with extreme depletion of incompatible elements in clinopyroxene from abyssal peridotites (Johnson, et al. 1990). On the other hand, moderately incompatible elements, e.g. MREE and HREE, are less affected by such late-stage processes and thus useful to infer the melting history of abyssal peridotites (Hellebrand et al. 2002). In this perspective, decompressional melting, melt segregation and melt migration assume an important role in driving the observed compositional heterogeneities in mantle residua, which consequently can be considered both source-inherited and melting-induced.

Petrographic evidences of magmatic reactive impregnation in the studied samples (chapter II) require an open-system scenario to be accounted for, which implies exotic migrating melts to percolate mantle rocks, since the large modal plagioclase (up to 15%) can not be explained by frozen pockets of local melts and/or spinel breakdown alone. Moreover, the studied rocks have major and trace elements compositions too enriched to be considered simple mantle residua, thus a refertilization process must be invoked.
Previous works (Seyler and Bonatti, 1997; Tartarotti et al., 2002.) documented that the Romanche FZ mantle peridotites did interact with transient melts. Other authors provided evidences for melt transport/retention to be a common mechanism experienced by upwelling mantle under slow mid-ocean ridges, which not necessarily leads to crystallization of plagioclase-bearing mineral assemblages, but also plagioclase-free, px pockets may precipitate, depending on the pressure conditions at which crystallization from the interstitial liquids occurs (Seyler et al. 2001, Dijkstra et al., 2001).
At the end of the melting process in the spinel stability field, the mantle parcel continues its upwelling. At a certain point, melting is forced to cease because the effects of conductive heat-loss overwhelm the advection of heat from below, i.e. the temperature first equals and then becomes lower than the peridotite solidus; this exactly occurs in correspondence to the base of the thermal boundary layer (TBL) (Niu, 1997; Niu & Hékinian, 1997). A continuous supply of exotic melt is thought to be a plausible process even at shallow depth. Dijkstra et al., 2001 suggested that plagioclase and px crystallize as cumulate phases as a result of a melt reactive impregnation process which occurred late in the deformation history of the host peridotite, at temperature well below the dry peridotite solidus.

5.2 Model setting and equations

5.2.1 Dynamic melting

Melting equations relate incompatible element concentrations in residual solids and derived liquids to the type and degree of melting, and can be used to test what type of melting abyssal peridotites have experienced and whether they are related to MORB by this melting processes.
Clinopyroxene trace element pattern are thus compared to models calculated for open-system, nonmodal dynamic melting.

Melting geometry is based on Ozawa and Shimizu (1995) and Brunelli et al. (2014); the amount of segregated melt depends linearly on the degree of melting but is also related to the amount of trapped melt from the requirement of mass balance.

Overall, the model aims to reproduce a mantle parcel experiencing exotic melt influx during progressive decompressional melting. Model input consists in a variably depleted, spinel-field equilibrated, mantle parcel with a bulk C_0 trace element concentration.
Each calculation step consists of the following stages:

1- The rock experiences a finite small amount of melting (F) and melt extraction (X)

2- Solid residue, residual mode, phase compositions and residual melt are calculated for a given critical mass porosity cmp (φ).

3- The residual melt composition is modified by assuming mixing with an exotic melt influx.

4- A new bulk solid is recalculated in equilibrium with the new residual melt.

5- Go to line 1.

Trace element compositions for the residue and the extracted melts were calculated following the equation set by Zou (1998). In a dynamic melting scenario the residual assemblage also includes a liquid phase. The concentration of a trace element in the residual assemblage is given by

$$C_{\text{res}} = C_0 \frac{1}{1-X}\left\{1 - \frac{X[P+\Phi(1-P)]}{D_0+\Phi(1-P)}\right\}^{1/[\Phi+(1-\Phi)P]} \quad (1)$$

where:

C_{res} is the concentration of a trace element in the residue (residual solid + residual melt);

C_0 is the concentration of a trace element in the source;

P is the weighted liquid partition coefficient:

$$P = \Sigma\, kd^{i/l}\, p^{i}$$

where p^i is the melting mode of the phase i;

D_0 is the initial bulk distribution coefficient of the source:

$$D_0 = \Sigma\, Kd^{i/l}\, X_{0,i}$$

where $X_{0,i}$ is the mode of the phase i in the source;

ϕ is the critical mass porosity, i.e. the minimum "critical" amount of partial melting required to allow segregation of the melt from the source; this also represents the amount of melt retained in the source after extraction;

X is the fraction of extracted melt; this is related to F (total degree of melting undergone by the source) and to the critical mass porosity ϕ by

$$X = 0 \quad \text{for } F \le \Phi$$
$$X = \frac{F-\Phi}{1-\Phi} \quad \text{for } F > \Phi$$

The relative concentration of a trace element in the extracted liquid is given by:

$$C_{\text{res}} = \frac{C_0}{X}\left\{1 - \left[1 - \frac{X[P+\Phi(1-P)]}{D_0+\Phi(1-P)}\right]^{1/[\Phi+(1-\Phi)P]}\right\} \quad (2)$$

Partition coefficients between mineral phase and melt are from Hellebrand et al. (2002) and Brunelli et al., 2006. Partition coefficients for olivine, orthopyroxene, clinopyroxene, garnet and spinel and all elements were compiled based on Blundy et al. (1998) and Suhr et al. (1998), with the exception of Gd obtained by averaging adjacent element values. Partition coefficients for plagioclase were compiled based on Aigner-Torres et al. (2007), except for La, Ce, Gd, Dy, Er and Yb which were corrected according to measured clinopyroxene to plagioclase ratios. Initial spinel mode is from Johnson et al. (1998), melting modes are from Kinzler (1997) (spinel), and Walter (1998) (garnet). Source composition is from Workman & Hart (2005).

Table 5.2.1. Source composition and partition coefficients (mineral/melt) used in this model.

	ol	opx	cpx (sp)	cpx (grt)	grt	sp	plag	S C/C1
SM	0.53	0.27	0.17	0	0	0.03		
MM GRT	0.04	-0.19		1.05	0.11			
MM SP	-0.06	0.28	0.67			0.11		
Ti	0.015	0.1	0.35	0.71	0.16	0.15	0.0014	1.82
Zr	0.004	0.024	0.12	0.27	0.4	0.07	0.0010	1.54
La	0.000007	0.0025	0.06	0.09	0.0035	0.0006	0.0566	1.08
Ce	0.00001	0.005	0.1	0.16	0.008	0.0006	0.0675	1.20
Nd	0.00007	0.01	0.2	0.36	0.05	0.0006	0.0250	1.55
Sm	0.001	0.02	0.3	0.67	0.22	0.001	0.0250	1.86
Eu	0.001	0.03	0.37	0.8	0.45	0.001	0.2600	1.93
Gd	0.0025	0.04	0.405	0.95	1.225	0.0015	0.0102	2.02
Dy	0.004	0.05	0.44	1.1	2	0.002	0.0052	1.76
Er	0.009	0.07	0.43	1.44	3.5	0.003	0.0036	1.20
Yb	0.014	0.09	0.41	1.43	5	0.005	0.0022	1.27
SM		source mode - (Johnson 1998)						
MM		melting mode - (Walter 1998) and (Kinzler 1997)						
S C/C1		source contents - (Workman and Hart 2005) normalized to C1 chondrite of Anders & Grevesse (1989)						

Measured clinopyroxene contents relate to mantle peridotites equilibrated in the spinel field. Thus, model trends for garnet-field equilibrated assemblages were recalculated to make them directly comparable with measured values, assuming an instantaneous garnet-spinel transition according to the following reaction (Johnson et al., 1990):

$$1Ol + 1Grt = 2.5Opx + 0.75Cpx + 1Sp$$

and considering the molar volume of each phase involved, listed in Table 5.2.2.

Table 5.2.2 - Molar volume of mineral phases

Forsterite	Enstatite	Diopside	Pyrope - Grossular	Spinel
$Mg_2(SiO_4)$	$MgSiO_3$	$CaMg(Si_2O_6)$	$Ca_{0.75}Mg_{2.25}Al_2(SiO_4)_3$	$MgAl_2O_4$
43.603	62.676	66.039	116.09	39.762

The following figures show modeling for REE ratios (fig. 5.2.1.1) and variations (fig. 5.2.1.2) in clinopyroxene during dynamic melting in garnet and spinel stability fields, at variable critical mass porosity of the system (ϕ=0.001 and ϕ=0.005). Increasing the critical mass porosity results in reduced depletion of the residue and a slight rotation of the melting paths in the Sm/Yb vs. Yb plot. The REE patterns of residual cpx (figs. 5.2.1.2 and 5.2.1.3) show the reduced depletion as upward compaction the patterns. A peculiar effect is that intermediate REEs mimic the compatible behavior of the HREE during melting in the garnet stability field (fig. 5.2.1.3). This effect depends on the extent of critical mass porosity.

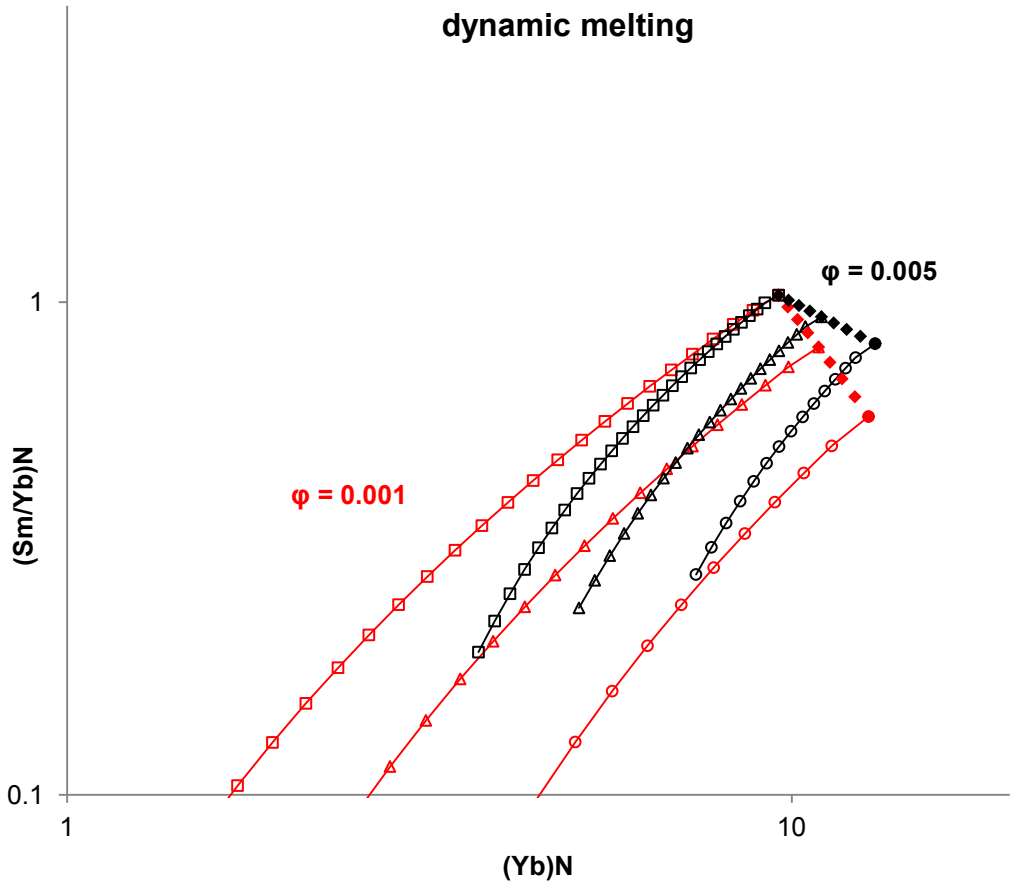

Fig. 5.2.1.1 - (Sm/Yb) vs Yb in cpx in a dynamic melting system, varying the critical mass porosity cmp of the system, assumed constant during the entire process: ϕ=0.001 (red curve) and ϕ=0.005 (black curve). Cpx compositions are assumed to be equilibrated in the spinel stability field: black solid diamonds represent the compositions in the garnet stability field, during melting from 0% to 8%, projected in the spinel stability field; black open squares represent compositions during melting in the spinel stability field with no previous melting in the garnet stability field; black open triangles represent compositions during melting in the spinel stability field after experiencing 4% melting in the garnet stability field; black open circles represent compositions during melting in the spinel stability field after experiencing 8% melting in the garnet stability field. Each melting step corresponds to 1% of melting (F=0.01). Each melting curves proceeds until cpx exhaustion. Values are normalized to C1 chondrite from Anders & Grevesse (1989).

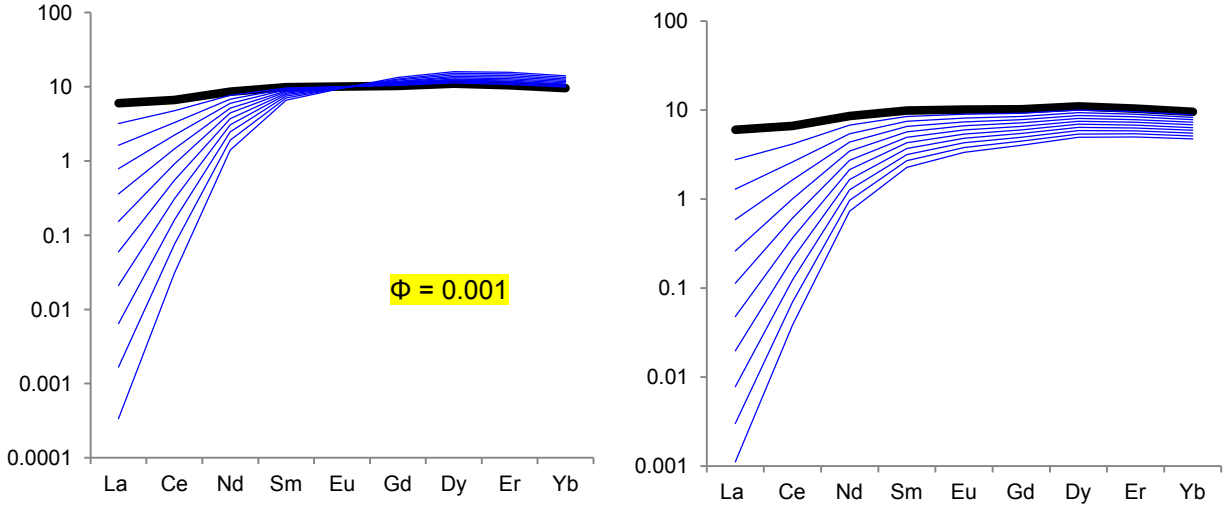

Fig. 5.2.1.2 - REE compositions in clinopyroxene during dynamic melting of a DMM source in the garnet stability field (left) and in the spinel stability field (right) from 0% to 10%. Black bold line represents the starting cpx composition. Each melting step corresponds to 1% of melting (F=0.01) and the critical mass porosity (ϕ) of the system is equal to 0.001. Values are normalized to C1 chondrite from Anders & Grevesse (1989).

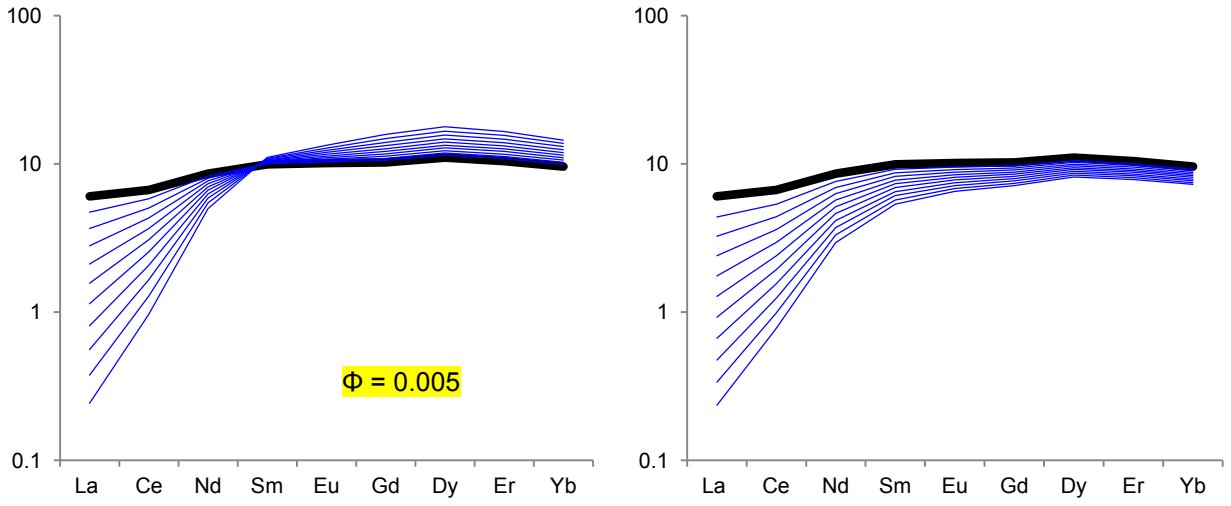

Fig. 5.2.1.3 - REE compositions in clinopyroxene during dynamic melting of a DMM source in the garnet stability field (left) and in the spinel stability field (right) from 0% to 10%. Black bold line represents the starting cpx composition. Each melting step corresponds to 1% of melting (F=0.01) and the critical mass porosity (ϕ) of the system is equal to 0.005. Values are normalized to C1 chondrite from Anders & Grevesse (1989).

5.2.2 Open-system melting

In the following computations we assumed that, during dynamic melting in the spinel stability field, the source experiences the inflow of a variable amount of exotic melt, a small amount of which mixes with the retained melt produced by one increment of partial melting undergone by the source itself.
The amount of the retained melt corresponds to the critical mass porosity ϕ, which has been considered constant during the entire melting and post-melting processes. The exotic melt is assumed to mix with the retained melt in equal parts. The total amount of refertilizing mixed melt corresponds to the critical mass porosity ϕ.

The composition of the melts are calculated according to the equation (2).

After refertilization, new whole rock trace element composition, new mineral modes and new distribution coefficients were recalculated following the equations from Hellebrand et al. (2002):

New whole rock composition:

$$C_{wr} = C_0(1-X)+C_{liq}X \quad (3)$$

Where X is the melt fraction added to the residual peridotite and C_{wr} and C_0 are the new and initial whole rock composition, respectively.

In the following figures results of open-system melting models are reported.

First we explore the case of open-system melting with refertilization due to the inflow of an exotic melt with variable compositions. We considered the occurrence of melts derived from melting of a DMM source both in the spinel stability field and in the garnet stability field.

The melt considered are:
i) instantaneous melt derived from 1% melting of a DMM source (melt1);
ii) instantaneous melt derived from 8% melting of a DMM source (melt2);
iii) aggregated melt derived from the aggregation of incremental melts from 1% to 8% melting of a DMM source (melt3).
The compositions of the melts used in models are listed in table 5.2.2.1.

Table 5.2.2.1 - Compositions (ppm) of the melts used in modeling of open-system melting.

ϕ=0.001		Ti	Zr	La	Ce	Nd	Sm	Eu	Gd	Dy	Er	Yb
SP	melt1	5309	41.36	0.06	0.95	3.50	2.12	0.89	3.53	4.84	3.27	3.31
	melt2	6046	86.31	0.25	3.06	6.99	3.19	1.19	4.41	5.76	3.78	3.75
	melt3	3393	8.13	0.00	0.03	0.73	0.85	0.45	1.95	2.88	2.04	2.12
GRT	melt1	5753	74.03	14.03	26.46	12.34	2.41	0.71	1.63	1.63	0.71	0.58
	melt2	5001	39.36	0.02	0.89	4.21	1.95	0.67	1.73	1.79	0.82	0.66
	melt3	6167	63.80	3.86	10.90	9.22	2.51	0.79	1.92	1.95	0.87	0.71
ϕ=0.005		Ti	Zr	La	Ce	Nd	Sm	Eu	Gd	Dy	Er	Yb
SP	melt1	7207	87.42	1.22	5.97	8.61	3.57	1.33	4.83	6.29	4.08	4.02
	melt2	7044	120.72	2.84	10.85	11.39	4.00	1.39	4.88	6.20	3.97	3.90
	melt3	5585	42.00	0.18	1.64	4.35	2.31	0.95	3.58	4.82	3.16	3.14
GRT	melt1	5732	72.88	13.00	25.13	12.10	2.40	0.71	1.64	1.63	0.72	0.58
	melt2	6334	58.29	1.35	6.96	9.00	2.69	0.84	1.94	1.93	0.85	0.67
	melt3	6868	74.97	6.63	17.29	12.14	2.89	0.88	2.03	2.02	0.89	0.71

The aggregated melts were calculated by linear mixing of all partial melt components according to the equation reported by Brunelli et al., (2006):

$$C_{\text{ref}} = \frac{\sum_{n=a}^{n=b} C_n}{b-a} \qquad (4)$$

In the following figures modeling of REE ratios and variations in clinopyroxene during open-system melting are reported. Results show that the composition of the exotic melt strongly influences the residual composition of the source during open-system melting. Overall, the most incompatible elements, i.e. the lighter LREEs, are the most susceptible to the effects of open-system melting and the extent of their compositional variation during melting is mainly dependent on the exotic melt composition. La and Nd

decreasing during melting will be slower if the exotic melt is relatively enriched (e.g. melts derived from low degree of melting of a garnet-lherzolite).

On the other hand, given that the critical mass porosity corresponds to the total amount of melt retained in the source after one increment of melting, the effect of the refertilizing melt on the source is emphasized with larger ϕ. The slope of the melting curve increases with the critical mass porosity in a dynamic melting system (fig. 5.2.2.1), whereas in an open-system melting MREE and HREE patterns may vary from a decreasing trend for small critical mass porosity (e.g. ϕ=0.001; fig. 5.2.1.1 and 5.2.1.4) to an increasing trend for large critical mass porosity (e.g. ϕ=0.005; fig. 5.2.1.2 and 5.2.1.5) a behavior opposite to that of the pure fractional or even dynamic melting. Thus, for sufficiently enriched influxing melts, the critical mass porosity is able to strongly influence MREE and HREE behavior during open-system melting. Moreover, it is noteworthy that, when the critical mass porosity is large (ϕ=0.005), the resulting patterns develop different MREE to HREE fractionation, depending on the exotic melt composition: spinel-lherzolite-derived melts induce residual clinopyroxene to develop a relative enrichment in the lighter HREE, whereas garnet-lherzolite melts lead to relative MREE enrichment. These effects are emphasized approaching the clinopyroxene exhaustion.

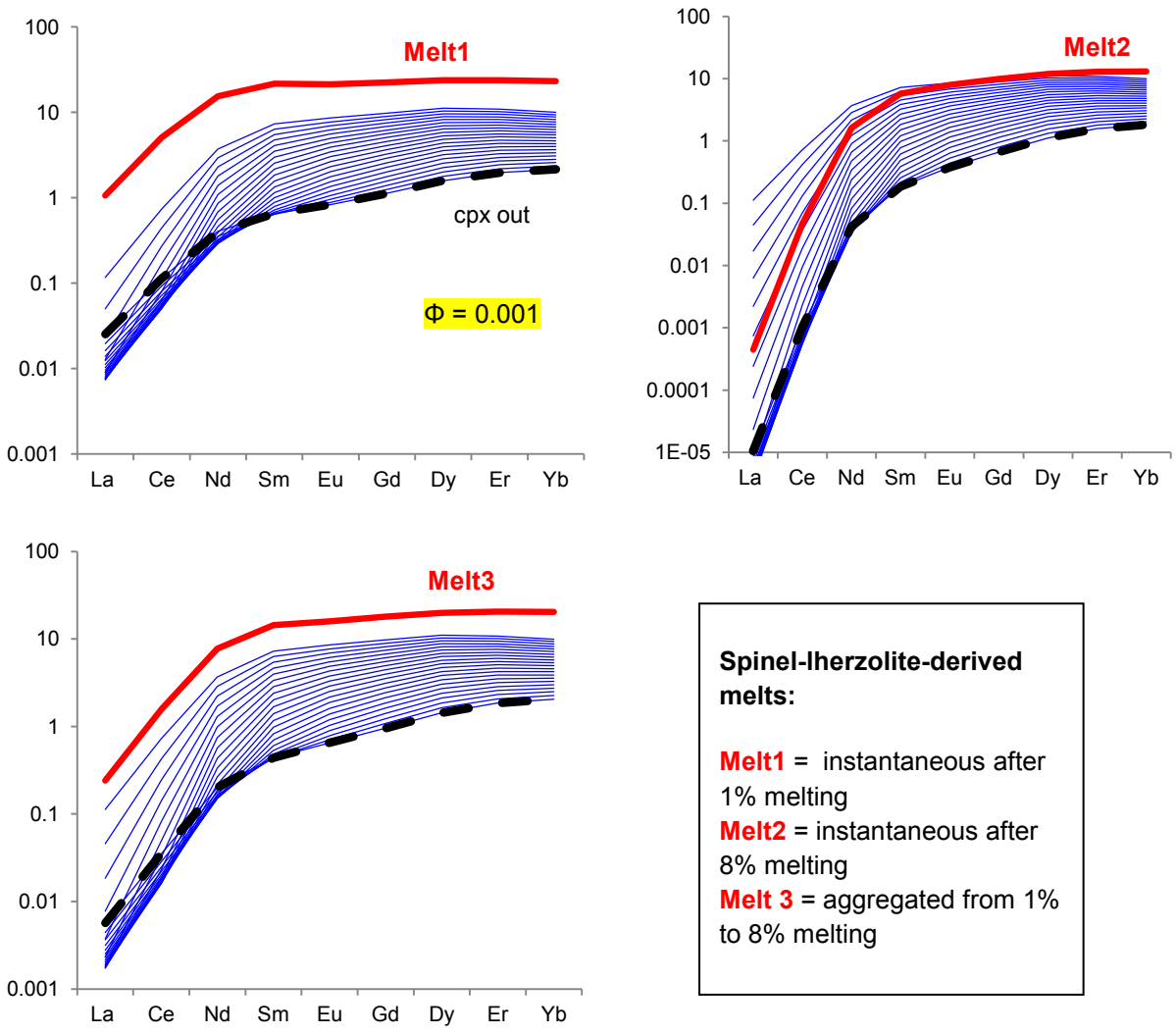

Fig. 5.2.2.1 - REE compositions in clinopyroxene during open-system melting in the spinel stability field of a DMM source which experienced 4% melting in the garnet stability field. Melting proceeds until the clinopyroxene exhaustion (black dashed line). The red bold line represents the exotic melt composition (see the small box for details). Each melting step corresponds to 1% of melting (F=0.01) and the critical mass porosity (ϕ) of the system is equal to 0.001. Values are normalized to C1 chondrite from Anders & Grevesse (1989).

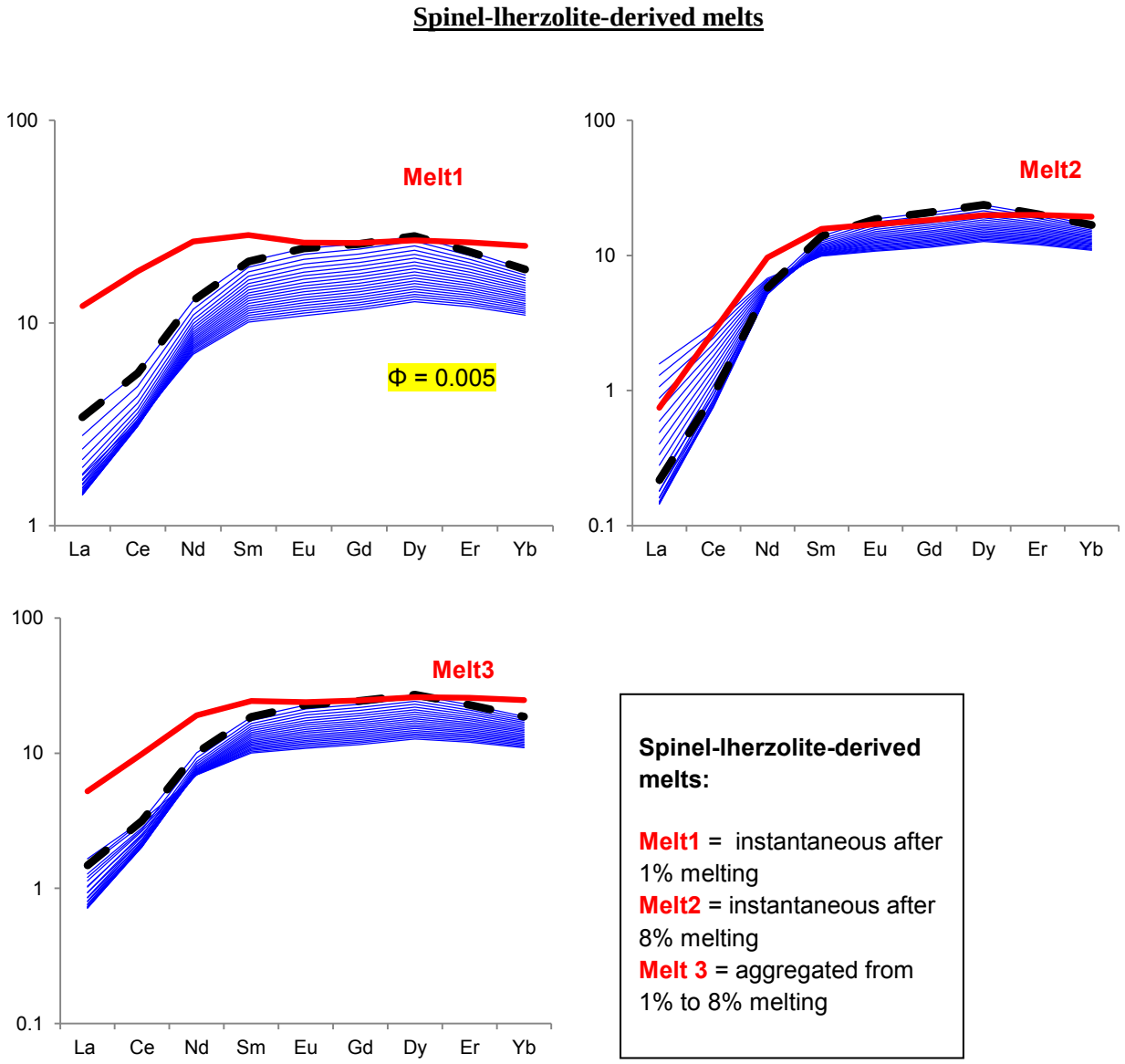

Fig. 5.2.2.2 - REE compositions in clinopyroxene during open-system melting in the spinel stability field of a DMM source which experienced 4% melting in the garnet stability field. Melting proceeds until the clinopyroxene exhaustion (black dashed line). The red bold line represents the exotic melt composition (see the small box for details). Each melting step corresponds to 1% of melting (F=0.01) and the critical mass porosity (ϕ) of the system is equal to 0.005. Values are normalized to C1 chondrite from Anders & Grevesse (1989).

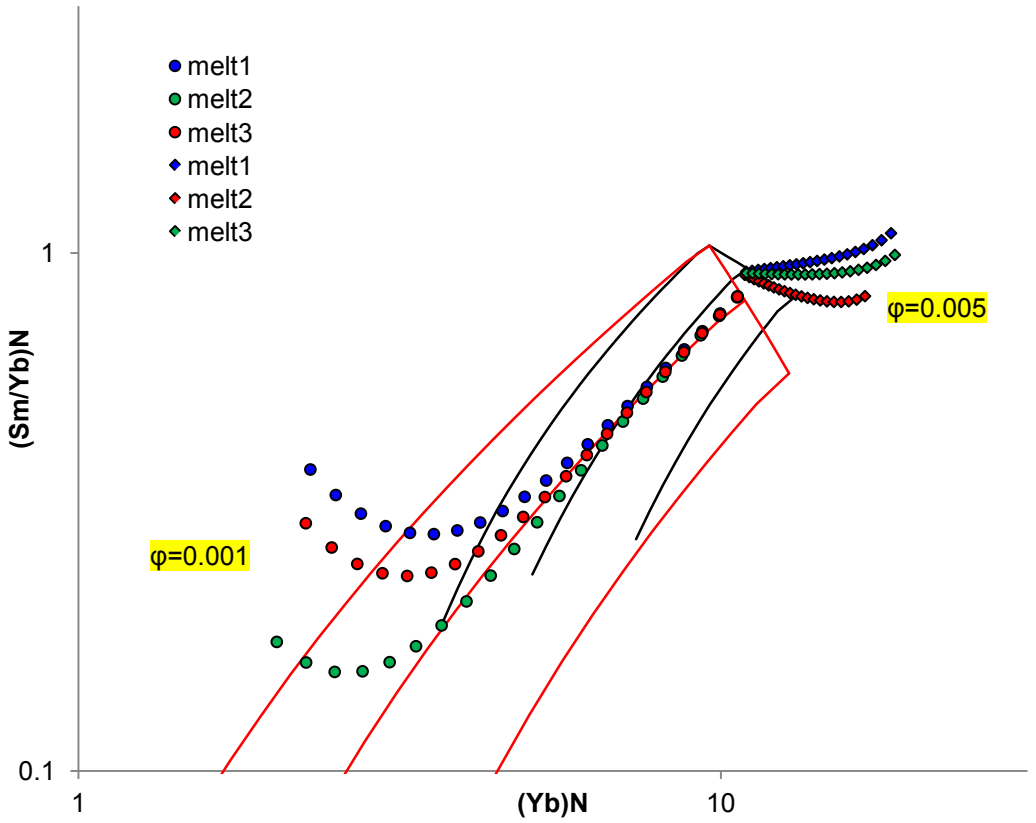

Fig. 5.2.2.3 - (Sm/Yb) vs Yb variation in clinopyroxene during continuous open-system melting in the spinel stability field of a DMM source which experienced 4% melting in the garnet stability field, varying the critical mass porosity of the system: ϕ =0.001 (circles) and ϕ =0.005 (diamonds). Refertilization is due to the inflow of variable spinel-lherzolite-derived melts: melt1 (blue symbols), melt2 (green symbols) and melt3 (red symbols) (for the melts composition, please refer to the previous figure). Melting proceeds until clinopyroxene exhaustion. Each melting step corresponds to 1% melting (F=0.01). Dynamic melting curves of a DMM source, varying the critical mass porosity of the system (red line: ϕ =0.001; black line: ϕ =0.001), are also reported for comparison. Values are normalized to C1 chondrite of Anders & Grevesse (1989).

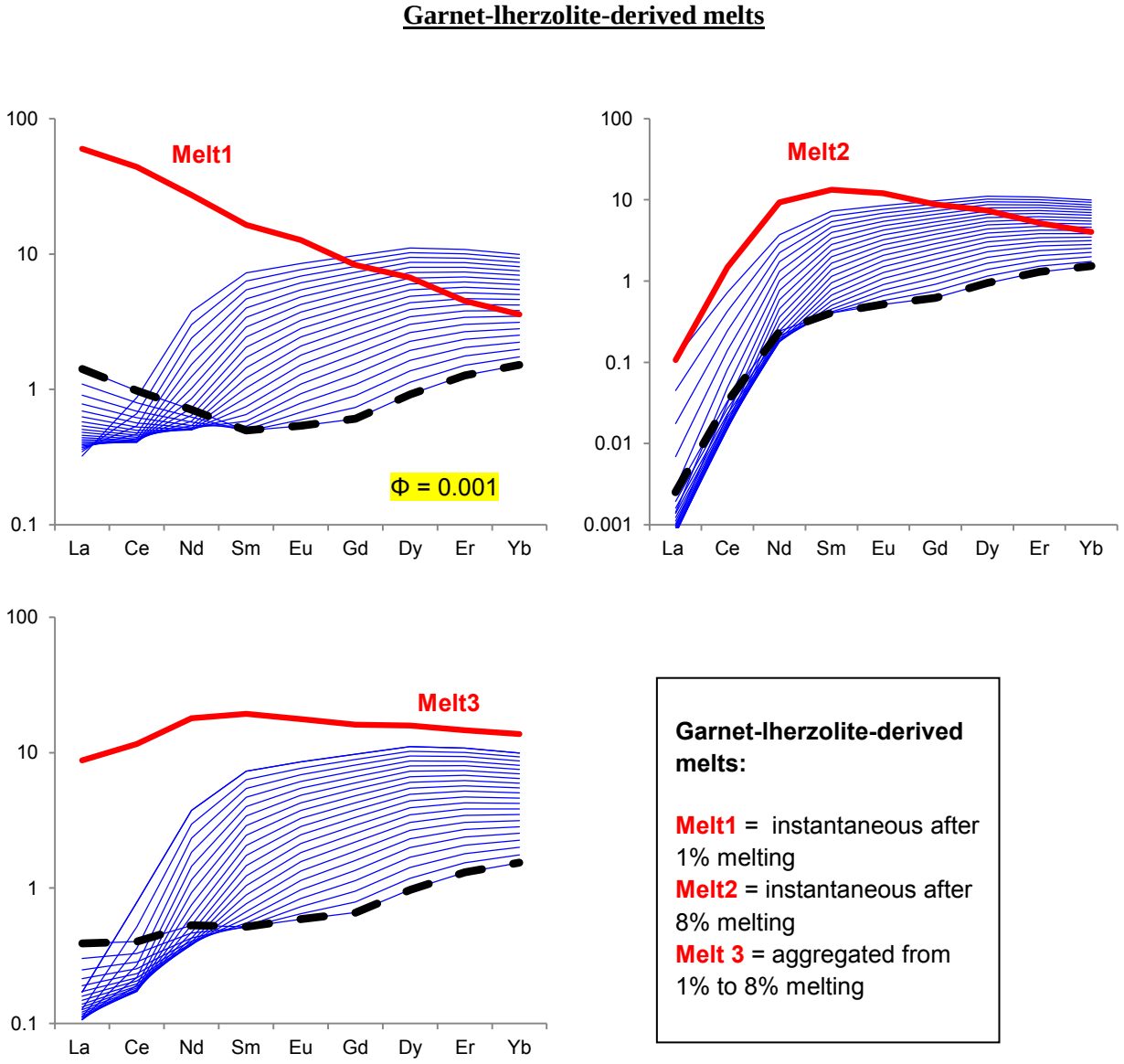

Fig. 5.2.2.4 - REE compositions in clinopyroxene during open-system melting in the spinel stability field of a DMM source which experienced 4% melting in the garnet stability field. Melting proceeds until the clinopyroxene exhaustion (black dashed line). The red bold line represents the exotic melt composition (see the small box for details). Each melting step corresponds to 1% of melting (F=0.01) and the critical mass porosity (ϕ) of the system is equal to 0.001. Values are normalized to C1 chondrite from Anders & Grevesse (1989).

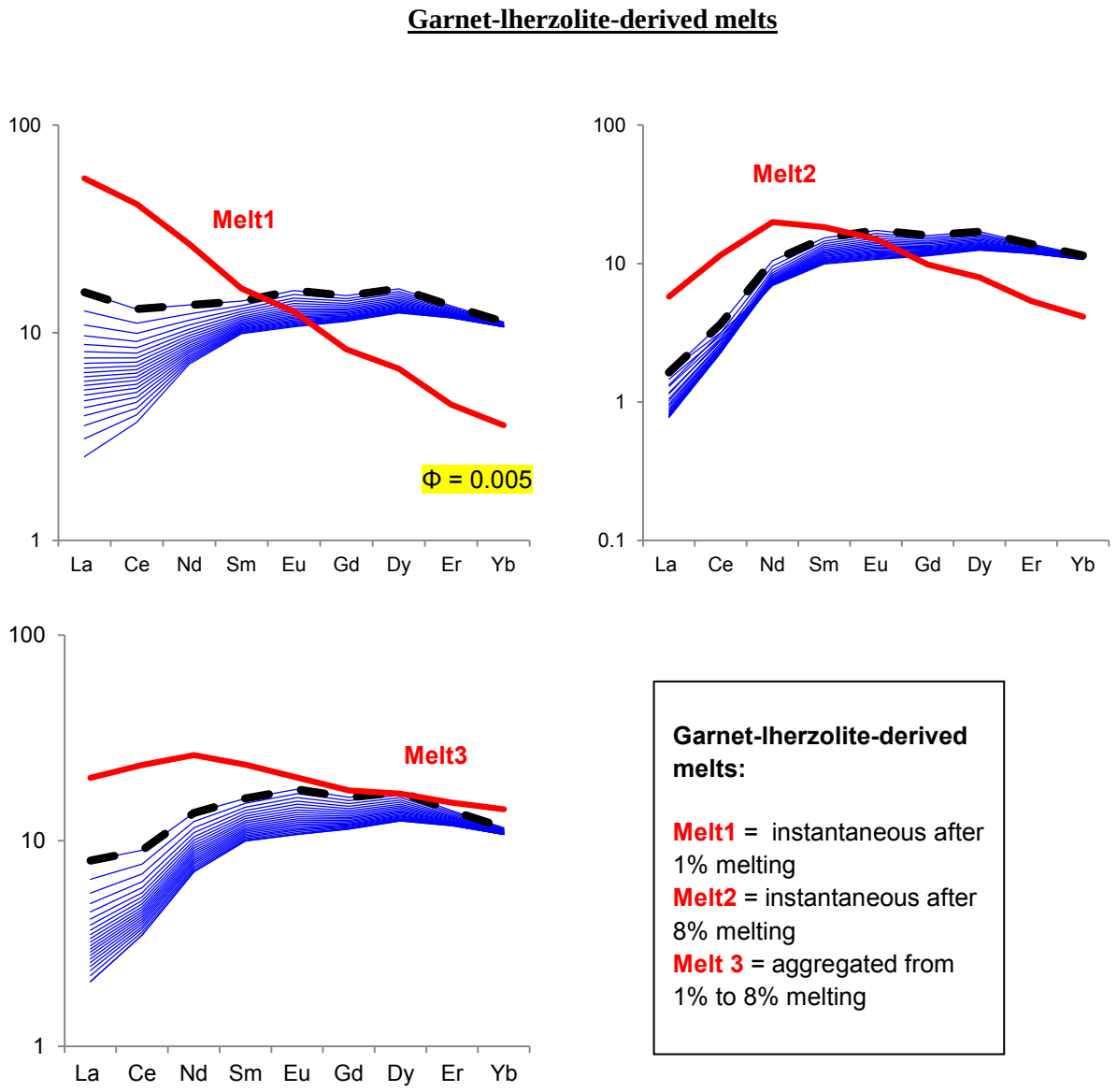

Fig. 5.2.2.5 - REE compositions in clinopyroxene during open-system melting in the spinel stability field of a DMM source which experienced 4% melting in the garnet stability field. Melting proceeds until the clinopyroxene exhaustion (black dashed line). The red bold line represents the exotic melt composition (see the small box for details). Each melting step corresponds to 1% of melting (F=0.01) and the critical mass porosity (ϕ) of the system is equal to 0.005. Values are normalized to C1 chondrite from Anders & Grevesse (1989).

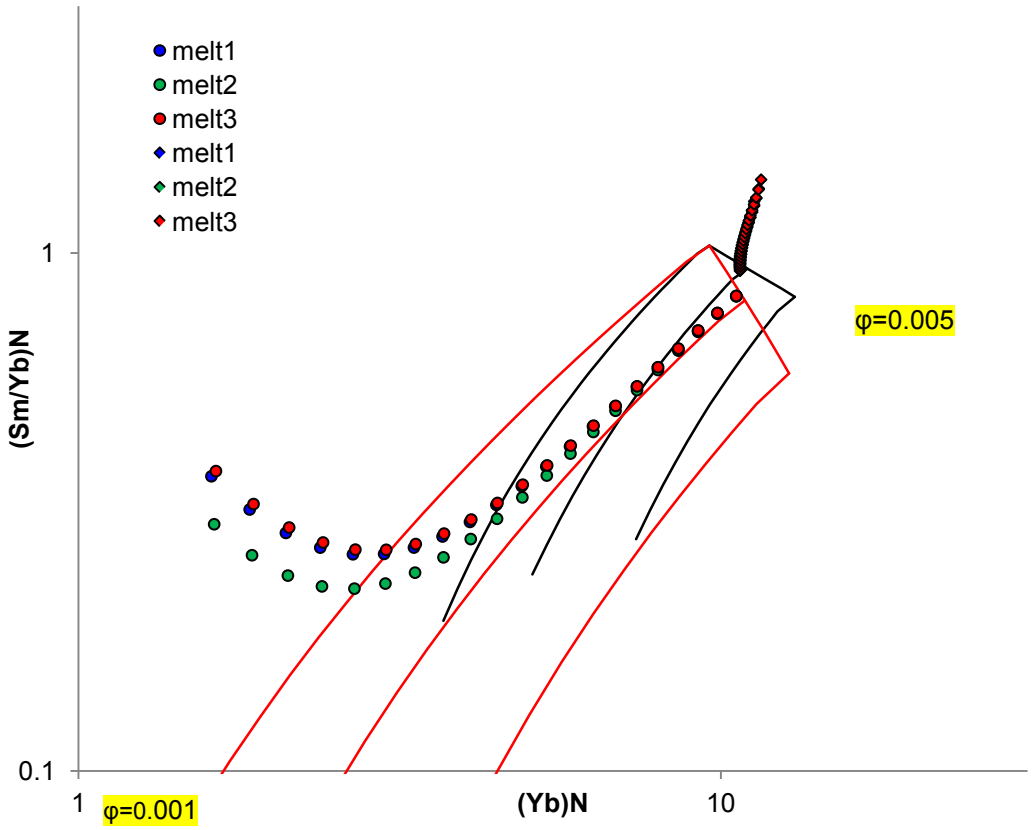

Fig. 5.2.2.6 - (Sm/Yb) vs Yb variation in clinopyroxene during continuous open-system melting in the spinel stability field of a DMM source which experienced 4% melting in the garnet stability field, varying the critical mass porosity of the system: ϕ =0.001 (circles) and ϕ =0.005 (diamonds). Refertilization is due to the inflow of variable garnet-lherzolite-derived melts: melt1 (blue symbols), melt2 (green symbols) and melt3 (red symbols) (for the melts composition, please refer to the previous figure). Melting proceeds until clinopyroxene exhaustion. Each melting step corresponds to 1% melting (F=0.01). Dynamic melting curves of a DMM source, varying the critical mass porosity of the system (black line: ϕ =0.001; red line: ϕ =0.005), are also reported for comparison. Values are normalized to C1 chondrite of Anders & Grevesse (1989).

5.2.3 Reactive impregnation

When the melting process ceases, inflow of exotic melts is assumed to continue as the mantle parcel continues its ascending path.

In this stage of reactive impregnation new phases crystallize in the source from the impregnating melts. Thus, after the addition of melt with concentration *C1*, trace elements are redistributed assuming that newly formed minerals that crystallized from the melt attain equilibrium with the pre-existing phases of the peridotite. The new mode *M* of phase *j* can be expressed as a function of the amount of impregnating melt (*X*) (Hellebrand et al. 2002):

$$M_j=M_0(1-X)+XZ_j$$

where Z_j is the crystallization mode of phase *j*, i.e. the proportions of new minerals that crystallize from the melt.

For the models here presented we considered that the studied rocks were affected by two distinct reactive impregnation processes: one due to the first impregnating melt which causes the crystallization of 0.3ol+0.7cpx (based on Elthon, 1992) and the other due to the second impregnating melt which causes the crystallization of 0.2cpx+0.8plag (based on petrographic observations of the studied samples). According to previous works (Seyler et al. 2001, Dijkstra et al., 2001) the crystallization of (cpx+ol) is assumed to occur before the crystallization of (plag+cpx).

After reactive impregnation, the new bulk distribution coefficient *D* was progressively recalculated according to the new modal composition.

In the computations we assumed that reactive impregnation is a continuous process and that each step corresponds to an amount of inflowing exotic melt (*X*) equal to 0.5%.

Melts used in the following models are i) an aggregated spinel-lherzolite-derived melt from 1% to 8% melting (melt1), ii) an aggregated garnet-lherzolite-derived melt from 1% to 8% melting (melt2) and iii) a depleted spinel-lherzolite derived melt (melt3); the composition of the melt used are listed in table 5.2.3.1.

Table 5.2.3.1 - Compositions (ppm) of the melts used in modeling of reactive impregnation.

φ=0.001	Ti	Zr	La	Ce	Nd	Sm	Eu	Gd	Dy	Er	Yb
melt1	3393	8.13	1.0E-04	0.03	0.73	0.85	0.45	1.95	2.88	2.04	2.12
melt2	6167	63.80	3.86	10.90	9.22	2.51	0.79	1.92	1.95	0.87	0.71
melt3	2815	3.73	6.6E-06	0.01	0.32	0.53	0.31	1.46	2.26	1.66	1.76
φ=0.005	**Ti**	**Zr**	**La**	**Ce**	**Nd**	**Sm**	**Eu**	**Gd**	**Dy**	**Er**	**Yb**
melt1	5585	42.00	0.18	1.64	4.35	2.31	0.95	3.58	4.82	3.16	3.14
melt2	6868	74.97	6.63	17.29	12.14	2.89	0.88	2.03	2.02	0.89	0.71
melt3	5188	29.89	0.07	0.87	3.11	1.91	0.83	3.22	4.43	2.93	2.92

In the following figures modeling for REE ratios and variations in clinopyroxene during reactive impregnation are reported. Results show that REEs compositional variations during reactive impregnation is strongly dependent on the exotic melt composition. The most incompatible elements are the most susceptible at the point that they will decrease if the impregnating melt is strongly depleted with respect to the clinopyroxene starting composition (fig. 5.2.3.1 E-F and fig. 5.23.3 E-F). MREE and HREE will increase anyhow, but at variable extent, depending not only on the melt composition but also on the modal clinopyroxene. Fractional crystallization of (cpx+ol) rather than (plag+cpx), in fact, implies a faster increase of the modal clinopyroxene and, at a same bulk C_0, this influences the REEs redistribution. Moreover, HREE are incompatible in plagioclase, thus not incorporated during the crystallization of plagioclase forcing the increase of Yb in clinopyroxene (figs. 5.2.3.2 and 5.2.3.4). On the contrary, La compatibility in plagioclase is similar to that of clinopyroxene, yielding a slower increase of La in clinopyroxene. Finally, MREE variation are rather susceptible to the modal plagioclase: crystallization of plagioclase, in fact, which has a strong compatibility for europium, induces the development of Eu negative anomaly in clinopyroxene, coupled with a faster increase of the other MREEs.

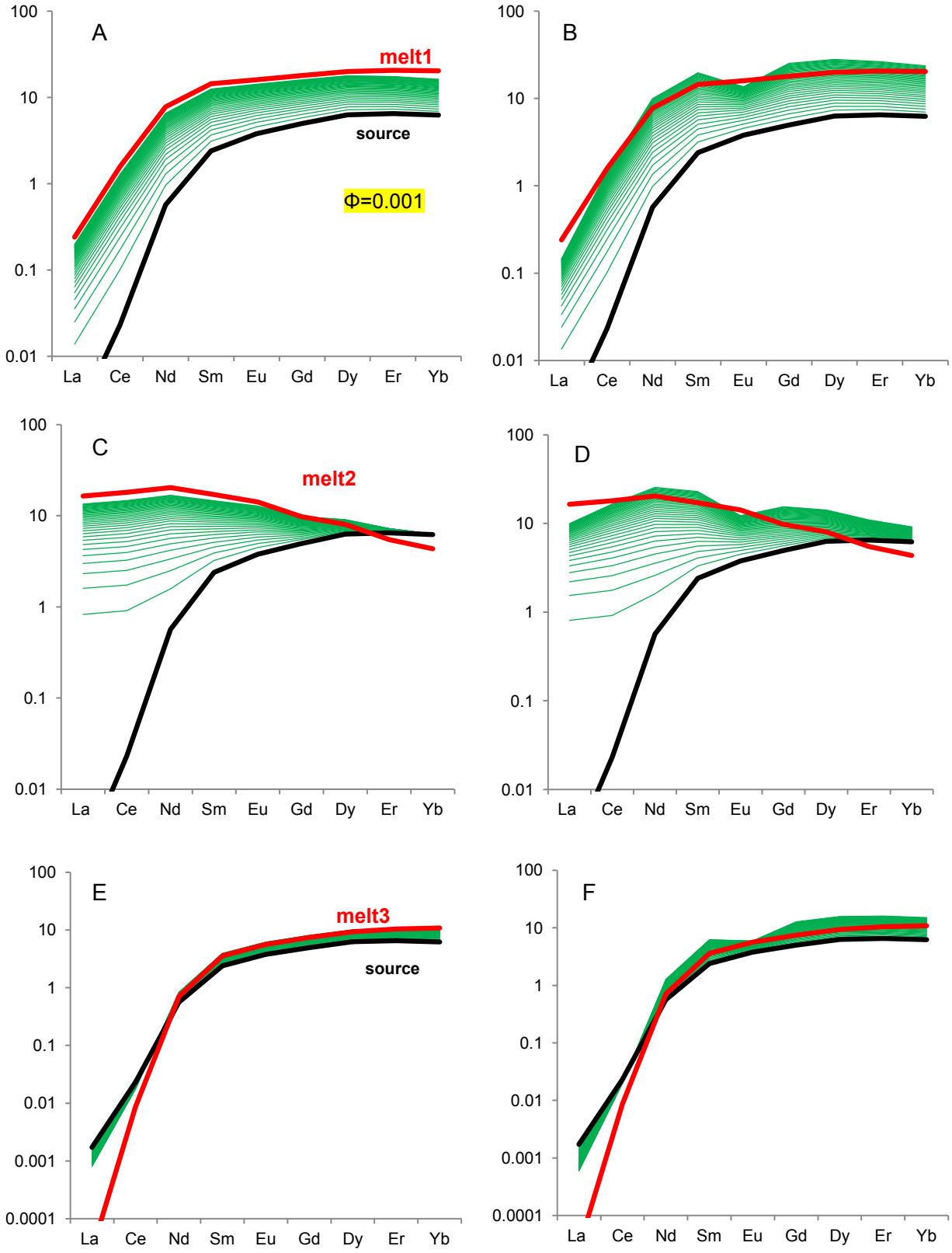
A
melt1
source
Φ=0.001
B
C
melt2
D
E
melt3
source
F
100
10
1
0.1
0.01
0.001
0.0001
La Ce Nd Sm Eu Gd Dy Er Yb

Fig. 5.2.3.1 - REE compositions in clinopyroxene during reactive impregnation of a DMM source which experienced 4% melting in the garnet stability field and 8% open-system melting in the spinel stability field (black bold line), due to inflow of variable melts (red bold line). Reactive impregnation causes fractional crystallization of (cpx+ol) (A-C-E) and (plag+cpx) (B-D-F) (see text for details). Each melting step corresponds to 1% melting (F=0.01) and the critical mass porosity is 0.001. Values are normalized to C1 chondrite of Anders & Grevesse (1989).

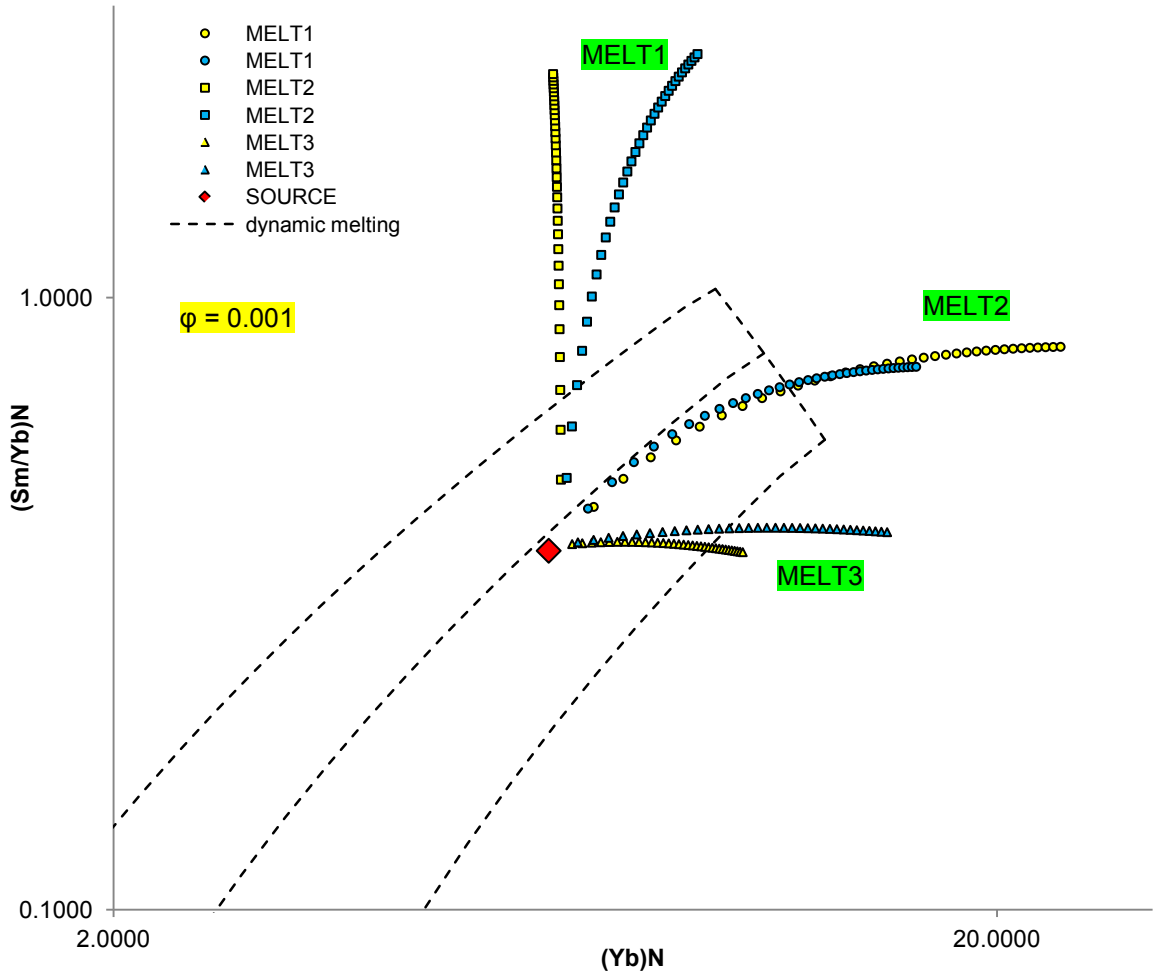

Fig. 5.2.3.2 - (Sm/Yb) vs Yb variation in clinopyroxene during reactive impregnation of a DMM source which experienced 4% melting in the garnet stability field and 8% open-system melting in the spinel stability field (red diamond); reactive impregnation is due to continuous inflow of variable exotic melts (for the melts compositions see previous figures), and causes fractional crystallization of (cpx+ol) (yellow symbols) and (plag+cpx) (light blue symbols). The critical mass porosity of the system is ϕ=0.001. Dynamic melting curves of a DMM source in garnet and spinel stability fields (black dashed line) are also reported for comparison. Values are normalized to C1 chondrite of Anders & Grevesse (1989).

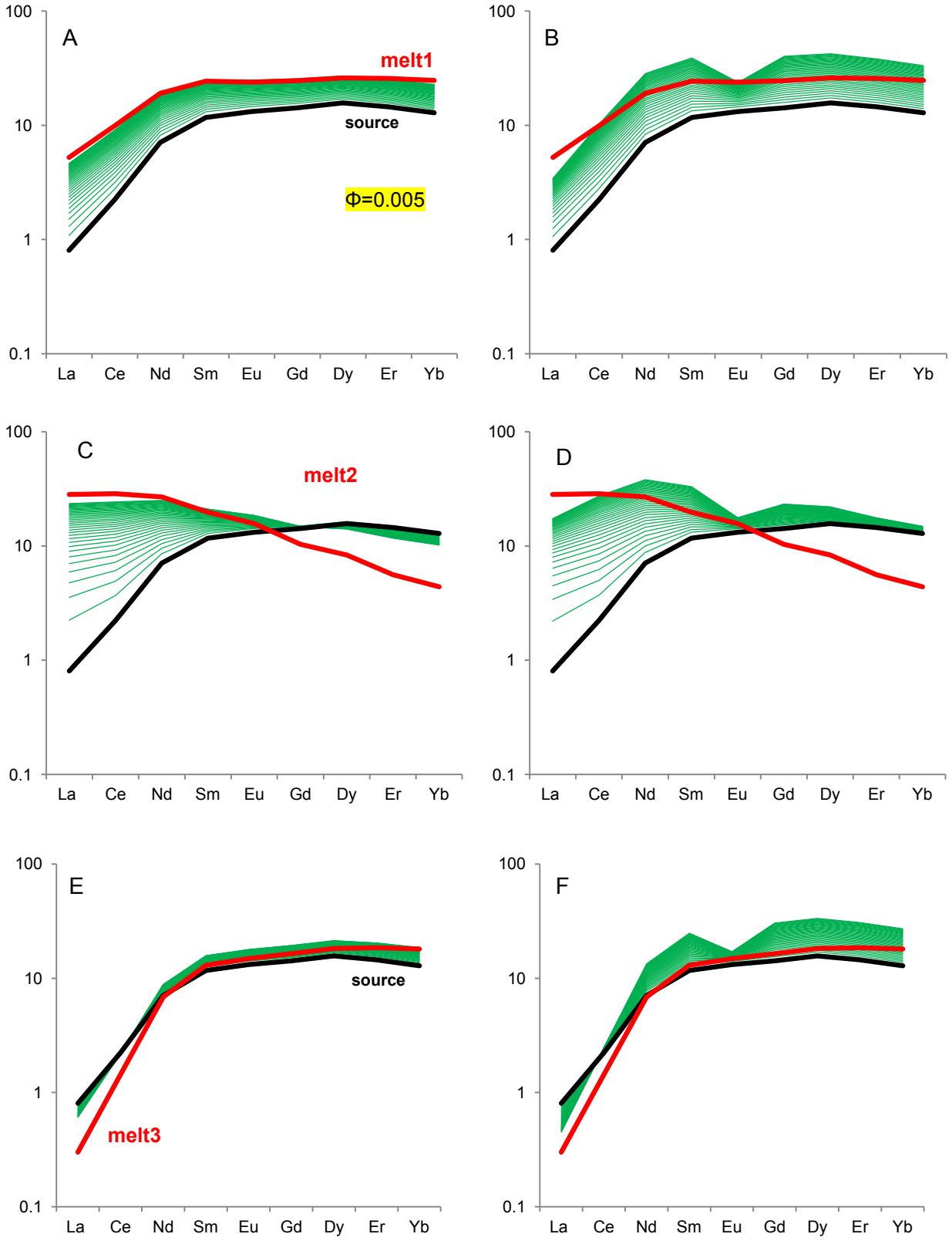
A
melt1
source
Φ=0.005
B
C
melt2
D
E
source
melt3
F
100
10
1
0.1
La Ce Nd Sm Eu Gd Dy Er Yb

Fig. 5.2.3.3 - REE compositions in clinopyroxene during reactive impregnation of a DMM source which experienced 4% melting in the garnet stability field and 8% open-system melting in the spinel stability field (black bold line), due to inflow of variable melts. Reactive impregnation causes fractional crystallization of (cpx+ol) (A-C-E) and (plag+cpx) (B-D-F) (see text for details). Red bold line represents the composition of the inflowing melt during reactive impregnation, corresponding to an aggregated melt derived from 1% to 8% melting of a garnet-lherzolite. Values are normalized to C1 chondrite of Anders & Grevesse (1989).

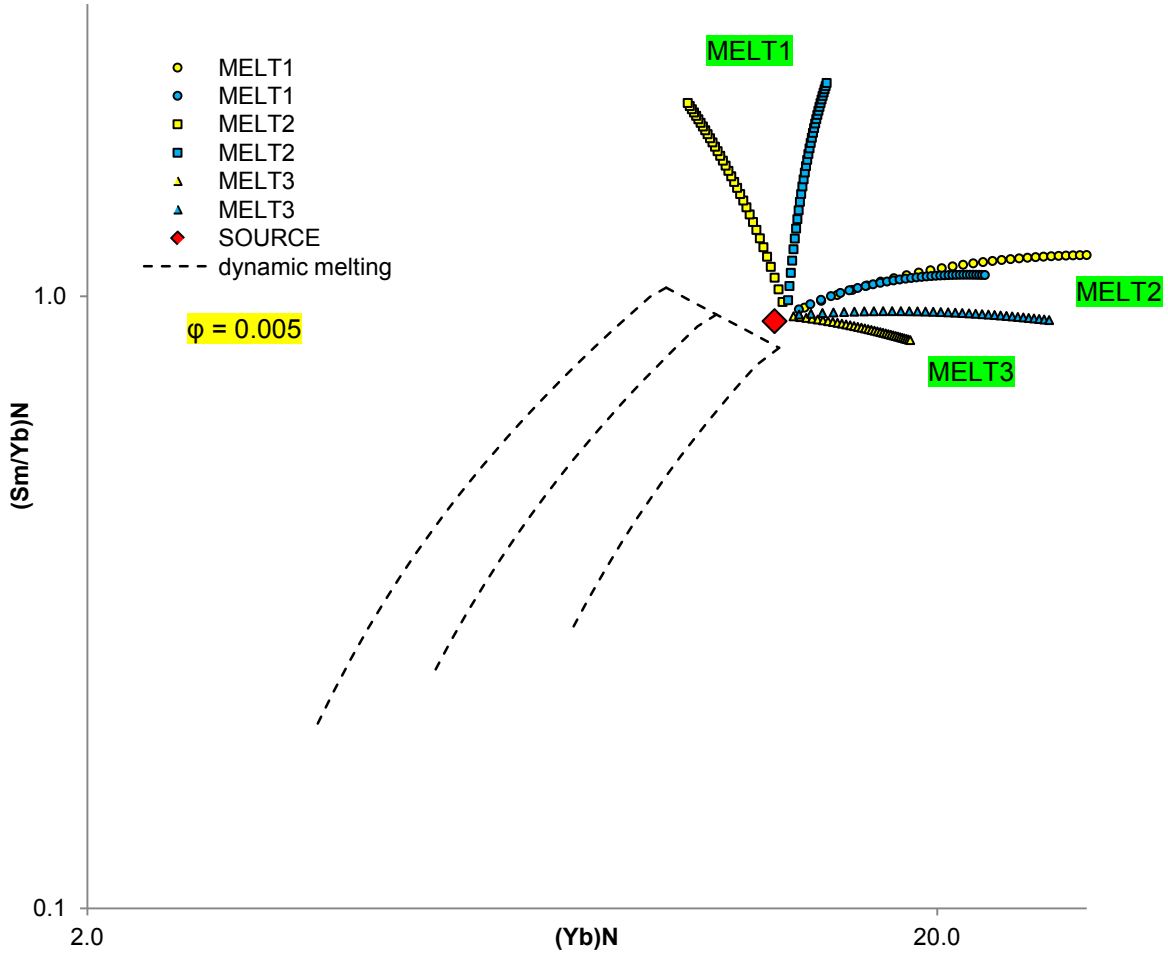

Fig. 5.2.3.4 - (Sm/Yb) vs Yb variation in clinopyroxene during reactive impregnation of a DMM source which experienced 4% melting in the garnet stability field and 8% open-system melting in the spinel stability field (red diamond); reactive impregnation is due to continuous inflow of variable exotic melts (for the melts compositions see previous figures), and causes fractional crystallization of (cpx+ol) (yellow symbols) and (plag+cpx) (light blue symbols). The critical mass porosity of the system is ϕ=0.005. Dynamic melting curves of a DMM source in garnet and spinel stability fields (black dashed line) are also reported for comparison. Values are normalized to C1 chondrite of Anders & Grevesse (1989).

5.3 Ti-Zr variation during melting and post-melting processes

Ti and Zr contents in clinopyroxene represent a useful tool to model both mechanisms and degree of partial melting of the source (Johnson et al., 1990; Brunelli et al., 2006), which are two important parameters for constraining the melting process.

The same model geometry described in the previous chapters is here applied to the Ti-Zr systematics. Results are displayed in the following figures for different mechanisms of melting.

In fig. 5.3.2 we can observe that, regardless of the inflowing melt composition, in an open-system melting process small critical mass porosity (e.g. ϕ=0.001) lowers the slope of the melting curve, inducing weak deviations up to 10% melting, followed by an abrupt deviation until a nearly vertical trend approaching the clinopyroxene exhaustion. When critical mass porosity is large (e.g. ϕ=0.005), the open-system melting trend is strongly modified, due to a fast increase of Ti coupled with a weaker increase, or decrease, depending on the melt composition, of Zr. In both cases (small cmp and large cmp), Zr varies with the composition of the inflowing melt, whereas Ti content variation is nearly negligible. It can be stressed that the smaller the critical mass porosity the higher the Zr variation. Irrespective to the chosen parameters dynamic melting and open-system melting fail to describe the observed Ti-Zr compositions of the studied samples. For the studied samples, therefore, Ti-Zr variation cannot be considered as an indicator of the degree of melting undergone by the rock; however, the measured Ti-Zr composition of the studied samples might derive from post-melting, continuous reactive impregnation, during which Ti-Zr increasing trends are expected because the continuous supply of exotic melt is not balanced by melting. In the following figures modeling of Ti-Zr variation during reactive impregnation is reported. Ti and Zr in the source increase at the proceeding of reacting impregnation. At a same degree of melting, the extent of Zr increase is dependent on the impregnating melt composition, whereas the effect on Ti increase is nearly negligible (fig. 5.3.2 and 5.3.3); on equal composition of the impregnating melt, instead, Ti-Zr increase is influenced by the degree of melting undergone by the rock source. This effect is minor for low extents of reactive impregnation.

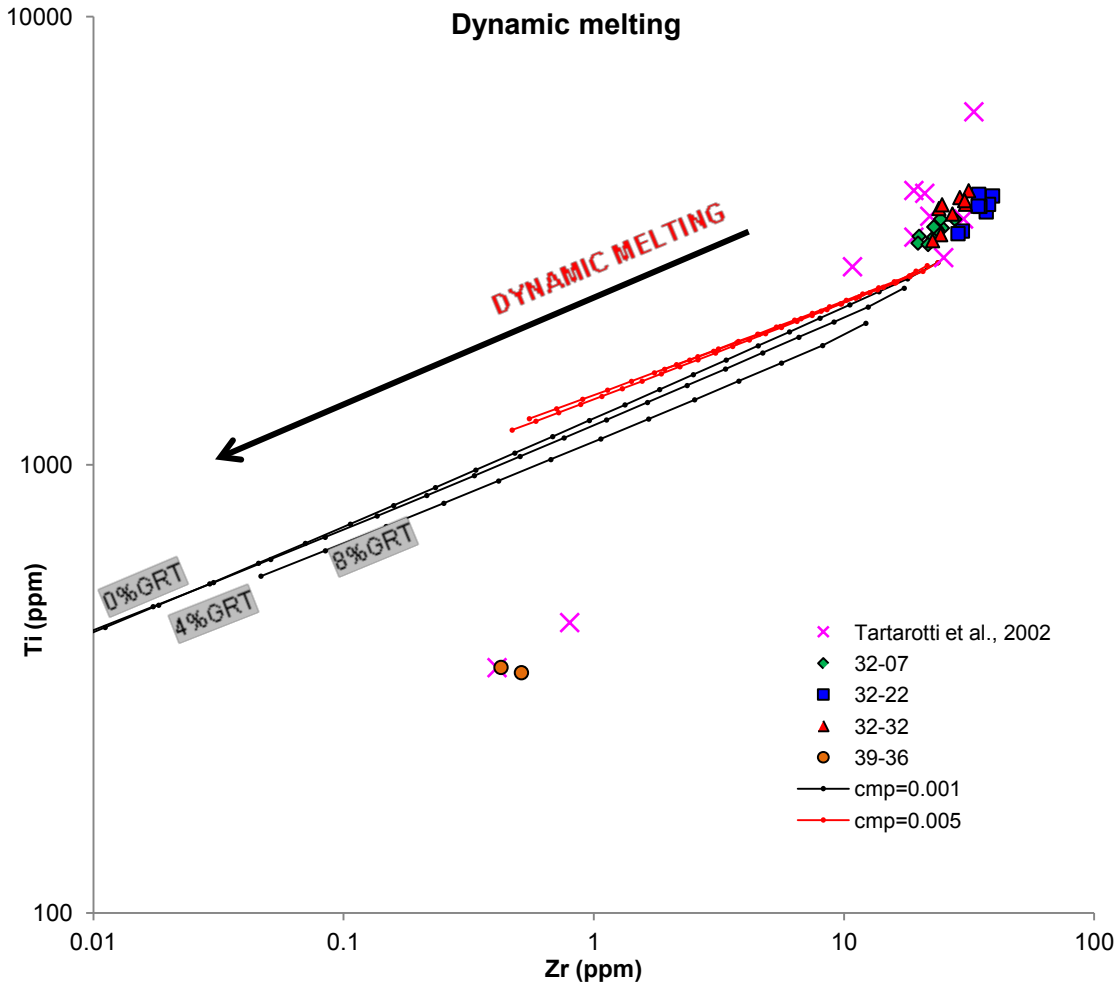

Fig. 5.3.1 - Ti-Zr composition in clinopyroxene during dynamic melting in the spinel stability field of a DMM source after 0%, 4% and 8% melting in the garnet stability field, varying the critical mass porosity (ϕ=0.001: black line and ϕ=0.005: red line)

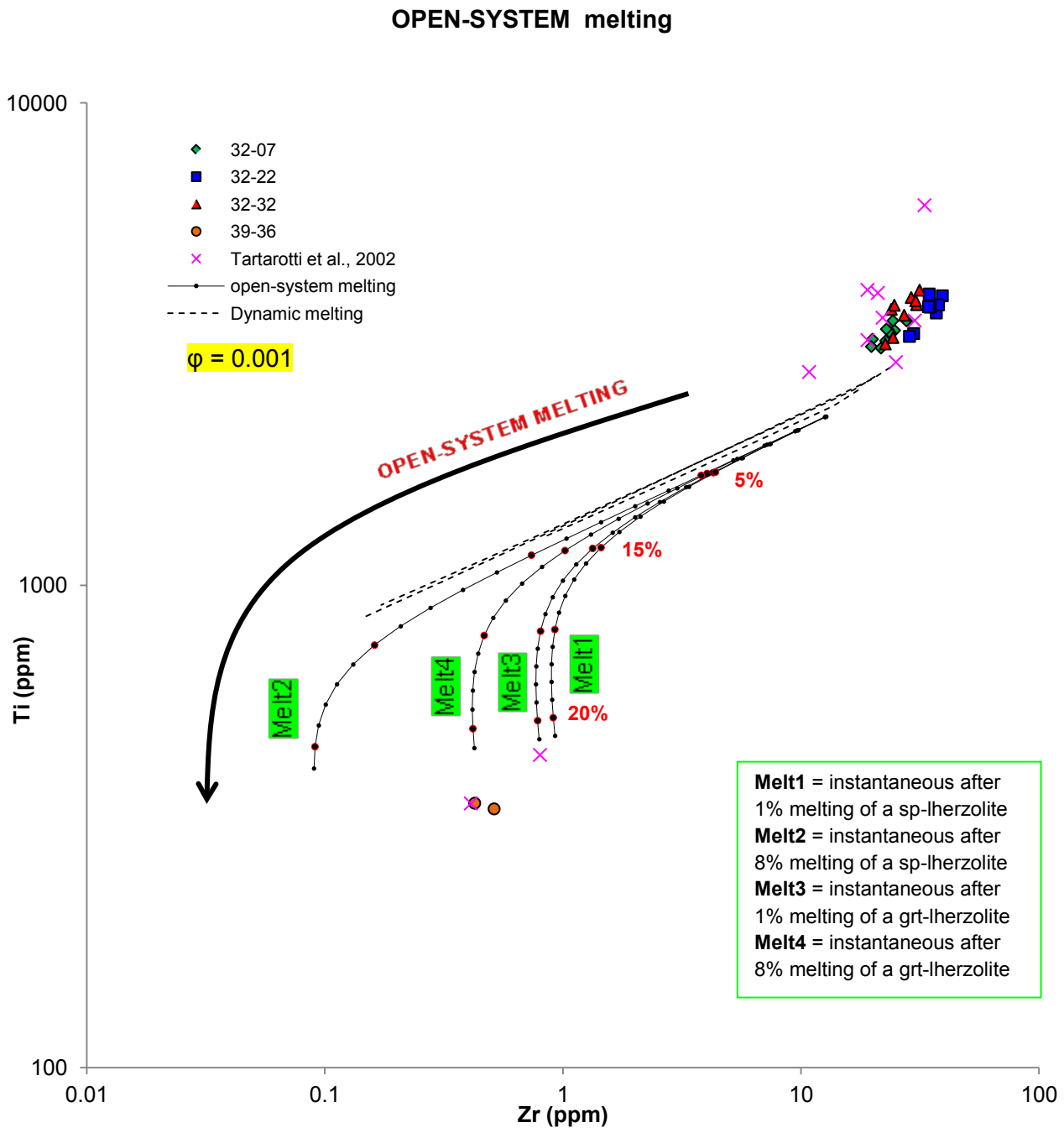

Fig. 5.3.2 - Ti (ppm) vs. Zr (ppm) composition in clinopyroxene during continuous open-system melting of a DMM source which experienced 4% melting in the garnet stability field, due to the inflow of variable exotic melts (for melt composition see the small inset); critical mass porosity of the system is equal to 0.001 and each step melting corresponds to f=0.01. Dynamic melting curve is also reported for comparison.

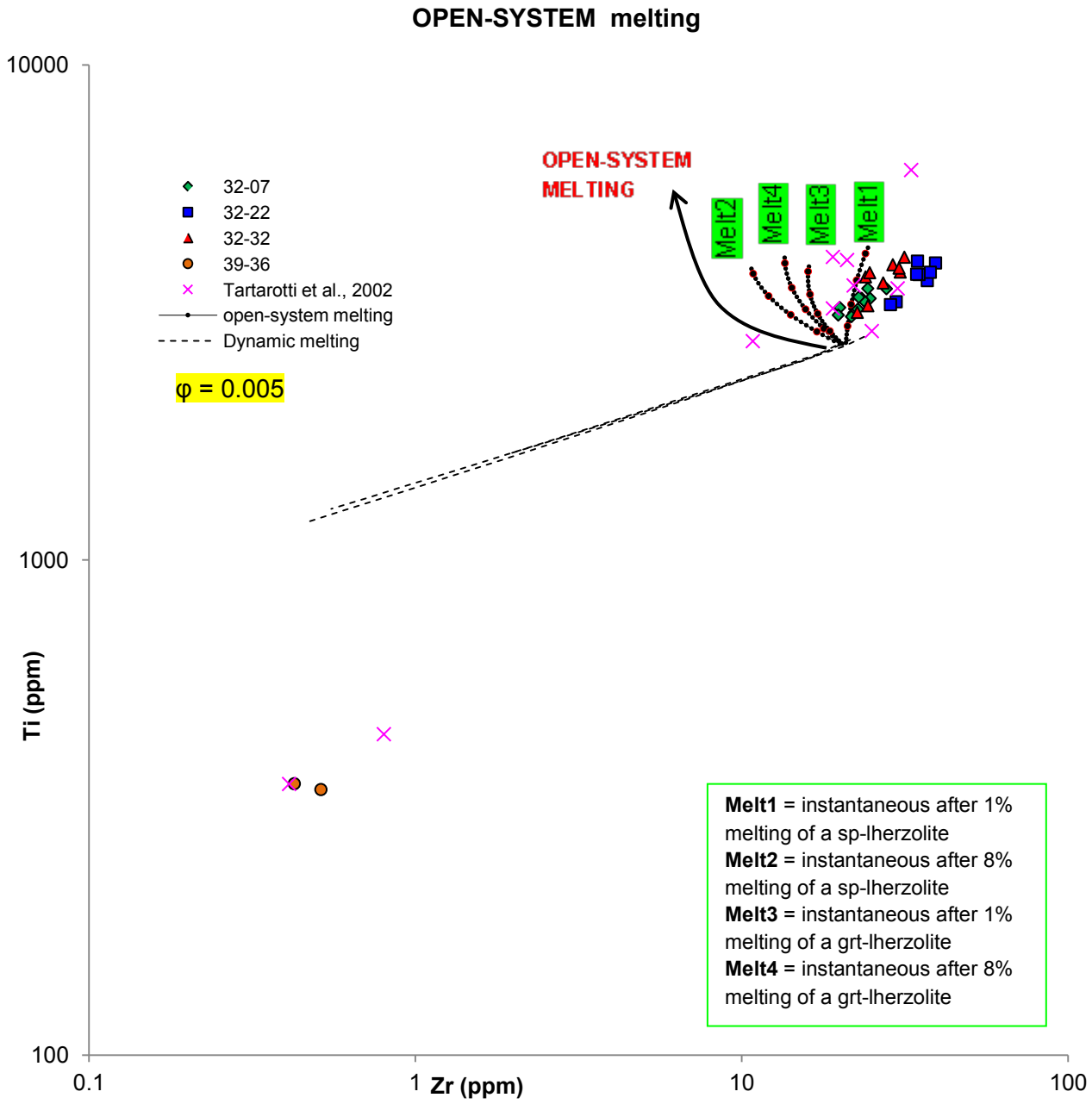

Fig. 5.3.3 - Ti (ppm) vs. Zr (ppm) composition in clinopyroxene during continuous open-system melting of a DMM source which experienced 4% melting in the garnet stability field, due to the inflow of variable exotic melts (for melt composition see the small inset); critical mass porosity of the system is equal to 0.005 and each step of melting corresponds to f=0.01. Dynamic melting curve is also reported for comparison.

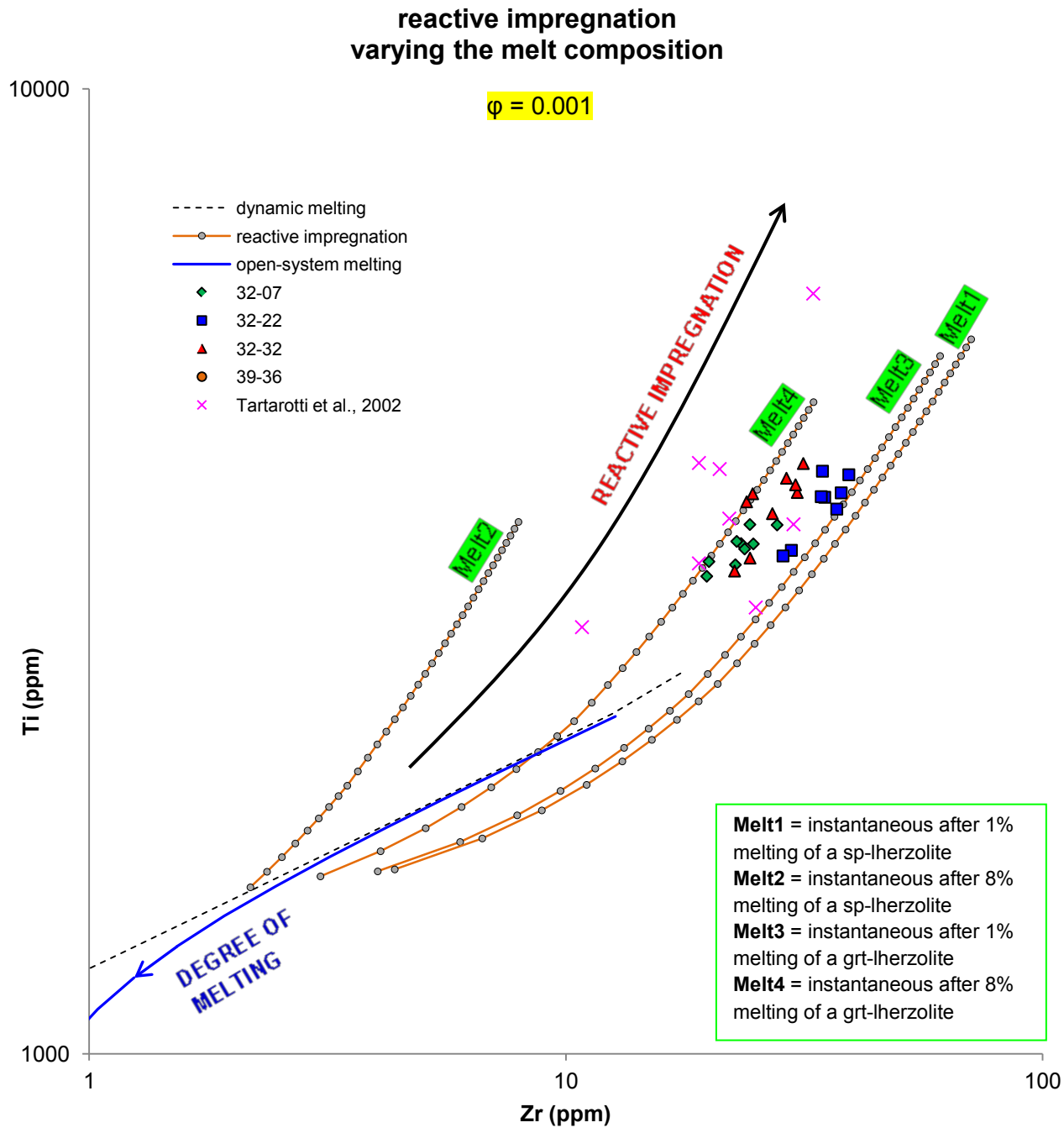

Fig. 5.3.4 - Ti (ppm) vs. Zr (ppm) composition in clinopyroxene during continuous reactive impregnation of a DMM source which experienced 4% melting in the garnet stability field and 8% open-system melting in the spinel stability field; reactive impregnation is due to the inflow of variable exotic melts (for melt composition see the inset) and causes the crystallization of (cpx+ol) and then (plag+cpx). Reactive impregnation proceeds until a total amount of modal plagioclase equal to 10%. Critical mass porosity of the system is ϕ=0.001 and each step of melting corresponds to 1% (f=0.01). Dynamic melting curve is also reported for comparison.

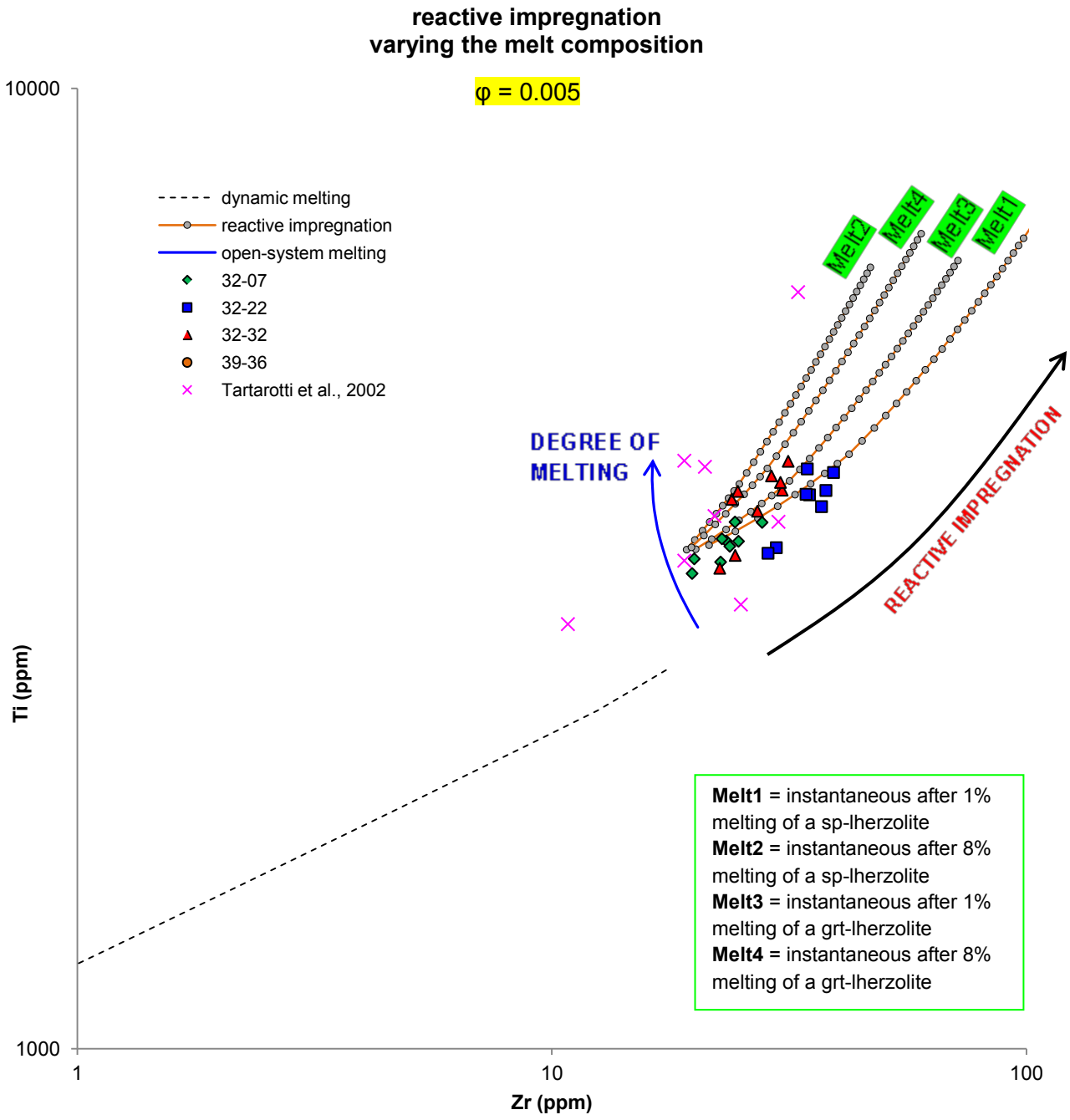

Fig. 5.3.5 - Ti (ppm) vs. Zr (ppm) composition in clinopyroxene during continuous reactive impregnation of a DMM source which experienced 4% melting in the garnet stability field and 8% open-system melting in the spinel stability field; reactive impregnation is due to the inflow of variable exotic melts (for melt composition see the inset) and causes the crystallization of (cpx+ol) and then (plag+cpx). Reactive impregnation proceeds until a total amount of modal plagioclase equal to 10%. Critical mass porosity of the system is ϕ=0.005 and each step of melting corresponds to 1% (f=0.01). Dynamic melting curve is also reported for comparison.

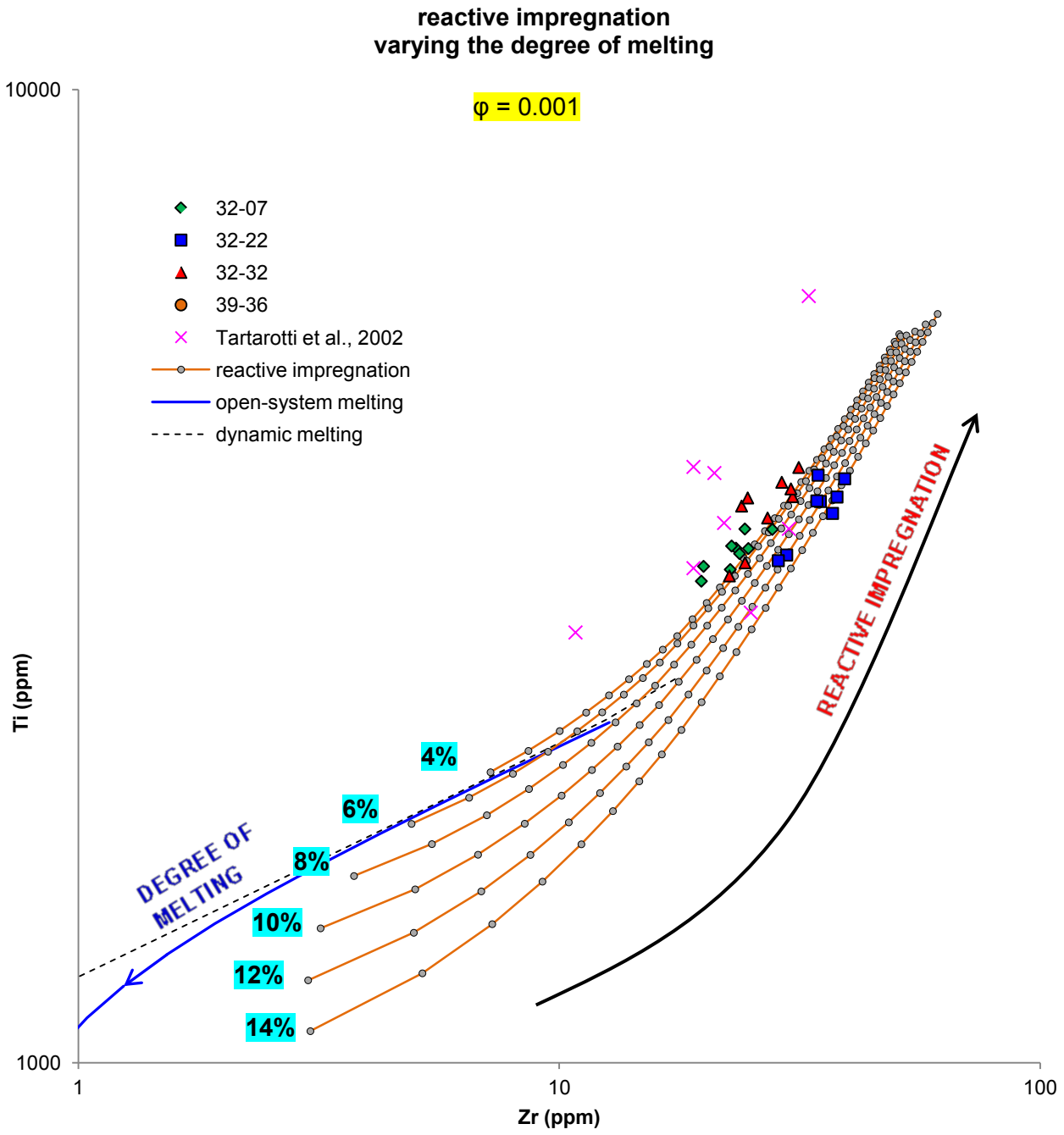

Fig. 5.3.6 -Ti (ppm) vs. Zr (ppm) composition in clinopyroxene during continuous reactive impregnation of a DMM source which experienced 4% melting in the garnet stability field and variable degrees of open-system melting in the spinel stability field; reactive impregnation is due to the inflow of a garnet-lherzolite derived aggregated melt from 1% to 8% of melting, and causes the crystallization of (cpx+ol) and then (plag+cpx). Reactive impregnation proceeds until a total amount of modal plagioclase equal to 10%. Critical mass porosity of the system is ϕ=0.001. Dynamic melting curve is also reported for comparison.

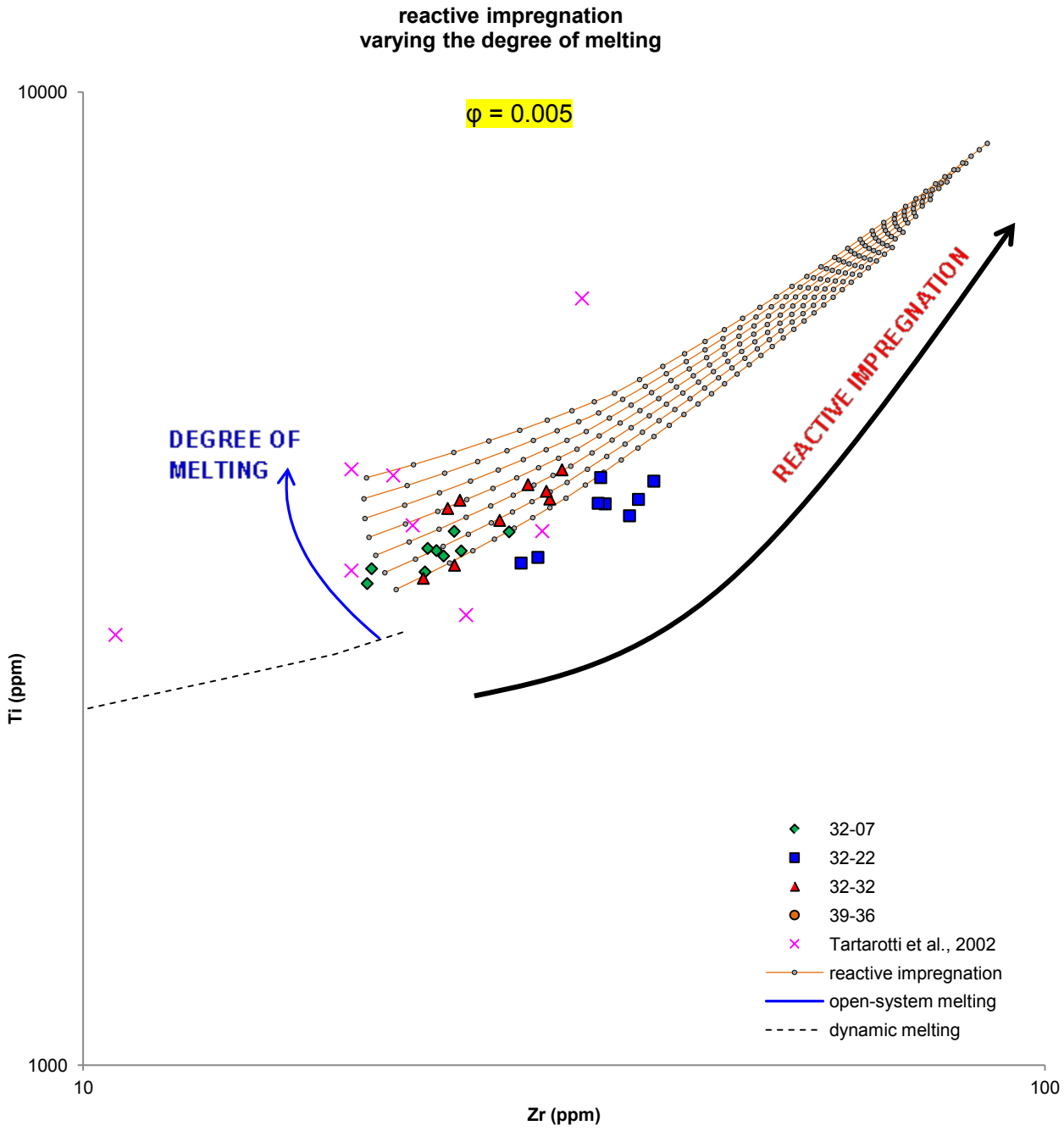

Fig. 5.3.7 - Ti (ppm) vs. Zr (ppm) composition in clinopyroxene during continuous reactive impregnation of a DMM source which experienced 4% melting in the garnet stability field and variable degrees of open-system melting in the spinel stability field; reactive impregnation is due to the inflow of a garnet-lherzolite derived aggregated melt from 1% to 8% of melting, and causes the crystallization of (cpx+ol) and then (plag+cpx). Reactive impregnation proceeds until a total amount of modal plagioclase equal to 10%. Critical mass porosity of the system is ϕ=0.005. Dynamic melting curve is also reported for comparison.

5.4 Modeling the studied samples

Reactive porous flow is able to change the behavior of trace elements during partial melting and upwelling towards the top of the mantle column under an oceanic ridge. First, the incoming exotic melt composition obviously plays a key role but, on the other hand, also the source composition is crucial. In fact, primary compositional heterogeneities are undoubtedly present in the MORB mantle source as shown by isotopic variability of MORBs and associated residual peridotites, even in ridge regions not influenced by hotspots (Salters & Dick, 2002; Cipriani et al. 2004; Graham et al., 2006; Hémond et al., 2006), thus the observed compositional variability of trace elements distribution are considered to be the product of both source-inherited and melting-induced heterogeneities.
In a general way decompressive mantle melting is always an open-system process in that the required porosity interconnection for melt extraction means open paths for melt to flow throughout the rock.
Many authors pointed out that highly incompatible elements are useful to assess late-stage processes, such as melt entrapment, melt-rock reactions and veining. Moderately incompatible trace elements are less affected by such late-stage processes and thus useful to infer the melting history of abyssal peridotites. It is noteworthy that in all samples measured rim Sm/Yb vs. Yb variations define a linear negative trend (fig 5.4.1.1) suggesting this as the trend more equilibrated and representative of the plagioclase impregnation stage. Accordingly REEs patterns and correlations measured in the clinopyroxene rims have been modeled using the melting systems described in the previous paragraphs in order to duplicate these observed trends.

In order to model the studied samples, the main governing parameters to be taken into account consist of: i) the critical mass porosity; ii) the total degree of melting; iii) the refertilizing melt composition and iv) the impregnating melts composition.

Modeling of the studied samples has been carried out according to the following:
- the lack of evidences for efficient melt extraction in correspondence to the Romanche FZ, i.e. the widespread scarcity of basaltic crust (Bonatti et al., 2001), may suggest low degrees of partial melting (Seyler & Bonatti, 1997; Bonatti et al., 2001; Tartarotti et al., 2002), or large critical mass porosity, or a combination of the two.

- Based on petrographic observations, sample 32-22 appears to be the only sample containing a large amount of coarse-grained clinopyroxene, i.e. residual clinopyroxene which underwent low dissolution and grain-size reduction during melting, which may suggest that sample 32-22 experienced lower degrees of melting with respect to the other samples. All samples of the dredge #32, moreover, contain small grains of interstitial clinopyroxene. Modal cpx is the highest in sample 32-32; however, this sample does not contain coarse-grained clinopyroxene. Modal clinopyroxene, therefore, cannot be considered dependent on the degree of melting alone.

- Modal plagioclase in samples of the dredge #32 is up to 15%; assuming that each step of reactive impregnation corresponds to an amount of inflowing melt equal to 0.5%, and that (plag+cpx) crystallize from the melt in the proportion 0.8:0.2, it results that reactive impregnation is a gradual and continuous process.

- La in samples of dredge #32 ranges from 0.7 x C1 to 1.5 x C1. La, and secondly Ce, is the most susceptible to the effect of the inflowing melt composition, thus La and Ce concentration in the studied samples is an important parameter in order to constrain the melts composition.

5.4.1 Modeling of Group1 samples

According to trace elements compositions, overall Group1 (samples 32-07, 32-22, 32-22TA and 32-32) is characterized by near-flat MREE to HREE patterns (Sm_N/Yb_N=1.19 and Dy_N/Yb_N=1.29), with relative moderate depletion in LREE (Ce_N/Yb_N=0.21) (see chapt. IV). In detail, sample 32-22 shows higher HREE compositions and accordingly lower Sm/Yb ratios with respect to samples 32-32 and 32-07 (Sm/Yb from 0.91 to 1.12 in sample 32-22, whereas Sm/Yb>1 always in samples 32-07 and 32-32), as shown in the Sm/Yb vs Yb plot in fig. (5.2), resulting in a slight bent in correspondence of the lighter HREE (fig. 5.4.1.1).

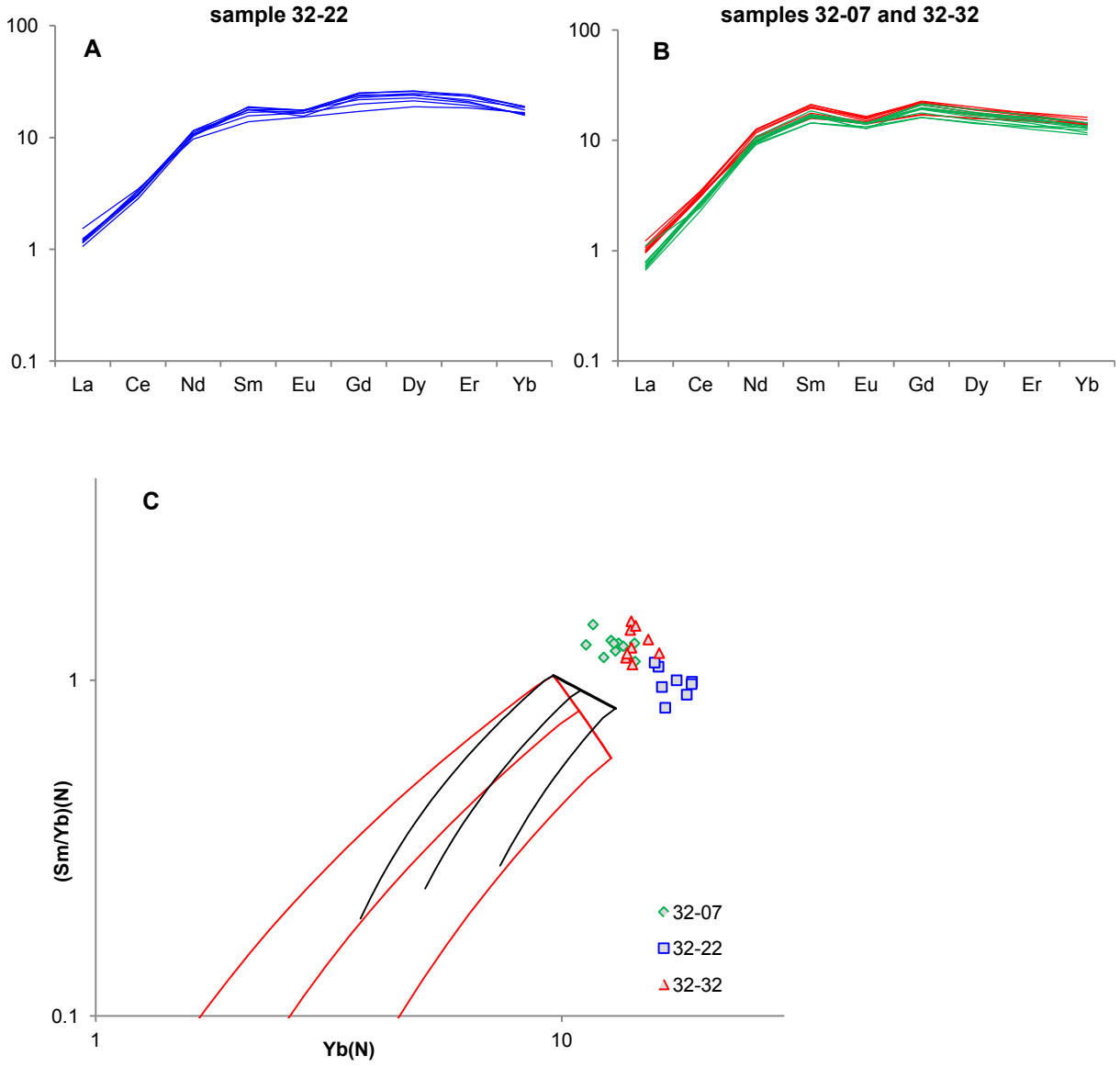

Fig. 5.4.1.1 - REE patterns in clinopyroxene in samples of group1 (A-B) and relative Sm/Yb vsYb variations (C). In C dynamic melting curves at variable critical mass porosity (ϕ=0.001: red line; ϕ=0.005: black line) are also reported for comparison. Values are normalized to C1 chondrite from Anders & Grevesse (1989).

Samples 32-07 and 32-32

According to the modeling proceedings described above, REE patterns of samples 32-07 and 32-32 can be reproduced by 4% melting in the garnet stability field; afterwards, melting proceeds in the spinel stability field as an open-system melting up to 10% for sample 32-07 and up to 8% for sample 32-32. In both cases, the refertilizing melts ("REF MELT" in fig. 5.4.1.1), which percolate the source during melting, were obtained by mixing spinel-lherzolite and garnet-lherzolite derived melts. The critical mass porosity during the entire process is ϕ=0.004, and the total amount of melting is 14% (sample 32-07) and 12% (sample 32-32).

During modeling of the measured values and trend the major difficulty is to contemporaneously match the rim trend and the observed shift with respect to the residual composition expected for “normal” melting in the sub-ridge mantle. In figure 5.4.1.1 it clearly appears that rim compositional trends run out of the field of the residual mantle rocks represented by the melting paths at different cmp. The over enrichment of the measured samples is coupled with a decreasing trend that requires Yb increasing at Sm/Yb decreasing values paralleling the melting trend in the garnet stability field. Being this trend coupled to the petrographic appearing of plagioclase a garnet effect is to be discharged.
The presence of a depleted melt during reactive impregnation is the only way to match the observed trend. At the same time this depleted melt cannot be used to model the shift toward higher compositional contents hence the necessity of accounting for a stage of percolation of an enriched melt that is able to displace the observed trend toward higher values. Matching the REE morphology is a further constraint to model the degree of melting and the percolating or refertilizing melt.
We have therefore decided to account for several stages of melt and melt percolation attributing all compositional shifts to a single stage irrespective of the meaning of each single stage.

In sample 32-07, 8% of the first impregnating melt ("IMPR MELT1" in fig. 5.4.1.1 A) is added, followed by an addition of the second, more depleted, impregnating melt ("IMPR MELT2" in fig. 5.4.1.1 A) equal to 15.5%, hence the total amount of added melt is equal to 23.5%. Impregnating melts were obtained by mixing partial melts derived from moderate to high degrees of melting of a garnet-lherzolite and a refertilized spinel-peridotite. Reactive impregnation leads to fractional crystallization of (cpx+ol) and subsequently (plag+cpx) up to a total amount of plagioclase equal to 9% and newly crystallized cpx equal to 3%. The results of modeling of REE compositions and ratios for sample 32-07 are reported in figs. 5.4.1.1 B, 5.4.1.2 and 5.4.1.3.

In sample 32-32, 12% of the first impregnating melt ("IMPR MELT1" in fig. 5.4.1.4 A) is added, followed by an addition of the second, more depleted, impregnating melt ("IMPR MELT2" in fig. 5.4.1.4 A) equal to 13%, hence the total amount of added melt is equal to 25%. Impregnating melts were obtained by mixing partial melts derived from moderate to high degrees of melting of a garnet-lherzolite and a refertilized spinel-

peridotite. Reactive impregnation leads to fractional crystallization of (cpx+ol) and subsequently (plag+cpx) up to a total amount of plagioclase equal to 12% and newly crystallized cpx equal to 7%. The results of modeling of REE compositions and ratios for sample 32-32 are reported in figs. 5.4.1.4 B, 5.4.1.5 and 5.4.1.6.

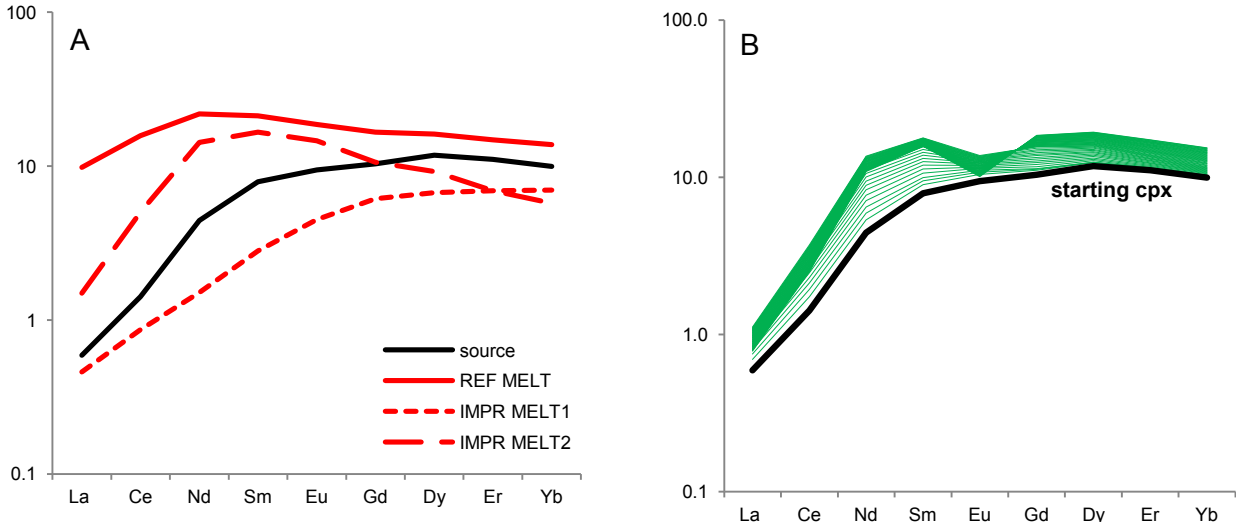

Fig. 5.4.1.1 - A) REE patterns of the melts used in modeling of sample 32-07; B) modeling for sample 32-07 (see text for details) which show REE variation in clinopyroxene during reactive impregnation from the starting composition at the end of melting; reactive impregnation proceeds until 16% of crystallized plagioclase and 3% of newly crystallized clinopyroxene, corresponding to a total amount of added melt equal to 23.5%. Impregnation steps corresponds to an addition of melt equal to 0.5% (X=0.005).

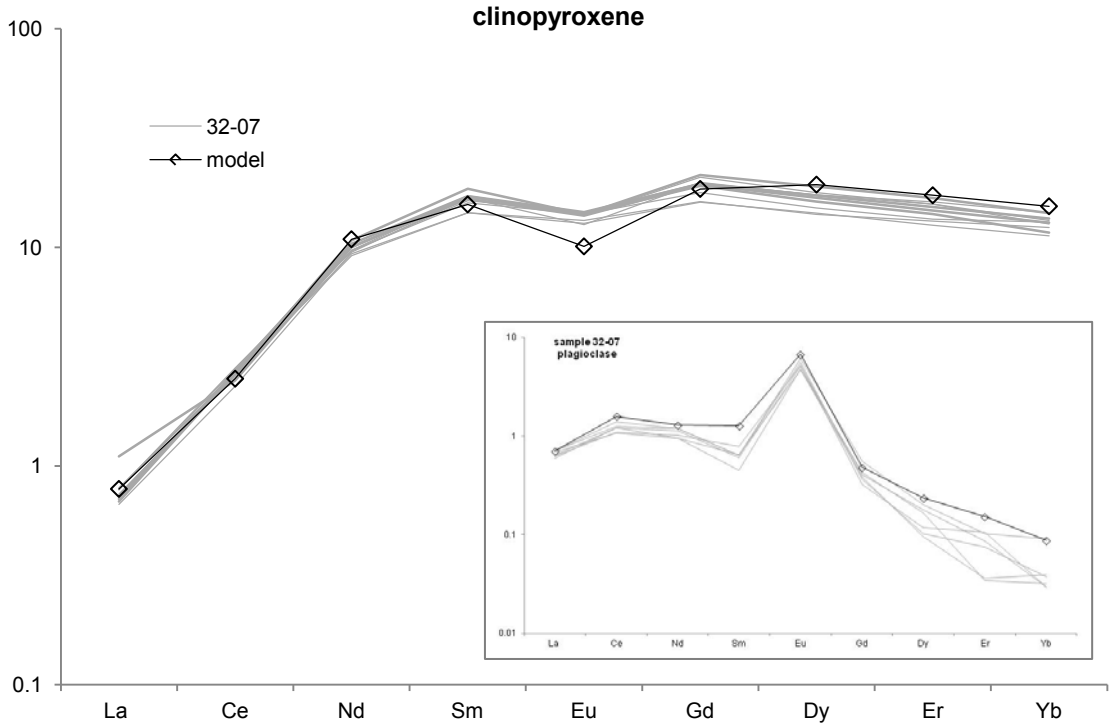

Fig. 5.4.1.2 - Modeled REE pattern for clinopyroxene in sample 32-07 (black open diamonds) at the end of reactive impregnation compared to measured contents (grey lines). Model represents the composition of the clinopyroxene after a total amount of added melt equal to 23.5%. In the small inset modeling REE composition of plagioclase compared to measured values is also reported. Values are normalized to C1 chondrite from Anders & Grevesse (1989)

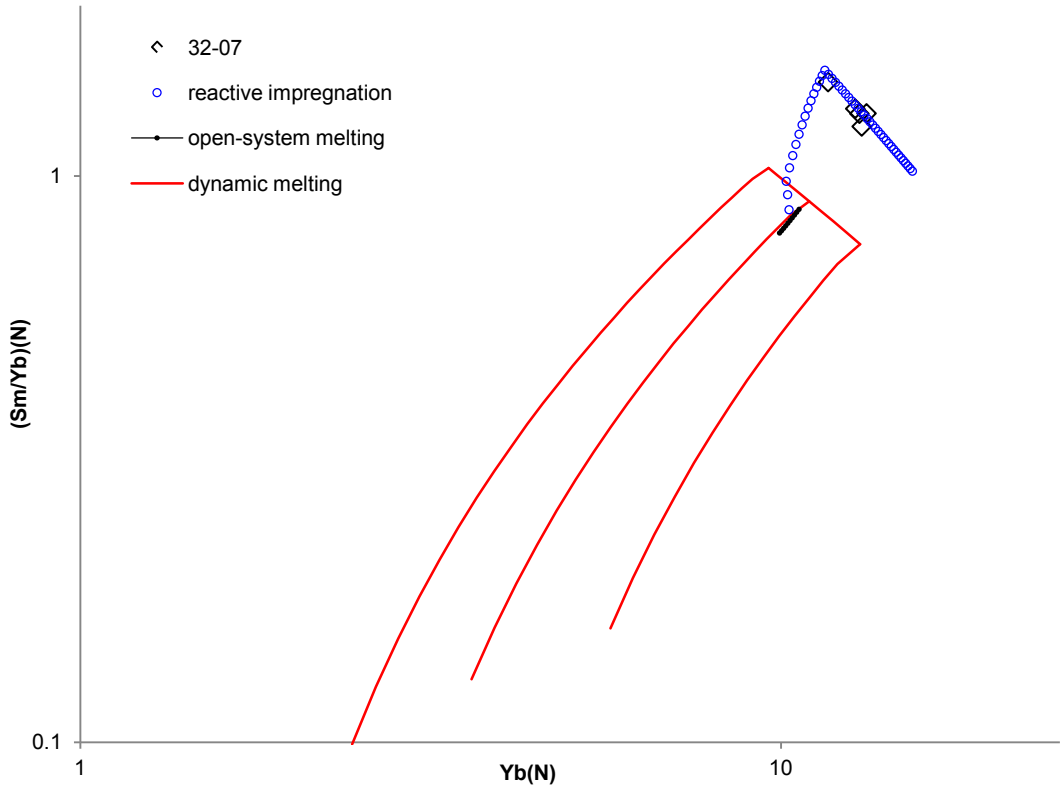

Fig. 5.4.1.3 - Modeled (Sm/Yb) vs Yb variations in clinopyroxene during reactive impregnation (blue open circles) for samples 32-07 (rims) compared to measured contents. Reactive impregnation proceeds until a total amount of added melt equal to 23.5%. Open-system melting (black-open circles) and dynamic melting (red line) curves are also reported for comparison. Values are normalized to C1 chondrite from Anders & Grevesse (1989)

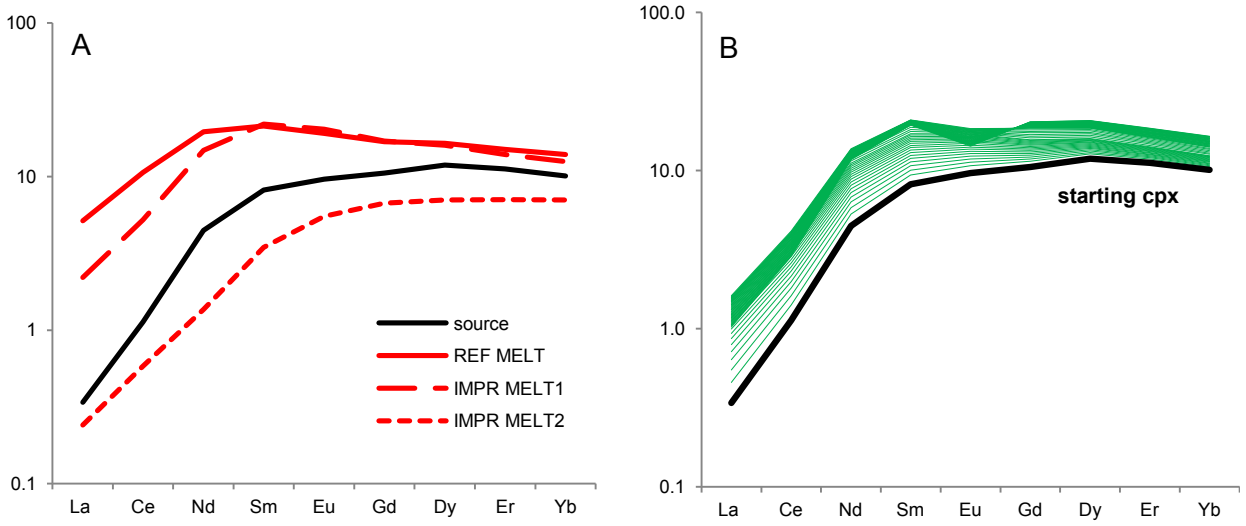

Fig. 5.4.1.4 - A) REE patterns of the melts used in modeling of sample 32-32; B) modeling for sample 32-07 (see text for details) which show REE variation in clinopyroxene during reactive impregnation from the starting composition at the end of melting; reactive impregnation proceeds until 12% of crystallized plagioclase and 7% of newly crystallized clinopyroxene, corresponding to a total amount of added melt equal to 25%. Impregnation steps corresponds to an addition of melt equal to 0.5% (X=0.005).

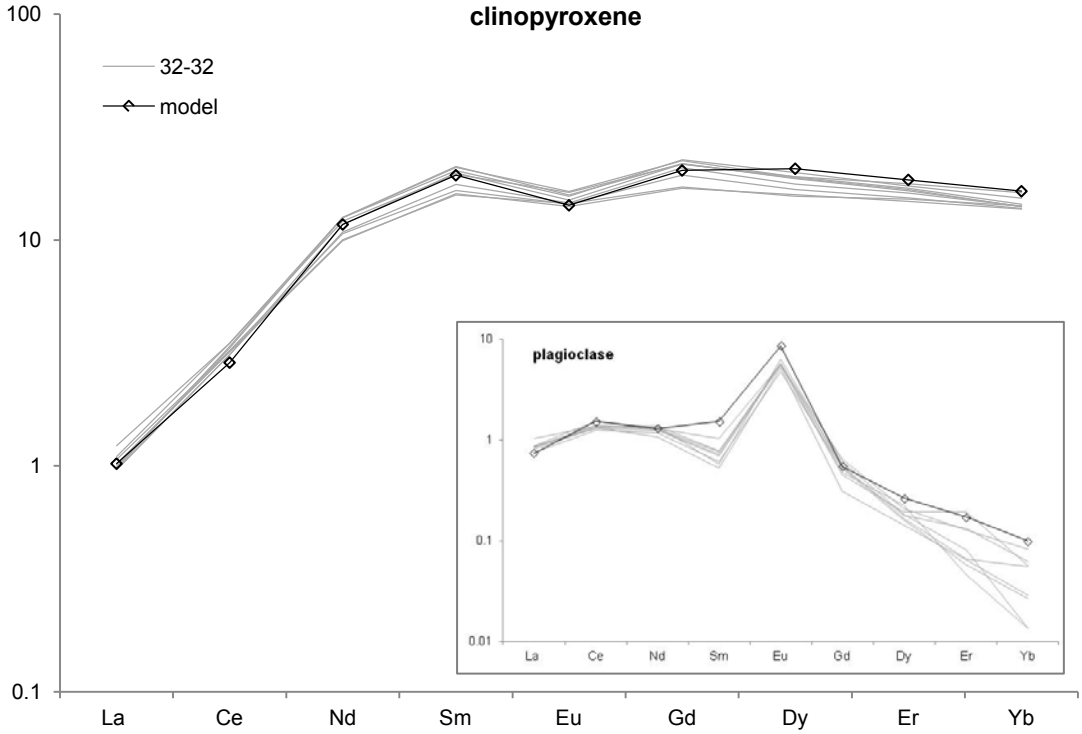

Fig. 5.4.1.5 - Modeled REE pattern for clinopyroxene in sample 32-32 (black open diamonds) at the end of reactive impregnation compared to measured contents (grey lines). Model represents the composition of the clinopyroxene after a total amount of added melt equal to 25%. In the small inset modeling REE composition of plagioclase compared to measured values is also reported. Values are normalized to C1 chondrite from Anders & Grevesse (1989)

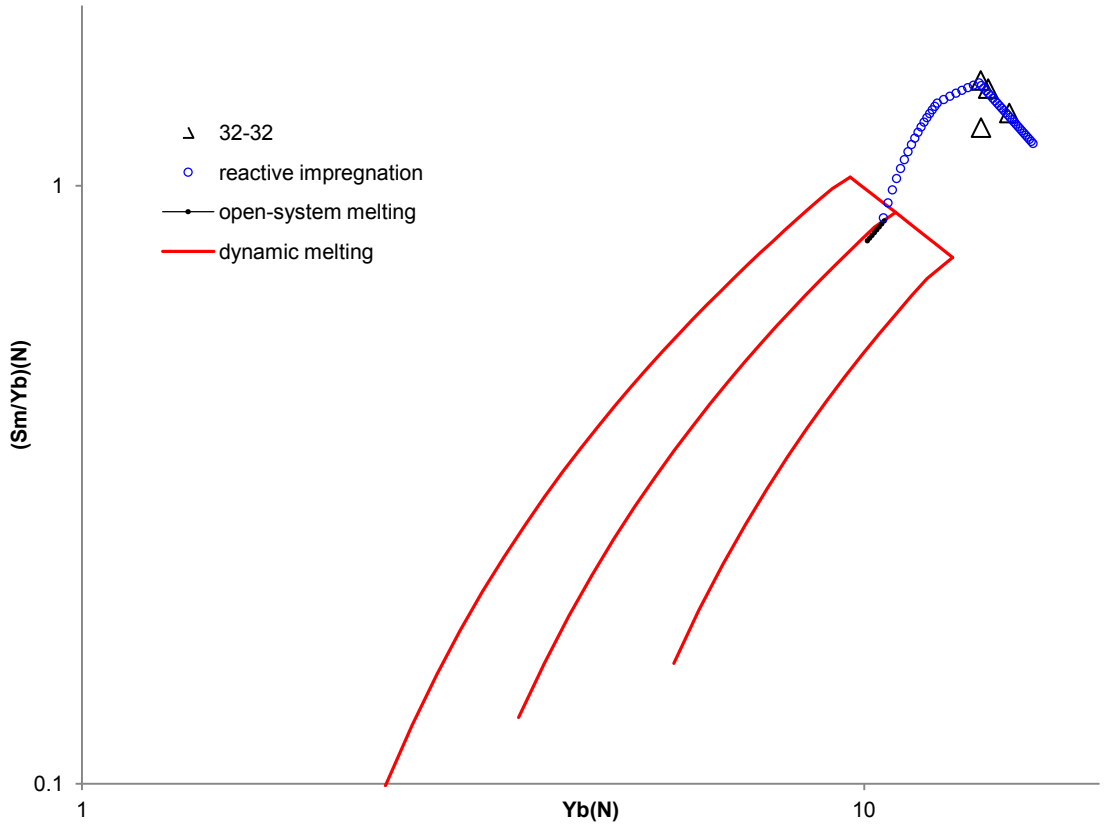

Fig. 5.4.1.6 - Modeled (Sm/Yb) vs Yb variations in clinopyroxene during reactive impregnation (blue open circles) for samples 32-32 (rims) compared to measured contents. Reactive impregnation proceeds until a total amount of added melt equal to 25%. Open-system melting (black-open circles) and dynamic melting (red line) curves are also reported for comparison. Values are normalized to C1 chondrite from Anders & Grevesse (1989)

Sample 32-22:

REE patterns of sample 32-22 can be reproduced by 1% melting in the garnet stability field followed by 7% open-system melting in the spinel stability field. The exotic melt ("REF MELT" in the following figures) which percolates the source during melting derives from low degree of melting of a spinel-lherzolite. The critical mass porosity during the entire process is ϕ=0.005, and the total amount of degree of melting is 7%. Reactive impregnation occurring after melting has been caused by two distinct melts: 3% of the first impregnating melt ("IMPR MELT1", fig. 5.4.1.7 A) is added, followed by an addition of the second, more depleted, impregnating melt ("IMPR MELT2", fig. 5.4.1.7 A) equal to 21.5%, hence the total amount of added melt is equal to 24.5%. Impregnating melts were obtained by mixing partial melts derived from moderate to high degrees of melting of a spinel-lherzolite and a refertilized spinel-peridotite. Reactive impregnation leads to fractional crystallization of (cpx+ol) and subsequently (plag+cpx) up to a total amount of plagioclase equal to 15% and newly crystallized clinopyroxene equal to 3%. The results of modeling of REE compositions and ratios for sample 32-22 are reported in figs. 5.4.1.7 B, 5.4.1.8 and 5.4.1.9.

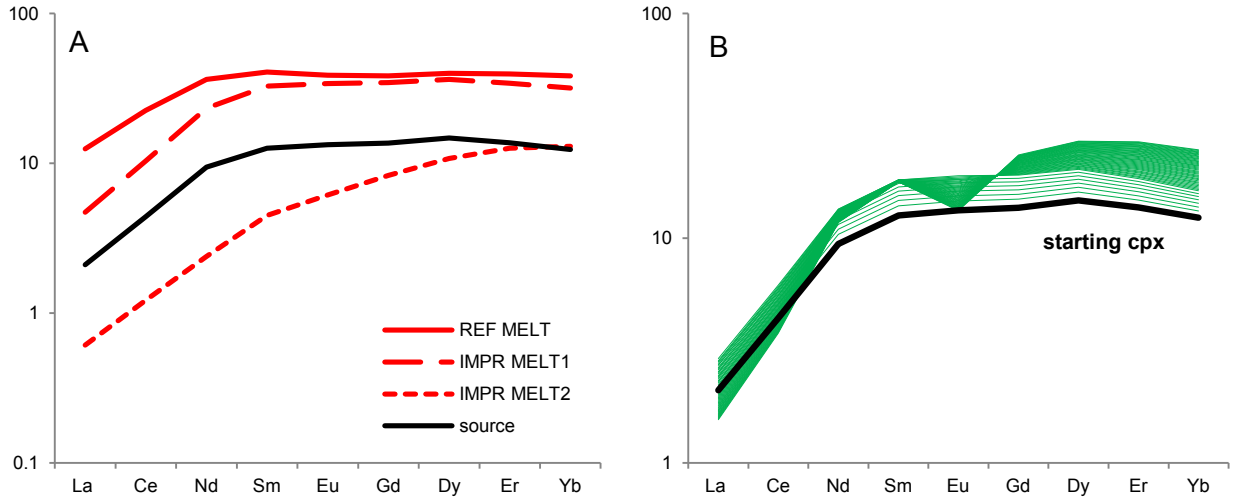

Fig. 5.4.1.7 - A) REE patterns of the melts used in modeling of sample 32-22; B) modeling for sample 32-22 (see text for details) which show REE variation in clinopyroxene during reactive impregnation from the starting composition at the end of melting; reactive impregnation proceeds until 15% of crystallized plagioclase and 3% of newly crystallized clinopyroxene, corresponding to a total amount of added melt equal to 24.5%. Impregnation steps corresponds to an addition of melt equal to 0.5% (X=0.005).

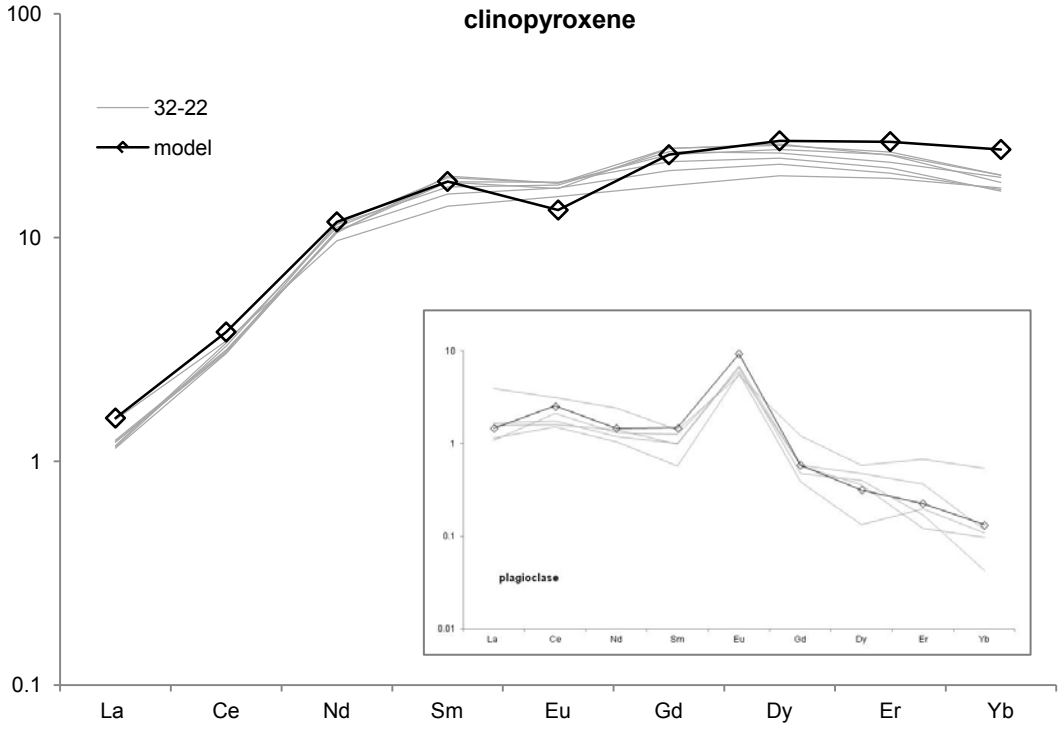

Fig. 5.4.1.8 - Modeled REE pattern for clinopyroxene in sample 32-22 (black open diamonds) at the end of reactive impregnation compared to measured contents (grey lines). Model represents the composition of the clinopyroxene after a total amount of added melt equal to 24.5%. In the small inset modeling REE composition of plagioclase compared to measured values is also reported. Values are normalized to C1 chondrite from Anders & Grevesse (1989)

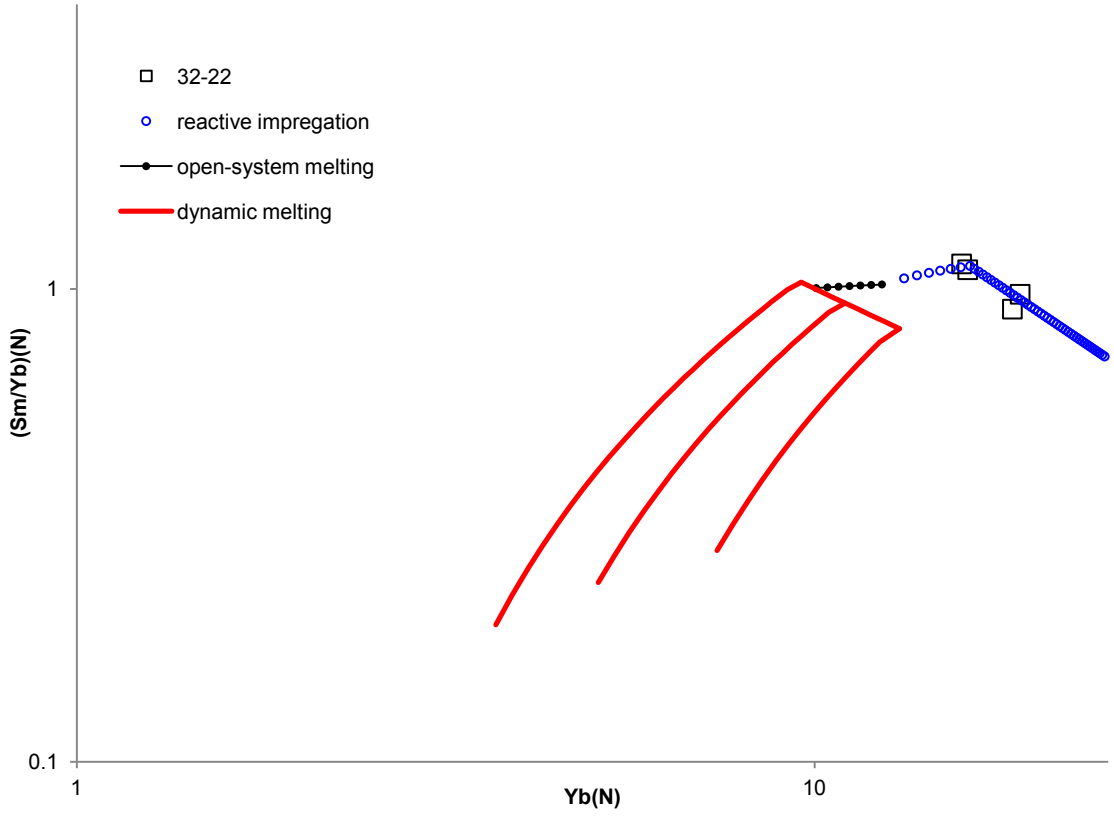

Fig. 5.4.1.9 - Modeled (Sm/Yb) vs Yb variations in clinopyroxene during reactive impregnation (blue open circles) for samples 32-22 (rims) compared to measured contents. Reactive impregnation proceeds until a total amount of added melt equal to 24.5%. Open-system melting (black-open circles) and dynamic melting (red line) curves are also reported for comparison. Values are normalized to C1 chondrite from Anders & Grevesse (1989).

Modeled sample have required a variety of melts (table 5.4.1.1) to justify the shape of REE patterns, the overenrichment and the rim trends. When plotted together (fig. 5.4.1.10 below) all these melts appear to pertain to two main compositional families: an enriched group of aggregated melts always related to the first phases of melting and refertilization and a second group of mets, strongly depleted, that are closely related to the last reactive percolation phases. Melts pertaining to the first group show variable garnet fingerprint: some present a clear MREE hump, attesting for a significant garnet-derived component, while others present a near-flat M- to HREE pattern attesting for a large degree of aggregation.

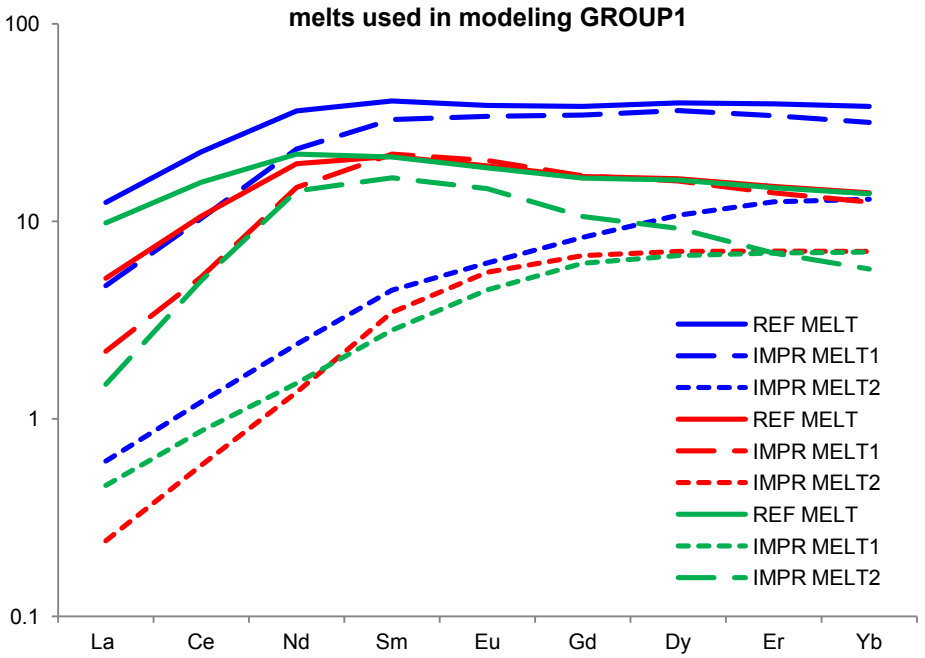

Fig. 5.4.1.10 - REE patterns of the melts used in modeling samples of Group1: sample 32-07 (green lines), sample 32-22 (blue lines) and sample 32-32 (red lines). Values are normalized to C1 chondrite from Anders & Grevesse (1989).

Table 5.4.1.1. Compositions (ppm) of melts used in the models for samples of Group1.

	GROUP1	Ti	Zr	La	Ce	Nd	Sm	Eu	Gd	Dy	Er	Yb
32-22	REF MELT	12485	147.45	2.93	13.56	16.40	5.98	2.16	7.51	9.66	6.25	6.21
	IMPR MELT1	10012	94.70	1.11	6.24	10.53	4.82	1.90	6.78	8.81	5.44	5.15
	IMPR MELT2	4159	18.27	0.14	0.74	1.08	0.66	0.34	1.63	2.61	2.00	2.10
32-07	REF MELT	6323	86.58	2.31	9.52	9.89	3.12	1.05	3.26	3.93	2.35	2.24
	IMPR MELT1	6042	48.88	0.35	3.03	6.46	2.45	0.82	2.08	2.23	1.10	0.93
	IMPR MELT2	2812	16.61	0.11	0.52	0.68	0.41	0.25	1.21	1.63	1.10	1.13
32-32	REF MELT	6381	82.35	1.21	6.40	8.85	3.14	1.07	3.32	3.99	2.38	2.26
	IMPR MELT1	7014	69.17	0.52	3.15	6.71	3.23	1.14	3.34	3.89	2.21	2.03
	IMPR MELT2	3178	18.15	0.06	0.35	0.62	0.51	0.31	1.32	1.71	1.12	1.14

5.4.2 Modeling of Group2 samples

Samples 39-28, 39-27 and 43-03:

REE patterns of samples of Group2 can be reproduced by 4% melting in the garnet stability field followed by 10% open-system melting in the spinel stability field. The exotic melt ("REF MELT" in the following figures) which percolates the source during melting was obtained by mixing melts derived from low degrees of melting of a spinel-lherzolite and a garnet-lherzolite. The critical mass porosity during the entire process is ϕ=0.004, and the total amount of degree of melting is 14%.

Reactive impregnation occurring after melting have been caused by two distinct melts: 6% of the first impregnating melt ("IMPR MELT1", fig. 5.4.2.1 A) is added, followed by an addition of the second, more depleted, impregnating melt ("IMPR MELT2", fig. 5.4.2.1 A) equal to 10%, hence the total amount of added melt is equal to 16%. Impregnating melts were obtained by mixing partial melts derived from moderate to high degrees of melting of a garnet-lherzolite and a refertilized spinel-peridotite, melts compositions are listed in table 5.4.2.1. Reactive impregnation leads to fractional crystallization of (cpx+ol) and subsequently (plag+cpx) up to a total amount of plagioclase equal to 9% and newly crystallized clinopyroxene equal to 3%. The results of modeling of REE compositions and ratios for sample of group2 are reported in figs. 5.4.2.1 B, 5.4.2.2 and 5.4.2.3.

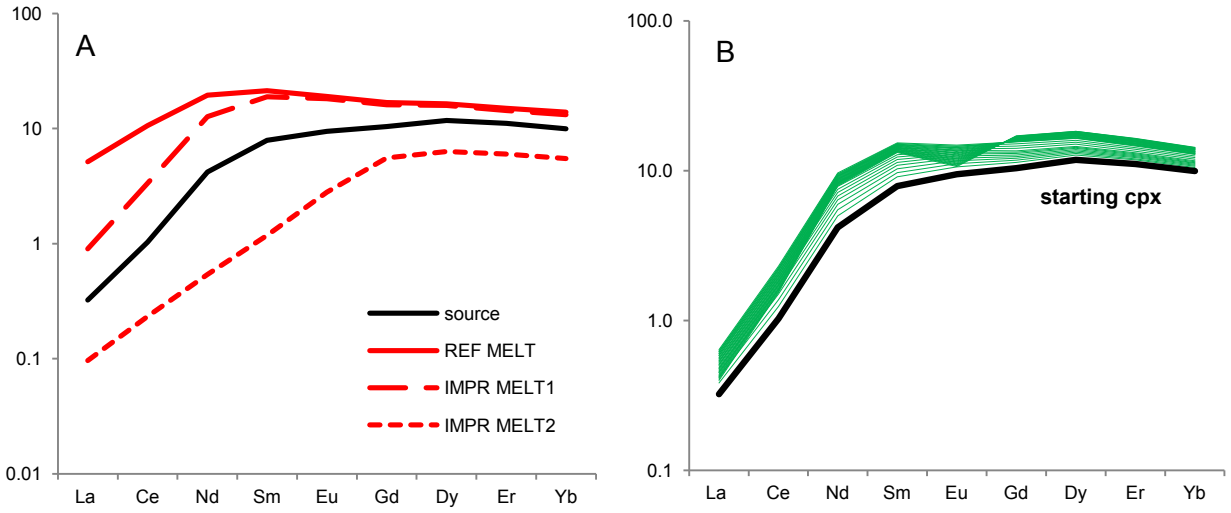

Fig. 5.4.2.1 - A) REE patterns of the melts used in modeling of sample of group2; B) modeling for sample of group2 (see text for details) which shows REE variation in clinopyroxene during reactive impregnation from the starting composition at the end of melting; reactive impregnation proceeds until 9% of crystallized plagioclase and 3% of newly crystallized clinopyroxene, corresponding to a total amount of added melt equal to 16%. Impregnation steps corresponds to an addition of melt equal to 0.5% (X=0.005).

Table 5.4.2.1. Compositions (ppm) of melts used in the models for samples of Group2.

	GROUP2	Ti	Zr	La	Ce	Nd	Sm	Eu	Gd	Dy	Er	Yb
39-27	REF MELT	6381	82.35	1.21	6.40	8.85	3.14	1.07	3.32	3.99	2.38	2.26
39-28 43-03	IMPR MELT1	6335	52.69	0.21	2.02	5.74	2.78	1.02	3.17	3.86	2.28	2.14
	IMPR MELT2	1605	8.54	0.02	0.14	0.24	0.17	0.16	1.09	1.53	0.95	0.89

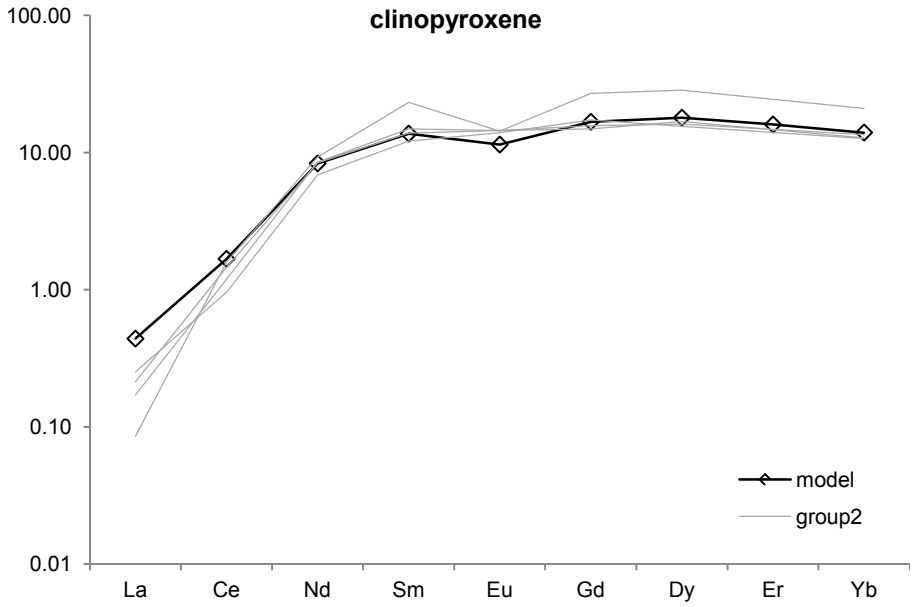

Fig. 5.4.2.2 - Modeled REE pattern for clinopyroxene in samples of group2 (black open diamonds) at the end of reactive impregnation compared to measured contents (grey lines). Model represents the composition of the clinopyroxene after a total amount of added melt equal to 16%. Plagioclase measured data for these samples are not available. Values are normalized to C1 chondrite from Anders & Grevesse (1989)

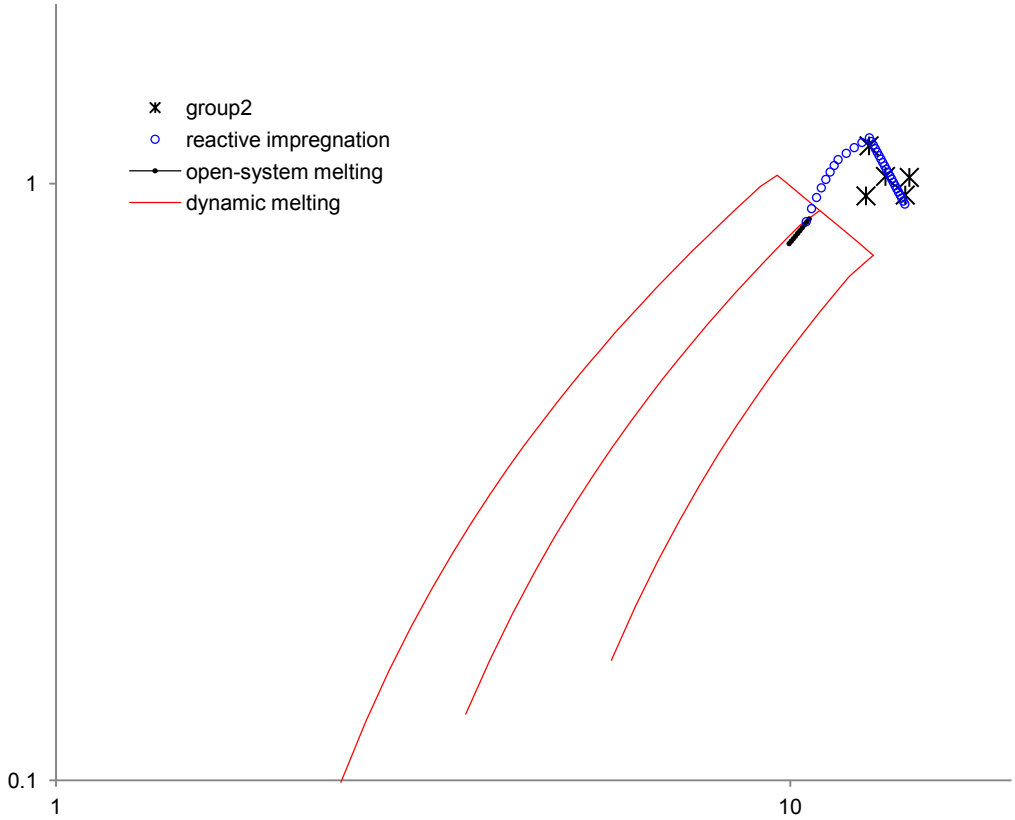

Fig. 5.4.2.3- Modeled (Sm/Yb) vs Yb variations in clinopyroxene during reactive impregnation (blue open circles) for samples of group2 compared to measured contents. Reactive impregnation proceeds until a total amount of added melt equal to 16%. Open-system melting (black-open circles) and dynamic melting (red line) curves are also reported for comparison. Values are normalized to C1 chondrite from Anders & Grevesse (1989)

5.4.3 Modeling of Group3 samples

Sample 39-36:

REE patterns of sample 39-36 can be reproduced by 8% melting in the garnet stability field followed by 10% open-system melting in the spinel stability field. The exotic melt ("REF MELT" in fig. 5.4.3.1) which percolates the source during melting is garnet-lherzolite-derived. The critical mass porosity during the entire process is ϕ=0.001, each step of melting corresponds to 2% (f=0.02) and the total amount of melting is 20%. Reactive impregnation occurring after melting have been caused by addition of 2% of an ultra-depleted melt ("IMPR MELT", fig. 5.4.3.1 A) which was obtained by mixing partial melts derived from high degrees of melting of a garnet-lherzolite and a refertilized spinel-peridotite; melts compositions are listed in table 5.4.3.1. Reactive impregnation leads to fractional crystallization of (plag+cpx) up to a total amount of plagioclase equal to 0.7% and newly crystallized clinopyroxene equal to 0.4%. The results of modeling of REE compositions and ratios for sample 39-36 are reported in figs. 5.4.3.1 B, 5.4.3.2 and 5.4.3.3.

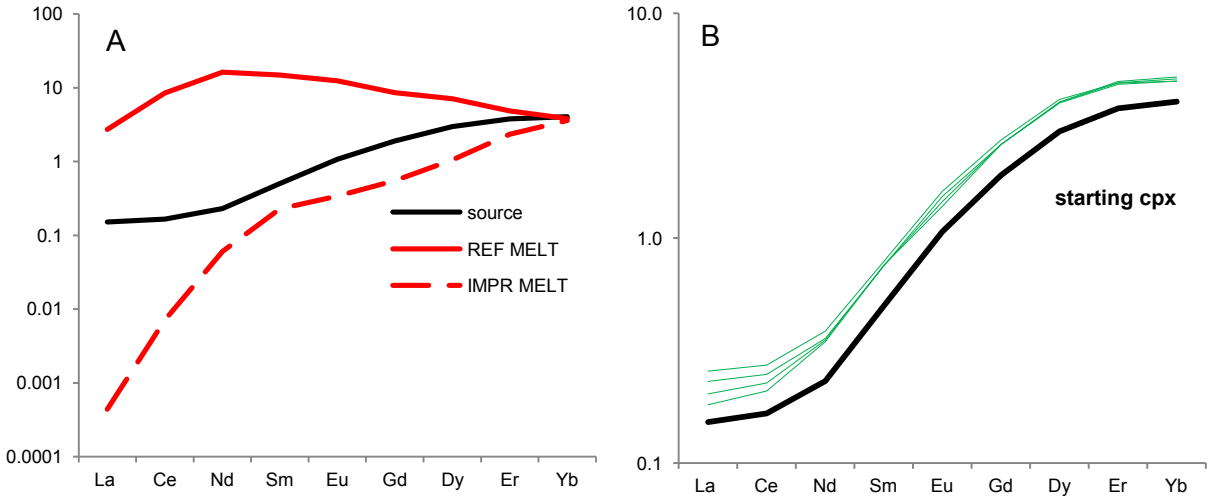

Fig. 5.4.3.1 - A) REE patterns of the melts used in modeling of sample 39-36; B) modeling for sample 39-36 (see text for details) which shows REE variation in clinopyroxene during reactive impregnation from the starting composition at the end of melting; reactive impregnation proceeds until 0.7% of crystallized plagioclase and 0.4% of newly crystallized clinopyroxene, corresponding to a total amount of added melt equal to 2%. Impregnation steps corresponds to an addition of melt equal to 0.5% (X=0.005).

Table 5.4.3.1. Compositions (ppm) of melts used in the models for samples of Group3.

	GROUP3	Ti	Zr	La	Ce	Nd	Sm	Eu	Gd	Dy	Er	Yb
39-36	REF MELT	5356	52.73	0.64	5.12	7.33	2.18	0.69	1.68	1.71	0.77	0.62
	IMPR MELT	265	1.02	0.00	0.00	0.01	0.01	0.02	0.39	0.67	0.44	0.40

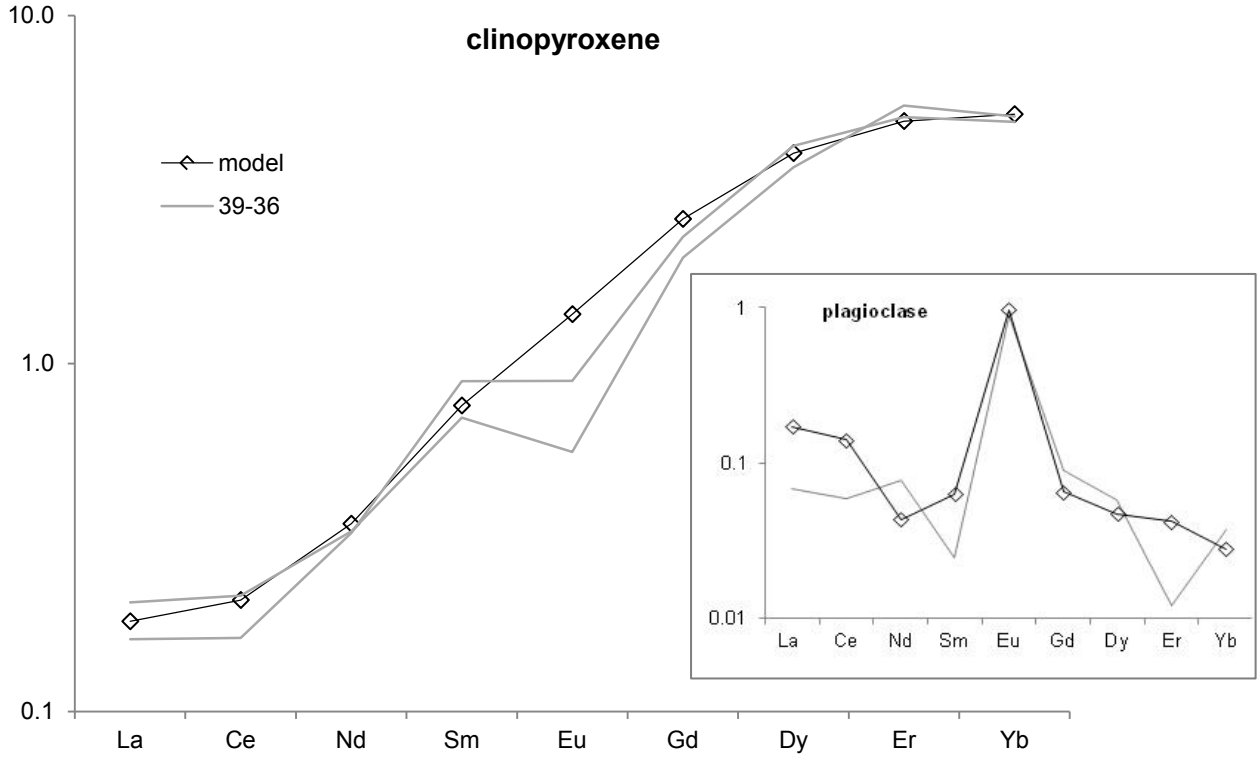

Fig. 5.4.3.2 - Modeled REE pattern for clinopyroxene in sample 39-36 (black open diamonds) at the end of reactive impregnation compared to measured contents (grey lines). Model represents the composition of the clinopyroxene after a total amount of added melt equal to 2%. In the small inset modeling REE composition of plagioclase compared to measured values is also reported. Values are normalized to C1 chondrite from Anders & Grevesse (1989).

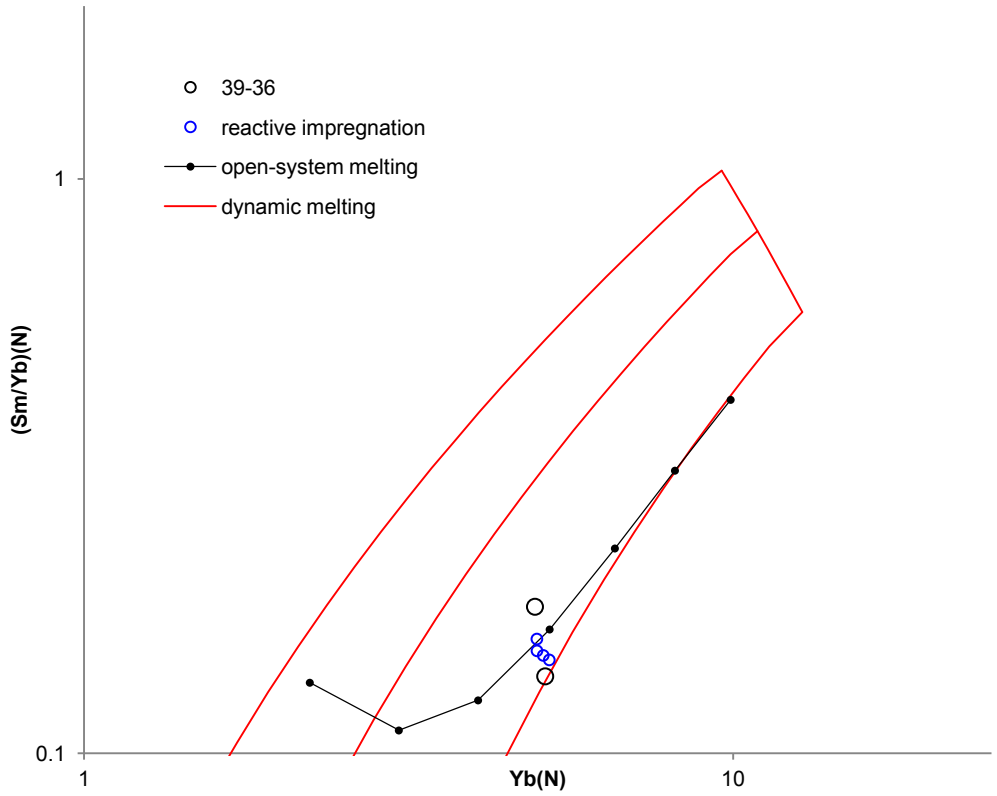

Fig. 5.4.3.3- Modeled (Sm/Yb) vs Yb variations in clinopyroxene during reactive impregnation (blue open circles) for sample 39-36 compared to measured contents. Reactive impregnation proceeds until a total amount of added melt equal to 2%. Open-system melting (black-open circles) and dynamic melting (red line) curves are also reported for comparison. Values are normalized to C1 chondrite from Anders & Grevesse (1989.

5.4.4 Modeling of Ti-Zr variations of the studied samples

The following figures report the results of modeling of Ti-Zr variation from open-system melting to the end of reactive impregnation for the studied samples, compared to measured compositions. Modeling assumptions and parameter are the same described in previous paragraphs. Figures 5.4.4.1 and 5.4.4.2 show that, accordingly, samples show increasing trends, but measured compositions appear slightly depleted in titanium with respect to the predicted models.

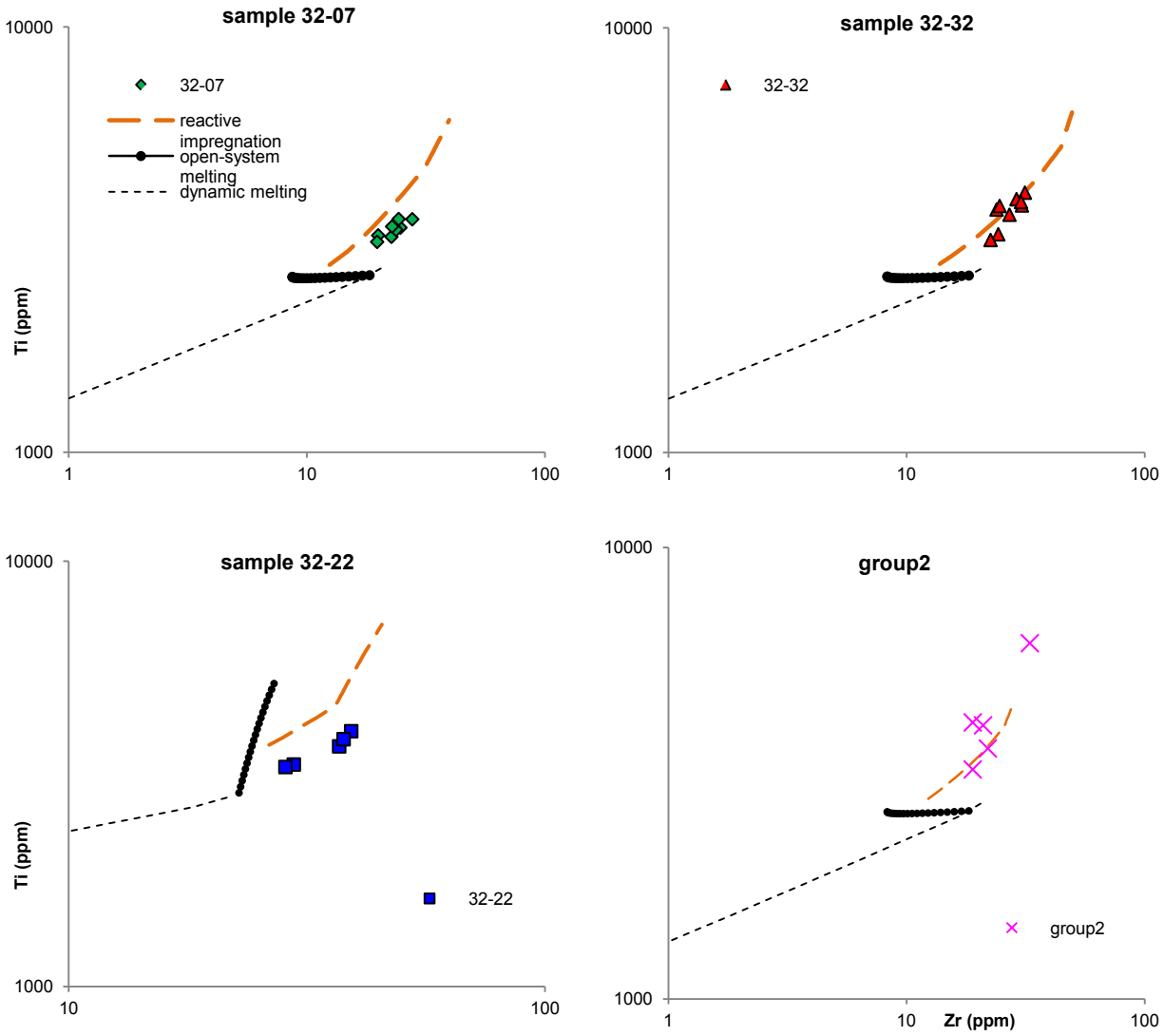

Fig. 5.4.4.1- Ti-Zr modeling of reactive impregnation for samples of group1 (samples 32-07, 32-32 and 32-22) and group2. See text for details.

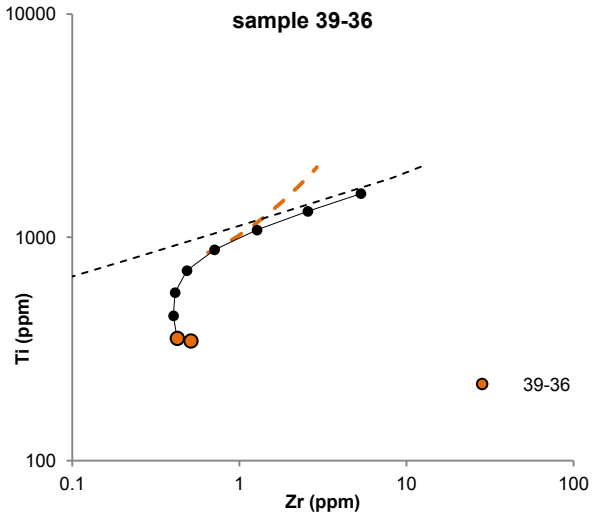

Fig. 5.4.4.2- Ti-Zr modeling of reactive impregnation for samples of group3 (sample 39-36). See text for details.

Chapter 6
Discussion and conclusions

6.1 Petrology of the Romanche FZ: state of the art

The Romanche FZ peridotites appear different from most abyssal peridotites collected along the Mid-Atlantic Ridge. Since the first oceanographic expeditions were carried out in the equatorial Atlantic, several works have been released through the last two decades, which have pointed out geological, petrographic and petrologic peculiarity characterizing this huge oceanic transform.

The Romanche Fracture Zone is a lens-shaped, 900 km-long, 100 km-wide multifault deformation zone, the major transform fault that offsets the Equatorial Mid-Atlantic Ridge and one of the longest of the worldwide ridge system. The geometry of the transform system thus looks different from "classic" oceanic transform boundaries, which are characterized by a single, few-kilometers-wide, strike-slip deformation zone, so that it has been defined as "megatransform" plate-boundary (Ligi et al., 2002). Other megatransforms have been observed elsewhere in the mid-ocean ridge system, e.g. the Andrew Bain Fracture Zone along the South West Indian Ridge (SWIR). For the detailed geological overview and the related debated issues, please refer to chapter 1.

Samples collecting throughout the equatorial Atlantic reveals a widespread scarcity of the basaltic crust in correspondence to the Romanche FZ, giving rise to an ~50-km-wide, >500-km-long strip of ocean floor mostly exposing mantle peridotites, south of the transform (Bonatti et al. 2001). As a rule, abyssal peridotites are usually sampled where amagmatic extension prevails over magmatic accretion, so that residual mantle exposure is allowed, as usual for slow and ultra-slow ridges, and many works have pointed out that this mechanism is supposed to be emphasized in the vicinity of oceanic transforms.

In the Romanche transform, the very large extension (900 km) of the fracture zone system coupled with the average half-spreading rate of 17 mm/yr (according to Cande et al., 1988) result in a large age offset, approximately 52 My (Bonatti et al. 2001); this means that the oceanic crust fronting each ridge axis (zero age) is aged of about 52 My. The oceanic lithosphere carried by plate motion in front of the opposite ridge axis has therefore experienced a ~52 My-long cooling time away from the thermal high of the ridge axis. Thermal modeling allows estimating a >30 km-thick lithosphere at this age. This may result in a strong cold

edge effect because of the thermal gradient from the hot-young ridge axis toward the thick-cold ancient lithosphere (Fox & Gallo, 1984). Numerical models (fig. 6.1.1) support the thesis that such cold-edge effect - although actually not mirrored by the non-deepening ridge axis approaching the Romanche transform, probably due to the serpentinization-related volume increase (Bonatti et al, 1996b; see chapter 1) - combined with the superposition of a regional thermal minimum (Bonatti et al., 1994; Schilling et al., 1995) lowers the extent of melting of the mantle in the vicinity of the ridge-transform intersection to the point that the complete development of the axial valley is prevented, while very small amounts of melt are produced and extruded at the seafloor. Bonatti et al. (2001) suggested a nearly continuous nonmagmatic, tectonic emplacement and extension of lithosphere at the Romanche ridge axis for more than 30 My.

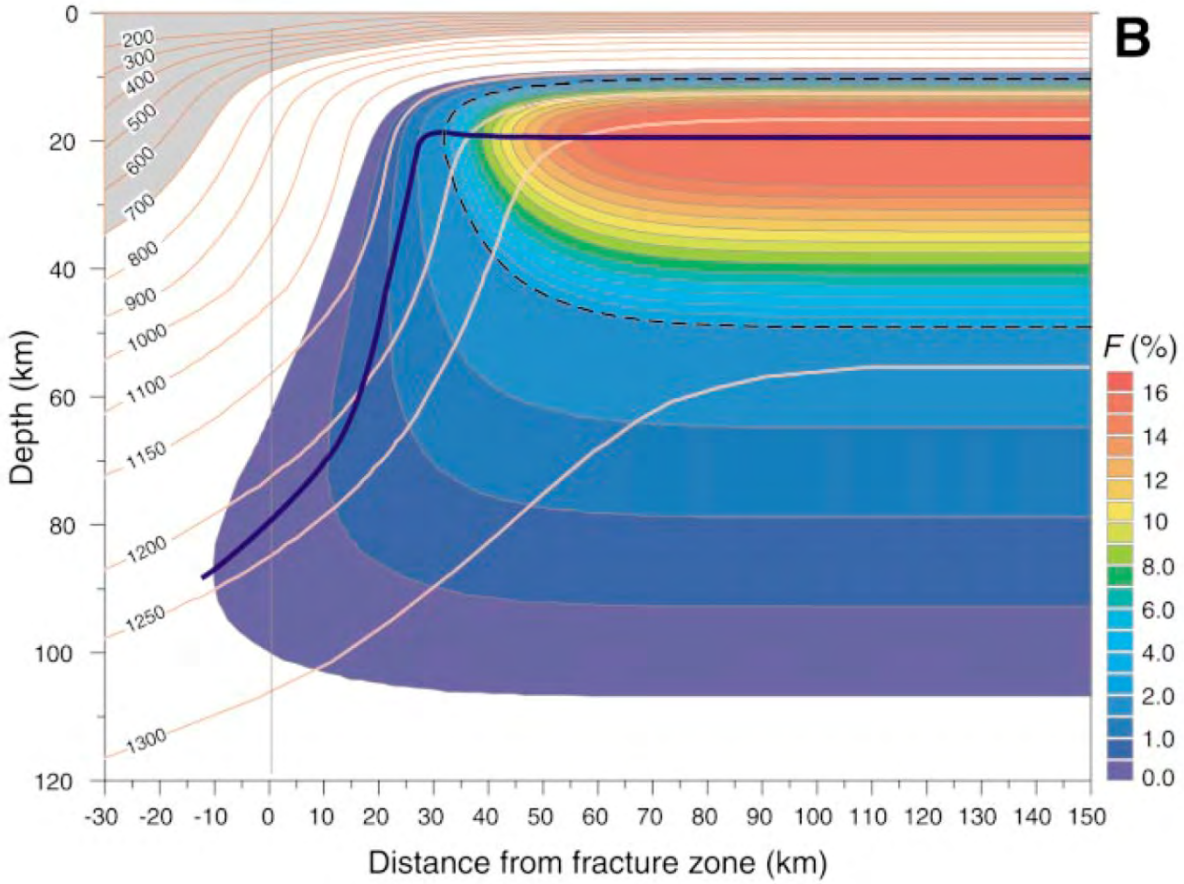

Fig. 6.1.1 - Melt production as a mid-ocean ridge segment approaches Romanche-type, slow-slipping transform, modeled by Bonatti et al. (2001). The gray area at the top corresponds to the lithosphere assuming its base at the 700° C isotherm. Worth noting the strong increase of the lithospheric thickness across the plate boundary due to the significant age contrast (>50 My). Coupling a cold plate to the tip of a hot segment results in heat transfer and depression of the isotherms at the boundary strongly limiting the melt production in the boundary region.

The residual character of abyssal peridotites is the reason why their incompatible elements contents are significantly more depleted than associated Mid-Ocean Ridge Basalts (MORB). However, abyssal peridotites allow to directly study mantle residua, revealing source compositional variability at a much shorter scale (m-km) than what can be inferred from the related MORBs. In fact, MORBs represent the aggregation of all instantaneous melt contributions from a large volume of mantle undergoing partial melting beneath a ridge segment. Under the physical conditions of a slow spreading ridge, such as the Mid-Atlantic Ridge, a $>10^6$ km^3 volume of the melting region can be estimated.

Sampling attests for chemical heterogeneities along the entire length of the Romanche FZ. Authors agree on the coexistence of simple mantle residua which underwent very low degrees of partial melting (<10%), mainly recovered in the western part of the transform, and "anomalous" peridotites, which prevail in the eastern part, characterized by anomalous contents of plagioclase (up to 16%) and clinopyroxene, and peculiar textures and microstructures, i.e. patches, pockets and veins/dikes of magmatic origin spread throughout the rock groundmass (Seyler & Bonatti, 1997; Bonatti et al., 2001; Tartarotti et al., 2002). The latter rock type, referred to as "metasomatic" in the sense of Bonatti et al., (2001), as well as "impregnated" in the sense of Tartarotti et al. (2002), have been interpreted to be the result of a porous flow of basaltic melt reacting with a slightly depleted, residual lherzolite, at a shallow level in the upper mantle, in the plagioclase stability field (above the depth of 25 km). Melt retention and consequent refertilization of the host peridotite are also suggested by Ti and Cr increase in spinel coupled with Ti, Sr, Zr, Y and LREE in residual clinopyroxene.
The Romanche FZ peridotites therefore may represent residual mantle after experiencing among the lowest degrees of melting (≤5%) of the whole mid-ocean ridge system, and frequently part of the percolating melts may be retained and crystallize within the lithospheric mantle.

6.2 Petrography

6.2.1 Peridotites residual textures

Sample 39-36 (and, to a lesser extent, sample 39-28) shows relics of coarse equigranular texture (Ceuleneer & Cannat, 1997) - i.e. coarse-grained olivine groundmass showing a preferred orientation and coarse orthopyroxene slightly concordant with the olivine foliation - co-existing with evidences of olivine grain-size reduction from coarse to medium, resulting in resorption of orthopyroxene, that is defined protogranular texture (Seyler et al, 2007; Dick et al 2010). Further pervasive grain-size reduction of olivine from medium to fine, clearly observed in sample 39-28 (and, to a lesser extent, in sample 39-36), locally leads to the development of porphyroclastic texture (Mercier & Nicholas, 1985; Ceuleneer & Cannat, 1997), i.e. relics of coarse to medium sub-rounded deformed orthopyroxene within an equigranular fine-grained groundmass.

As a whole, we can assert that all the studied samples show similar textures, i.e. transitional textures from protogranular to porphyroclastic, with occasional relics of coarse equigranular texture.
In a mid-ocean ridge setting, considering the ascending mantle, which is gradually rafted to the top of the oceanic crust column, the physical conditions at which the peridotite were deformed can be constrained by measurements of grain size and by the morphology and substructure of the olivine matrix (Ceuleneer & Cannat, 1997), and according to occurring olivine microstructures, "asthenospheric" vs. "lithospheric" microstructures have been distinguished (Nicolas, 1986; Ceuleneer et al., 1988; Ildefonse et al., 1998a, 1998b, Dijkstra et al., 2003). Coarse equigranular texture may be indicative of asthenospheric environment, i.e. high T, low strain (about 1000-1200° C; <5-10 MPa) and is referred to as "asthenospheric" microstructure; the development of medium-grained olivine, i.e. protogranular texture, instead, is considered to be the result of subsequent asthenosphere incorporation in the lithosphere, which triggers a high-temperature, quasi-static re-crystallization, occurring simultaneously with melt percolation. Finally, "lithospheric" microstructure occurs in response to a further grain-size reduction of olivine due to relatively higher stress (>10 MPa) and lower temperature deformation in lithospheric conditions, with concurrent brittle deformation of coarse-grained residual pyroxene resulting in kink banding and fracturing (porphyroclastic texture). For example, Dijkstra et al. (2003) by means of paleopiezometer found that some coarse tectonites from the Othris Peridotite Massif, which locally preserves ‘‘asthenospheric’’ microstructures with recrystallized olivine grain sizes >0.5 mm, underwent deformation stresses <13 MPa, whereas the recrystallized olivine grain size from 0.1 to 0.6 mm in the fine-grained tectonites of the same massif suggests deformation stresses of 10 - 40 MPa.

6.2.2 Evidences of melt percolation and impregnation textures

As observed in samples of dredge #39, plagioclase patches tend to gather in medium-to fine-grained zones due to the higher porosity (fig. 2.3.1.3, see chapter 2); as regards samples of dredges #32 and #33, in which the olivine fabric appears totally obscured by alteration, it can be inferred that local assemblages of plagioclase patches might reveal the presence of previous zones of higher porosity, i.e. medium- to fine-grained textures. On the other hand, if we consider plagioclase as a product of melt percolation, the occurrence of plagioclase also should depend on melt availability; therefore, if occurrence of plagioclase might suggest higher porosity, the lack of plagioclase can't be considered as an evidence of lower porosity. Petrographic observations also reveal propensity of plagioclase patches to gather within brittle and ductile deformation structures, i.e. fractures, kinkbands, micro-faults and so on. Hence, such lithospheric deformation may be able to locally increase the rock porosity and thus ease melt entrapment, similarly to a "lithospheric sponge" (Müntener et al. 2010).

Plagioclase-bearing peridotites is a subject matter which claims a wide literature; they have been recovered and described in extensional settings both in oceanic and continental environments. Porous flow percolation

of migrating melts throughout the upper mantle and consequent melt-rock reaction is widely accepted to be a common mechanism affecting the upwelling asthenosphere towards the shallow lithospheric mantle. Part of the migrating melt may be retained within the rock porosity and crystallize plagioclase±px pockets at the P-T conditions of the plagioclase stability field (above the depth of 25 km), i.e. at shallow and relatively cold lithospheric environments. On the other hand, several works highlighted the key-role of the adiabatic upwelling, which may trigger metamorphic recrystallization of spinel, as a consequence of phase subsolidus transition, independently of the occurrence of partial melting and/or percolation of migrating melts, according to the reaction:

clinopyroxene + orthopyroxene + spinel --> anorthite + 2forsterite

Such "metamorphic" plagioclase-bearing peridotites are scarce in oceanic settings; they likely require an early fertile composition before the breakdown of spinel-bearing mineral assemblage occurs, being in fact more frequent in extensional settings related to lithospheric mantle exhumation in response to lithospheric thinning and rifting, in which the exhumed mantle did not experience partial melting.

Thin plagioclase coronas surrounding spinel crystals have been interpreted as an evidence of transition from spinel- to plagioclase-facies, whereas plagioclase interconnected patches clearly attest for melt-rock reaction involving exotic migrating melts since the high plagioclase modal content (up to 15%) could not be explained by neither spinel breakdown nor in situ melting alone. In the studied samples plagioclase mainly occurs as partially interconnected plagioclase±px patches which permeate the whole rock, and plagioclase coronas surrounding spinel have been recognized only in samples 39-28, though coexisting with interconnected patches. Thus the moderately depleted mantle expected to underlie oceanic transforms may allow the development of spinel-breakdown textures; however, this process may be negligible and most modal plagioclase can be considered as a result of crystallization from exotic melts.

It is worth noting that modal composition of crystallized pockets from interstitial melts strongly depends on pressure conditions and the host peridotite composition (Seyler et al., 2001; Dijkstra et al., 2001). Accordingly, usually plagioclase appears almost undeformed, contrary to residual pyroxenes, strongly suggesting that plagioclase must have escaped most lithospheric deformation processes, i.e. plagioclase crystallization occurred during the late stages of mantle upwelling. Several studies have provided evidences for a small proportion of clinopyroxene in abyssal plagioclase-free peridotites to be not residual, but crystallized from melt as the partially molten mantle enters into the conductive thermal layer (Seyler et al. 2001) (Hellebrand et al. 2002) (Brunelli et al. 2006). The precipitation of clinopyroxene associated with Al-rich spinel rather than plagioclase indicates that this process occurred at relatively high pressure (>0.9 GPa --> about 35 km, spinel field). Interstitial small px grains have been widely recovered in samples of dredge #32.

The main and ubiquitous texture characterizing the studied rocks concerns the coarse-grained orthopyroxene crystals which are affected by a peculiar "corroded" appearance, resulting from penetration and partial replacement by other mineral phases (fig. 6.2.2.1). In most cases, orthopyroxene replacement occurs on the benefit of olivine, but also of plagioclase±clinopyroxene though at a less extent. Orthopyroxene replacement on the benefit of olivine may be considered as a reaction product of opx+cpx+sp incongruent melting occurring in asthenospheric environment during mantle upwelling (Kinzler and Grove, 1992), but also as a consequence of reactive porous flow, i.e. the reaction product between adiabatically ascending melts that become saturated in ol and undersaturated in opx (Kelemen, 1990). Opx undersaturated melts may derive from high-P partial melts that extensively reacted with wall peridotites, beyond the point of exhaustion of clinopyroxene (Kelemen et al., 1995a, b) or if they are silica-rich, low-P melts produced by partial melting of a depleted peridotite, in equilibrium with a cpx-free residue. Moreover, if the melt is undersaturated in opx and also saturated in clinopyroxene, orthopyroxene resorption occurs on the benefit of clinopyroxene ± spinel (Seyler et al., 2007).

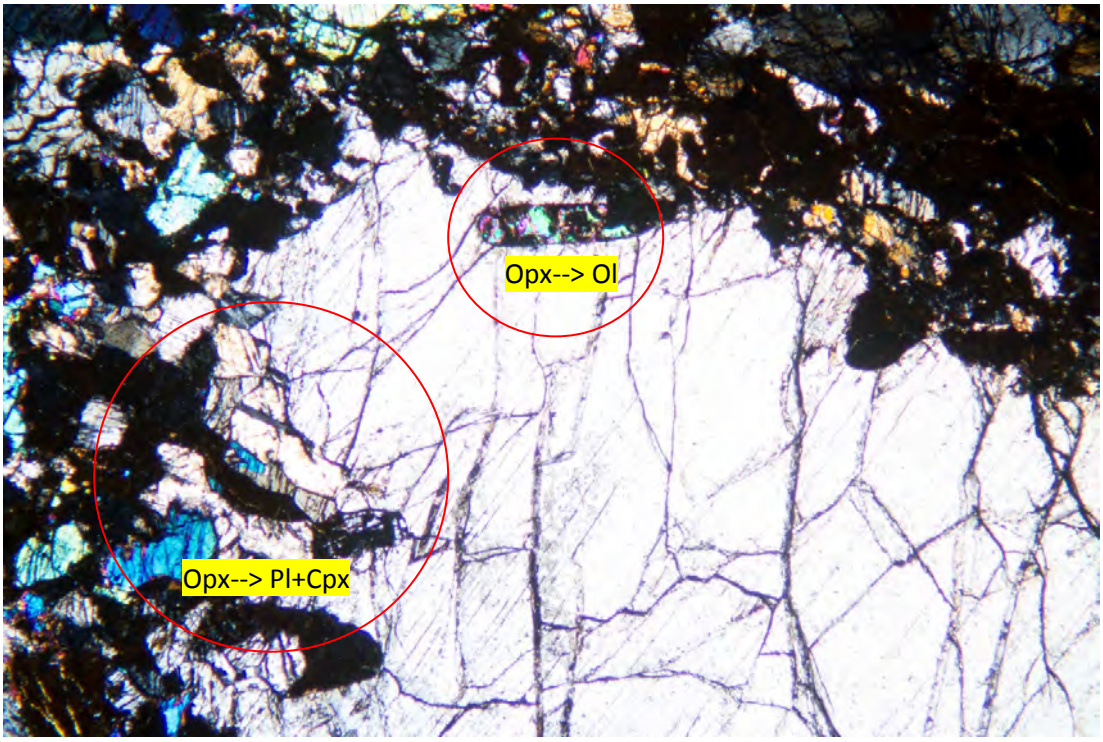

Fig. 6.2.2.1 - Coarse-grained opx with evidences of resorption: replacement by olivine and replacement by pl+clinopyroxene. Sample 32-32. Crossed nicols. 2x

6.3 Major elements

As mentioned above, reactive porous flow and refertilization are two important and common processes that are potentially able to deeply modify textures, mineral modes and, consequently, chemical composition of residual peridotites.

Olivine Mg# in plagioclase-bearing peridotites is expected to be lower or, at least, more variable than in plagioclase-free peridotites (89.3-91; Dick, 1989), due to intrusion of gabbroic veins (Tartarotti et al., 1995; Cannat et al. 1997; Dick, et al., 2010). Fe enrichment effect approaching gabbroic dikelets may occur up to distances around 3 cm from a dikelet, reaching olivine Mg# values lower than 80% (Cannat et al., 1997). In the studied samples measurements in medium- to coarse-grained olivine have been performed both close to and away from plagioclase-bearing mineral assemblages, but extremely homogeneous Mg# (from 89 to 90) have been observed (fig. 6.2.1).

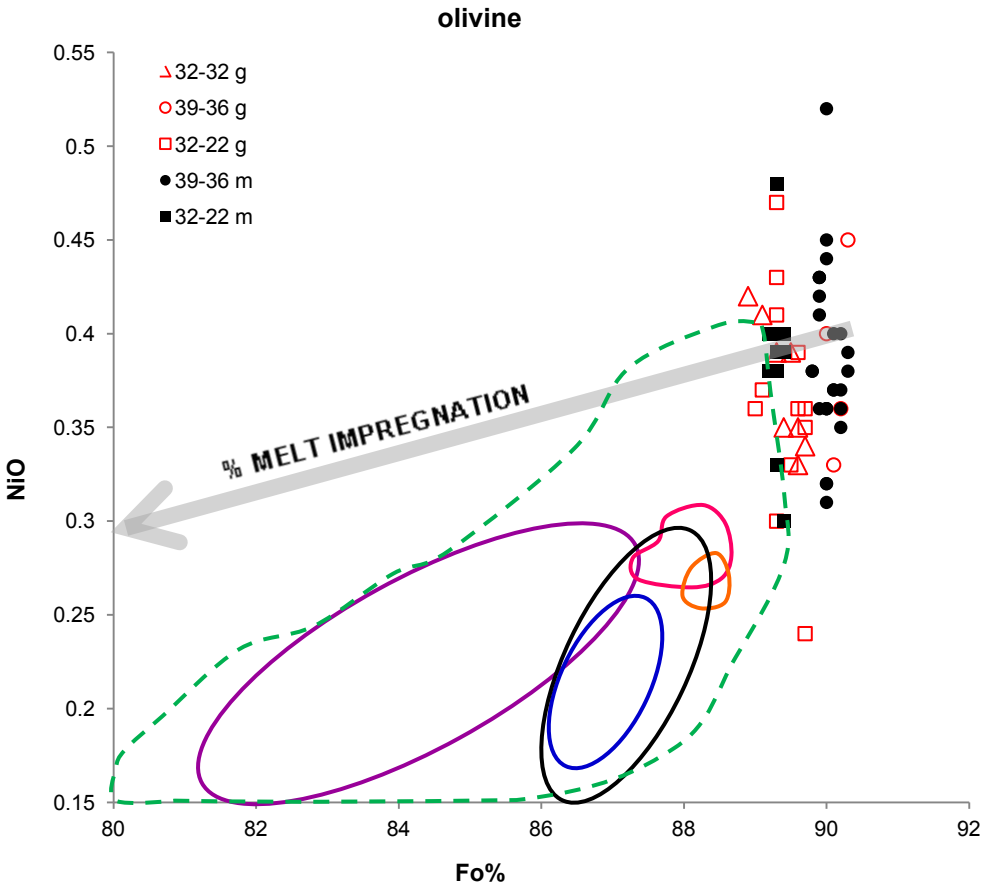

Figure 6.2.1 - NiO vs Mg# in olivine. Red outlined symbols represent fine-grained crystals whereas black full-colored symbols represent medium and coarse crystals. Grey arrow defines the inferred NiO vs. Mg# trend at the increasing melt impregnation whereas green dotted lines represents calculated MORB-equilibrated olivine (from Dick et al., 2010). Data of the olivine-rich troctolites from the Internal Ligurian ophiolites (pink line; (Renna and Tribuzio 2011), the Pineto gabbroic sequence (orange line; Sanfilippo and Tribuzio, 2013), the Atlantis Massif (violet line; Suhr et al., 2008; Drouin et al., 2009), the Kane Megamullion (black line; Dick et al., 2010) and Godzilla Megamullion (blue line; Sanfilippo et al., 2013) are also reported for comparison.

Generally, Al_2O_3 content in abyssal peridotites pyroxene is used as an indicator of re-equilibration to lower temperature; decreasing Al_2O_3 from plagioclase-free to plagioclase-bearing peridotites (Rampone et al., 1993; Seyler et al. 2003) is consistent with re-equilibration to lower temperature in presence of plagioclase; in the studied samples this effect is emphasized when plagioclase-bearing mineral aggregates fill fractures inside coarse orthopyroxenes, resulting in Al_2O_3 decreasing of opx approaching the fracture. Fertile (higher Al) cores of some coarse pyroxene crystals may suggest re-equilibration effect to be more efficient at the rims of the crystals.

In the studied samples Al_2O_3 and Cr_2O_3 in opx are positively correlated, contrary to how generally observed during partial melting (Jacques & Green, 1980). The Cr-loss moving from core to rim has been interpreted as a consequence of the development of symplectitic opx+sp intergrowths along opx-ol grain boundaries in presence of percolating melts (Seyler et al. 2007), or as a consequence of the transition from spinel to plagioclase stability field during mantle upwelling, which triggers Cr-spinel breakdown and thus Cr re-distribution among px and pl (Rampone et al., 1993). Such spinel-bearing symplectites, indeed, have been clearly recognized only in sample 39-36; however, petrographic observations of the studied samples suggest the spinel tiny grains, occurring in the poly-mineralic fine-grained aggregates, to likely represent hosts for Cr.

TiO_2<0.2 wt.% in spinel is considered as a typical signature of residual abyssal peridotites (Dick, 1989); higher TiO_2 contents in spinel usually found in plagioclase-bearing peridotites suggest TiO_2>0.2% wt. to be an indicator of melt-induced refertilization. On the other hand, interstitial melt-derived minerals does not record TiO_2 increase in spinel as well as LREEs increase in clinopyroxene. According to Seyler and co-authors (2001) the lack of Ti-enrichment in spinel and the lack of light rare earth elements re-enrichment in the primary clinopyroxene grains suggest that the composition of this liquid was not simply that of MORB but rather interstitial liquids represent incremental partial melts produced within the upper pressure range of the spinel stability field.

6.4 Trace elements and model

Reactive porous flow is able to change the behavior of trace elements during partial melting and upwelling towards the top of the mantle column under an oceanic ridge. First, the incoming exotic melt composition obviously plays a key role but, on the other hand, also the source composition is crucial. In fact, primary compositional heterogeneities are undoubtedly present in the MORB mantle source as shown by isotopic variability of MORBs and associated residual peridotites, even in ridge regions not influenced by hotspots (Salters & Dick, 2002; Cipriani et al. 2004; Graham et al., 2006; Hémond et al., 2006), thus the observed compositional variability of trace elements distribution are considered to be the product of both source-inherited and melting-induced heterogeneities.

In a general way decompressive mantle melting is always an open-system process in that the required porosity interconnection for melt extraction means open paths for melt to flow throughout the rock.
Many authors pointed out that highly incompatible elements are useful to assess late-stage processes, such as melt entrapment, melt-rock reactions and veining. Moderately incompatible trace elements are less affected by such late-stage processes and thus useful to infer the melting history of abyssal peridotites. From measured Sm/Yb vs Yb variations it is noteworthy that in all samples the rims of the crystals define a linear negative trend, thus REEs patterns and correlations measured in the clinopyroxene rims have been modeled according to the melting systems described in the previous paragraphs.

On the basis of trace elements patterns, the studied samples and those from Tartarotti et al. (2002) have been divided into three groups (§ 4.4).
Group1 (samples 32-07, 32-22 and 32-32) is characterized by near-flat MREE to HREE patterns with relative moderate depletion in LREE. Group2 (samples 39-27, 39-28 and 43-03) is characterized by near-flat HREE patterns, showing abundances similar to those of Group1, with relative strong depletion in LREE. Group1 and Group2 are also characterized by Ti and Zr enrichment. Group3 (sample 39-36 and 39-36TA) is characterized by strong trace elements depletion with respect to the other groups and by REE regular increasing from LREE to MREE to HREE.
From the results of modeling we can observe that samples 32-07 and 32-32 (Group1) underwent significant degrees of melting (14% and 12% respectively) and that they have interacted with melts with a garnet signature. The estimated extent of melting falls in the lower end of those estimated for the Mid-Ocean Ridge systematics that usually span from 15 to 25 % in thermally normal stretches of the oceanic ridges.
Interaction with garnet-derived melts is responsible for the relative MREE enrichment with respect to HREE resulting in Sm to Yb ratios >1. Relative HREE enrichment with respect to MREE recorded in sample 32-22, instead, can be explained by the interaction with garnet-free melts. Moreover, sample 32-22 might have experienced a very low degree of melting in the garnet stability field (1%), and the lowest total amount of melting (8%). This agrees with the high modal coarse-grained clinopyroxene (about 15% of total clinopyroxene from modal counting, chapter 2). Samples 32-07 and 32-32 experienced, instead, 4% of melting in the garnet stability field. Slightly higher total degree of melting (14%) inferred for sample 32-07 might be responsible for the lowest modal clinopyroxene (about 6.5% from modal counting). Sample 32-32 does not contain coarse-grained clinopyroxene; however, the high modal clinopyroxene (about 21% from modal counting) may be explained by a deep reactive impregnation in the spinel stability field resulting in the crystallization of a large amount of clinopyroxene. The critical mass porosity of the system for samples of Group1 is rather high (ϕ=0.004 for samples 32-07 and 32-32 and ϕ=0.005 for sample 32-22).
Sample 39-36 (Group 3) represents a peculiar case: the strongly depleted concentrations of trace elements, in fact, may derive from very high degrees of melting (18%), combined with melting steps of 2% and a very low melt retention (ϕ=0.001).

Finally, samples 39-27, 39-28 and 43-03 (Group 2) experienced melting and post-melting histories similar to those of samples 32-07 and 32-32, i.e. a total amount of melting of 14%, critical mass porosity equal to 0.004 and interaction with exotic melts with a garnet signature, except for a further depletion of the impregnating melts resulting in stronger La and Ce depletion and slightly lower Sm to Yb ratios.

In a general way, in all samples it comes to light that the rock source during upwelling has interacted with compositionally variable melts which became more depleted approaching the shallower levels of the mantle column. In fig. 6.4.1 we can observe that the first impregnating melt is still enriched enough to lead a fast increase in Yb and a variably Sm/Yb increase, depending on the melt genesis. Such melts also lead to a considerable La and Ce increasing. Afterwards, ultra-depleted melts are required to finally reproduce Sm/Yb vs Yb negative trends affecting the rims of the clinopyroxene and to drop down La concentrations.

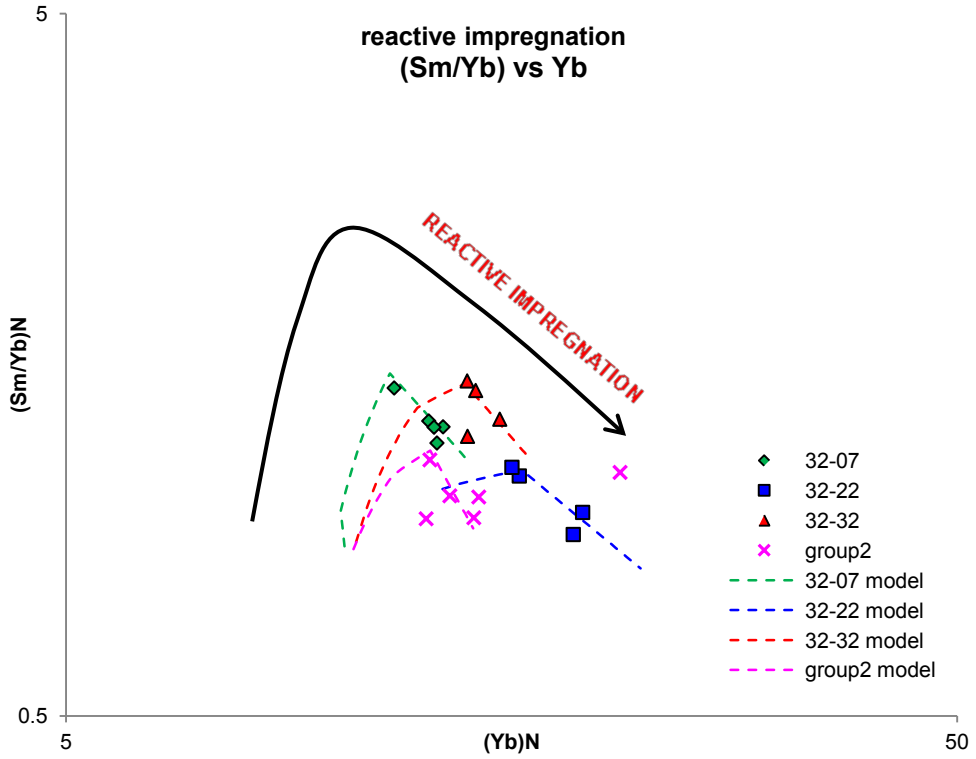

Fig. 6.4.1 - Modeled Sm/Yb vs Yb trends in clinopyroxene for the studied samples during reactive impregnation compared to measured values (rims). Values are normalized to C1 chondrite from Anders and Grevesse (1989).

By comparing measured compositions of Ti and Zr in the studied samples to the relative Ti-Zr modeling for reactive impregnation (fig 6.3.2), we can stress that, accordingly, samples show increasing trends, but measured compositions appear slightly depleted in titanium with respect to the predicted models. Sample 32-22 records the lowest values of Ti and the highest values of Zr, according to impregnation due to relatively enriched spinel-derived melts instead of garnet-derived melts (figs. 5.3.4 and 5.3.5, chapter 5). Samples of Group2 record the lowest concentrations in Zr according to strongly depleted impregnating melts. The

observed Ti-loss in the studied samples with respect to the predicted models (fig. 6.4.2) can be explained by the crystallization of tiny grains of spinel related to impregnation products, which have been widely attested by petrographic observations (chapter 2).

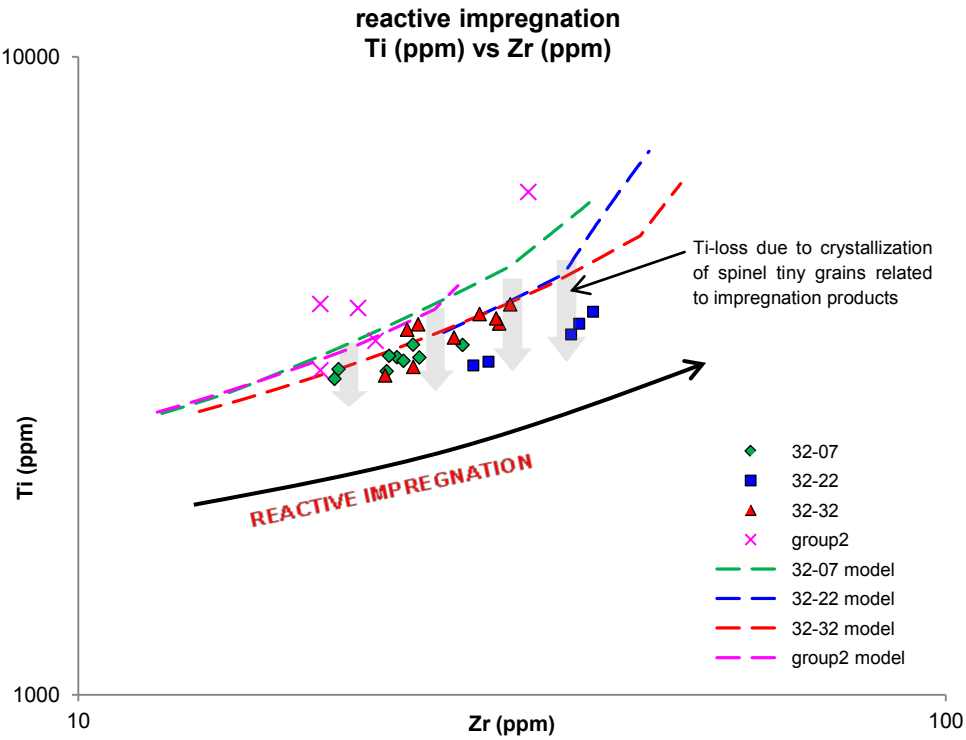

Fig. 6.4.2 - Modeled Ti-Zr variation in clinopyroxene for the studied samples during reactive impregnation compared to measured values (rims). Values are normalized to C1 chondrite from Anders and Grevesse (1989).

6.5 General discussion and conclusions

The scant and discontinuous basaltic coverage throughout the Romanche FZ indicates that melt extraction process is not efficient. Ligi et al. (2005) reported the presence in this region of water-rich basalts characterized by a garnet signature, i.e. Na-enrichment and high ratios of light versus heavy rare earth elements, and thus suggested these melts to derive from low degrees of "wet" melting greater than 60 km deep in the mantle, with minor dilution by melts produced by shallower "dry" melting. However, low degrees of partial melting (up to 10%) inferred for this region by previous works (§ 6.1) are not in agreement with modeling of trace elements patterns of the studied samples, which suggests moderate to significant degrees of partial melting also in the spinel stability field (from 7% to 10%). In this perspective we consider plagioclase-bearing peridotites to be the result of refertilization of previously depleted peridotites rather than pure residues after low degree of partial melting (Müntener et al. 2010; Dijkstra, et al. 2001). Such a deep reactive impregnation resulting in the high amount of newly crystallized plagioclase and clinopyroxene, in fact, will lead to as much deep re-enrichment in most incompatible elements; thus, a relatively depleted starting source is required to match the observed trace elements patterns.

Generally, compositions of basalts erupted in correspondence to mid-ocean ridges can be closely approximate by polybaric, near-fractional melting models (Johnson et al., 1990), i.e. MORBs represent aggregated melts that preserve evidence for partial melting of a mantle peridotite over a range of pressures. Geochemical disequilibrium between MORBs and residual harzburgite (Johnson et al., 1990) requires melt extraction from the adiabatically upwelling mantle to occurs by focused flow in dunite conduits rather than reactive porous flow throughout residual peridotite; however, small amounts of melt likely migrate by reactive porous flow around these conduits (Kelemen et al. 1997). Chemically isolated melt transport by focused flow in spatially restricted conduits versus diffuse, reactive porous flow beneath spreading ridges require different porosities governing the two systems. The non-extraction of the produced melts observed in the Romanche region can be therefore explained considering that a large amount of melt is held in the residual porosity of the rock during melting. This is what we can observe in model results for samples of Group1 and Group2, characterized by large critical mass porosity ranging from 0.004 to 0.005 and degrees of melting ranging from 8% to 14%. On the other hand, sample 39-36 (Group3) attests for high melting degree (18%) combined with very small amounts of retained melts (ϕ=0.001), suggesting efficient mechanisms of melt production and extraction, thus a scenario more similar to channeled melt transport rather than diffuse porous flow. Furthermore, modeling Romanche samples presented in the previous chapter reveals that the rock source during its melting and post-melting history has interacted with melt fractions derived from different degrees of melt aggregation and variable degrees of melting of a partially depleted peridotite, instead of with MORB-type melts. All model melt patterns are plotted in figure 6.5.1. It appears that mainly two type of melts percolate through the system: i) enriched melts relatively aggregated with strongly variable garnet fingerprint and ii) markedly depleted melts.

The first melt type, the enriched one, is necessary to obtain the right starting point before shallow percolative reaction starts, while the second kind of melts is strictly related to the crystallization of plagioclase in the late stages.

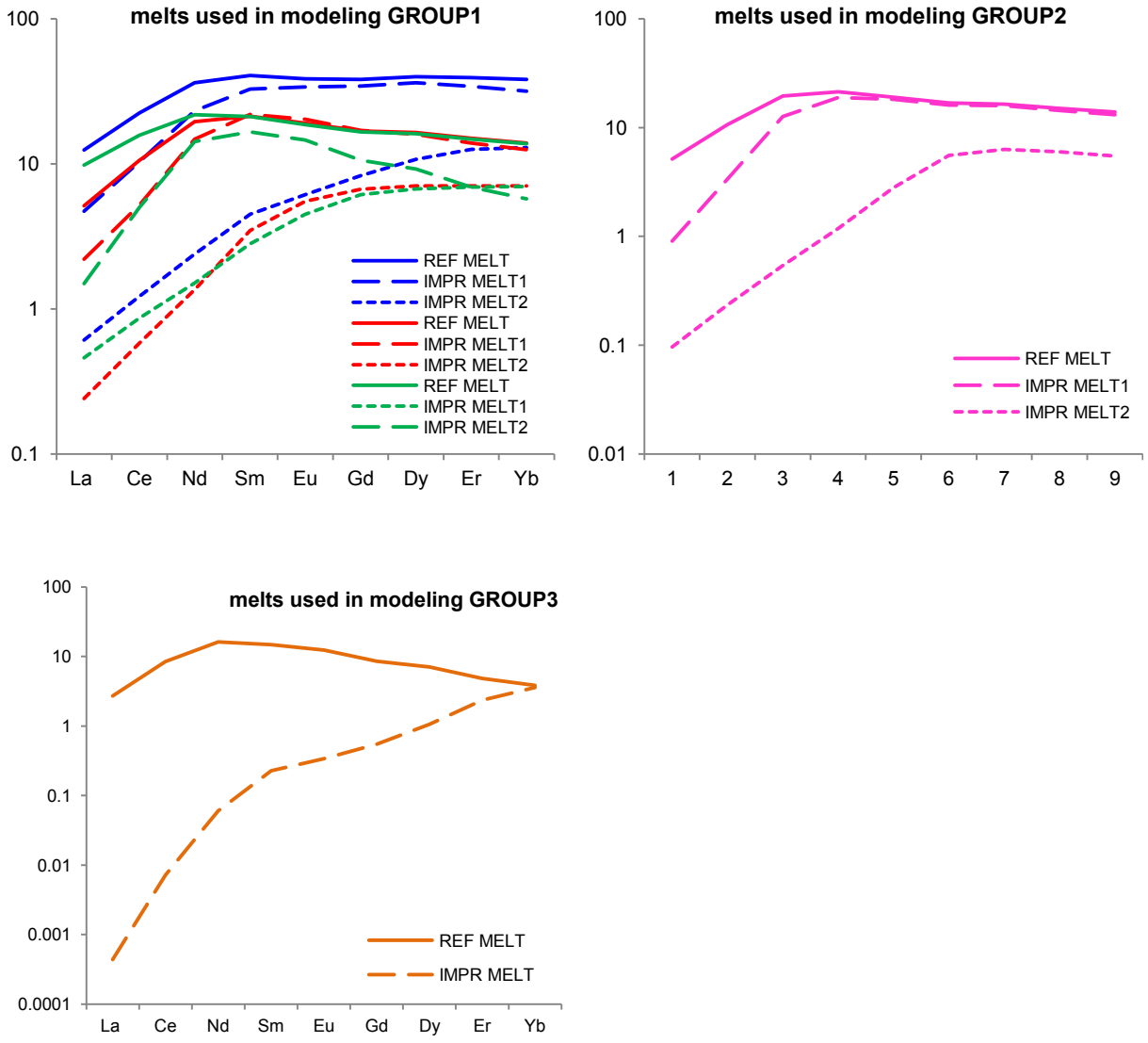

Fig 6.5.1 - REE patterns of melts used in modeling of samples of Group1 (sample 32-07, green lines; sample 32-22, blue lines; sample 32-32, red lines), samples of Group2 and sample of Group3.

Reactive impregnation, which deeply affects samples of Group1 and Group2, is hence the result of diffuse porous flow of percolating melts produced by fractional melting within the shallowest part of the melting column. Melting ceases as the mantle enters the conductive lithosphere and starts to cool below the peridotite solidus. At this point, a certain amount of melt (about 2% according to Seyler et al., 2001) might be present in the interstices of the rock, from which clinopyroxene and olivine start to crystallize. Melt supply by diffuse porous flow during upwelling proceeds beyond the thermal boundary layer: (cpx+ol) pockets continue to crystallize from the percolating melts until pressure is still relatively high (about 0.9 GPa, i.e. 35 km deep; Seyler et al., 2001), otherwise (plag+cpx) may crystallize. During this step the percolating melts

derive from the last fractions of partial melting, eventually mixed with deeper and more enriched melt which were able to migrate along the entire melting column (e.g. garnet-lherzolite-derived melts).
Further post-deformation percolation of ultra-depleted, more evolved melts leads to (plag+cpx) fractional crystallization. Percolating melts will exploit the residual porosity of the rock; higher-porosity zones are mainly due to pervasive grain-size reduction and lithospheric deformation structures, e.g. fractures, gashes, kink bands, micro-faults. Reactive impregnation may involve total amounts of impregnating melts up to 25%. Previous works (Kelemen at al., 1997; Djkistra et al., 2003) suggested ultra-depleted melts to percolate mantle at this stage, resembling those observed in glass inclusions within some olivine phenocrysts in MORBs (Sobolev & Shimizu 1993), i.e. low-pressure melt fractions from the melting column underneath a spreading center produced by shallow melting of refractory peridotites, unable to create their own high permeability melt channels.

The need of melting and refertilizing the source in order to obtain a “reasonable” starting point before plagioclase crystallization possibly represents the evidence for the reactive percolation process to be active starting from the spinel field when the system is fed by deep variably aggregated melts, and continuing into the plagioclase stability field where the system is fed by shallower less aggregated melts (fig. 6.5.1).
Moreover, the strong garnet fingerprint of some melts require short aggregation lengths to preserve the garnet-derived compositional character. Thus, early channeling of garnet-derived melt is required to transport these melt fractions to shallow levels. This in turn requires low regional temperatures to reduce the overall degree of melting, otherwise the large amount of melts produced in the spinel field will dilute and erase the garnet compositional fingerprint.

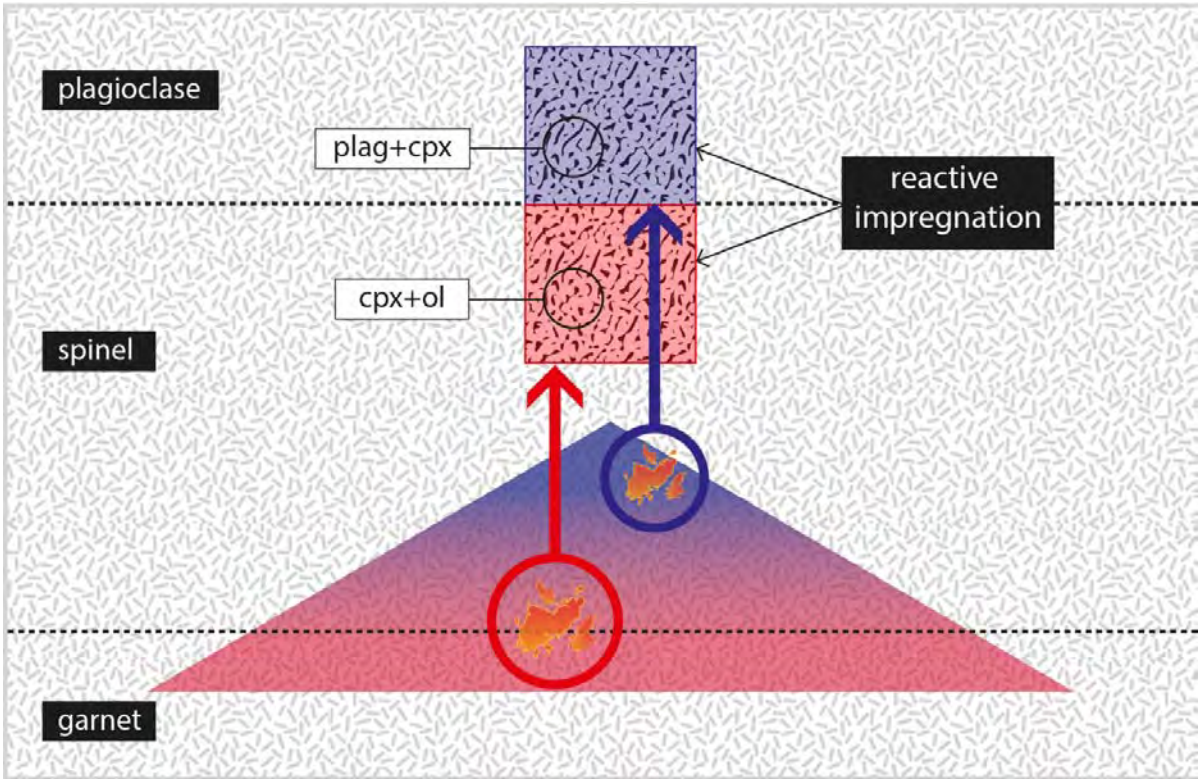

Fig 6.5.1 - Sketch of possible mechanisms of production, segregation and percolation of impregnating melts throughout mantle in correspondence to the Romanche FZ. Refertilization and crystallization from transient melts covers a wide range; however, trapped melts are more enriched and aggregated at depth (red arrows) whereas more depleted and less aggregated when reactive percolation occurs in the plagioclase stability field (blue arrows).

On the other hand, melt extraction must be efficient somewhere in the Romanche region (e.g. sample 39-36, group3), in which significant degrees of melting combined with very low melt retention and weak, nearly negligible post-melting reactive impregnation results in the extrusion at the seafloor of enriched basalts (E-MORBs) with a strong garnet-signature (Ligi et al., 2005). Modeling confirms sample 39-36 to have interacted with garnet-derived melts during its melting and post melting history. This can be an evidence for efficiently channelized melt extraction that early collects deep melts and re-distributes them partially into the rock. The presence of E-MORB erupted at the seafloor with significant garnet-fingerprint (Ligi et al., 2005) confirms that channelization of deep melt portions is strongly efficient in the region.

References

Aigner-Torres, Mario, Jon Blundy, Peter Ulmer, and Thomas Pettke. 2007. “Laser Ablation ICPMS Study of Trace Element Partitioning between Plagioclase and Basaltic Melts: An Experimental Approach.” Contributions to Mineralogy and Petrology 153 (6): 647–67. doi:10.1007/s00410-006-0168-2.

Albarède E., 1995. Introduction to Geochemical Modeling, Cambridge Univ. Press.

Anders, E. & Grevesse, N., 1998. Abundances of the elements: meteoritic and solar. Geochimica et Cosmochimica Acta 53, 197.

Aumento, F., Loubat, H., 1971. The Mid-Atlantic ridge near 45jN. XVI. Serpentinized ultramafic intrusions. Can. J. Earth Sci. 8, 631–663.

Blundy, J., Robinson, J. A. C. & Wood, B., 1998. Heavy REE are compatible in clinopyroxene on the spinel lherzolite solidus. Earth and Planetary Science Letters 160, 493–504.

Bohnenstiehl, D.R., Tolstoy, M., Smith,, D.K., Fox, C.G., 2000. Earthquake sequences detected using autonomous underwater hydrophones. Data from the northern Mid-Atlantic Ridge: February 1999–February 2000. Eos Trans. Am. Geophys. Union 81, p. 1077.

Bonatti, E., Honnorez, J., 1976. Sections of the Earth’s crust in the equatorial Atlantic. J. Geophys. Res. 81, 4104–4116.

Bonatti, E., Chermak, A., 1981. Formerly emerging crustal blocks in the equatorial Atlantic. Tectonophysics 72, 165–180.

Bonatti, E., Crane, K., 1982. Oscillatory spreading explanation of anomalously old uplifted crust near oceanic transforms. Nature 300, 343-345.

Bonatti, E., Raznitsin, Y., Bertoluzzi, G., Boudillon, F., De Alteriis,G., Gasperini, L., Gasperini, M., Giaquinto, G., Ligi, M., Lodolo, E., Mazarovich, A., Peyve, A., Sacchi, M., Skolotnev, S., Trofimov,

V., Turko, N., Zacharov, M., Auzende, J.M., Mamaloukas-Frangoulis, V., Searle, S., 1991. Geological studies of the eastern part of the Romanche transform (equatorial Atlantic): a first report. G. Geol. 53/2, 31–48.

Bonatti, E., Seyler, M., Sushevskaya, N., 1993. A Cold Suboceanic Mantle Belt at the Earth's Equator. Science 261, 315–320.

Bonatti, E., Ligi, M., Gasperini, L., Peyve, A., Raznitsin, Y., Chen, Y.J., 1994. Transform migration and vertical tectonics at the Romanche fracture zone, equatorial Atlantic. J. Geophys. Res. Solid Earth 99, 21779–21802.

Bonatti, E., Ligi, M., Borsetti, A.M., Gasperini, L., Negri, A., Sartori, R., 1996a. Lower Cretaceous deposits trapped near the equatorial Mid-Atlantic Ridge. Nature 380, 518–520.

Bonatti E., Ligi M., Carrara G., Gasperini L., Turko N., Perfiliev N., Peyve A., Sciuto P.F., 1996b. Diffuse impact of the Mid-Atlantic Ridge with the Romanche transform: An ultracold ridge-transform intersection. J. Geophys. Res. 101, 8043–8054.

Bonatti, E., Brunelli, D., Fabretti, P., Ligi, M., Asunta Portaro, R., Seyler, M., 2001. Steady-state creation of crust-free lithosphere at cold spots in mid-ocean ridges. Geology 29, 979.

Brunelli, D., Seyler, M, Cipriani, A., Ottolini, L., Bonatti, E. 2006. "Discontinuous Melt Extraction and Weak Refertilization of Mantle Peridotites at the Vema Lithospheric Section (Mid-Atlantic Ridge)." Journal of Petrology, 47 (4): 745–71. doi:10.1093/petrology/egi092.

Brunelli, D., Paganelli, E., Seyler, M.,. 2014. "Percolation of Enriched Melts during Incremental Open-System Melting in the Spinel Field: A REE Approach to Abyssal Peridotites from the Southwest Indian Ridge." Geochimica et Cosmochimica Acta,127 (February): 190–203. doi:10.1016/j.gca.2013.11.040.

Bryan, W.B., Dick, H.J.B., 1982. Contrasted abyssal basalt liquidus trends: evidence for mantle major element heterogenity. Earth Planet. Sci. Lett. 58, 15-26.

Cande, S.C., LaBrecque, J.L., Haxby, W.F., 1988. Plate Kinematics of the South Atlantic: Chron C34 to Present. J. Geophys. Res. Solid Earth 93, 13479–13492.

Cannat, M., Chatin, F., Whitechurch, H. & Ceuleneer, G. (1997). Gabbroic rocks trapped in the upper mantle at the Mid-Atlantic Ridge. In: Karson, J. A., Cannat, M., Miller, D. J. & Elthon, D. (eds) Ocean Drilling Program, Scientific Results, 153. College Station,

Ceuleneer, G., Nicolas, A. & Boudier, F., 1988. Mantle flow patterns at an oceanic spreading centre: the Oman peridotites record. Tectonophysics 151, 1-26.

Ceuleneer, G. and Cannat, M., 1997. High-temperature ductile deformation of Site 920 peridotites. In: Karson, J. A., Cannat, M.m Miller, D. J.. & Elthon, D. (eds) Proceedings of the Ocean Drilling Program, Scientific Results. 153, College Station, TX: Ocean Drilling Program, 23-24.

Cipriani, A., Brueckner, H.K., Bonatti, E., Brunelli, D. 2004. "Oceanic Crust Generated by Elusive Parents: Sr and Nd Isotopes in Basalt-Peridotite Pairs from the Mid-Atlantic Ridge." Geology 32 (8): 657–60. doi:10.1130/G20560.1.

Dick, H.J.B., 1989. Abyssal peridotites, very slow spreading ridges and oceanic ridge magmatism. In: Saunedrs, A.D., Morris, M.J. (Eds.), Magmatism in the Ocean Basins. Spec. Publ. -Geol. Soc. London, vol. 42, pp. 71-105.

Dick, H.J.B., Lissenberg, C.J., Warren, J.M., 2010. Mantle Melting, Melt Transport, and Delivery Beneath a Slow-Spreading Ridge: The Paleo-MAR from 23°15′N to 23°45′N. J. Petrol. 51, 425–467. doi:10.1093/petrology/egp088

Dijkstra, A.H., Drury, M.R., Vissers, R.L.M., 2001. Structural Petrology of Plagioclase Peridotites in the West Othris Mountains (Greece): Melt Impregnation in Mantle Lithosphere. J. Petrol. 42, 5–24. doi:10.1093/petrology/42.1.5

Dijkstra, Arjan H., Matthias G. Barth, Martyn R. Drury, Paul R. D. Mason, and Reinoud L. M. Vissers. 2003. "Diffuse Porous Melt Flow and Melt-Rock Reaction in the Mantle Lithosphere at a Slow-Spreading Ridge: A Structural Petrology and LA-ICP-MS Study of the Othris Peridotite Massif (Greece)." Geochemistry, Geophysics, Geosystems 4 (8): 8613. doi:10.1029/2001GC000278.

Drouin, M., Godard, M., Ildefonse, B., Bruguier, O., and Garrido, C.J. 2009. "Geochemical and Petrographic Evidence for Magmatic Impregnation in the Oceanic Lithosphere at Atlantis Massif, Mid-Atlantic Ridge (IODP Hole U1309D, 30°N)." Chemical Geology 264 (1–4): 71–88. doi:10.1016/j.chemgeo.2009.02.013.

Elthon, Don. 1992. "Chemical Trends in Abyssal Peridotites: Refertilization of Depleted Suboceanic Mantle." Journal of Geophysical Research: Solid Earth 97 (B6): 9015–25. doi:10.1029/92JB00723.

England, P.C., Houseman, G.A., Sonder, L.J., 1985. Length scales for continental deformation in convergent, divergent and strike-slip environments: Analogical and approximate solutions for a thin viscous sheet model. J. Geophys. Res. 90, 3551–3557.

Forsyth, D.W., Wilson, B., 1984. Three-dimensional temperature structure of a ridge-transform-ridge system. Earth Planet. Sci. Lett. 70, 355–362.

Forsyth, D.W., Bechtel, T.D., Stewart, L.M., 1986. Rupture of separate en-echelon segments of an oceanic transform fault in a single earthquake. Eos Trans. Am. Geophys. Union 67, 359.

Fox, P.J., Gallo, D.G., 1984. A tectonic model for ridge-transform-ridge plate boundaries: Implications for the structure of oceanic lithosphere. Tectonophysics 104, 205–242.

Gasperini, L., Bonatti, E., Brunelli, D., Carrara, G., Cipriani, A., Fabretti, P., Gilod, D., Ligi, M., Peyve, A., Skolotnev, S., Susini, S., Tartarotti, P., Turko, N., 1997a. New data on the geology of the Romanche FZ, equatorial Atlantic: PRIMAR-96 cruise report. G. Geol. 59, 3 –18.

Gasperini, L., Bonatti, E., Ligi, M., Sartori, R., Borsetti, A., Negri, A., Ferrari, A., Sokolov, S., 1997b. Stratigraphic numerical modelling of a carbonate platform on the Romanche transverse ridge, equatorial Atlantic. Mar. Geol. 136, 245–257.

Gasperini, L., Bernoulli, D., Bonatti, E., Borsetti, A.M., Ligi, M., Negri, A., Sartori, R., von Salis, K., 2001. Lower Cretaceous to Eocene sedimentary transverse ridge at the Romanche Fracture Zone and the opening of the equatorial Atlantic. Mar. Geol. 176, 101–119.

Gast, Paul W. 1968. “Trace Element Fractionation and the Origin of Tholeiitic and Alkaline Magma Types.” Geochimica et Cosmochimica Acta 32 (10): 1057–86. doi:10.1016/0016-7037(68)90108-7.

Graham, D. W., J. Blichert-Toft, C. J. Russo, K. H. Rubin, and F. Albarède. 2006. “Cryptic Striations in the Upper Mantle Revealed by Hafnium Isotopes in Southeast Indian Ridge Basalts.” Nature 440 (7081): 199–202. doi:10.1038/nature04582.

Gorini, M.A., 1977. The tectonic fabric of the equatorial Atlantic and adjoining continental margins: Gulf of Guinea to northeastern Brazil. PhD thesis, Columbia Univ., New York, 116 p.

Hellebrand, E., Snow, J.E., Hoppe, P., Hofmann, A.W. 2002. “Garnet-Field Melting and Late-Stage Refertilization in ‘Residual’ Abyssal Peridotites from the Central Indian Ridge.” Journal of Petrology 43 (12): 2305–38. doi:10.1093/petrology/43.12.2305.

He`mond C., Hofmann A. W., Heusser G., Condomines M., Raczek I., and Rhodes J. M., 1994. U-Th-Ra systematics in Kilauea and Mauna Loa basalts, Hawaii. Chem. Geol. 116, 163–180.

Hémond, C., Hofmann, A.W., Vlastélic, I., Nauret, F. 2006. “Origin of MORB Enrichment and Relative Trace Element Compatibilities along the Mid-Atlantic Ridge between 10° and 24°N.” Geochemistry, Geophysics, Geosystems 7 (12): Q12010. doi:10.1029/2006GC001317.

Honnorez, J., Mascle, J., Basile, C., Tricart, P., Villeneuve, M., Bertrand, H., 1991. Mapping of a segment of the Romanche Fracture Zone: A morphostructural analysis of a major transform fault of the equatorial Atlantic Ocean. Geology 19, 795.

Ildefonse, B., F. Boudier, and A. Nicolas, 1998a .Asthenospheric deformation in ophiolitic peridotite, in Fault-Related Rocks: A Photographic Atlas, edited by A. W. Snoke, J. Tullis, and V. R. Todd, pp. 588–589, Princeton Univ. Press, Princeton, N. J.

Ildefonse, B., F. Boudier, and A. Nicolas, 1998b. Lithospheric deformation in ophiolitic peridotite, in Fault-Related Rocks: A Photographic Atlas, edited by A. W. Snoke, J. Tullis, and V. R. Todd, pp. 590–591, Princeton Univ. Press, Princeton, N. J.

Jacques, A.L., Green D.H., 1980. Anhydrous melting of peridotite at 0–15 kb pressure and the genesis of tholeiitic basalts. Contrib Mineral Petrol 73:287–310

Johnson, K.T. M., Dick, H. J. B, Shimizu, N., 1990. "Melting in the Oceanic Upper Mantle: An Ion Microprobe Study of Diopsides in Abyssal Peridotites." Journal of Geophysical Research: Solid Earth 95 (B3): 2661–78. doi:10.1029/JB095iB03p02661.

Johnson, K. T. M. & Dick, H. J. B., 1992. Open system melting and spatial variation of peridotite and basalt at the Atlantis II Fracture Zone. Journal of Geophysical Research 97, 9219–9241.

Johnson, K. T. M. 1998. "Experimental Determination of Partition Coefficients for Rare Earth and High-Field-Strength Elements between Clinopyroxene, Garnet, and Basaltic Melt at High Pressures." Contributions to Mineralogy and Petrology 133 (1-2): 60–68. doi:10.1007/s004100050437.

Kelemen, P.B. 1990. Reaction between ultramafic rock and fractionating basaltic magma, I. Phase relations, the origin of calc-alkaline magma series, and the formation of discordant dunite. J Petrol 31:51–98

Kelemen, P.B., Shimizu, N., Salters, V.J.M .1995a. Extraction of midocean-ridge basalt from the upwelling mantle by focused flow of melt in dunite channels. Nature 375:747–753.

Kelemen, P.B., Whitehead, J.A., Aharonov, E., Jordahl, K.A., 1995b. Experiments on flow focusing in soluble porous media, with applications to melt extraction from the mantle. J Geophys Res 100:475–496.

Kelemen, P. B., Hirth, G., Shimizu, N., Spiegelman, M., Dick, H. J. B., 1997. "A Review of Melt Migration Processes in the Adiabatically Upwelling Mantle beneath Oceanic Spreading Ridges." Philosophical Transactions of the Royal Society of London. Series A: Mathematical, Physical and Engineering Sciences 355 (1723): 283–318. doi:10.1098/rsta.1997.0010.

Kinzler, R.J., Grove, T.L., 1992. Primary magmas of mid-ocean ridge basalts, 2. Applications J Geophys Res 97:6907–6926.

Kinzler, R. J., 1997. "Melting of Mantle Peridotite at Pressures Approaching the Spinel to Garnet Transition: Application to Mid-Ocean Ridge Basalt Petrogenesis." Journal of Geophysical Research: Solid Earth 102 (B1): 853–74. doi:10.1029/96JB00988.

Langmuir C.H., Bender J.F., Bence A.E., Hanson G.N., Taylor S.R., 1977. Petrogenesis of basalts from the FAMOUS area: Mid-Atlantic Ridge, Earth and Planetary Science Letters, Volume 36, Issue 1, 133-156.

Langmuir C. H., Klein E. M., and Plank T., 1992. Petrological systematics of mid-ocean ridge basalts: Constraints on melt generation beneath ocean ridges. In Mantle Flow and Melt Generation at Mid-ocean Ridges (ed. J. Phipps Morgan et al.), 183–280. AGU.

Liang, Yan. 2008. "Simple Models for Dynamic Melting in an Upwelling Heterogeneous Mantle Column: Analytical Solutions." Geochimica et Cosmochimica Acta 72 (15): 3804–21. doi:10.1016/j.gca.2008.05.050.

Ligi, M., Bonatti, E., Gasperini, L., Poliakov, A.N.B., 2002. Oceanic broad multifault transform plate boundaries. Geology 30, 11.

Ligi, M., Bonatti, E., Cipriani,A., Ottolini, L. 2005. "Water-Rich Basalts at Mid-Ocean-Ridge Cold Spots." Nature 434 (7029): 66–69. doi:10.1038/nature03264.

Lundstrom, C. C, J Gill, and Q Williams. 2000. "A Geochemically Consistent Hypothesis for MORB Generation." Chemical Geology 162 (2): 105–26. doi:10.1016/S0009-2541(99)00122-9.

McGuire, J.J., Ihmle, P.F., Jordan, T.H., 1996. Time-Domain Observations of a Slow Precursor to the 1994 Romanche Transform Earthquake. Science 274, 82–85.

Mckenzie, D., 1985. The generation and compaction of partially molten rock, Journal of Petrology, 25(3), 713-65 CODEN: JPTGAD; ISSN: 0022-3530.

Michael, P.J., Bonatti, E., 1985. Peridotite composition from the north Atlantic: Regional and tectonic variations and implications for partial melting, Earth and Planetary Science Letters, 73, 91–104.

Monti, S., Mecier, H., 1991. Carte bathymetrique de la zone de fracture de la Romanche (1/1.000.000, Seabeam EM12). Brest: IFREMER DRO/GM, Cartographie.

Morgan, J.P., Forsyth, D.W., 1988. Three-dimensional flow and temperature perturbations due to a transform offset: Effects on oceanic crustal and upper mantle structure. J. Geophys. Res. Solid Earth 93, 2955–2966.

Müntener, Othmar, Gianreto Manatschal, Laurent Desmurs, and Thomas Pettke. 2010. "Plagioclase Peridotites in Ocean–Continent Transitions: Refertilized Mantle Domains Generated by Melt Stagnation in the Shallow Mantle Lithosphere." Journal of Petrology 51 (1-2): 255–94. doi:10.1093/petrology/egp087.

Nicolas, A., 1986. A melt extraction model based on structural studies in mantle peridotites. J. Petrol. 27, 999–1022.

Niu, Y., 1997. Mantle Melting and Melt Extraction Processes beneath Ocean Ridges: Evidence from Abyssal Peridotites. Journal of Petrology, 38, 1047–1074.

Niu, Y., He´kinian, R., 1997. Spreading-rate dependence of the extent of mantle melting beneath ocean ridges, Nature, 385, 320–326.

Nürnberg, D., Müller, R.D., 1991. The tectonic evolution of the South Atlantic from Late Jurassic to present. Tectonophysics 191, 27–53.

Ozawa, K., Shimizu, N. 1995. "Open-System Melting in the Upper Mantle: Constraints from the Hayachine-Miyamori Ophiolite, Northeastern Japan." Journal of Geophysical Research: Solid Earth 100 (B11): 22315–35. doi:10.1029/95JB01967.

Parsons, B., Sclater, J.G., 1977. An analysis of the variation of ocean floor bathymetry and heat flow with age. J. Geophys. Res. 82, 803-827.

Piccardo, G. B., A. Zanetti, and O. Müntener. 2007. "Melt/peridotite Interaction in the Southern Lanzo Peridotite: Field, Textural and Geochemical Evidence." Lithos 94 (1–4). Melting, Metasomatism and Metamorphic Evolution in the Lithospheric Mantle Symposium Held at the 32nd International Geological Congress: 181–209. doi:10.1016/j.lithos.2006.07.002.

Prichard, H.M., 1979. A petrographic study of the process of serpentinization in ophiolites and ocean crust. Contrib. Mineral. Petrol. 68, 231– 241.

Rabinowitz, P.D., LaBrecque, J., 1979. The Mesozoic South Atlantic Ocean and evolution of its continental margins. J. Geophys. Res. Solid Earth 84, 5973–6002.

Rampone, E., Piccardo, G. B., Vannucci, R., Bottazzi, P., Ottolini, L. 1993. "Subsolidus Reactions Monitored by Trace Element Partitioning: The Spinel- to Plagioclase-Facies Transition in Mantle Peridotites." Contributions to Mineralogy and Petrology 115 (1): 1–17. doi:10.1007/BF00712974.

Rampone, E., Piccardo, G.B., Hofmann, A.W. 2008. "Multi-Stage Melt–rock Interaction in the Mt. Maggiore (Corsica, France) Ophiolitic Peridotites: Microstructural and Geochemical Evidence." Contributions to Mineralogy and Petrology 156 (4): 453–75. doi:10.1007/s00410-008-0296-y.

Renna, Maria Rosaria, and Riccardo Tribuzio. 2011. "Olivine-Rich Troctolites from Ligurian Ophiolites (Italy): Evidence for Impregnation of Replacive Mantle Conduits by MORB-Type Melts." Journal of Petrology 52 (9): 1763–90. doi:10.1093/petrology/egr029.

Richter, F.M., McKenzie, D., 1984. Dynamical models for melt segregation from a deformable matrix. The Journal of Petrology, Vol. 92, No 6, 729-740.

Ribe N. M., 1988. Dynamical geochemistry of the Hawaiian plume. Earth Planet. Sci. Lett. 88, 37–46.

Salters, Vincent J. M., and Henry J. B. Dick. 2002. "Mineralogy of the Mid-Ocean-Ridge Basalt Source from Neodymium Isotopic Composition of Abyssal Peridotites." Nature 418 (6893): 68–72. doi:10.1038/nature00798.

Sanfilippo, A., Tribuzio, R. 2013. Origin of olivine-rich troctolites from the oceanic lithosphere: a comparison between the Alpine Jurassic ophiolites and modern slow spreading ridges. Ofioliti, 38 (1), 89-99 - doi: 10.4454/ofioliti.v38i1.418 89.

Sanfilippo, Alessio, Henry J. B. Dick, and Yasuhiko Ohara. 2013. "Melt–Rock Reaction in the Mantle: Mantle Troctolites from the Parece Vela Ancient Back-Arc Spreading Center." Journal of Petrology 54 (5): 861–85. doi:10.1093/petrology/egs089.

Schilling, J.-G., Ruppel, C., Davis, A.N., McCully, B., Tighe, S.A., Kingsley, R.H., Lin, J., 1995. Thermal structure of the mantle beneath the equatorial Mid-Atlantic Ridge: Inferences from the spatial variation of dredged basalt glass compositions. J. Geophys. Res. 100, 10057.

Schilling, J.G. AND Winchester, J.W., 1967. Rare-earth fractionation and magmatic processes. In: Runcorn, F.R.S.S.K., Editor, , 1967. Mantles of Earth and Terrestrial Planets, Interscience, 267–283.

Searle, R.C., 1981. The active part of the Charlie-Gibbs fracture zone: a study using sonar and other geophysical techniques. J. Geophys. Res. 86, 243–262.

Searle, R.C., Thomas, M.V., Jones, E.J.W., 1994. Morphology and tectonics of the Romanche Transform and its environs. Mar. Geophys. Res. 16, 427–453.

Seyler, M. & Bonatti, E. 1997. “Regional-Scale Melt-Rock Interaction in Lherzolitic Mantle in the Romanche Fracture Zone (Atlantic Ocean).” Earth and Planetary Science Letters 146 (1–2): 273–87. doi:10.1016/S0012-821X(96)00220-8.

Seyler, M., Toplis, M.J., Lorand, J-P, Luguet, A., Cannat, M. 2001. “Clinopyroxene Microtextures Reveal Incompletely Extracted Melts in Abyssal Peridotites.” Geology 29 (2): 155–58. doi:10.1130/0091-7613(2001)029<0155:CMRIEM>2.0.CO;2.

Seyler M., Cannat M., Mével, C., 2003. Evidence for major element heterogeneity in the mantle source of abyssal peridotites from the Southwest Indian Ridge (52° to 68°E).Geochem Geophys Geosyst. DOI: 10.1029/2002GC000305.

Seyler, M., Lorand, J.-P., Dick, H. J. B., Drouin, M. 2007. “Pervasive Melt Percolation Reactions in Ultra-Depleted Refractory Harzburgites at the Mid-Atlantic Ridge, 15° 20′N: ODP Hole 1274A.” Contributions to Mineralogy and Petrology 153 (3): 303–19. doi:10.1007/s00410-006-0148-6.

Seyler, M., Brunelli, D., Toplis, M.J., and Mével, C. 2011. “Multiscale Chemical Heterogeneities beneath the Eastern Southwest Indian Ridge (52°E–68°E): Trace Element Compositions of along-Axis Dredged Peridotites.” Geochemistry, Geophysics, Geosystems 12 (9).

Shaw, D. M., 1970. “Trace Element Fractionation during Anatexis.” Geochimica et Cosmochimica Acta 34 (2): 237–43. doi:10.1016/0016-7037(70)90009-8.

Shaw, D. M. 2000. “Continuous (dynamic) Melting Theory Revisited.” The Canadian Mineralogist 38 (5): 1041–63. doi:10.2113/gscanmin.38.5.1041.

Sobolev, A. V., Shimizu, N., 1993. Ultra-depleted primary melt included in an olivine from the Mid-Atlantic Ridge, Nature, 363, 151–154. Q0AC15. doi:10.1029/2011GC003585.

Spiegelman M., Elliott, T., 1993. Consequences of melt transport for uranium series disequilibrium in young lavas. Earth Planet. Sci. Lett. 118, 1–20.

Suhr, G., Seck, H. A., Shimizu, N., Gu¨nther, D. & Jenner, G., 1998. Infiltration of refractory melts into the lowermost oceanic crust: evidence from dunite- and gabbro-hosted clinopyroxenes in the Bay of Islands Ophiolite. Contributions to Mineralogy and Petrology, 131, 136–154.

Suhr G., Hellebrand E., Johnson K. and Brunelli D., 2008. Stacked gabbro units and intervening mantle: A detailed look at a section of IODP Leg 305, Hole U1309D. Geochem. Geophys. Geosyst., 9, Q10007, doi:101029/2008GC002012.

Tartarotti, P., Cannat, M., Mevel, C., 1995. Gabbroic dikelets in serpentinized peridotites from the Mid-Atlantic ridge at 23j20VN. In: Vissers, R.L.M., Nicolas, A. (Eds.), Mantle and Lower Crust Exposed in Oceanic Ridges and in Ophiolites. Kluwer Academic Publishing, Dordrecht, pp. 35– 69.

Tartarotti, P., Susini, S., Nimis, P., Ottolini, L. 2002. "Melt Migration in the Upper Mantle along the Romanche Fracture Zone (Equatorial Atlantic)." Lithos 63 (3–4): 125–49. doi:10.1016/S0024-4937(02)00116-0.

Walter, M.J. 1998. "Melting of Garnet Peridotite and the Origin of Komatiite and Depleted Lithosphere." Journal of Petrology 39 (1): 29–60. doi:10.1093/petroj/39.1.29.

Williams R. W., Gill, J. B., 1989. Effect of partial melting on the uranium decay series. Geochim. Cosmochim. Acta 53, 1607–1619.

Wilson, J.T., 1965. A new class of faults and their bearing on continental drift. Nature 207, 343–347.

Workman, Rhea K., and Stanley R. Hart. 2005. "Major and Trace Element Composition of the Depleted MORB Mantle (DMM)." Earth and Planetary Science Letters 231 (1–2): 53–72. doi:10.1016/j.epsl.2004.12.005.

Zou, H., Zindler, A., 1996. Constraints on the degree of dynamic partial melting and source composition using concentration ratios in magma. Geochim. Cosmochim. Acta, 60, 711–717.

Zou, H., 1998. "Trace Element Fractionation during Modal and Nonmodal Dynamic Melting and Open-System Melting: A Mathematical Treatment." Geochimica et Cosmochimica Acta 62 (11): 1937–45. doi:10.1016/S0016-7037(98)00115-X.

Appendix A

Major elements analysis

Major elements contents (% wt.) of Romanche FZ minerals

Olivine

sample 39-36	SiO2	TiO2	Al2O3	Cr2O3	FeO	MnO	NiO	MgO	CaO	Na2O
Z36C0101m	41.08	0	0	0	9.2	0.07	0.36	48.75	0.06	0
Z36C0103m	40.83	0.02	0.01	0	9.12	0.13	0.4	49.15	0.03	0
Z36C0104m	40.68	0	0	0	9.2	0.13	0.41	48.7	0.05	0
Z36C0105m	40.83	0.03	0.02	0.04	8.83	0.15	0.38	48.99	0.02	0
Z36C0106m	40.88	0	0.03	0.01	9.23	0.2	0.38	48.88	0.05	0
Z36C0107m	41.04	0	0.02	0	8.97	0.19	0.37	49.11	0.05	0
Z36C0108m	40.83	0	0.03	0	9.04	0.17	0.52	49.47	0.03	0.03
Z36C0109m	40.52	0.04	0.01	0	9.25	0.11	0.36	48.82	0.03	0
Z36C0110m	40.89	0	0	0.01	9.08	0.12	0.45	48.79	0.05	0
Z36C0111m	40.88	0	0	0.03	9.02	0.15	0.37	49.15	0.04	0
Z36C0112m	40.8	0	0	0	9.09	0.17	0.31	48.7	0.03	0.01
Z36C0201m	40.5	0.07	0.02	0.05	8.94	0.09	0.36	48.94	0.05	0.02
Z36C0205m	40.54	0	0	0.05	9.19	0.24	0.42	49.5	0.03	0.02
Z36C0206m	40.8	0	0	0	8.99	0.11	0.35	49.11	0.08	0.03
Z36C0403m	40.53	0	0.03	0	8.88	0.12	0.39	49.04	0.04	0
Z36C0504m	40.79	0	0.01	0	9.18	0.12	0.43	49.04	0.04	0.01
Z36C0505m	40.83	0	0	0	9	0.16	0.36	48.61	0.06	0
Z36C0506m	40.66	0	0	0.01	9.1	0.19	0.32	48.65	0.06	0
Z36C0701m	40.75	0	0	0.04	8.93	0.1	0.4	48.94	0.02	0.01
Z36C0702m	41.11	0	0	0	9.02	0.16	0.44	48.9	0.03	0.02
Z36C1103m	40.92	0.01	0	0	8.86	0.12	0.37	48.77	0.08	0.03
Z36C1403m	40.73	0.04	0	0	9.17	0.18	0.43	48.79	0.02	0.01
Z36C1404m	41.06	0.06	0	0	9.2	0.16	0.43	49.04	0.04	0.01
Z36C1405m	40.7	0	0	0	9.2	0.11	0.36	48.86	0.02	0.02
Z36C1406m	40.87	0	0	0	9.26	0.14	0.38	48.68	0.04	0
Z36C1407m	41.04	0.01	0.01	0.05	9.14	0.19	0.32	48.62	0.03	0.02
Z36C0604g	40.76	0	0	0.07	8.8	0.12	0.45	48.98	0.01	0
Z36C0608g	40.62	0	0	0	9.13	0.1	0.4	48.55	0.01	0.02
Z36C0902g	40.79	0.01	0.03	0.02	9.09	0.14	0.33	49.09	0.04	0
Z36C0903g	40.45	0.04	0	0.08	9.04	0.08	0.36	48.86	0.02	0.04
sample 32-22	**SiO2**	**TiO2**	**Al2O3**	**Cr2O3**	**FeO**	**MnO**	**NiO**	**MgO**	**CaO**	**Na2O**
Y22C1401m	40.68	0	0.01	0	9.8	0.14	0.38	48.47	0.07	0.01
Y22C1402m	40.52	0.01	0	0.01	9.66	0.22	0.33	48.2	0.04	0.02
Y22C1403m	40.47	0	0	0	9.67	0.15	0.39	48.12	0.03	0.01

Y22C1801m	40.43	0	0	0	9.73	0.19	0.4	48.43	0.07	0.01
Y22C1802m	40.19	0.03	0	0	9.76	0.15	0.3	48.42	0.06	0.03
Y22C1803m	40.19	0	0	0	9.66	0.17	0.48	48.38	0.05	0
Y22C1804m	40.47	0.04	0	0.05	9.7	0.17	0.4	48.52	0.03	0.02
Y22C1805m	40.57	0.03	0.01	0	9.69	0.14	0.39	48.43	0.04	0.02
Y22C1806m	40.42	0	0	0	9.8	0.12	0.4	47.82	0.03	0
Y22C1807m	40.7	0	0.02	0.01	9.75	0.18	0.38	47.73	0.04	0
Y22C0210g	40.6	0.03	0.04	0	9.47	0.12	0.33	47.84	0.03	0.01
Y22C0211g	40.69	0.05	0.05	0.04	9.41	0.11	0.36	48.26	0.04	0
Y22C0312g	40.2	0.01	0	0.01	9.71	0.16	0.43	48.03	0.01	0
Y22C0313g	40.54	0.03	0.02	0	9.38	0.12	0.35	48.36	0.05	0.02
Y22C0315g	40.58	0	0.02	0.06	9.68	0.16	0.41	48.14	0.04	0
Y22C0714g	41	0	0.02	0.03	9.46	0.12	0.39	48.08	0.03	0.04
Y22C0715g	40.8	0.02	0	0	9.49	0.12	0.24	48.07	0	0
Y22C0716g	40.6	0.01	0.03	0.02	9.39	0.12	0.36	47.9	0	0
Y22C0801g	40.52	0.01	0.03	0.01	9.65	0.2	0.47	48.31	0.02	0.01
Y22C0804g	40.98	0.01	0.02	0	9.73	0.13	0.3	47.69	0.03	0
Y22C1904g	40.69	0.01	0.01	0.02	9.87	0.14	0.37	47.98	0.05	0.01
Y22C1905g	40.66	0.02	0.02	0	9.91	0.15	0.36	47.74	0.05	0
sample 32-32	**SiO2**	**TiO2**	**Al2O3**	**Cr2O3**	**FeO**	**MnO**	**NiO**	**MgO**	**CaO**	**Na2O**
Y32C0403g	40.3	0	0.02	0.01	9.96	0.13	0.41	48.51	0.03	0
Y32C0711g	40.42	0.05	0.02	0	9.85	0.13	0.39	48.42	0.02	0
Y32C0712g	40.34	0	0.03	0.05	9.55	0.14	0.33	48.64	0.05	0
Y32C0917g	40.72	0.01	0.01	0	9.81	0.08	0.35	48.33	0.02	0.01
Y32C1213g	40.06	0.01	0	0.02	9.55	0.16	0.39	48.74	0.04	0.03
Y32C2010g	40.45	0.03	0	0.08	9.23	0.19	0.34	48.51	0.11	0.01
Y32C2011g	40.07	0.01	0.01	0.01	9.95	0.19	0.42	47.92	0.09	0.06
Y32C2019g	40	0.02	0.04	0.08	9.4	0.15	0.35	48.24	0.09	0

Orthopyroxene

sample 32-22	**SiO2**	**TiO2**	**Al2O3**	**Cr2O3**	**Fe2O3**	**FeO**	**MnO**	**NiO**	**MgO**	**CaO**	**Na2O**
Y07C0206g	55.18	0.25	2.02	0.44	0	6.66	0.18	0.08	32.41	1.05	0.04
Y07C0501g	56.05	0.24	1.76	0.39	0.02	6.58	0.15	0.06	32.49	1.09	0.01
Y07C0503g	55.71	0.18	1.81	0.41	0	6.53	0.13	0.09	32.91	0.69	0
Y07C1111g	55.16	0.22	2.08	0.48	0	6.91	0.12	0.06	32.53	0.8	0
Y07C1112g	55.25	0.16	2.08	0.54	0.08	6.64	0.16	0.05	32.09	1.05	0.03
Y07C0505t core	54.92	0.21	2.91	0.76	0	6.71	0.15	0	31.27	1.48	0.04
Y07C0705c	54.75	0.24	2.67	0.77	0	6.74	0.16	0.09	31.88	1.3	0.04
Y07C0710t core	54.47	0.21	3.75	0.82	0	6.72	0.18	0.12	31.2	1.34	0
Y07C0720t core	54.05	0.25	3.09	0.85	1	5.8	0.13	0.06	31.5	1.92	0.05
Y07C0508t rim	54.97	0.23	2.52	0.73	0.66	5.72	0.14	0.13	31.26	1.99	0.05
Y07C0704r	55.74	0.21	2.16	0.55	0	6.73	0.18	0.03	32.66	0.79	0.05
Y07C0707t rim	54.9	0.24	2.69	0.69	0.19	6.6	0.1	0.04	31.87	1.26	0.02
Y07C0715t rim	54.73	0.22	3.08	0.72	0	6.27	0.18	0.11	30.71	2.41	0.07
Y07C0716t rim	54.38	0.26	2.48	0.78	0	6.68	0.18	0.15	31.98	1.32	0.03
Y07C0725t rim	55.27	0.18	1.97	0.55	0.15	6.37	0.16	0.1	32.39	1.26	0.01
sample 32-22	**SiO2**	**TiO2**	**Al2O3**	**Cr2O3**	**Fe2O3**	**FeO**	**MnO**	**NiO**	**MgO**	**CaO**	**Na2O**
Y22C0207g	55.01	0.28	2.58	0.71	0	6.32	0.14	0.06	31.76	1.15	0.03
Y22C0208g	55.21	0.26	2.18	0.74	0	6.47	0.14	0	31.91	1.13	0
Y22C0306g	55.47	0.25	2.63	0.78	0	6.46	0.18	0.12	32.1	1.11	0
Y22C0406g	54.93	0.25	2.24	0.7	0	6.77	0.11	0.06	31.9	1.07	0
Y22C0408g	55.27	0.24	2.47	0.72	0	6.76	0.17	0.1	31.94	1.1	0.01
Y22C0409g	55.37	0.16	2.51	0.69	0	6.54	0.12	0.06	32.14	1.01	0.04
Y22C0421g	55.32	0.23	2.44	0.67	0	6.75	0.13	0.06	32.17	0.92	0

Y22C0712g	55.48	0.21	2.3	0.74	0	6.44	0.14	0.07	32.71	1.06	0.03
Y22C0713g	55.5	0.26	2.38	0.68	0	6.54	0.15	0.17	32.82	0.96	0.01
Y22C1107g	54.85	0.2	2.21	0.67	0	6.39	0.18	0.17	32.25	1.17	0.06
Y22C1117g	55.45	0.22	2.04	0.6	0	6.52	0.15	0.04	32.49	1.1	0.05
Y22C1501g	55.49	0.25	2.08	0.56	0	6.44	0.1	0.07	32.36	1.33	0
Y22C1502g	56.09	0.27	2.07	0.48	0	6.67	0.17	0.04	32.11	1.17	0
Y22C1510g	56.05	0.31	1.96	0.38	0	6.33	0.19	0.01	32.63	0.99	0.03
Y22C1513g	56.53	0.21	1.78	0.48	0	6.53	0.15	0.07	32.37	1	0.04
Y22C1605g	55.98	0.22	1.66	0.29	2.23	4.55	0.22	0.14	33.14	0.56	0.04
Y22C1609g	55.29	0.25	2.36	0.76	0	6.86	0.17	0.08	32.15	1.14	0.01
Y22C1612g	55.02	0.21	2.61	0.82	0	6.82	0.21	0.06	31.97	1.17	0.05
Y22C1613g	54.81	0.23	3.17	0.89	0	6.93	0.18	0.07	32.19	0.87	0.03
Y22C1616g	54.84	0.3	2.9	0.82	0	6.68	0.17	0.06	31.51	1.67	0.03
Y22C1617g	55.25	0.18	2.55	0.68	0	6.61	0.18	0.07	32.19	1.17	0.02
Y22C1808g	56.06	0.24	1.92	0.48	0	6.62	0.14	0.07	32.73	0.89	0.07
Y22C1809g	55.99	0.23	1.91	0.51	0	6.35	0.19	0.1	32.09	1.28	0.03
Y22C1810g	54.8	0.23	2.75	0.8	0	6.35	0.09	0.15	32.06	1.39	0.06
Y22C1907g	55.32	0.23	2.28	0.62	0.2	6.44	0.13	0.1	32.01	1.46	0.05
Y22C0111t core	54.24	0.19	3.36	0.87	0	6.52	0.14	0.05	31.36	1.23	0.04
Y22C0812t core	54.66	0.21	3.25	0.85	0	6.33	0.13	0.09	31.69	1.25	0.03
Y22C1101t core	54.94	0.2	3.14	0.78	0	6.24	0.14	0.01	31.44	1.55	0.04
Y22C1112t core	53.67	0.21	4.09	0.75	0	6.29	0.19	0.14	30.99	1.72	0.06
Y22C0107t rim	55.47	0.22	2.26	0.66	0	6.29	0.16	0.03	31.75	1.31	0.02
Y22C0718r	55.61	0.31	2.36	0.6	0	6.56	0.17	0.13	32.41	1.34	0
Y22C0719r	54.9	0.23	2.55	0.76	0	6.53	0.17	0.07	32.23	1.13	0.05
Y22C0809t rim	55.18	0.2	2.52	0.67	0.12	6.46	0.21	0.08	31.85	1.06	0.03
Y22C0813r	55.23	0.18	2.6	0.72	0	6.43	0.13	0.16	32.15	1.41	0.02
Y22C1105t rim	55.48	0.22	1.94	0.46	0	6.25	0.18	0.09	32.58	0.93	0.02
Y22C1108t rim	54.67	0.27	2.81	0.82	0	6.42	0.14	0.07	32.02	1.23	0
sample 32-32	**SiO2**	**TiO2**	**Al2O3**	**Cr2O3**	**Fe2O3**	**FeO**	**MnO**	**NiO**	**MgO**	**CaO**	**Na2O**
Y32C0104g	55.93	0.22	2.06	0.43	0	7.02	0.15	0.11	32.44	1.24	0.02
Y32C0105g	56.08	0.2	1.68	0.43	0	6.7	0.16	0.11	33.35	0.76	0
Y32C0106g	55.73	0.21	2.07	0.5	0.03	6.39	0.15	0.12	32.3	1.11	0
Y32C0214g	54.78	0.23	2.21	0.49	0	6.5	0.09	0.03	33.1	0.73	0.03
Y32C0215g	55.3	0.25	2.31	0.51	0.59	5.79	0.16	0.12	32.67	0.77	0
Y32C0216g	55.78	0.2	2.08	0.51	0	6.55	0.19	0.09	32.61	0.94	0.02
Y32C0304g	53.98	0.17	3.57	0.85	0.38	5.99	0.17	0.11	30.96	2.2	0.08
Y32C0509g	55.64	0.15	2.37	0.64	0	6.43	0.17	0.05	32.44	0.85	0.05
Y32C0510g	55.39	0.19	2.12	0.72	0	6.51	0.18	0.03	32.23	0.83	0.06
Y32C0605g	55.33	0.19	2.56	0.79	0	6.42	0.12	0.11	32.28	1.09	0
Y32C0606g	55.17	0.15	2.7	0.86	0	6.48	0.12	0.11	32.4	1.09	0.02
Y32C0710g	55.87	0.21	2.2	0.61	0.07	6.5	0.19	0.1	32.22	1.38	0.03
Y32C0804g	55.16	0.22	2.39	0.76	0	6.57	0.16	0.15	32.37	1.07	0.01
Y32C0805g	55.78	0.17	1.7	0.54	0.24	6.17	0.15	0.12	33.09	0.98	0.02
Y32C0915g	55.03	0.22	2.19	0.52	0	6.42	0.19	0.07	32.91	1.08	0.03
Y32C0916g	55.56	0.19	2.03	0.54	0.74	5.59	0.13	0.09	32.69	1.22	0.04
Y32C1001g	55.79	0.23	2.27	0.6	0	6.64	0.13	0.03	32.11	1.11	0.01
Y32C1005g	56.18	0.2	1.9	0.49	0	6.47	0.12	0.12	32.63	0.93	0.02
Y32C1006g	55.98	0.22	1.69	0.43	0	6.45	0.14	0.1	32.71	1.05	0.03
Y32C1212g	55.24	0.24	2.13	0.47	0.16	6.41	0.14	0.11	32.61	1.14	0.05
Y32C1403g	55.32	0.24	2.49	0.77	0	6.55	0.12	0.19	32.07	1.29	0
Y32C1406g	55.9	0.17	2.05	0.63	0	6.66	0.14	0.11	32.28	1.49	0.03
Y32C1407g	54.98	0.23	2.82	0.81	0	6.75	0.2	0.16	31.52	1.35	0.03
Y32C1408g	55.53	0.26	2.06	0.61	0	6.36	0.12	0.15	32.26	1.41	0.05
Y32C1606g	55.8	0.23	1.87	0.47	0	6.54	0.14	0.09	32.05	1.19	0.04

Y32C1607g	55.93	0.19	1.97	0.54	0	6.46	0.12	0.07	32.53	1.21	0.02
Y32C1608g	55.43	0.22	2.43	0.66	0	6.54	0.11	0.11	31.86	1.53	0.03
Y32C2001g	55.22	0.27	2.25	0.8	0.12	6.41	0.19	0.14	32.42	1.17	0.04
Y32C2003g	54.91	0.28	2.7	0.77	0	6.46	0.13	0.05	32.58	0.81	0
Y32C2013g	55.4	0.24	1.64	0.54	0.24	6.18	0.17	0.03	33.28	0.91	0.02
Y32C2015g	55.55	0.19	1.96	0.56	0.62	5.86	0.19	0.07	33.3	0.88	0.03
Y32C2101g	55.97	0.24	2.02	0.53	0.38	6.21	0.16	0.04	32.39	1.12	0
Y32C2102g	55.7	0.21	1.94	0.5	0	6.3	0.14	0.13	32.42	1.37	0.03
Y32C2106g	54.94	0.23	2.36	0.67	0	6.43	0.13	0.09	31.77	1.42	0.03
Y32C2107g	55.49	0.26	2.23	0.5	0	6.35	0.16	0.12	32.15	1.48	0.04
Y32C0204t core	55.04	0.28	2.66	0.83	0	6.57	0.12	0.09	31.87	1.51	0.01
Y32C0208t core	54.77	0.22	3.41	0.78	0	6.26	0.15	0.04	31.7	1.26	0.08
Y32C0303c	54.16	0.23	3.61	0.83	0	6.67	0.16	0.14	31.69	1.21	0.04
Y32C0412c	54.63	0.2	4	0.81	0	6.51	0.16	0.03	31.86	1.13	0.01
Y32C0413c	53.63	0.21	5.26	0.82	0	6.65	0.11	0.1	30.89	1.13	0.03
Y32C0904c	54.48	0.18	3.23	0.76	0.42	6.08	0.18	0.01	31.41	1.52	0.06
Y32C0905c	54.38	0.24	3.91	0.94	0	6.55	0.18	0.08	31.45	1.59	0.01
Y32C0906c	54.36	0.19	3.94	0.91	0.01	6.51	0.12	0.08	31.55	0.96	0.05
Y32C1011t core	53.41	0.14	4.9	0.76	0	6.49	0.1	0.1	31.19	1.33	0.02
Y32C1016t core	53.04	0.16	5.47	0.84	0	6.7	0.11	0.1	30.67	1.44	0.07
Y32C0101r	55.35	0.24	2.43	0.6	0.17	6.4	0.16	0.04	32.36	1.1	0.04
Y32C0102r	55.78	0.22	2.69	0.72	0	6.82	0.15	0.07	31.74	1.11	0
Y32C0201t rim	55.53	0.25	2.09	0.59	0	6.48	0.18	0.11	32.21	0.87	0.01
Y32C0205t rim	55.63	0.27	2.51	0.71	0	6.43	0.21	0.03	32.47	0.87	0.03
Y32C0305r	55.6	0.23	1.9	0.52	0.37	6.25	0.19	0.07	32.88	0.92	0.05
Y32C0901r	55.14	0.26	2.54	0.81	0	6.57	0.13	0.07	31.69	1.34	0.04
Y32C0902r	54.31	0.24	3.48	0.94	0	6.74	0.14	0.04	31.8	0.86	0.01
Y32C0903r	54.68	0.28	2.99	0.9	0	6.12	0.16	0.07	31.99	1.64	0.03
Y32C0907r	55.21	0.26	2.18	0.54	0	6.6	0.19	0.08	32.43	1.03	0.01
Y32C0908r	55.53	0.19	2.83	0.69	0	6.56	0.16	0.12	32.04	1.34	0.06
Y32C0909r	55.05	0.29	2.94	0.83	0	6.56	0.13	0.03	31.82	1.37	0.02
Y32C1007t rim	54.12	0.2	4.39	0.77	0	6.14	0.15	0.13	30.39	2.79	0.08
Y32C1012t rim	55.07	0.27	2.43	0.61	0	6.65	0.13	0.17	32.31	1.09	0
Y32C1106r	54.8	0.26	2.62	0.78	0	6.53	0.13	0.11	31.99	1.32	0.04
Y32C1107r	54.88	0.21	3.02	0.81	0	6.72	0.22	0.06	32.05	1.2	0.01
Y32C1108r	54.24	0.32	3.13	0.84	0	6.01	0.14	0.08	30.65	2.94	0.05
Y32C1402r	54.76	0.2	3.14	0.77	0.07	6.49	0.16	0.16	31.8	1.26	0.06
Y32C1903r	54.37	0.24	3.4	0.89	0	6.51	0.16	0.18	31.52	1.28	0.02
Y32C1904r	54.29	0.24	4.11	0.77	0	6.48	0.14	0.14	31.46	1.24	0.02
Y32C1905r	53.57	0.11	4.82	0.73	0	6.61	0.14	0.1	31.37	1.46	0.04
sample 39-36	**SiO2**	**TiO2**	**Al2O3**	**Cr2O3**	**Fe2O3**	**FeO**	**MnO**	**NiO**	**MgO**	**CaO**	**Na2O**
Z36C0114g	55.94	0.07	2.51	0.71	0	5.85	0.14	0.05	32.5	1.41	0.03
Z36C0115g	56.77	0.09	2.35	0.7	0	5.71	0.2	0.06	32.63	1.2	0.02
Z36C0116g	55.17	0.03	3.24	1.01	0	5.72	0.11	0.1	32.38	1.4	0.03
Z36C0117g	55.57	0.01	2.38	0.75	0.01	5.8	0.14	0.07	32.73	1.34	0.03
Z36C0404g	55.68	0	2.23	0.64	0	5.89	0.08	0.16	33.36	0.76	0
Z36C0501g	56.37	0.06	2.1	0.59	0.02	5.82	0.1	0.08	33.15	0.93	0.04
Z36C0502g	56.59	0.01	2.16	0.66	0	5.71	0.13	0.1	33.05	1.13	0.04
Z36C0904g	55.55	0.05	2.44	0.76	0	5.94	0.15	0.06	32.64	1.08	0.04
Z36C0905g	56.31	0.06	2.16	0.73	0	5.77	0.13	0.1	32.86	1.05	0.02
Z36C1101g	56.38	0.04	1.99	0.63	0	5.92	0.12	0.06	33.22	0.97	0.02
Z36C1102g	56.11	0.02	1.59	0.5	0	5.85	0.14	0.11	33.14	0.83	0.02
Z36C0303c	55.47	0.03	2.9	0.97	0	5.93	0.16	0.04	32.38	1.44	0.04
Z36C0605c	54.83	0.03	3.31	0.89	0	5.81	0.11	0.06	32.14	1.2	0.06
Z36C0606c	54.64	0.03	3.49	0.97	0	5.7	0.13	0.07	32.35	1.4	0.03

Z36C0704c	55.25	0.04	3.02	0.87	0	5.98	0.11	0.14	32.93	1.16	0.03
Z36C0906c	56	0.01	1.71	0.55	0	5.89	0.14	0.07	33.61	0.89	0.01
Z36C0302r	55.36	0	2.32	0.67	0	5.72	0.14	0.12	33.13	0.98	0.05
Z36C0607r	55.03	0	2.94	0.87	0.3	5.23	0.12	0.05	32.02	2.02	0.04
Z36C0703r	55.81	0	2.35	0.67	0	5.93	0.15	0.11	32.85	1	0.03
Z36C0907r	56.73	0.07	1.76	0.52	0.07	5.77	0.15	0.03	33.1	0.89	0

Clinopyroxene

sample 32-07	**SiO2**	**TiO2**	**Al2O3**	**Cr2O3**	**Fe2O3**	**FeO**	**MnO**	**NiO**	**MgO**	**CaO**	**Na2O**
Y07C0301g	51.88	0.49	3.38	1.06	0	3.77	0.13	0.06	17.67	19.87	0.42
Y07C0302g	51.77	0.57	3.2	0.9	0	3.61	0.16	0.07	16.88	20.67	0.42
Y07C0305g	51.05	0.71	3.9	1.29	0	3.12	0.04	0	15.9	22.49	0.56
Y07C0306g	51.8	0.64	3.6	1.33	0	3.2	0.07	0.05	16.36	21.39	0.46
Y07C0502g	51.19	0.86	3.78	1.02	0	3.28	0.13	0.1	15.98	21.94	0.45
Y07C0504g	51.21	0.73	3.6	1.09	0	3.13	0.05	0.02	16.05	22.94	0.42
Y07C0702g	53	0.36	2.12	0.79	0	2.7	0.13	0.07	16.81	22.08	0.55
Y07C0703g	50.82	0.72	4.24	1.36	0	3.3	0.09	0	15.77	21.77	0.53
Y07C0801g	50.58	0.92	4.57	1.35	0	3.28	0.07	0.14	15.8	21.88	0.52
Y07C0806g	50.8	0.59	4.18	1.3	0	3.43	0.07	0.08	15.64	21.85	0.52
Y07C1004g	52.18	0.6	3.02	0.93	0	2.96	0.1	0.01	16.58	21.95	0.44
Y07C1104g	50.34	0.56	5.2	1.22	0	3.42	0.03	0.04	15.33	21.68	0.55
Y07C1113g	51.08	0.69	4	1.34	0	3.22	0.07	0	15.73	22.09	0.51
Y07C1114g	51.47	0.65	3.66	1.32	0	3.26	0.01	0.07	16.43	21.35	0.44
Y07C1115g	51.6	0.58	3.23	1.18	0	3.3	0.09	0.02	17.33	20.96	0.43
Y07C1116g	51.31	0.55	3.25	1.12	0	3.32	0.1	0.04	17.11	20.99	0.47
Y07C0803 core	50.02	0.53	6.22	1.05	0	3.72	0.02	0.13	15.54	20.52	0.46
Y07C1001 core	49.76	0.58	6.16	1.09	0	3.48	0.12	0.05	14.74	21.98	0.51
Y07C1006 core	50.13	0.53	6.11	1.09	0	3.37	0.1	0.06	14.89	21.8	0.5
Y07C1102 core	49.84	0.53	6.34	1.22	0	3.51	0.1	0.21	14.66	22	0.5
Y07C1105 core	50.09	0.64	4.85	1.3	0	3.42	0.05	0.01	15.63	21.77	0.48
Y07C0802r	50.13	0.68	5.36	1.24	0	3.2	0.06	0.1	15.1	22.05	0.57
Y07C1002r	52.1	0.52	3.03	0.96	0	3.31	0.17	0.1	16.73	21.52	0.48
Y07C1005r	50.58	0.78	4.82	1.25	0	3.35	0.09	0	15.74	21.73	0.59
Y07C1103r	50.73	0.59	3.84	1.25	0	3.05	0.1	0.11	15.83	21.98	0.52
Y07C1106r	51.31	0.52	3.43	1.06	0	2.98	0.07	0.05	16.09	22.36	0.53
Y07C1110r	50.71	0.61	4.54	1.33	0	3.23	0.1	0.02	15.75	21.56	0.55
sample 32-22	**SiO2**	**TiO2**	**Al2O3**	**Cr2O3**	**Fe2O3**	**FeO**	**MnO**	**NiO**	**MgO**	**CaO**	**Na2O**
Y22C0710g	52.05	0.4	2.47	0.78	0	2.68	0.09	0.08	16.75	22.7	0.44
Y22C0711g	51.77	0.66	3.28	1.25	0	2.85	0.05	0.1	16.03	22.57	0.5
Y22C0802g	51.37	0.63	3.96	1.28	0	3.13	0.07	0.05	15.59	21.86	0.47
Y22C0803g	49.16	1.07	6.22	1.7	0	3.35	0.09	0	14.7	21.9	0.52
Y22C1119g	51.81	0.62	3.2	1.04	0	3.13	0.06	0.04	16.27	21.63	0.47
Y22C1120g	50.55	0.98	4.27	1.31	0	3.07	0.06	0	15.54	22.06	0.4
Y22C1407g	51.89	0.55	3.35	1.01	0	3.29	0.11	0.08	16.52	21.39	0.42
Y22C1408g	51.62	0.65	3.57	1.27	0	2.98	0.08	0	16.16	22.03	0.49
Y22C1709g	51.7	0.61	3.64	1.15	0	3.27	0.12	0.01	16.27	21.5	0.48
Y22C1710g	51.63	0.63	3.69	1.28	0	2.98	0.09	0.06	15.9	21.84	0.43
Y22C1711g	52.65	0.38	2.6	1.09	0	2.88	0.08	0.04	16.44	22.54	0.42
Y22C1906g	51.54	0.65	3.91	1.33	0	3.59	0.14	0.09	17.07	20.3	0.52
Y22C0401t core	49.83	0.49	6	1.14	0	3.45	0.08	0.16	14.65	21.94	0.58
Y22C0412t core	49.81	0.54	6.68	1.05	0	3.33	0.07	0.07	14.9	21.99	0.52
Y22C0413t core	49.54	0.47	7.25	0.96	0	3.53	0.16	0.03	14.25	22.43	0.55
Y22C0424t core	49.7	0.53	7.17	0.97	0	3.66	0.06	0	14.82	21.42	0.55
Y22C1702t core	51.39	0.55	4.75	1.27	0	3.63	0.14	0.11	16.71	20.37	0.41
Y22C1703t core	51.04	0.62	4.65	1.27	0	3.11	0.06	0.03	15.48	21.7	0.5
Y22C1706t core	49.6	0.6	6.95	1.02	0	3.97	0.09	0.04	15.87	20.09	0.49
Y22C1707t core	49.68	0.63	6.28	1.14	0	3.26	0.08	0	14.52	22.24	0.6

Y22C0403t rim	51.3	0.56	3.63	1.3	0	3.14	0.09	0.05	16.38	21.43	0.49
Y22C0410t rim	50.93	0.6	4.87	1.23	0	3.8	0.04	0.08	17.1	19.77	0.46
Y22C0415t rim	51.12	0.56	4.07	1.12	0	3.23	0.03	0	15.27	22.18	0.51
Y22C0422t rim	51.17	0.56	3.87	1.24	0	3	0.11	0.03	15.7	22.22	0.45
Y22C1701t rim	51.05	0.49	4.23	1.41	0	3.04	0.12	0.06	15.81	21.71	0.53
Y22C1704t rim	51.24	0.53	4.82	1.32	0	3.2	0.16	0	15.33	21.98	0.49
Y22C1705t rim	50.37	0.78	5.35	1.16	0	3.16	0.09	0	15.19	21.97	0.53
Y22C1708t rim	51.95	0.59	3.29	1.08	0	3.09	0.08	0.12	16.25	21.83	0.45
sample 32-32	**SiO2**	**TiO2**	**Al2O3**	**Cr2O3**	**Fe2O3**	**FeO**	**MnO**	**NiO**	**MgO**	**CaO**	**Na2O**
Y32C0103g	51.68	0.55	3.46	1.08	0	3.25	0.16	0.05	16.08	21.87	0.49
Y32C0212g	51.63	0.59	3.27	1.04	0	3.18	0.11	0.01	16.52	21.93	0.43
Y32C0302e	51.36	0.58	4.06	1.31	0	2.96	0.1	0.1	15.5	22.26	0.58
Y32C0511g	51.5	0.6	3.62	1.28	0	3.05	0.16	0	15.89	21.93	0.57
Y32C0512g	51.48	0.48	3.23	1.22	0	3.05	0.1	0.09	16.45	21.86	0.48
Y32C0811g	51.46	0.66	3.59	1.3	0	2.95	0.09	0.08	15.94	22.19	0.46
Y32C0812g	51.34	0.67	3.58	1.19	0	3.14	0.13	0.05	16.65	21.43	0.48
Y32C1003g	51.74	0.62	3.36	1.06	0	3.32	0.05	0.08	16.58	21.8	0.42
Y32C1004g	52.01	0.65	3.05	0.89	0	3.23	0.07	0.04	16.32	21.9	0.46
Y32C1104g	51.3	0.6	4.16	1.39	0	3.1	0.11	0.03	16.04	21.77	0.52
Y32C1105g	51.45	0.6	3.67	1.09	0	3.1	0.06	0.08	15.7	22.31	0.51
Y32C1409g	50.94	0.63	3.96	1.33	0	3.18	0.07	0.03	15.77	21.72	0.52
Y32C1410g	51.38	0.56	3.67	1.17	0	2.91	0.1	0	15.89	21.92	0.54
Y32C2012g	50.75	0.6	4.04	1.37	0	2.93	0.06	0.07	15.53	22.27	0.51
Y32C2014g	51.45	0.67	3.24	1.17	0	2.78	0.07	0.05	16.16	22.58	0.51
Y32C2111g	52.01	0.55	3	1.02	0	3.04	0.08	0.05	16.46	22.16	0.52
Y32C0501t core	49.62	0.54	7.08	1.13	0	3.61	0.14	0.11	15.85	20.47	0.54
Y32C2007t core	49.46	0.52	6.74	1.04	0	3.53	0.11	0.17	15.42	21.25	0.55
Y32C2008r	51.06	0.59	4.21	1.38	0	3.47	0.08	0	16.64	20.86	0.47
Y32C2009r	50.48	0.62	5.13	1.29	0	3.28	0.06	0.18	15.84	21.37	0.54
Y32C0504t rim	49.95	0.7	5.97	1.17	0	3.11	0.12	0.04	15.02	21.98	0.52
Y32C0503t rim	50.52	0.65	5.95	1.11	0	3.89	0.09	0	16.68	19.57	0.48
Y32C2004t rim	51.86	0.56	3.57	1.26	0	3.04	0.06	0.09	15.87	22.11	0.46
sample 39-36	**SiO2**	**TiO2**	**Al2O3**	**Cr2O3**	**Fe2O3**	**FeO**	**MnO**	**NiO**	**MgO**	**CaO**	**Na2O**
Z36C0301g	53.5	0.03	2.33	1.11	0	1.86	0.06	0.14	16.51	23.35	0.32
Z36C0401g	52.87	0.01	2.85	1.06	0	2.44	0.12	0.07	17.02	22.25	0.32
Z36C0405g	52.46	0.07	3.15	1.3	0	2.58	0.14	0.05	17.14	21.92	0.29
Z36C0603g	51.17	0.08	4.38	1.57	0	2.08	0.11	0.04	15.74	23	0.37
Z36C0203c	51.71	0.03	3.86	1.45	0	2.26	0.14	0.01	16.56	22.14	0.33
Z36C0204c	51.22	0.05	4.44	1.46	0	2.45	0.03	0.01	16.77	21.72	0.43
Z36C0601c	50.91	0.05	5.76	1.49	0	2.19	0.08	0.08	15.42	22.76	0.42
Z36C0808t core	51.49	0.07	5.41	1.56	0	2.97	0.05	0.05	17.24	20.11	0.33
Z36C0813t core	52.52	0.12	3.36	1.3	0	2.03	0.13	0	16.25	22.84	0.38
Z36C0202r	53	0.05	2.44	0.87	0	2.23	0.09	0.13	17.28	22.38	0.32
Z36C0304r	51.76	0.03	4.47	1.57	0	2.37	0.05	0.03	16.08	22.54	0.31
Z36C0602r	51.33	0.04	4.99	1.46	0	2.39	0.1	0.09	16.04	21.93	0.33
Z36C0804t rim	52.33	0.05	2.95	1.3	0	2.14	0.08	0.1	16.45	22.94	0.36
Z36C0809t rim	52.34	0.1	3.87	1.42	0	2.33	0.05	0.06	16.19	22.38	0.37

Spinel

sample 32-07	**SiO2**	**TiO2**	**Al2O3**	**Cr2O3**	**Fe2O3**	**FeO**	**MnO**	**NiO**	**MgO**	**CaO**	**Na2O**
Y07C0901 core	0.03	0.92	26.19	35.71	6.93	18.2	0.13	0.19	12.16	0	0
Y07C5a01 core	0.06	0.95	25.49	36.04	7.22	17.97	0.12	0.19	12.12	0.02	0.02
Y07C5a03 rim	0.04	0.95	24.67	37.27	6.46	17.8	0.1	0.2	12.02	0.03	0.03
Y07C0903 rim	0.08	0.91	25.13	38.18	6.25	18.37	0.18	0.16	12.02	0.04	0.03
Y07C0902 l	0.03	0.94	25.49	35.63	7.08	18.1	0.17	0.21	11.93	0	0
Y07C5a02 l	0.02	0.97	25.59	36.28	6.81	17.29	0.14	0.19	12.38	0	0.05
sample 32-22	**SiO2**	**TiO2**	**Al2O3**	**Cr2O3**	**Fe2O3**	**FeO**	**MnO**	**NiO**	**MgO**	**CaO**	**Na2O**

Y22C2001 l	0	0.87	26.89	36.34	6.03	17.3	0.14	0.19	12.78	0	0
Y22C2002 l	0.05	0.93	26.05	36.87	6.39	17.59	0.13	0.27	12.51	0	0.03
Y22C2003 l	0.01	0.91	25.49	37.44	6.12	17.51	0.13	0.1	12.4	0	0.03
Y22C2101 l	0	0.94	25.91	37.73	5.8	16.64	0.16	0.2	13.03	0	0.03
Y22C2102 l	0	0.89	25.92	37.67	5.76	16.59	0.11	0.12	13.1	0	0.02
Y22C2103 l	0.03	0.92	25.73	38.08	5.84	16.83	0.16	0.19	12.98	0	0.03
Y22C1409 l	0.04	0.81	25.99	36.67	6.16	18.87	0.19	0.09	11.67	0.01	0
Y22C1410 l	0	0.86	26	36.6	6.15	18.47	0.15	0.17	11.79	0	0.02
Y22C0314 g	0.08	0.66	23.25	37.06	6.77	22.08	0.25	0.1	8.84	0.11	0
Y22C0717 g	0.04	0.89	23.62	36.73	7.14	22.3	0.18	0.22	8.93	0.08	0.03
Y22C1122 g	0.1	0.91	24	34.24	8.06	22.15	0.2	0.2	8.88	0.19	0
Y22C1123 g	0.29	0.46	24.39	38.79	4.29	18.85	0.19	0.16	11	0.02	0.02
Y22C1508 g	0.01	1.18	23.98	37.52	7.04	18.28	0.17	0.22	11.66	0.07	0.07
Y22C1509 g	0	1.06	24.04	37.64	7.21	18.71	0.16	0.21	11.47	0.06	0.04
sample 32-32	**SiO2**	**TiO2**	**Al2O3**	**Cr2O3**	**Fe2O3**	**FeO**	**MnO**	**NiO**	**MgO**	**CaO**	**Na2O**
Y32C0701 l	0.07	1	26.21	36.98	6.43	16.91	0.11	0.09	13.28	0.02	0
Y32C0702 l	0	0.93	25.21	37.81	6.22	17.45	0.06	0.12	12.47	0.02	0.04
Y32C0703 l	0	0.99	26.83	36.78	5.59	16.38	0.07	0.21	13.31	0.01	0.03
Y32C2201 l	0.03	0.96	27.22	35.16	6.04	17.93	0.18	0.17	12.37	0	0
Y32C2202 l	0.06	0.85	27.59	34.98	6.57	17.73	0.11	0.25	12.64	0	0
Y32C2203 l	0.02	0.82	27.31	35.45	6.32	17.29	0.21	0.19	12.64	0.01	0.02
Y32C1801 core	0.03	0.93	27.3	35.39	6.62	17.28	0.14	0.22	12.87	0.02	0.01
Y32C1803 core	0.06	0.88	26.29	35.69	6.73	16.94	0.1	0.21	12.72	0.04	0.03
Y32C1802 rim	0	0.68	27.43	35.71	6.4	17.04	0.11	0.15	12.74	0.02	0.04
Y32C1804 rim	0.01	0.94	23.5	39.17	7.12	17.28	0.16	0.19	12.31	0.07	0.05
Y32C0213 g	0.09	0.83	24.99	35.11	7.1	19.73	0.26	0.21	10.55	0.06	0.01
Y32C0402 g	0.04	1.24	22.52	35.77	8.39	20.32	0.11	0.27	10.17	0.01	0
Y32C2108 g	0.04	0.94	26.14	33.81	8.05	20.1	0.22	0.12	10.68	0.03	0.05
Y32C0301 e	0.44	0.43	32.58	31.49	4.44	14.96	0.17	0.28	14.59	0.08	0.03
sample 39-36	**SiO2**	**TiO2**	**Al2O3**	**Cr2O3**	**Fe2O3**	**FeO**	**MnO**	**NiO**	**MgO**	**CaO**	**Na2O**
Z36C0402 l	0.06	0.05	30.65	38.62	1.12	15.55	0.1	0.1	13.77	0.1	0.03
Z36C0406 l	0	0.04	30.76	39.24	0.2	16.49	0.1	0	13.2	0.05	0.03
Z36C1201 l	0.08	0	31.92	37.23	0.46	16.66	0.14	0.12	13.07	0.03	0.03
Z36C1202 l	0.08	0.08	32.66	36.33	0.15	16.85	0.06	0.14	13.07	0.02	0.03
Z36C1301 l	0.05	0.02	30.87	39.11	0.46	15.77	0.16	0.13	13.69	0	0.02
Z36C1302 l	0	0.04	31.73	39	0.16	15.67	0.08	0.13	14	0	0.01
Z36C1303 l	0.03	0.06	31.96	38.71	0.04	15.58	0.21	0.05	14.08	0	0.01

Plagioclase

sample 32-07	**SiO2**	**TiO2**	**Al2O3**	**Cr2O3**	**Fe2O3**	**FeO**	**MnO**	**NiO**	**MgO**	**CaO**	**Na2O**
Y07C0201o	47.9	0.04	33	0	0.2	0	0	0	0.03	15.68	2.65
Y07C0202o	48.15	0.07	32.88	0.02	0.21	0	0	0	0.02	15.67	2.72
Y07C0203o	48.46	0	32.79	0	0.18	0	0	0	0.03	15.5	2.76
Y07C0204o	48.3	0.04	32.87	0	0.23	0	0.01	0	0.03	15.75	2.64
Y07C0205o	48.23	0.03	32.93	0.02	0.18	0	0.04	0.04	0.04	15.49	2.75
Y07C0804o	48.18	0.02	32.89	0	0.15	0	0	0.02	0.02	15.45	2.61
Y07C0805o	48.68	0	32.61	0	0.19	0	0.02	0.05	0.01	15.47	2.81
Y07C1003o	49.38	0.03	32.73	0.01	0.19	0	0	0.04	0.03	15.03	2.96
Y07C0701a	47.81	0.03	33.24	0.01	0.12	0	0	0	0.03	16.14	2.45
Y07C1101a	48.85	0	32.67	0.02	0.04	0.05	0.01	0	0.04	15.56	2.62
Y07C1109a	47.14	0.05	33.39	0	0.31	0	0	0.03	0.03	15.89	2.42
Y07C0303v	47.85	0.02	33.51	0	0.22	0	0	0	0.04	15.89	2.52
Y07C0304v	46.89	0.05	33.82	0	0.27	0	0	0	0.05	16.48	2.18
sample 32-22	**SiO2**	**TiO2**	**Al2O3**	**Cr2O3**	**Fe2O3**	**FeO**	**MnO**	**NiO**	**MgO**	**CaO**	**Na2O**
Y22C0805o	49.55	0.05	32.08	0.04	0.15	0	0.01	0	0.01	14.98	3.14
Y22C0806o	49.91	0.01	32.49	0.04	0.05	0.11	0	0.05	0.02	14.84	3.04
Y22C0807o	49.7	0.06	31.78	0.01	0.27	0	0	0	0.01	14.56	3.39

Y22C0808o	49.84	0	31.54	0	0.22	0	0	0	0	14.57	3.31
Y22C1005o	48.63	0.05	33.06	0.04	0.22	0	0	0.04	0.01	15.78	2.55
Y22C1006o	50.05	0.05	32.46	0.03	0.16	0	0	0.04	0	14.97	3.08
Y22C1007o	48.89	0.08	32.8	0	0	0.21	0.02	0	0.01	15.69	2.57
Y22C1008o	48.9	0.06	32.69	0.04	0.25	0	0	0.06	0.05	15.39	2.72
Y22C1013o	48.86	0.08	32.59	0	0.19	0	0	0.02	0.02	15.2	2.93
Y22C1014o	48.96	0	32.82	0.05	0.18	0	0.03	0.11	0.03	15.44	2.73
Y22C1404o	49.07	0	32.11	0.04	0.19	0	0.04	0	0.03	14.91	3.15
Y22C1405o	49.02	0.07	32.5	0	0.18	0	0	0	0.06	15.15	3.01
Y22C1406o	48.59	0.04	32.39	0	0.33	0	0.01	0.01	0.02	15.45	2.83
Y22C1503o	47.98	0.06	32.86	0	0.25	0	0.01	0.02	0.02	15.98	2.43
Y22C1504o	48.58	0.02	32.6	0	0.31	0	0	0	0.02	15.44	2.9
Y22C1505o	49.64	0.06	32.14	0	0.25	0	0	0.01	0.04	15.04	3.11
Y22C1506o	49.21	0.05	32.41	0	0.2	0	0	0.01	0.02	15.19	3.03
Y22C1507o	48.48	0.04	32.8	0.04	0.37	0	0	0.05	0.04	15.74	2.58
Y22C1511o	49.72	0.04	32.24	0.01	0.27	0	0	0.01	0.02	14.87	3.07
Y22C1512o	49.4	0.02	32.02	0	0.14	0	0.01	0.02	0.01	14.95	3.1
Y22C0202a	47.84	0.05	32.44	0.01	0.25	0	0	0	0.02	15.17	2.77
Y22C0203a	48.63	0.01	32.09	0	0.14	0	0	0.01	0.03	14.82	2.93
Y22C0204a	48.23	0.06	32.11	0.03	0.32	0	0	0.06	0.03	15.11	2.86
Y22C0205a	48.8	0.03	31.75	0	0.15	0	0.04	0	0.03	14.79	2.98
Y22C0206a	48.27	0	32.33	0	0	0.2	0	0	0.01	15.03	2.61
Y22C1113a	47.96	0.03	32.48	0	0.21	0	0.02	0.08	0.05	15.24	2.72
Y22C1114a	50.09	0.01	31.41	0	0.16	0	0	0	0.04	13.82	3.68
Y22C1115a	48.57	0.01	32.08	0	0.15	0	0.01	0	0.05	14.65	3.21
Y22C1901a	49.15	0.01	32.31	0	0.23	0	0	0.11	0.03	15.27	3.01
Y22C1902a	49.58	0	32.48	0	0.19	0	0.04	0	0.02	15.01	2.97
Y22C1903a	49.84	0	32.01	0	0.22	0	0	0	0.01	14.66	3.3
Y22C0307e	47.28	0	33.67	0	0.24	0	0	0.05	0.01	16.29	2.24
Y22C0308e	47.7	0.01	33.52	0	0.29	0	0	0	0.02	16.18	2.42
Y22C0404e	47.51	0.03	33.43	0	0.28	0	0.03	0.04	0.05	16.16	2.41
Y22C0405e	47.94	0.04	33.18	0.02	0.31	0	0.05	0	0.01	15.84	2.46
Y22C0407e	47.38	0	33.52	0	0.24	0	0.04	0	0.05	16.13	2.33
Y22C0416e	48.27	0.02	33.43	0	0.27	0	0.02	0	0.03	16.06	2.54
Y22C0417e	47.41	0.03	33.67	0	0.19	0	0.02	0.03	0.02	16.68	2.2
Y22C0419e	47.39	0.04	33.32	0	0.21	0	0	0	0.02	16.44	2.2
Y22C1608e	47.51	0.02	33.41	0.07	0.27	0	0.02	0	0.02	16.06	2.44
Y22C1610e	47.54	0.07	33.82	0	0.24	0	0	0.02	0.02	16.35	2.24
Y22C1611e	47.75	0.08	33.02	0	0.17	0	0	0	0.04	15.78	2.54
Y22C0704v	48.96	0.06	32.44	0	0.26	0	0	0	0.02	15.35	2.9
Y22C0705v	49.4	0.03	32.63	0	0.22	0	0	0.05	0.03	15.02	3.14
Y22C0706v	48.26	0	32.88	0	0.28	0	0	0.01	0.04	15.45	2.68
Y22C0720v	48.62	0	32.97	0.03	0.29	0	0	0	0	15.61	2.72
Y22C0721v	49.74	0.05	31.98	0.03	0.18	0	0.01	0.06	0.03	14.76	3.3
Y22C0102 d-opx	50.05	0.01	31.44	0	0.14	0	0	0.06	0.05	14.25	3.34
Y22C0103 d-opx	49.3	0.09	32.09	0	0	0.16	0	0	0.03	14.87	2.94
Y22C0104 d-opx	48.39	0.07	32.51	0.05	0.24	0	0	0.02	0.03	15.27	2.82
Y22C0105 d-opx	49.05	0.06	32.52	0.03	0.19	0	0.02	0.08	0.05	15.15	3.02
sample 32-32	**SiO2**	**TiO2**	**Al2O3**	**Cr2O3**	**Fe2O3**	**FeO**	**MnO**	**NiO**	**MgO**	**CaO**	**Na2O**
Y32C2103o	48.96	0.04	32.16	0	0.22	0	0	0	0.03	15.2	2.89
Y32C2104o	49.34	0.08	31.72	0	0.1	0	0	0	0.02	14.5	3.39
Y32C2105o	48.44	0	32.98	0	0.24	0	0.02	0.05	0.01	15.67	2.67
Y32C2109o	48.2	0.05	32.66	0	0.28	0	0	0	0.03	15.46	2.78
Y32C2110o	48.68	0.03	32.06	0	0.29	0	0	0.02	0.03	15.33	2.84
Y32C2112o	49.14	0.07	32.14	0.02	0.23	0	0	0	0.03	15.11	3.08
Y32C0707o	49.1	0.05	31.92	0	0.18	0	0.02	0	0.02	15.17	3.02
Y32C0709o	48.54	0.04	32.59	0.02	0.25	0	0	0	0.05	15.7	2.7
Y32C1601o	49.09	0	31.95	0.04	0.2	0	0.01	0	0	14.96	3.18
Y32C1602o	49.28	0.02	32.17	0.01	0.2	0	0	0.05	0.04	14.84	3.12

Y32C1603o	48.34	0.02	32.17	0	0.22	0	0.01	0	0.04	15.53	2.72
Y32C1604o	49.54	0.01	31.69	0.02	0.18	0	0.02	0.01	0.03	14.82	3.24
Y32C1605o	48.97	0.03	32.35	0	0.24	0	0.02	0.03	0.03	15.25	2.9
Y32C1609o	49.65	0.05	31.88	0	0.29	0	0	0	0.02	14.6	3.3
Y32C1610o	49.24	0.03	32.04	0.03	0.22	0	0.02	0.01	0.03	15.01	3.09
Y32C1611o	48.03	0	32.64	0.01	0.35	0	0	0.01	0.03	15.75	2.57
Y32C1612o	48.41	0.06	32.6	0	0.36	0	0.01	0	0.03	15.44	2.84
Y32C1613o	48.36	0.01	32.43	0	0.12	0	0	0	0.02	15.61	2.82
Y32C1614o	48.93	0.04	32.16	0.03	0.26	0	0	0	0.01	15.25	3.02
Y32C1808o	47.88	0	32.92	0.16	0.43	0	0	0.06	0.04	15.73	2.73
Y32C1809o	48.3	0.08	32.65	0.02	0.29	0	0	0	0.03	15.8	2.72
Y32C1805o sp	48.34	0.05	32.64	0.11	0.31	0	0	0.03	0.05	15.44	2.77
Y32C1806o sp	47.42	0.06	33.39	0.08	0.33	0	0.07	0.05	0.03	16.56	2.12
Y32C1807o sp	48.17	0.05	32.98	0.09	0.4	0	0	0.01	0.06	15.85	2.63
Y32C0704o sp	48.46	0.04	32.55	0.06	0.22	0	0	0.02	0.03	15.59	2.64
Y32C0705o sp	48.26	0.01	32.49	0	0.14	0	0	0	0.04	15.21	3.06
Y32C0706o sp	48.89	0.02	32.5	0.01	0.25	0	0	0	0.02	15.37	3.01
Y32C0209a	47.58	0.08	33.13	0.06	0.23	0	0	0.01	0.04	16.08	2.46
Y32C0210a	48.6	0.02	32.68	0	0.23	0	0	0	0	15.21	3.04
Y32C0507a	48.81	0.05	32.39	0.03	0.23	0	0.04	0.03	0.03	15.48	2.88
Y32C0508a	48.58	0.02	32.42	0	0.14	0	0	0.03	0.02	15.29	2.91
Y32C0806a	48.51	0.02	32.65	0.01	0.2	0	0.01	0	0.03	15.26	2.81
Y32C0807a	48	0.03	32.64	0.08	0.24	0	0.04	0	0.03	15.48	2.93
Y32C0914a	47.88	0.02	33.06	0.01	0.19	0	0	0.04	0.03	15.8	2.68
Y32C2002a	48.75	0.03	32.18	0	0.24	0	0	0	0.03	14.88	3.08
Y32C2016a	48.26	0.05	32.9	0	0.22	0	0	0.03	0.02	15.42	2.72
Y32C2017a	48.22	0.03	32.96	0.01	0.14	0	0.05	0.08	0.02	15.73	2.63
Y32C2018a	47.7	0.02	33.04	0	0.19	0	0	0	0.03	15.86	2.63
Y32C1404a	48.67	0.07	32.12	0.03	0.14	0	0	0	0.03	15.12	2.88
Y32C1405a	49.14	0	31.98	0.02	0.19	0	0.01	0.07	0.02	14.71	3.07
Y32C0611e	47.49	0	33.58	0	0.33	0	0	0	0	16.09	2.43
Y32C0612e	47.9	0.05	32.84	0.05	0.29	0	0.03	0	0.01	15.78	2.63
Y32C0613e	48.51	0.03	32.13	0	0.22	0	0	0	0.02	14.99	2.97
Y32C0614e	48.7	0.04	32.37	0.02	0.19	0	0	0	0.01	14.99	3.02
Y32C0401 d-opx	50.21	0.04	31.57	0	0.38	0	0.01	0.05	0	14.27	3.44
Y32C0404 d-opx	49.29	0	32.25	0.02	0.59	0	0.01	0	0.04	14.87	3.05
Y32C0405 d-opx	49.25	0.02	32.11	0.04	0.63	0	0.01	0.03	0.04	14.69	3.11
Y32C0910 d-opx	48.58	0.03	32.34	0	0.17	0	0	0	0.03	15.5	2.85
Y32C0911 d-opx	48.96	0.07	32.45	0	0.24	0	0	0.06	0.04	15.3	2.86
Y32C0912 d-opx	48.85	0.06	32.35	0	0.27	0	0	0	0.02	15.01	3.04
Y32C0913 d-opx	48.59	0	32.98	0.03	0.32	0	0.01	0.03	0.01	15.52	2.83
Y32C1102 d-opx	49.18	0.03	32.07	0	0.19	0	0	0	0.01	15.1	3.17
Y32C1103 d-opx	49.41	0.05	32.32	0	0.25	0	0	0.01	0.03	15.22	2.99
Y32C1201 d-opx	48.96	0.04	32.08	0.05	0.3	0	0.02	0	0.01	15.09	3
Y32C1202 d-opx	48.95	0.04	32.11	0	0.17	0	0	0	0.04	15	3
Y32C1203 d-opx	48.41	0.08	32.69	0	0.32	0	0.01	0	0.01	15.7	2.64
Y32C1204 d-opx	48.51	0.01	32.2	0	0.17	0	0.03	0.05	0.01	15.42	2.79
Y32C1208 d-opx	48.4	0.04	32.89	0.03	0.12	0	0.01	0	0.01	15.17	2.89
Y32C1214 d-opx	48.5	0.04	32.77	0.07	0.33	0	0.02	0.01	0.01	15.38	2.83
Y32C1901 d-opx	48.64	0	32.57	0.03	0.3	0	0.01	0.01	0.02	15.37	2.94
Y32C1902 d-opx	49.08	0.05	32.56	0.04	0.26	0	0.02	0.02	0.04	15.1	2.88
sample 39-36	**SiO2**	**TiO2**	**Al2O3**	**Cr2O3**	**Fe2O3**	**FeO**	**MnO**	**NiO**	**MgO**	**CaO**	**Na2O**
Z36C0102o	46.31	0	34.54	0.02	0	0	0.04	0.02	0.03	17.6	1.6
Z36C0113o	46.01	0	34.67	0.04	0.07	0	0	0	0.01	17.39	1.56
Z36C0118o	46.06	0	34.59	0	0.06	0	0.04	0.07	0.03	17.54	1.57

Appendix B

Trace elements analysis

Trace elements contents (ppm) of Romanche FZ minerals

Orthopyroxene

sample 32-07		Ti	Zr	Sr	La	Ce	Nd	Sm	Eu	Gd	Dy	Ho	Er	Yb	Lu
3207_C3opx1	c	920	2.876	0.121	0.000	0.018	0.068	0.075	0.034	0.174	0.318	0.082	0.303	0.454	0.064
3207_C3opx1	c	865	2.718	0.107	0.004	0.013	0.065	0.075	0.030	0.170	0.291	0.085	0.276	0.365	0.060
3207_C3opx1		1048	2.926	0.164	0.005	0.015	0.088	0.040	0.031	0.230	0.374	0.093	0.342	0.463	0.066
3207_C3opx1	r	2603	4.181	0.084	0.000	0.020	0.100	0.079	0.036	0.342	0.689	0.171	0.694	0.956	0.142
3207_C3opx1	g	1439	1.704	0.226	0.000	0.008	0.035	0.027	0.024	0.161	0.259	0.083	0.321	0.443	0.062
3207_C3opx1	r	1557	3.889	0.065	0.002	0.028	0.097	0.120	0.041	0.300	0.482	0.134	0.493	0.632	0.100
3207_C4opx3a		1092	3.182	0.080	0.003	0.015	0.069	0.079	0.031	0.192	0.377	0.098	0.346	0.485	
3207_C4opx3d	r	1664	3.877	0.451	0.017	0.022	0.081	0.095	0.037	0.254	0.491	0.134	0.499	0.654	0.098
3207_C1opx4	c	1000	2.662	0.154	0.001	0.019	0.071	0.070	0.025	0.174	0.320	0.083	0.292	0.396	0.054
3207_C1opx4d		1488	3.117	0.105	0.001	0.015	0.074	0.068	0.037	0.202	0.412	0.111	0.401	0.505	
3207_C1opx4e	r	1139	2.576	0.081	0.000	0.026	0.073	0.063	0.030	0.196	0.388	0.094	0.361	0.441	0.065
3207_C1opx5	r	1602	3.171	0.141	0.006	0.015	0.091	0.072	0.030	0.190	0.426	0.115	0.425	0.587	0.084
3207_C1opx5	c	1102	2.890	0.087	0.002	0.017	0.086	0.082	0.031	0.211	0.364	0.095	0.331	0.446	0.066
sample 32-22		**Ti**	**Zr**	**Sr**	**La**	**Ce**	**Nd**	**Sm**	**Eu**	**Gd**	**Dy**	**Ho**	**Er**	**Yb**	**Lu**
32_22C3opx1	r	1294	3.288	0.317	0.006	0.024	0.047	0.071	0.050	0.198	0.457	0.138	0.490	0.555	0.088
32_22C3opx1	c	1673	3.208	2.409	0.009	0.022	0.058	0.080	0.033	0.239	0.477	0.113	0.509	0.694	0.110
sample 32-32		**Ti**	**Zr**	**Sr**	**La**	**Ce**	**Nd**	**Sm**	**Eu**	**Gd**	**Dy**	**Ho**	**Er**	**Yb**	**Lu**
3232A_C2opx1	c	1186	4.337	0.023	0.005	0.019	0.090	0.074	0.037	0.214	0.434	0.113	0.411	0.633	0.089
3232A_C2opx1	r	1871	3.679	0.171	0.003	0.013	0.072	0.073	0.039	0.257	0.499	0.135	0.521	0.752	0.106
3232A_C4opx2	c	1984	7.053	0.073	0.007	0.040	0.190	0.169	0.061	0.389	0.774	0.196	0.752	1.001	0.135
3232A_C4opx2	r	1939	4.387	0.189	0.009	0.023	0.111	0.097	0.044	0.280	0.573	0.150	0.553	0.836	0.114
3232A_C6opx3	c	2026	5.613	0.056	0.000	0.047	0.179	0.156	0.058	0.378	0.668	0.172	0.607	0.922	0.122
3232A_C6opx3	r	1893	3.414	0.068	0.004	0.020	0.071	0.075	0.034	0.209	0.439	0.123	0.467	0.743	0.101
sample 39-36		**Ti**	**Zr**	**Sr**	**La**	**Ce**	**Nd**	**Sm**	**Eu**	**Gd**	**Dy**	**Ho**	**Er**	**Yb**	**Lu**
3232B_C4opx1	r	1325	2.619	0.301	0.017	0.290	0.057	0.046	0.021	0.168	0.367	0.102	0.405	0.546	0.080
3232B_C4opx1	c	1107	2.767	0.014	0.003	0.032	0.078	0.073	0.029	0.178	0.345	0.090	0.333	0.488	0.067
3232B_C2opx2	c	1356	4.792	0.197	0.001	0.025	0.123	0.120	0.040	0.293	0.494	0.152	0.494	0.666	0.092
3232B_C2opx2	r	1676	2.858	0.180	0.002	0.020	0.057	0.070	0.023	0.208	0.383	0.105	0.407	0.530	0.082
3232B_C3opx3	c	1790	4.688	0.031	0.008	0.040	0.158	0.109	0.046	0.326	0.579	0.160	0.528	0.704	0.101

3232B_C3opx3	r	1897	3.093	0.119	0.000	0.013	0.066	0.080	0.029	0.196	0.428	0.110	0.458	0.697	0.102
sample 32-07		**Ti**	**Zr**	**Sr**	**La**	**Ce**	**Nd**	**Sm**	**Eu**	**Gd**	**Dy**	**Ho**	**Er**	**Yb**	**Lu**
39_36C5opx1	r	134	0.059	0.005	0.001	0.005	0.002	0.007	0.000	0.028	0.093	0.034	0.159	0.248	0.035
39_36C5opx1	c	157	0.122	0.039	0.006	0.012	0.008	0.015	0.002	0.033	0.166	0.045	0.174	0.307	0.044
39_36C2opx	r	168	0.091	0.041	0.012	0.015	0.005	0.005	0.002	0.013	0.106	0.040	0.157	0.273	0.041
39_36C2opx2	c	100	0.074	0.013	0.008	0.008	0.005	0.005	0.002	0.025	0.099	0.033	0.145	0.177	0.026
39_36C3opx2	r	182	0.073	0.068	0.009	0.008	0.004	0.011	0.006	0.037	0.115	0.040	0.205	0.237	0.029
39_36C3opx2	c	108	0.043	0.006	0.003	0.000	0.004	0.001	0.000	0.025	0.084	0.019	0.100	0.155	0.026

Clinopyroxene

sample 32-07		**Ti**	**Zr**	**Sr**	**La**	**Ce**	**Nd**	**Sm**	**Eu**	**Gd**	**Dy**	**Ho**	**Er**	**Yb**	**Lu**
3207_C6cpx1	c	3214	22.659	2.755	0.185	1.692	4.362	2.406	0.807	3.867	4.212	0.900	2.567	2.335	0.278
3207_C2cpx3	c	3238	19.939	2.330	0.186	1.586	4.228	2.116	0.720	3.163	3.485	0.708	2.002	1.832	0.224
3207_C7cpx2	c	3126	19.730	2.819	0.186	1.601	4.135	2.118	0.744	3.185	3.437	0.731	2.094	1.999	0.238
3207_C11cpx5	c	3377	24.712	2.748	0.166	1.639	4.688	2.518	0.811	3.824	4.182	0.858	2.432	2.203	0.252
3207_C10cpx4		3534	27.716	2.337	0.172	1.588	4.871	2.720	0.791	4.206	4.596	0.986	2.667	2.328	0.274
3207_C2cpx3	r	3380	23.287	2.018	0.162	1.597	4.540	2.516	0.795	3.759	3.923	0.813	2.254	1.897	0.232
3207_C6cpx1	r	3337	23.692	2.485	0.174	1.549	4.390	2.514	0.784	4.113	4.319	0.932	2.500	2.152	0.255
3207_C7cpx2	r	3398	22.806	2.546	0.182	1.670	4.365	2.346	0.795	3.494	3.670	0.779	2.134	2.118	0.235
3207_C11cpx5	r	3537	24.300	4.623	0.260	1.483	4.535	2.453	0.781	3.804	4.093	0.830	2.339	2.102	0.235
3207_C6cpx1	g	3104	21.652	12.019	0.156	1.397	4.301	2.469	0.711	3.890	4.209	0.909	2.505	2.074	0.244
sample 32-22		**Ti**	**Zr**	**Sr**	**La**	**Ce**	**Nd**	**Sm**	**Eu**	**Gd**	**Dy**	**Ho**	**Er**	**Yb**	**Lu**
32_22C4cpx1	c	3326	29.690	2.814	0.269	1.830	4.870	2.305	0.932	3.917	5.154	1.044	3.075	2.665	0.365
32_22C2cpx2	c	3282	28.520	5.370	0.360	2.084	4.371	2.032	0.852	3.356	4.579	0.966	2.918	2.709	0.379
32_22C5cpx2	c	3983	39.189	3.390	0.292	1.895	4.823	2.596	0.926	4.904	6.353	1.255	3.709	2.866	0.407
32_22C1cpx3	c	3670	36.973	2.813	0.287	1.880	4.758	2.772	0.980	4.609	6.003	1.216	3.732	3.092	0.398
32_22C1cpx3	r	3815	37.773	3.972	0.286	1.847	5.217	2.723	0.981	4.926	6.260	1.242	3.833	3.087	0.402
32_22C4cpx1	r	3775	34.881	2.310	0.272	1.972	5.181	2.472	0.962	4.753	5.794	1.256	3.448	3.013	0.356
32_22C2cpx2	r	4017	34.505	2.934	0.276	2.043	5.021	2.605	0.991	4.296	5.494	1.088	3.240	2.621	0.337
32_22C5cpx2	r	3780	34.302	3.203	0.249	1.712	4.663	2.630	0.871	4.479	5.852	1.115	3.329	2.571	0.346
sample 32-32		**Ti**	**Zr**	**Sr**	**La**	**Ce**	**Nd**	**Sm**	**Eu**	**Gd**	**Dy**	**Ho**	**Er**	**Yb**	**Lu**
3232A_C5cpx1	c	3265	24.319	3.339	0.240	1.930	4.488	2.358	0.787	3.330	3.860	0.780	2.354	2.231	0.263
3232B_C5cpx1	c	3734	23.924	1.639	0.251	1.957	4.829	2.441	0.810	3.808	4.063	0.886	2.445	2.245	0.247
3232B_C1cpx2	c	3166	22.567	2.525	0.238	1.941	4.530	2.325	0.812	3.381	3.794	0.811	2.413	2.303	0.270
3232A_C2cpx2	c	3818	30.550	1.908	0.226	1.876	5.286	2.914	0.840	4.271	4.564	0.910	2.661	2.280	0.260
3232B_C3CPX3	c	3630	27.095	1.456	0.258	2.107	5.489	2.870	0.909	4.257	4.628	0.935	2.817	2.630	0.292
3232B_C5cpx1	r	3807	24.633	1.915	0.226	1.873	4.902	2.596	0.818	4.110	4.289	0.884	2.568	2.293	0.251
3232B_C1cpx2	r	4092	31.455	3.594	0.234	2.009	5.679	3.081	0.920	4.410	4.605	0.959	2.692	2.341	0.283
3232B_C3CPX3	r	3951	28.997	1.341	0.229	2.042	5.681	2.984	0.874	4.455	4.826	0.988	2.760	2.492	0.286
3232A_C5cpx1	r	3889	30.298	10.484	0.289	2.107	5.699	3.110	0.887	4.291	4.538	0.891	2.628	2.291	0.254
sample 39-36		**Ti**	**Zr**	**Sr**	**La**	**Ce**	**Nd**	**Sm**	**Eu**	**Gd**	**Dy**	**Ho**	**Er**	**Yb**	**Lu**
39_36C6cpx1	r	353	0.425	0.196	0.038	0.098	0.147	0.131	0.050	0.455	1.025	0.242	0.813	0.804	0.099
39_36C6cpx1	c	344	0.513	0.204	0.048	0.130	0.149	0.103	0.031	0.396	0.890	0.233	0.877	0.834	0.094

Plagioclase

sample 32-07	Ti	Zr	Sr	La	Ce	Nd	Sm	Eu	Gd	Dy	Ho	Er	Yb	Lu
3207_C9plag1	259	0.018	182.10	0.166	0.843	0.540	0.093	0.343	0.109	0.049	0.006	0.016	0.015	0.001
3207_C6plag2	224	0.018	112.64	0.150	0.737	0.511	0.089	0.287	0.079	0.044	0.006	0.014	0.005	0.001
3207_C8plag3	190	0.013	181.77	0.165	0.763	0.541	0.093	0.314	0.071	0.025	0.004	0.012	0.006	0.002
3207_C5plag4	211	0.017	203.36	0.140	0.728	0.428	0.096	0.262	0.076	0.023	0.004	0.006	0.006	0.001
3207_C10plag5a	181	0.021	74.435	74.44	0.659	0.463	0.115	0.291	0.064	0.029	0.004	0.017	0.005	-
3207_C10plag5d	193	0.019	85.918	85.92	0.644	0.430	0.066	0.270	0.085	0.041	0.007	0.005	0.005	-
sample 32-22	**Ti**	**Zr**	**Sr**	**La**	**Ce**	**Nd**	**Sm**	**Eu**	**Gd**	**Dy**	**Ho**	**Er**	**Yb**	**Lu**
32_22C5plag1	220	0.037	83.70	0.269	0.907	0.474	0.085	0.318	0.076	0.033	0.002	0.031	0.018	0.001
32_22C6plag2a	264	1.113	146.05	0.367	0.959	0.634	0.144	0.374	0.093	0.098	0.019	0.027	0.007	0.001
32_22C6plag2d	284	9.904	108.88	0.922	1.910	1.095	0.206	0.303	0.237	0.141	0.054	0.108	0.089	-
32_22C7plag3	241	1.797	164.34	0.390	1.064	0.535	0.149	0.389	0.113	0.087	0.014	0.019	0.016	0.003
32_22C7plag3	248	4.524	133.33	0.252	1.287	0.590	0.185	0.339	0.116	0.115	0.029	0.058	0.019	0.001
sample 32-32	**Ti**	**Zr**	**Sr**	**La**	**Ce**	**Nd**	**Sm**	**Eu**	**Gd**	**Dy**	**Ho**	**Er**	**Yb**	**Lu**
3232A_C2plag1	222	0.017	60.59	0.202	0.775	0.561	0.101	0.312	0.093	0.054	0.004	0.007	0.002	-
3232A_C3plag2	207	0.012	94.63	0.191	0.794	0.488	0.078	0.294	0.060	0.034	0.010	0.010	0.005	-
3232A_C6plag3	218	0.016	63.23	0.177	0.753	0.534	0.089	0.268	0.103	0.039	0.010	0.009	0.004	-
3232A_C6plag4	224	0.019	84.53	0.200	0.796	0.619	0.115	0.312	0.089	0.047	0.004	0.031	0.009	-
3232A_C6plag5a	194	0.017	56.30	0.199	0.824	0.571	0.107	0.323	0.110	0.040	0.008	0.010	0.009	-
3232A_C6plag5d	248	0.028	74.14	0.204	0.921	0.591	0.152	0.316	0.127	0.051	0.009	0.020	0.013	-
3232B_C1plag1a	237	0.008	272.42	0.200	0.837	0.583	0.113	0.324	0.105	0.043	0.003	0.021	0.010	-
3232B_C3plag2	200	0.016	60.59	0.242	0.822	0.619	0.084	0.357	0.119	0.044	0.006	0.013	0.002	-
sample 39-36	**Ti**	**Zr**	**Sr**	**La**	**Ce**	**Nd**	**Sm**	**Eu**	**Gd**	**Dy**	**Ho**	**Er**	**Yb**	**Lu**
39_36C1plag1	16	0.088	8.827	0.016	0.036	0.035	0.004	0.050	0.018	0.014	0.000	0.002	0.006	0.000